DISSERTATIONS IN
FORESTRY AND
NATURAL SCIENCES

OSSI LEHTIKANGAS

Approximations and Hybrid Models for Modeling Light Propagation in Biological Tissues

PUBLICATIONS OF THE UNIVERSITY OF EASTERN FINLAND
Dissertations in Forestry and Natural Sciences

UNIVERSITY OF
EASTERN FINLAND

OSSI LEHTIKANGAS

Approximations and hybrid models for modeling light propagation in biological tissues

Publications of the University of Eastern Finland
Dissertations in Forestry and Natural Sciences
No 164

Academic Dissertation
To be presented by permission of the Faculty of Science and Forestry for public examination in the Auditorium SN200 in Snellmania Building at the University of Eastern Finland, Kuopio, on November, 29, 2014,
at 12 o'clock noon.

Department of Applied Physics

Grano Oy
Kuopio, 2014
Editors: Prof. Pertti Pasanen,
Prof. Kai Peiponen, Prof. Matti Vornanen, Prof. Pekka Kilpeläinen

Distribution:
University of Eastern Finland Library / Sales of publications
PO. Box 107, FI-80101 Joensuu, Finland
tel. +358-50-3058396
`http://www.uef.fi/kirjasto`

ISBN: 978-952-61-1627-3 (printed)
ISBN: 978-952-61-1628-0 (PDF)
ISSNL: 1798-5668
ISSN: 1798-5668
ISSN: 1798-5676 (PDF)

Author's address:
University of Eastern Finland
Department of Applied Physics
P.O.Box 1627
FI-70211 KUOPIO
Finland
email: `Ossi.Lehtikangas@uef.fi`

Supervisors:
Docent Tanja Tarvainen, Ph.D.
University of Eastern Finland
Department of Applied Physics
P.O.Box 1627
FI-70211 KUOPIO
FINLAND
email: `Tanja.Tarvainen@uef.fi`

Professor Jari P. Kaipio, Ph.D.
University of Auckland
Department of Mathematics
Private Bag 92019
AUCKLAND 1142
NEW ZEALAND
email: `jari@math.aucland.ac.nz`

Reviewers:
Associate Professor Kui Ren, Ph.D.
University of Texas at Austin
Department of Mathematics
2515 Speedway, Stop C1200
AUSTIN, TX 78712-1202
UNITED STATES
email: `ren@math.utexas.edu`

Assistant Professor Cosimo D'Andrea, Ph.D.
Politecnico di Milano
Dipartimento di Fisica
and
Istituto di Fotonica e Nanotecnologie (IFN-CNR)
Piazza Leonardo da Vinci 32
I-20133 MILAN
ITALY
email: `Cosimo.Dandrea@polimi.it`

Opponent:
Lecturer Oliver Dorn, Ph.D.
University of Manchester
School of Mathematics
Alan Turing Building
Oxford Rd
MANCHESTER M13 9PL
UNITED KINGDOM
email: `Oliver.Dorn@manchester.ac.uk`

ABSTRACT

Diffuse optical tomography is a non-invasive imaging modality in which images of the optical properties of tissues are reconstructed based on boundary measurements of transmitted near-infrared light. The reconstructed tomographic images of the optical properties are linked to physiologically interesting quantities such as blood volume and oxygenation level. Medical applications of diffuse optical tomography include breast cancer detection, neonatal brain imaging and functional brain activation studies.

Reconstruction of the tomographic images requires an accurate and computationally feasible mathematical model for light propagation inside tissues. Light propagation in tissues can be modeled using the radiative transport equation (RTE). Solving the RTE is computationally expensive, and therefore it is often approximated by using the diffusion approximation (DA). However, the DA does not describe light propagation accurately close to the boundary and sources or in low-scattering regions such as the cerebrospinal fluid in the brain.

In this thesis, computational methods for modeling light propagation in tissue-like media are developed utilizing four approaches. In the first approach, a recently introduced corrected diffusion approximation is numerically implemented. In the corrected diffusion approximation, an additive correction term is computed for the DA near the boundary to enhance the accuracy. In the second approach, Fokker-Planck-Eddington (FPE) approximations are utilized as light transport models. The FPE approximations take into account forward-peaked scattering analytically, and therefore are computational less expensive than the RTE. As the third approach, hybrid models which utilize the FPE and the DA as light transport models in different subdomains are developed. Finally, in the fourth approach, a RTE based coupled model is developed which is applicable when the refractive index is not constant inside the tissues. The developed models are numerically approximated using a finite element method.

The proposed models are tested with numerical simulations and are compared against the conventional light transport models, the RTE and the DA. The results show that the corrected DA is more accurate than the DA near the boundary without significant increase in computation time. In addition, the FPE approximations and the hybrid FPE-DA models are computationally less expensive than the RTE and more accurate than the DA especially if the medium contains low-scattering regions. Furthermore, the coupled RTE model can be utilized when the refractive index is not constant within the medium.

Universal Decimal Classification: 519.6, 535.3, 535.4
National Library of Medicine Classification: QT 36, WN 195, WN 206

INSPEC Thesaurus: biomedical optical imaging; optical tomography; light propagation; radiative transfer; light scattering; refractive index; biological tissues; turbidity; finite element analysis; boundary value problems; computational physics; inverse problems; image reconstruction; simulation; modelling; numerical analysis; Fokker-Planck equation; Galerkin method

Yleinen suomalainen asiasanasto: kuvantaminen; tomografia; pehmytkudokset; optiset ominaisuudet; mallintaminen; numeeriset menetelmät; elementtimenetelmä; approksimointi; simulointi; integraaliyhtälöt; osittaisdifferentiaaliyhtälöt

Acknowledgements

This work was carried out in the Department of Applied Physics at the University of Eastern Finland during 2010-2014.

First, and most of all, I would like to thank my main supervisor Docent Tanja Tarvainen, Ph.D., for her excellent guidance and all the help during this work. You always managed to have enough time for me while giving me freedom to learn. I am very grateful to second supervisor Professor Jari Kaipio, Ph.D., for the guidance and ideas, and for giving the opportunity to work in his world famous Inverse Problems group.

I want to thank the official reviewers Associate Professor Kui Ren, Ph.D., and Assistant Professor Cosimo D'Andrea, Ph.D., for carefully reading the thesis, and giving positive feedback.

I am honored and looking forward to have Lecturer Oliver Dorn, Ph.D., as my dissertation opponent.

I am very grateful to Professor Simon Arridge, Ph.D., from the University College London, Centre for Medical Image Computing (CMIC), for having the opportunity to visit CMIC and for his advice during this work. I want to express my gratitude to Professor Arnold D. Kim, Ph.D., from the University of California, Merced, for welcoming me to visit Merced and for fruitful collaboration.

I want to thank all the current and former members of the Inverse Problems and Mathematical Modeling groups. You are excellent (as indicated by the Centre of Excellence status)! Especially, I want to thank all of my former and current roommates. Special thanks go to Aki Pulkkinen, Ph.D., for providing an outstanding Monte Carlo simulation solver. I am grateful to Antti Lipponen, Ph.D., for discussion concerning academic and non-academic life, and for peer support during morning coffee after poorly slept nights with young kids. Moreover, I want to thank Jussi Toivanen, M.Sc., and Pekka Kuoppa, M.Sc., for friendship and lunch company.

I want to thank my mother Anneli for supporting and encouraging me during my whole life. *Kiitos äiti.* I also want to thank all the relatives, especially my parents-in-law Seija and Ilkka, for support and interest towards my work. Finally, my dearest thanks go to my family: my wife Maija and son Eino, for love and support, and for keeping my feet on the ground.

This thesis was financially supported by the Finnish Doctoral Programme in Computational Sciences (FICS), the Magnus Ehrnrooth Foundation, the Academy of Finland, and by the strategic funding of the University of Eastern Finland.

Kuopio, November 3, 2014 *Ossi Lehtikangas*

ABBREVIATIONS

1D	One-dimensional
2D	Two-dimensional
3D	Three-dimensional
cDA	Corrected diffusion approximation
cFP-DA	Coupled Fokker-Planck-diffusion
cFPE-DA	Coupled Fokker-Planck-Eddington-diffusion
cRTE	Coupled RTE
DA	Diffusion approximation
DG	Discontinuous Galerkin
DOM	Discrete ordinate method
DOT	Diffuse optical tomography
FD	Frequency domain
FDM	Finite difference method
FE	Finite element
FEM	Finite element method
FP	Fokker-Planck
FPE	Fokker-Planck-Eddington
FVM	Finite volume method
MC	Monte Carlo
NIR	Near infrared
RTE	Radiative transport equation
SDM	Streamline diffusion modification
TD	Time domain

NOMENCLATURE

$\mathbb{R}^d$	d-dimensional real space
$\mathbb{C}^d$	d-dimensional complex space
$\mathbb{S}^{d-1}$	Angular space
$\mathcal{L}$	Scattering operator
$\mathcal{P}$	Projection operator in the cDA
$\lvert \cdot \rvert$	Absolute value
$\arg(\cdot)$	Phase angle
α	Vector of radiances in the RTE, FP, or FPE discretization
α_{cDA}	Scaled absorption coefficient in the cDA
δ	Streamline diffusion parameter
$\delta(\hat{s}-\hat{s}')$	Delta function
$\delta^{(2)}(\hat{s}-\hat{s}')$	Second order derivative of the delta function
$\Delta_{\hat{s}}$	Laplace operator in spherical coordinates
ϵ	Asymptotic parameter
f	Modulation frequency
$\Gamma(\mathbf{r})$	Exitance
Γ	Interface between sub-domains
$\Gamma_{k,m}$	Interface between the sub-domains Ω_k and Ω_m
γ_d	Dimension-dependent constant ($\gamma_2 = 1/\pi$, $\gamma_3 = 1/4$)
I_s	Inward directed diffuse boundary current
κ	Diffusion coefficient
κ_{cDA}	Diffusion coefficient in the cDA
λ	Eigenvalue in the plane wave solution
μ	Cosine of angle with respect to the inward unit normal
μ_{s}	Scattering coefficient
μ_{a}	Absorption coefficient
μ'_{s}	Reduced scattering coefficient
$\hat{\mathbf{n}}$	Outward unit normal
$\mathbf{r}$	Position vector
$\phi(\mathbf{r},\hat{s})$	Radiance
$\phi_0(\mathbf{r},\hat{s})$	Boundary source
$\Phi(\mathbf{r})$	Fluence
Φ_{cDA}	Interior solution in the cDA
Ω	Spatial domain
Ω_k	Spatial sub-domain k

$\partial\Omega$	Boundary of the spatial domain
$\Psi(\mathbf{r})$	Test function for fluence
Ψ_{cDA}	Boundary layer solution in the cDA
$\psi(\mathbf{r})$	Spatial basis function for the radiance
$\psi(\hat{s})$	Angular basis function for the radiance
Ω_{ϕ}	RTE, FP, or FPE spatial sub-domain
$\partial\Omega_{\phi}$	Boundary of the RTE, FP, or FPE sub-domain
$\partial\Omega_{\phi,\text{out}}$	Outer boundary of the RTE, FP, or FPE sub-domain
Ω_{Φ}	DA spatial sub-domain
$\partial\Omega_{\Phi}$	Boundary of the DA sub-domain
$\partial\Omega_{\Phi,\text{out}}$	Outer boundary of the DA sub-domain
ω	Angular modulation frequency of the input signal
σ_{cDA}	Scaled scattering coefficient in the cDA
$\Theta(\hat{s},\hat{s}')$	Scattering phase function
$\vartheta(\mathbf{r})$	Spatial basis function for the fluence
ξ	Scaled coordinate along $-\hat{\mathbf{n}}$
a	Vector of fluences in the DA discretization
a_0^{FP}	Coefficient in the FP approximation
a_1^{FP}	Coefficient in the FP approximation
a_0^{FPE}	Coefficient in the FPE approximation
a_1^{FPE}	Coefficient in the FPE approximation
a_{cDA}	Coefficient in the Robin boundary condition in the cDA
A	Reflection parameter
b_0^{FPE}	Coefficient in the FPE approximation
b_1^{FPE}	Coefficient in the FPE approximation
b_{cDA}	Coefficient in the Robin boundary condition in the cDA
c	Speed of light in the medium
c_k	Speed of light in the sub-domain Ω_k
$\hat{\mathbf{s}}$	Unit vector in the direction of interest
$\hat{\mathbf{s}}_r$	Direction of reflected radiance
$\hat{\mathbf{s}}_t$	Direction of radiance before transmission
$\hat{\mathbf{s}}_{\perp}$	Perpendicular direction
d	Dimension of the domain
f_{cDA}	Coefficient in the Robin boundary condition in the cDA

g_m	Angular moment of the scattering phase function of order m
g	Scattering anisotropy parameter
H	Reflection mapping
i	Imaginary unit
K	Transmission mapping (Snell's law)
K^{-1}	Inverse transmission mapping (inverse Snell's law)
l^*	Transport mean free path
l_s	Scattering mean free path
n_{in}	Refractive index of the medium
n_{out}	Refractive index of the exterior
n_k	Refractive index of the sub-domain Ω_k
N_s	Number of spatial nodes in the RTE, FP, or FPE discretization
N_a	Number of angular nodes in the RTE, FP, or FPE discretization
$N_{a,k}$	Number of angular nodes in the sub-domain Ω_k
$N_{s,k}$	Number of spatial nodes in the sub-domain Ω_k
N_Φ	Number of spatial nodes in the DA discretization
P_k	Legendre polynomial of order k
R	Fresnel reflection coefficient
T	Fresnel transmission coefficient
$v(\mathbf{r}, \hat{\mathbf{s}})$	Test function for the radiance
$V_n(\mu)$	Eigenvector in the plane wave solution
z	Coordinate along $-\hat{\mathbf{n}}$

LIST OF PUBLICATIONS

This thesis consists of an overview and the following four original articles, which are referred to in the text by their Roman numerals **I–V**.

- **I** O. Lehtikangas, T. Tarvainen, V. Kolehmainen, A. Pulkkinen, S.R. Arridge, J.P. Kaipio, "Finite element approximation of the Fokker–Planck equation for diffuse optical tomography," *Journal of Quantitative Spectroscopy and Radiative Transfer* **111,** 1406–1417 (2010).
- **II** O. Lehtikangas, T. Tarvainen, A.D. Kim, "Modeling boundary measurements of scattered light using the corrected diffusion approximation," *Biomedical Optics Express* **3,** 552–571 (2012).
- **III** O. Lehtikangas, T. Tarvainen, "Hybrid forward-peaked-scattering-diffusion approximations for light propagation in turbid media with low-scattering regions," *Journal of Quantitative Spectroscopy and Radiative Transfer* **116,** 132–144 (2013).
- **IV** O. Lehtikangas, T. Tarvainen, A.D. Kim, S.R. Arridge, "Finite element approximation of the radiative transport equation in a medium with piece-wise constant refractive index," Submitted for publication.

The original articles have been reproduced with permission of the copyright holders.

AUTHOR'S CONTRIBUTION

All publications are result of collaboration with the supervisors and co-authors. The author implemented all the numerical computations using MATLAB® and computed all the results in **I-IV**. The author of this thesis has been the principal author in all of the publications but the guidance and contribution of the supervisors and co-authors has been significant.

In publication **I**, the author implemented the numerical solution of the Fokker-Planck equation using the finite element method by utilizing in part the existing numerical implementations of the radiative transport equation developed by the supervisor. The author computed all the results presented in the article and wrote most of the article with comments from the supervisors and co-authors.

In publication **II**, the author implemented the numerical solution of the corrected diffusion approximation and implemented a boundary condition for the radiative transport equation which takes into account a mismatch in refractive indices at the boundary. The author computed all the results presented in the article and wrote approximately a half of the article with comments from the supervisor and co-author.

In publication **III**, the author derived and implemented the finite element approximation of the hybrid Fokker-Planck-diffusion and hybrid Fokker-Planck-Eddington-diffusion models. The author computed all the results presented in the article and wrote the article with comments from the supervisor.

In publication **IV**, the author formulated the coupled radiative transport equation model with piece-wise constant refractive index. In addition, the author derived and implemented the finite element approximation. The author computed all the results presented in the article and wrote the article with comments from the supervisor and co-authors.

Contents

1 Introduction

Diffuse optical tomography (DOT) is a biomedical imaging modality that is used to reconstruct three dimensional (3D) images of spatially distributed optical parameters. The tomographic images are reconstructed based on boundary measurements of transmitted light. The imaging modality has potential applications for example in detection of breast cancer, neonatal brain imaging and functional brain activation studies [1, 2]. In DOT, low energy visible or near infra-red (NIR) light, 650–950 nm in wavelength, is used for imaging tissues. Hence, the method is non-ionizing in contrast to high energy radiation imaging modalities such as x-ray computed tomography (CT) and positron emission tomography (PET).

In the experimental setup of DOT, highly scattering (turbid) medium is illuminated by a laser beam and the transmitted light is measured on the boundary of the target. Therefore, the imaging modality is non-invasive. The measurements can be done either in time-domain (TD) using pulsed lasers and time resolved detectors measuring the temporal distribution of photon counts (temporal point spread function) or in frequency-domain (FD) using intensity modulated sources and frequency resolved detectors measuring the amplitude and the phase shift. In continuous wave (CW) systems, constant or low frequency modulated light sources are used and only the intensity of light at the boundary is measured [3]. Moreover, the illumination can be either a narrow collimated beam [4, 5] or wide-field illumination with spatial structure [6–9], and the imaging system can be fiber-optics based in contact with the target or non-contact using CCD cameras [10–12]. For more details about the instrumentation and hardware of DOT modalities, see e.g. [3–5, 13–15].

The imaging modality is relatively low-cost compared to other medical imaging modalities such as magnetic resonance imaging (MRI). Furthermore, the instrumentation can be portable and no special environment, such as magnetically shielded room in MRI, is needed. Hence, the modality is suitable for continuous bedside monitoring of infants and adults [2]. Disadvantages of the modality include low spatial resolution and poor depth sensitivity due to strong scattering of NIR light in tissues. Therefore, the accuracy of structural information of DOT images is lower than in CT and MRI [2]. However, temporal resolution and contrast between different tissues types can be quite good and the modality is suitable for functional imaging in addition to MRI [16–18].

Light propagation in tissues is dominated by scattering over absorption. Human tissues consist mostly of water and the relatively low absorption of water at wavelengths which are used in DOT enables imaging of tissues. The most important absorbers are bone tissue, fat tissue, and oxygenated and deoxygenated haemoglobin. Since different physiologically interesting molecules, such as oxygenated and deoxygenated haemoglobin and cytochrome oxidase, absorb light at different wavelengths it is possible to distinguish between them. In particular, haemoglobin provides an indicator of blood volume and oxygenation level whereas the cytochrome indicates tissues oxygenation level [2]. This difference in spectral dependence of absorption is routinely exploited in non-tomographic monitoring techniques such as pulse oximetry and near infrared spectroscopy [2]. In DOT, reconstruction of 3D images of absorption inside tissues can enable functional imaging of different physiological processes. For example, increased blood volume and oxygenation are indicators of increased physiological activity such as a cognitive task [19, 20].

There are several non-invasive optical imaging modalities which are similar to DOT. In fluorescence diffuse optical tomography (fDOT), fluorescent contrast agent is injected into the target, excited with NIR light at an excitation wavelength and the emitted fluorescent light is detected at an emission wavelength at the boundary of the target [12, 21]. Specific fluorescence contrast agents, which target specific molecules, enable molecular imaging. The reconstructed quantity is then the position and the strength of the fluorescent source inside the target assuming that the optical properties are known. In fluorescence lifetime imaging (FLIM), not only the source but also the lifetime of the fluorescent contrast agent is reconstructed. Similar imaging modality to fDOT is bioluminance optical tomography (BDOT) in which images of luciferase activity inside the target are reconstructed based on boundary measurements of spontaneous emission of internal bioluminescence sources. In quantitative photoacoustic tomography (QPAT), one seeks to estimate concentration of absorbers inside tissues by combining the optical contrast and ultrasound propagation [22].

Image reconstruction problems in DOT, fDOT and QPAT are non-linear ill-posed inverse problems. Thus, even small errors in measurements or modeling can cause large errors in the reconstructed images. There are no direct methods for the solution of these problems, and thus they are typically stated as optimization problems such as regularized output least squares or maximum a posterior estimate of the posterior distribution in the Bayesian framework [12, 23, 24]. The iterative solution of these problems requires repetitive solutions of the forward model. Therefore, it is essential to have a computationally feasible forward model that describes light propagation in tissues accurately.

Light propagation in tissues can be modeled using the radiative transport equation (RTE) [1,25–27]. The RTE takes into account absorption and multiple scattering due to inhomogeneities in tissues. The RTE does not have an analytical solution in arbitrary geometry and numerical methods are computationally expensive due to a large number of variables in the RTE. Therefore, the RTE is often approximated by some computationally less demanding model.

The most often used approximation to the RTE in turbid media is the diffusion approximation (DA). In the DA framework, one assumes that light becomes almost isotropic due to strong scattering. In addition, scattering must be much stronger than absorption. Due to these limitations, the DA fails to describe light propagation accurately close to the boundary, sources, and in low-scattering and non-scattering regions [1,28–30]. A typical low-scattering region encountered in optical imaging of the brain is the cerebrospinal fluid surrounding the brain and in the ventricles.

In cases when the employed (computational) light transport model does not take into account all the relevant physical phenomena, significant modeling errors may be caused [23, 31–33]. These modeling errors can exceed the errors caused by measurement devices [32]. Moreover, the errors may be amplified even more (by an order of magnitude) when solving the inverse problem leading to intolerably large errors in the reconstructed tomographic images. Therefore, developing light transport models which take into account the relevant physical effects, and developing reliable and computationally feasible solution methods is crucial for the tomographic image reconstruction.

Aims and contents of the thesis

In this thesis, computational methods for modeling light propagation in tissue-like media are developed. The goal of this thesis is to develop methods which are computationally less expensive to solve than the RTE but still more accurate than the DA. In this thesis, four different approaches were taken.

As the first approach, the corrected diffusion approximation (cDA) is numerically implemented in publication **II**. The cDA was introduced in [34] and it is based an asymptotic analysis of the RTE when scattering is much stronger than absorption. In the cDA, an additive correction term is computed for the DA near the boundary to enhance the accuracy.

In tissues, scattering is typically forward dominated and the direction of photons is most likely to change only a little in scattering events. In the second approach, Fokker-Planck-Eddington (FPE) approximations [35, 36] are utilized as light transport models. The FPE approximations take into account forward dominated scattering analytically when approximating the RTE. As a result, FPE approximations are computational less expensive than the RTE. In this thesis, the Fokker-Planck (FP) equation is used as a light transport model in publication **I**, and the FP and Fokker-Planck-Eddington equations are used in publication **III**.

In the third approach, hybrid models which utilize the FPE and the DA as light transport models in different subdomains are developed in publication **III**. The FPE approximations are used in those parts of the domain in which the DA is not valid, such as in low-scattering regions and near the boundaries, and the DA was used elsewhere. The models are coupled on the interfaces between the subdomains. The developed models are numerically approximated using a finite element method (FEM).

The refractive index is assumed to be constant inside tissues in the RTE. However, the refractive index can change between different tissues types inside the target. As the fourth approach, a RTE based coupled model which is applicable when the refractive index is piecewise constant inside tissues is developed in publication **IV**. In the coupled RTE (cRTE) model, light propagation in each subdomain with constant refractive index is modeled using the RTE and the equations are coupled using boundary conditions describing Fresnel reflection and transmission on the interfaces between the subdomains. The resulting coupled system of RTEs is numerically approximated using the FEM.

This thesis is organized as follows. In Chapter 2, modeling of light propagation in tissues is discussed using the RTE and the DA. Then, the cDA is shortly derived and the forward-peaked scattering approximations including the FP and FPE are presented. In addition, the proposed hybrid forward-peaked scattering–diffusion model is presented. At the end of the chapter, the cRTE model is derived.

In Chapter 3, the numerical implementations of the models are described. First, the numerical approximation methods of the light transport models are reviewed and the numerical implementation of the cDA is described. Then, the FE approximations of the hybrid forward-peaked scattering–diffusion and the cRTE models are derived.

In Chapter 4, the simulation results of the proposed light transport models are presented and discussed. The proposed models are compared to the RTE and DA. In addition, computational load of the models is investigated.

Finally, the summary of results and the conclusion of the thesis are given in Chapter 5.

2 Light transport models

Maxwell's equations describe the propagation of electromagnetic radiation, such as light, in medium. Solving the Maxwell's equations to describe light propagation in tissues is applicable on a microscopic scale but quickly becomes a tedious task on mesoscopic and macroscopic scales. Mesoscopic scale is the regime where multiple scattering starts to dominate and creates a superposition of an infinite number of wave fronts propagating essentially in every direction [37]. As a result, accurate spatial information is lost and wave phenomena become negligible.

Light propagation in random media can be described using the transport theory. This approach can be derived by investigating photon conservation within a small volume element of phase space [38–40]. Within the phase space element, the number of photons is increased through incoming scattering from other directions and through internal radiation sources, and decreased through outgoing scattering and absorption events. For the derivation of the transport theory starting from the Maxwell's equations, see e.g. [37, 41–43], and as a high frequency limit (as wavelength tends to zero) of wave equations using asymptotic analysis and Wigner transforms, see [44,45]. Applications of the transport theory can be found in atmospheric and oceanological optics [46], astrophysics [47], nuclear reactor physics [48] and biomedical optics [26].

The transport theory can be derived using stochastic or deterministic approaches [49]. In light transport modeling, the most often used stochastic method is Monte Carlo (MC) method. In the approach, path of individual photons are traced as the photons are scattered and absorbed within the medium [50,51]. The photon interactions are modeled using appropriate probability distributions, such as the exponential distribution, from which samples can be drawn. Finally, quantities of interest can be computed based on cumulative contribution of all simulated photons. Several versions of MC implementations have been proposed, see e.g. [52–55]. Recently, developments in parallel computing and utilization graphics processing units have lead into a significant increase in applicability of MC methods for modeling light propagation in realistic 3D objects, see [56–60] and the references therein.

In this thesis, deterministic transport methods are considered. The basic equation of the transport theory is radiative transport equation [27, 38, 39]. The RTE is a linear one-speed approximation to the Boltzmann equation, and thus the energy is assumed to be preserved in scattering events and the refractive index is assumed to be constant within the medium. It neglects wave phenomena, such as diffraction and interference, and treats photons as particles which propagate along straight lines between scattering and absorption events.

2.1 RADIATIVE TRANSPORT EQUATION

Let $\Omega \subset \mathbb{R}^d$ be the physical domain, and d = 2,3 be the dimension of the domain. In addition, let $\hat{\mathbf{s}} \in \mathbb{S}^{d-1}$ denote a unit vector in the direction of interest on the unit sphere $\mathbb{S}^{d-1}$. The frequency domain version of the RTE without internal sources is

$$\frac{\mathrm{i}\omega}{c}\phi(\mathbf{r},\hat{\mathbf{s}}) + \hat{\mathbf{s}} \cdot \nabla\phi(\mathbf{r},\hat{\mathbf{s}}) + \mu_{\mathrm{a}}\phi(\mathbf{r},\hat{\mathbf{s}}) = \mu_{\mathrm{s}}\mathcal{L}\phi(\mathbf{r},\hat{\mathbf{s}}), \qquad (2.1)$$

where i is the imaginary unit, $\omega = 2\pi f$ is the angular modulation frequency of the input signal (the units of Hz), f is the modulation frequency (the units of Hz), c is the speed of light in the medium (the units of m/s), $\phi(\mathbf{r},\hat{\mathbf{s}})$ is the radiance (the units of $\mathrm{Wm}^{-2}\mathrm{sr}^{-1}$ in 3D and $\mathrm{Wm}^{-1}\mathrm{rad}^{-1}$ in 2D), and $\mu_{\mathrm{s}} = \mu_{\mathrm{s}}(\mathbf{r})$ and $\mu_{\mathrm{a}} = \mu_{\mathrm{a}}(\mathbf{r})$ are the scattering and absorption coefficients of the medium (the units of m^{-1}), respectively [1, 38, 39]. The inverse of the scattering and absorption coefficients, which are called the scattering mean free path $l_{\mathrm{s}} = \mu_{\mathrm{s}}^{-1}$ and the absorption mean free path $l_{\mathrm{a}} = \mu_{\mathrm{a}}^{-1}$, describes the average length between scattering and absorption events, respectively. These quantities are related to the lifetime of the photons which is the expected value of the exponential distribution.

The scattering operator $\mathcal{L}_{\mathrm{RTE}}$ is defined as

$$\mathcal{L}\phi(\mathbf{r},\hat{\mathbf{s}}) = \mathcal{L}_{\mathrm{RTE}}\phi(\mathbf{r},\hat{\mathbf{s}}) = -\phi(\mathbf{r},\hat{\mathbf{s}}) + \int_{\mathbb{S}^{d-1}} \Theta(\hat{\mathbf{s}}\cdot\hat{\mathbf{s}}')\phi(\mathbf{r},\hat{\mathbf{s}}')\mathrm{d}\hat{\mathbf{s}}', \quad (2.2)$$

where the scattering phase function $\Theta(\hat{\mathbf{s}}\cdot\hat{\mathbf{s}}')$ is the probability density for a photon to scatter from direction $\hat{\mathbf{s}}'$ in direction $\hat{\mathbf{s}}$. In this work, the Henyey-Greenstein scattering function [61] is used

$$\Theta(\hat{\mathbf{s}}\cdot\hat{\mathbf{s}}') = \frac{1}{|\mathbb{S}^{d-1}|}\frac{1-g^2}{(1+g^2-2g\hat{\mathbf{s}}\cdot\hat{\mathbf{s}}')^{d/2}}, \quad (2.3)$$

where $|\mathbb{S}^{d-1}|$ is the surface measure of $\mathbb{S}^{d-1}$ ($|\mathbb{S}^1| = 2\pi$ and $|\mathbb{S}^2| = 4\pi$) and $g \in]-1,1[$ is the anisotropy parameter defining the shape of the probability distribution. The angular moments of the scattering phase function are

$$g_m = \int_{\mathbb{S}^{d-1}} (\hat{\mathbf{s}}\cdot\hat{\mathbf{s}}')^m \Theta(\hat{\mathbf{s}}\cdot\hat{\mathbf{s}}')d\hat{\mathbf{s}}. \quad (2.4)$$

In the case of the Henyey-Greenstein phase function angular moments are $g_m = g^m$. In biological tissues, scattering is forward dominated and the first moment g_1 is close to unity [62]. Thus, the direction of photons is most likely to change only a little in one scattering event. However, although forward dominated scattering is the most important scattering mechanism in biological tissues also large-angle scattering (back-scattering) is possible [63,64].

In this work, a boundary condition which takes into account a boundary source and reflection of light due to a mismatch in refractive indices on the boundary is used

$$\phi(\mathbf{r},\hat{\mathbf{s}}) = \phi_0(\mathbf{r},\hat{\mathbf{s}}) + R\phi(\mathbf{r},H\hat{\mathbf{s}}), \quad \mathbf{r}\in\partial\Omega, \quad \hat{\mathbf{s}}\cdot\hat{\mathbf{n}} < 0, \quad (2.5)$$

where $\phi_0(\mathbf{r},\hat{\mathbf{s}})$ is the source, R is the Fresnel reflection coefficient and $\hat{\mathbf{n}}$ is an outward unit normal. The mapping H gives the change in direction due to reflection (see forward Section 2.6, Eq. (2.39)). The above choice of the boundary condition ensures an unique solution of the RTE [38]. Quantities of interest include the fluence defined as an integral of the radiance over angular directions [1]

$$\Phi(\mathbf{r}) = \int_{\mathbb{S}^{d-1}} \phi(\mathbf{r},\hat{\mathbf{s}})\mathrm{d}\hat{\mathbf{s}}, \quad (2.6)$$

and the exitance which is the measurable quantity at the boundary

$$\Gamma(\mathbf{r}) = \int_{\hat{\mathbf{s}}\cdot\hat{\mathbf{n}}>0} T(\hat{\mathbf{s}}\cdot\hat{\mathbf{n}})\phi(\mathbf{r}, K(\hat{\mathbf{s}}))\mathrm{d}\hat{\mathbf{s}}, \quad \mathbf{r} \in \partial\Omega, \tag{2.7}$$

where $T = 1 - R$ is the Fresnel transmission coefficient and K is a mapping which gives the change in direction due refraction according to the Snell's law (see forward Section 2.6, Eq. (2.42)).

2.2 DIFFUSION APPROXIMATION

To derive the diffusion approximation to the RTE, the radiance, the source term, and the phase function are expanded into series using the spherical harmonics leading to the P_n approximation [1,27]. The P_n approximation is a coupled system of partial differential equations. If the series is truncated at first order, the P_1 approximation is obtained. The DA is obtained as a special case of the P_1 approximation assuming that the light source is isotropic and scattering is much stronger than absorption [1]. The DA can also be derived using an asymptotic analysis when scattering is strong and absorption is weak [34,65,66]. This derivation is reviewed later in Section 2.3 when the corrected diffusion approximation is derived. In the DA framework, the approximation that is used for the radiance is [1,27,67]

$$\phi(\mathbf{r}, \hat{\mathbf{s}}) \approx \frac{1}{|S^{d-1}|}\Phi(\mathbf{r}) - \frac{d}{|S^{d-1}|}(\hat{\mathbf{s}} \cdot \kappa\nabla\Phi(\mathbf{r})), \tag{2.8}$$

where $\kappa = \kappa(\mathbf{r})$ is the diffusion coefficient

$$\kappa = (d(\mu_\mathrm{a} + \mu_\mathrm{s}(1 - g_1)))^{-1}. \tag{2.9}$$

In the frequency domain, the DA without internal sources is of the form [1]

$$-\nabla \cdot \kappa\nabla\Phi(\mathbf{r}) + \mu_\mathrm{a}\Phi(\mathbf{r}) + \frac{\mathrm{i}\omega}{c}\Phi(\mathbf{r}) = 0. \tag{2.10}$$

The DA can not satisfy the boundary condition (2.5) exactly. Generally, the boundary condition is approximated with a Robin-type boundary condition

$$\Phi(\mathbf{r}) + \frac{1}{2\gamma_d}\kappa A \frac{\partial \Phi(\mathbf{r})}{\partial \hat{\mathbf{n}}} = \frac{I_s}{\gamma_d}, \quad \mathbf{r} \in \partial\Omega, \tag{2.11}$$

where γ_d is a dimension dependent constant ($\gamma_2 = 1/\pi$, $\gamma_3 = 1/4$), and I_s is an inward directed diffuse boundary current [68,69]. The parameter A takes into account the mismatch in refractive indices on the boundary and it can be derived from the Fresnel's law [69, 70].

In addition to the DA, other approximations based on the P_n approximation include the simplified spherical harmonics method (SP_n) [71], and the telegraph equation (TE) [1]. The SP_n method can be derived either heuristically from the one-dimensional (1D) version of the P_n approximation or using asymptotic analysis, see [71,72]. The advantage of the SP_n method is that it yields a set of coupled diffusion equations with only Laplacian operators. The P_n method includes also mixed spatial derivatives and therefore it requires more computational resources compared to the SP_n [71]. The drawback of the SP_n is that it converges to the solution of the RTE as $n \to \infty$ only in 1D where the P_n and the SP_n equations are identical. Despite its limitations, the SP_n method have been studied and applied in DOT and BDOT [73–76]. The TE is based on the P_1 approximation and it has been applied in few studies, e.g. [77–79]. The SP_n method and the TE typically model light propagation more accurately in highly absorbing and low-scattering regions than the DA. In the following section, the accuracy of the DA near the boundaries is discussed leading to the corrected diffusion approximation.

2.3 CORRECTED DIFFUSION APPROXIMATION

Within the DA framework, different forms of the boundary conditions [80–85] and source terms [86–88] have been introduced. The derivation of the DA as an asymptotic limit of the RTE when scattering is much stronger than absorption was established in the early

1970's in the context of neutron transport [65,66]. Later, the boundary conditions of the DA were studied using this asymptotic analysis [89].

Recently, an asymptotic analysis of the RTE in a steady state case ($\omega = 0$) leading to the so-called corrected diffusion approximation (cDA) was presented [34]. The cDA consists of solving a diffusion equation and an additive correction term at the boundary. This additive boundary layer solution satisfies 1D RTE in a half space, and it vanishes rapidly away from the boundary (on the order of one scattering mean free path) so that the DA approximates the radiance deep inside the domain.

This approach can overcome some of the limitations of the DA near boundaries but is not applicable in low-scattering or highly absorbing regions. A similar correction term can also be derived for the DA near the sources [90,91]. The analysis can also be applied to the time or frequency domain problems but in that case additional correction terms (initial and initial-boundary layers) are needed to correct for the error made by the DA at short time instances [65]. Next, the cDA is shortly reviewed based on [34] and publication **II**.

2.3.1 Asymptotic analysis of the RTE

Let $0 < \epsilon \ll 1$ be a small dimensionless parameter and let us define scaled absorption and scattering coefficients α_{cDA} and σ_{cDA}

$$\mu_{\text{a}} = \epsilon \alpha_{\text{cDA}}, \quad \mu_{\text{s}} = \epsilon^{-1} \sigma_{\text{cDA}}. \tag{2.12}$$

The parameter ϵ can be chosen, for example, as the ratio of the total mean free path $l = (\mu_s + \mu_a)^{-1}$ to the size of the domain L [92]

$$\epsilon = \frac{(\mu_s + \mu_a)^{-1}}{L}. \tag{2.13}$$

By substituting Eq. (2.12) into the RTE (2.1) and assuming that $\omega = 0$, we obtain

$$\epsilon \hat{\mathbf{s}} \cdot \nabla \phi(\mathbf{r}, \hat{\mathbf{s}}) + \epsilon^2 \alpha_{\text{cDA}} \phi(\mathbf{r}, \hat{\mathbf{s}}) - \sigma_{\text{cDA}} \mathcal{L} \phi(\mathbf{r}, \hat{\mathbf{s}}) = 0. \tag{2.14}$$

We seek an asymptotic solution of the RTE (2.14) in the limit as $\epsilon \to 0^+$ separated into two parts

$$\phi(\mathbf{r}, \hat{\mathbf{s}}) = \Phi_{\mathrm{cDA}}(\mathbf{r}, \hat{\mathbf{s}}) + \Psi_{\mathrm{cDA}}(\mathbf{r}, \hat{\mathbf{s}}), \tag{2.15}$$

where $\Phi_{\mathrm{cDA}}(\mathbf{r}, \hat{\mathbf{s}})$ denotes the interior solution and $\Psi_{\mathrm{cDA}}(\mathbf{r}, \hat{\mathbf{s}})$ the boundary layer solution.

2.3.2 Interior solution

Expanding the interior solution $\Phi_{\mathrm{cDA}}(\mathbf{r}, \hat{\mathbf{s}})$ as a power series in ϵ

$$\Phi_{\mathrm{cDA}}(\mathbf{r}, \hat{\mathbf{s}}) = \Phi_0(\mathbf{r}, \hat{\mathbf{s}}) + \epsilon \Phi_1(\mathbf{r}, \hat{\mathbf{s}}) + O(\epsilon^2), \tag{2.16}$$

it is found that $\Phi_0(\mathbf{r}, \hat{\mathbf{s}}) = \Phi_0(\mathbf{r})$ and $\Phi_1(\mathbf{r}, \hat{\mathbf{s}}) = -d\kappa_{\mathrm{cDA}} \hat{\mathbf{s}} \cdot \nabla \Phi_0(\mathbf{r})$ with $\Phi_0(\mathbf{r})$ satisfying the diffusion equation

$$\nabla \cdot (\kappa_{\mathrm{cDA}} \nabla \Phi_0(\mathbf{r})) - \alpha_{\mathrm{cDA}} \Phi_0(\mathbf{r}) = 0. \tag{2.17}$$

The diffusion coefficient $\kappa_{\mathrm{cDA}} = \kappa_{\mathrm{cDA}}(\mathbf{r})$ is defined as

$$\kappa_{\mathrm{cDA}} = \left(d\sigma_{\mathrm{cDA}}(1 - g_1) \right)^{-1}. \tag{2.18}$$

Note the absence of absorption coefficient in Eq. (2.18) compared to the diffusion coefficient given by the DA, Eq. (2.9).

2.3.3 Boundary layer solution

To compute $\Psi_{\mathrm{cDA}}(\mathbf{r}, \hat{\mathbf{s}})$ at a point $\mathbf{r}_b \in \partial\Omega$ on the boundary, consider a coordinate system (ρ, z) where ρ is a vector parallel to the tangent plane at $\mathbf{r}_b$ and z is the coordinate along $-\hat{\mathbf{n}}$. Then, let $z = \epsilon\zeta$, $\mu = \hat{\mathbf{s}} \cdot (-\hat{\mathbf{n}})$ and $\hat{\mathbf{s}}_\perp = \hat{\mathbf{s}} + \mu\hat{\mathbf{n}}$. The boundary layer solution $\Psi_{\mathrm{cDA}}(\rho, \zeta, \hat{\mathbf{s}}) = \Psi_0(\zeta, \mu) + \epsilon\Psi_1(\zeta, \mu) + O(\epsilon^2)$ satisfies the one-dimensional RTE in a half-space

$$\mu \partial_\zeta \Psi_{\mathrm{cDA}}(\zeta, \mu) - \sigma_{\mathrm{cDA}} \mathcal{L} \Psi_{\mathrm{cDA}}(\zeta, \mu) = 0, \quad \zeta > 0, \tag{2.19}$$

$$\begin{aligned} \Psi_{\mathrm{cDA}}(0, \mu) &= \phi_0(\mathbf{r}_b, \mu) + R(\mu)\Psi(0, -\mu) \\ -[1 - R(\mu)]\Phi_0(\mathbf{r}_b) &+ \epsilon d\kappa_{\mathrm{cDA}} \mu [1 + R(\mu)] \hat{\mathbf{n}} \cdot \nabla \Phi_0(\mathbf{r}_b), \quad 0 < \mu \leq 1. \end{aligned} \tag{2.20}$$

The boundary layer solution $\Psi_{\mathrm{cDA}}(\zeta,\mu)$ must satisfy the asymptotic matching condition

$$\Psi_{\mathrm{cDA}}(\zeta,\mu) \to 0, \quad \zeta \to \infty. \tag{2.21}$$

As a result, a Robin boundary condition for $\Phi_0(\mathbf{r})$ is obtained

$$a_{\mathrm{cDA}}\Phi_0(\mathbf{r}) + b_{\mathrm{cDA}}\kappa_{\mathrm{cDA}}\hat{\mathbf{n}}\cdot\nabla\Phi_0(\mathbf{r}) = f_{\mathrm{cDA}}, \quad \text{on } \partial\Omega, \tag{2.22}$$

with

$$a_{\mathrm{cDA}}(\mathbf{r}_b) = \mathcal{P}[1 - R(\mu)], \tag{2.23}$$
$$b_{\mathrm{cDA}}(\mathbf{r}_b) = \epsilon d\mathcal{P}[\mu(1 + R(\mu))], \tag{2.24}$$
$$f_{\mathrm{cDA}}(\mathbf{r}_b) = \mathcal{P}[\phi_0(\mathbf{r}_b,\mu)], \tag{2.25}$$

where $\mathcal{P}$ is a projection operator derived in [34] and $R(\mu)$ is the Fresnel reflection coefficient. The projection operator $\mathcal{P}$ is given in terms of plane wave solution of the half-space Green's function. Once $\mathcal{P}$ is available, the coefficients of the Robin boundary condition (2.22) can be evaluated given the optical coefficients and the source. Then, the interior solution $\Phi_{\mathrm{cDA}}(\mathbf{r})$ satisfying the diffusion equation (2.17) can be computed. Finally, the additive boundary layer correction $\Psi_{\mathrm{cDA}}(\zeta,\mu)$ can be computed from Eq. (2.19) and the approximation to the radiance on the boundary is obtained as

$$\phi(\mathbf{r}_b,\hat{\mathbf{s}}) \sim \Phi_0(\mathbf{r}_b) - \epsilon d\kappa_{\mathrm{cDA}}\hat{\mathbf{s}}\cdot\nabla\Phi_0(\mathbf{r}_b) + \Psi_{\mathrm{cDA}}(0,\mu). \tag{2.26}$$

2.4 FORWARD-PEAKED-SCATTERING APPROXIMATIONS

The numerical solution of the RTE with forward dominated scattering is challenging due to dense angular discretization needed to describe scattering accurately. Motivated by that, forward-peaked scattering approximations have been proposed to approximate the RTE [35,36,93–100].

2.4.1 Fokker-Planck approximation

The FP equation can be derived either i) using the Taylor expansion of the scattering operator $\mathcal{L}$ at $\hat{\mathbf{s}} \approx \hat{\mathbf{s}}'$ [94], ii) using the asymptotic analysis when the scattering mean free path l_s is small while the transport mean free path $l^* = (\mu_\mathrm{s}(1-g_1))^{-1}$ is necessarily not small [25, 93], or iii) by approximating the eigenvalues of the scattering operator [35, 36]. In the following, the third approach is shortly reviewed.

When scattering is forward dominated, one can approximate the scattering phase function $\Theta(\hat{\mathbf{s}} \cdot \hat{\mathbf{s}}')$ using a linear combination of the delta function and its even (weak) derivatives [36]. The FP approximation of the scattering phase function $\Theta(\hat{\mathbf{s}} \cdot \hat{\mathbf{s}}')$ is

$$\Theta(\hat{\mathbf{s}} \cdot \hat{\mathbf{s}}') \approx \Theta_\mathrm{FP}(\hat{\mathbf{s}} \cdot \hat{\mathbf{s}}') = a_0^\mathrm{FP}\delta(\hat{\mathbf{s}} - \hat{\mathbf{s}}') + a_1^\mathrm{FP}\delta^{(2)}(\hat{\mathbf{s}} - \hat{\mathbf{s}}'), \tag{2.27}$$

where coefficients $a_0^\mathrm{FP} = 1$ and $a_1^\mathrm{FP} = (d-1)^{-1}(1-g_1)$ can be determined from the eigenvalues of the original scattering operator $\mathcal{L}$ (2.2), δ is the delta function, and $\delta^{(2)}$ is the second order derivative of the delta function [36, 95]. The resulting approximate scattering operator $\mathcal{L}_\mathrm{FP}$ is

$$\mathcal{L}\phi(\mathbf{r}, \hat{\mathbf{s}}) \approx \mathcal{L}_\mathrm{FP}\phi(\mathbf{r}, \hat{\mathbf{s}}) = \frac{1}{d-1}(1-g_1)\Delta_{\hat{\mathbf{s}}}\phi(\mathbf{r}, \hat{\mathbf{s}}), \tag{2.28}$$

where $\Delta_{\hat{\mathbf{s}}}$ is the Laplacian operator in spherical coordinates (or Laplace-Beltrami operator) on the unit sphere $\mathbb{S}^{d-1}$. The FP equation is obtained by substituting Eq. (2.28) into RTE (2.1). The existence, uniqueness and positivity of the solution of the FP equation was proved in [101].

In tissues, there is a small but important large-angle scattering component which can not be modeled using only forward dominated scattering. In fact, it has been shown that the FP equation is not an asymptotic limit of the RTE if the phase function includes significant the large-angle scattering part which is the case for the Henyey-Greenstein phase function even with large values of g [93]. If the phase function is sufficiently peaked without the large-angle scattering part, such as the exponential phase function, then the FP is a valid asymptotic limit of the RTE [35].

2.4.2 Fokker-Planck-Eddington approximation

In the presence of both forward dominated and large-angle scattering, (smoothly varying) Legendre polynomials can be used to approximate the scattering phase function in addition to the delta function and its even derivatives [36]. The FPE approximation is

$$\begin{aligned}\Theta(\hat{\mathbf{s}}\cdot\hat{\mathbf{s}}') \approx \Theta_{\mathrm{FPE}}(\hat{\mathbf{s}}\cdot\hat{\mathbf{s}}') = a_0^{\mathrm{FPE}}\delta(\hat{\mathbf{s}}-\hat{\mathbf{s}}') + a_1^{\mathrm{FPE}}\delta^{(2)}(\hat{\mathbf{s}}-\hat{\mathbf{s}}') \\ + \frac{1}{|\mathbb{S}^{d-1}|}(b_0^{\mathrm{FPE}}P_0(\hat{\mathbf{s}}\cdot\hat{\mathbf{s}}') + d b_1^{\mathrm{FPE}}P_1(\hat{\mathbf{s}}\cdot\hat{\mathbf{s}}')),\end{aligned} \tag{2.29}$$

where P_k is the Legendre polynomial of order k and the coefficients a_0^{FPE}, a_1^{FPE}, b_0^{FPE}, and b_1^{FPE} can be determined from the eigenvalues of the original scattering operator [36, 95]. As a result, one obtains in 2D

$$a_0^{\mathrm{FPE}} = \frac{g_2}{5}(9-4g_1), \tag{2.30a}$$

$$a_1^{\mathrm{FPE}} = \frac{g_2}{5}(1-g_1), \tag{2.30b}$$

$$b_0^{\mathrm{FPE}} = 1 - \frac{9}{5}g_2 + \frac{4}{5}g_3, \tag{2.30c}$$

$$b_1^{\mathrm{FPE}} = g_1 - \frac{8}{5}g_2 + \frac{3}{5}g_3 \tag{2.30d}$$

and in 3D

$$a_0^{\mathrm{FPE}} = 2g_2 - g_3, \tag{2.31a}$$

$$a_1^{\mathrm{FPE}} = \frac{g_2 - g_3}{6}, \tag{2.31b}$$

$$b_0^{\mathrm{FPE}} = 1 - 2g_2 + g_3, \tag{2.31c}$$

$$b_1^{\mathrm{FPE}} = g_1 - \frac{5g_2}{3} + \frac{2g_3}{3}. \tag{2.31d}$$

The resulting approximate scattering operator is

$$\begin{aligned}\mathcal{L}\phi(\mathbf{r},\hat{\mathbf{s}}) \approx & \mathcal{L}_{\mathrm{FPE}}\phi(\mathbf{r},\hat{\mathbf{s}}) = -(1-a_0^{\mathrm{FPE}})\phi(\mathbf{r},\hat{\mathbf{s}}) + a_1^{\mathrm{FPE}}\Delta_{\hat{\mathbf{s}}}\phi(\mathbf{r},\hat{\mathbf{s}}) \\ & + \frac{1}{|\mathbb{S}^{d-1}|}\int_{\mathbb{S}^{d-1}}\left(b_0^{\mathrm{FPE}}P_0(\hat{\mathbf{s}}\cdot\hat{\mathbf{s}}') + n b_1^{\mathrm{FPE}}P_1(\hat{\mathbf{s}}\cdot\hat{\mathbf{s}}')\right)\phi(\mathbf{r},\hat{\mathbf{s}}')\mathrm{d}\hat{\mathbf{s}}'.\end{aligned} \tag{2.32}$$

The FPE equation is obtained by substituting Eq. (2.32) into RTE (2.1). It has been shown that the FPE (also called the Boltzmann-Fokker-Planck) equation is a formal asymptotic limit of the RTE [102].

2.4.3 Other approximations based on forward-peaked scattering

Other approximations based on forward-peaked scattering include the delta-Eddington (dE), the generalized Fokker-Planck (gFP), and the generalized Fokker-Planck-Eddington (gFPE) approximations [95]. The dE utilizes the delta function for approximating the forward dominated part and the zeroth order Legendre polynomial for the large-angle part. It was introduced in [103] for calculating radiative fluxes in an absorbing-scattering atmosphere. The dE has been utilized for modeling light propagation in tissues in [36, 104–107]. The gFP utilizes the higher order derivatives of the delta function for approximating the phase function and it was introduced for particle transport with forward dominated scattering in [35, 108, 109]. If the large-angle scattering part using Legendre polynomials is included then the gFPE approximation is obtained. A comparison of the dE, FP, gFP, FPE, gFPE equations for DOT reconstructions was presented in [95].

2.5 HYBRID MODELS

To combine the computational efficiency of the DA and the accuracy of the high order approximations, different hybrid models have been proposed. These hybrid models can overcome some of the limitations of the DA.

The radiosity diffusion model combines the diffusion theory with a ray-tracing algorithm and is applicable in highly scattering medium with non-scattering regions [30, 110]. The hybrid Monte Carlo-diffusion models can be used in complex heterogeneous media but often require iterative mapping between the models in order to take into account back-scattering between the subdomains leading to computationally expensive problems [29, 111–113].

In the hybrid radiative transport-diffusion models [67,114–117], light propagation is modelled using the RTE in subdomains in which the DA is not valid. The DA is used in the rest of the domain and the models are coupled with boundary conditions on the interfaces between the subdomains. The variable order spherical harmonics approximation uses different orders of the P_n approximation in each subdomain depending on the local scattering and absorption coefficients [118,119].

2.5.1 Coupled transport–diffusion model

In this thesis, the FPE approximations are utilized to approximate the RTE part of the coupled RTE-DA model [67,115,120] in publication **III**. In particular, the coupled Fokker-Planck-diffusion (cFP-DA) and coupled Fokker-Planck-Eddington-diffusion (cFPE-DA) models for modeling light propagation in tissues are introduced.

In the coupled model, the domain Ω is divided into two disjoint subsets Ω_ϕ and Ω_Φ. The subdomain Ω_ϕ covers the regions in which the DA is not valid such as the vicinity of the source and the boundaries, and regions with low-scattering. Light propagation in subdomain Ω_ϕ is modelled using either the FP equation, FPE equation, or RTE depending on the chosen scattering operator. The DA is used in the subdomain $\Omega_\Phi = \Omega \setminus \Omega_\phi$ which covers the rest of the domain. The boundaries of the subdomains are denoted by $\partial\Omega_\phi$ and $\partial\Omega_\Phi$. Furthermore, the interface of subdomains is denoted by $\Gamma = \partial\Omega_\phi \cap \partial\Omega_\Phi$. The external boundaries are denoted by $\partial\Omega_{\phi,\mathrm{out}} = \partial\Omega_\phi \setminus \Gamma$ and $\partial\Omega_{\Phi,\mathrm{out}} = \partial\Omega_\Phi \setminus \Gamma$.

The models are coupled through boundary conditions on the interface Γ. The location of the interface Γ should be chosen such that the radiance is almost isotropic in Ω_Φ. Then, the DA is a valid approximation and the coupling between the models is feasible. Usually, this criterion can be fulfilled in diffuse media with distances greater than three transport mean free paths l^* from the boundaries, sources and low-scattering regions. The coupled model can be written in a general form allowing the use of any scattering operator $\mathcal{L}$ and it takes the form

$$
\begin{aligned}
&\frac{\mathrm{i}\omega}{c}\phi(\mathbf{r},\hat{\mathbf{s}}) + \hat{\mathbf{s}}\cdot\nabla\phi(\mathbf{r},\hat{\mathbf{s}}) + \mu_{\mathrm{a}}\phi(\mathbf{r},\hat{\mathbf{s}}) = \mu_{\mathrm{s}}\mathcal{L}\phi(\mathbf{r},\hat{\mathbf{s}}), \quad \mathbf{r}\in\Omega_\phi && \text{(2.33a)}\\
&\phi(\mathbf{r},\hat{\mathbf{s}}) = \phi_0(\mathbf{r},\hat{\mathbf{s}}) + R\phi(\mathbf{r},H\hat{\mathbf{s}}), \quad \mathbf{r}\in\partial\Omega_{\phi,\mathrm{out}}, \quad \hat{\mathbf{s}}\cdot\hat{\mathbf{n}} < 0, && \text{(2.33b)}\\
&\phi(\mathbf{r},\hat{\mathbf{s}}) = \frac{1}{|\mathbb{S}^{d-1}|}\Phi(\mathbf{r}) - \frac{n}{|\mathbb{S}^{d-1}|}\hat{\mathbf{s}}\cdot(\kappa\nabla\Phi(\mathbf{r})), \quad \mathbf{r}\in\Gamma && \text{(2.33c)}\\
&-\nabla\cdot\kappa\nabla\Phi(\mathbf{r}) + \mu_{\mathrm{a}}\Phi(\mathbf{r}) + \frac{\mathrm{i}\omega}{c}\Phi(\mathbf{r}) = 0, \quad \mathbf{r}\in\Omega_\Phi && \text{(2.33d)}\\
&\Phi(\mathbf{r}) + \frac{1}{2\gamma_d}\kappa A\frac{\partial\Phi(\mathbf{r})}{\partial\hat{\mathbf{n}}} = \frac{I_s}{\gamma_d}, \quad \mathbf{r}\in\partial\Omega_{\Phi,\mathrm{out}} && \text{(2.33e)}\\
&\Phi(\mathbf{r}) = \int_{\mathbb{S}^{d-1}}\phi(\mathbf{r},\hat{\mathbf{s}})\mathrm{d}\hat{\mathbf{s}}, \quad \mathbf{r}\in\Gamma, && \text{(2.33f)}
\end{aligned}
$$

where the coupled RTE-DA, FP-DA, and FPE-DA models are obtained by using the corresponding scattering operator Eq. (2.2), (2.28), or (2.32), respectively.

2.6 RADIATIVE TRANSPORT EQUATION WITH PIECEWISE CONSTANT REFRACTIVE INDEX

The refractive index is assumed to be constant in the RTE (2.1) within Ω. However, in practice, the refractive index can change between different tissues types inside the target. A more general version of the RTE which allows spatially varying refractive index was derived in [121], and more recently was investigated in [122–130]. This model allows curved photon paths between absorption and scattering events based on the gradient field of the refractive index. Therefore, the refractive index is assumed to be a smooth continuous function such that the gradient is well defined. However, in biomedical applications the refractive index can have jumps between different tissue types, such as between skull and cerebrospinal fluid in the brain, and a smooth function may not approximate these correctly.

As an alternative, the RTE with piecewise constant refractive index with Fresnel reflection and transmission between the regions has been considered. This approach was developed for a one di-

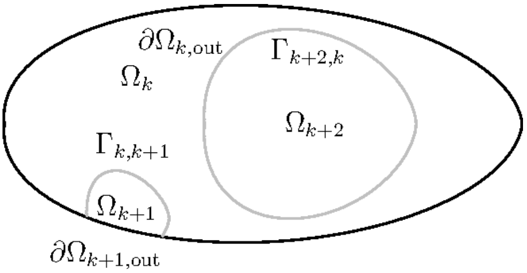

Figure 2.1: A sketch of subdomains having different refractive indices. The interfaces Γ *between the subdomains are marked with gray color and the outer boundaries* $\partial\Omega_{\mathrm{out}}$ *with black color.*

mensional spherically symmetric case in [131, 132] and for multilayered media in [133–136]. Furthermore, one dimensional plane paraller geometry with multilayered media was considered in [137]. This approach was extended to general geometry in publication **IV**.

Let the refractive index n be a piecewise constant within N disjoint subdomains Ω_k, $k = 1, ..., N$. An interface between the subdomains Ω_k and Ω_m with different refractive indices n_k and n_m is denoted by $\Gamma_{k,m} = \partial\Omega_k \cap \partial\Omega_m$ as shown in Figure 2.1. Further, the union of the interfaces of the subdomain Ω_k can be written as $\Gamma_k = \cup_{m=1, m\neq k}^{N} \Gamma_{k,m}$. With these notations, the boundary of the subdomain Ω_k can be divided into the outer boundary and the union of the interfaces $\partial\Omega_k = \partial\Omega_{k,\mathrm{out}} \cup \Gamma_k$. Light propagation in each subdomain Ω_k can be modeled using the RTE and the equations are coupled using the boundary conditions on the interfaces $\Gamma_{k,m}$.

2.6.1 Boundary conditions

The boundary condition in the subdomain Ω_k on the interface $\Gamma_{k,m}$ in an inward direction $\hat{\mathbf{s}}_{r,k}$ takes into account the reflected radiance from a direction $\hat{\mathbf{s}}_{i,k}$ and the transmitted radiance from the subdomain Ω_m from a direction $\hat{\mathbf{s}}_{t,k}$ as shown in Figure 2.2. The boundary condition can be written as

$$\phi_k(\mathbf{r}, \hat{\mathbf{s}}) = R_{k,m}\phi_k(\mathbf{r}, H_k^{-1}\hat{\mathbf{s}}) + T_{m,k}\phi_m(\mathbf{r}, K_{m,k}^{-1}(\hat{\mathbf{s}})), \quad \mathbf{r} \in \Gamma_{k,m}, \quad \hat{\mathbf{s}} \cdot \hat{\mathbf{n}}_k < 0, \tag{2.34}$$

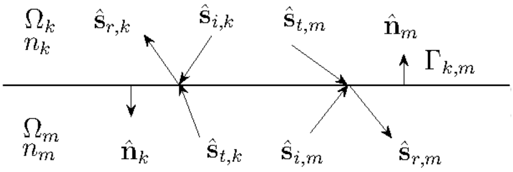

Figure 2.2: Interface $\Gamma_{k,m}$ between the subdomains Ω_k and Ω_m with different refractive indices n_k and n_m. The direction of incoming radiance to the interface is denoted by $\hat{\mathbf{s}}_i$, the direction of reflected radiance by $\hat{\mathbf{s}}_r$ and the direction of radiance which transmits through the interface is denoted by $\hat{\mathbf{s}}_t$. Outward unit normal is denoted by $\hat{\mathbf{n}}$.

where $R_{k,m} = R_{k,m}(\hat{\mathbf{s}}_{i,k}, \hat{\mathbf{n}}_k, n_k, n_m)$ is the Fresnel reflection coefficient between the subdomain Ω_k and Ω_m

$$R_{k,m} = \frac{1}{2}\left(\frac{n_k \cos\theta_k - n_m \cos\theta_m}{n_k \cos\theta_k + n_m \cos\theta_m}\right)^2 + \frac{1}{2}\left(\frac{n_k \cos\theta_m - n_m \cos\theta_k}{n_k \cos\theta_m + n_m \cos\theta_k}\right)^2, \tag{2.35}$$

where

$$\cos\theta_k = \hat{\mathbf{n}}_k \cdot \hat{\mathbf{s}}_{i,k}, \tag{2.36}$$

$$\cos\theta_m = \sqrt{1 - \left(\frac{n_k}{n_m}\right)^2 (1 - (\cos\theta_k)^2)}. \tag{2.37}$$

Further, $T_{m,k}$ is the Fresnel transmission coefficient between the subdomains Ω_m and Ω_k

$$T_{m,k} = 1 - R_{m,k}. \tag{2.38}$$

Figure 2.3 shows the Fresnel reflection coefficient R and the transmission coefficient T as a function of an incident angle.

The mapping H_k^{-1} is the inverse reflection law giving the initial direction of the radiance $\hat{\mathbf{s}}_{i,k}$ for a given direction of the reflected radiance $\hat{\mathbf{s}}_{r,k}$. The reflection law can be written in a vector form as $H_k : \hat{\mathbf{s}}_{i,k} \to \hat{\mathbf{s}}_{r,k}$

$$\hat{\mathbf{s}}_{r,k} = H_k \hat{\mathbf{s}}_{i,k}, \tag{2.39}$$

$$H_k = \left(\mathbf{I} - 2\hat{\mathbf{n}}_k \hat{\mathbf{n}}_k^T\right), \tag{2.40}$$

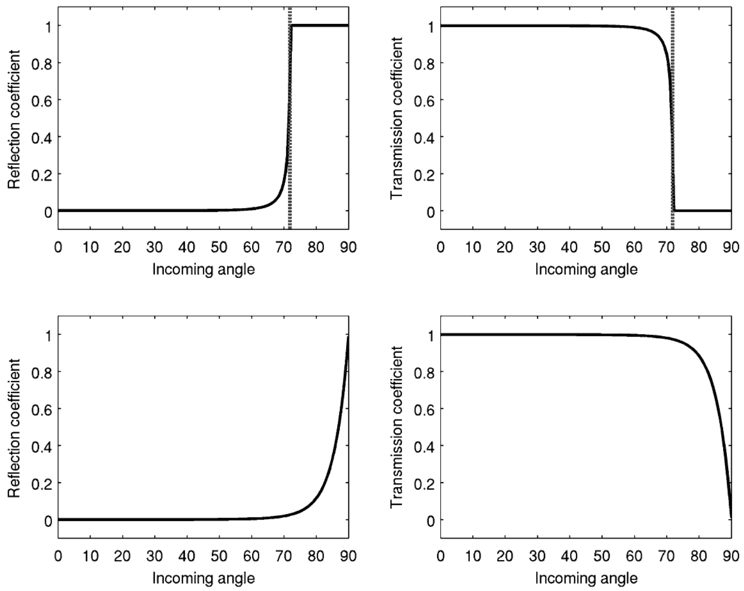

Figure 2.3: Fresnel reflection coefficient R (left column) and transmission coefficient T (right column) between subdomains with refractive indices $n_1 = 1.4$ *and* $n_2 = 1.33$ *(top row) and refractive indices* $n_1 = 1.33$ *and* $n_2 = 1.4$ *(bottom row) as a function of incoming angle. The critical angle* $\theta_{\text{crit}} = \sin^{-1}(n_2/n_1)$ *is marked with a gray vertical line when total internal reflection occurs.*

where $\mathbf{I}$ is an identity matrix. The inverse reflection law H_k^{-1} can be computed

$$\hat{\mathbf{s}}_{i,k} = H_k^{-1}\hat{\mathbf{s}}_{r,k} = H_k\hat{\mathbf{s}}_{r,k}, \tag{2.41}$$

since it can be shown that the matrix H_k is a Householder transformation and thus $H_k^{-1} = H_k$.

The mapping $K_{m,k}^{-1}$ is the inverse Snell's law giving the direction $\hat{\mathbf{s}}_{t,k}$ from which the radiance is transmitted from the subdomain Ω_m into the subdomain Ω_k for a given direction $\hat{\mathbf{s}}_{r,k}$. The Snell's law for the refraction of the radiance between the subdomains Ω_m and Ω_k can be written in a vector form $K_{m,k} : (\hat{\mathbf{s}}_{\text{t,k}}, \hat{\mathbf{n}}_m, n_m, n_k) \to \hat{\mathbf{s}}_{r,k}$

$$\hat{\mathbf{s}}_{r,k} = \frac{n_m}{n_k}\hat{\mathbf{s}}_{t,k} + \left(\cos\varphi_k - \frac{n_m}{n_k}\cos\varphi_m\right)\hat{\mathbf{n}}_m, \tag{2.42}$$

where

$$\cos \varphi_m = \hat{\mathbf{n}}_m \cdot \hat{\mathbf{s}}_{t,k}, \tag{2.43}$$

$$\cos \varphi_k = \sqrt{1 - \left(\frac{n_m}{n_k}\right)^2 (1 - (\cos \varphi_m)^2)}. \tag{2.44}$$

The inverse Snell's law $K_{m,k}^{-1} : (\hat{\mathbf{s}}_{r,k}, \hat{\mathbf{n}}_m, n_m, n_k) \rightarrow \hat{\mathbf{s}}_{t,k}$ can be computed as $K_{m,k} : (-\hat{\mathbf{s}}_{r,k}, -\hat{\mathbf{n}}_m, n_k, n_m) \rightarrow -\hat{\mathbf{s}}_{t,k}$ due to the reciprocity principle of light propagation.

The boundary condition for the outer boundary in the subdomain Ω_k takes into account a boundary source $\phi_{0,k}(\mathbf{r}, \hat{\mathbf{s}})$ and the reflection of the radiance due to a mismatch in refractive indices on the outer boundary

$$\phi_k(\mathbf{r}, \hat{\mathbf{s}}) = \phi_{0,k}(\mathbf{r}, \hat{\mathbf{s}}) + R_{k,\text{out}} \phi_k(\mathbf{r}, H_k \hat{\mathbf{s}}), \quad \mathbf{r} \in \partial\Omega_{k,\text{out}}, \quad \hat{\mathbf{s}} \cdot \hat{\mathbf{n}}_k < 0 \tag{2.45}$$

where $R_{k,\text{out}} = R_{k,\text{out}}(\hat{\mathbf{s}}_{i,k}, \hat{\mathbf{n}}_k, n_k, n_{\text{out}})$ is the reflection coefficient between the subdomain Ω_k and the exterior of the domain Ω with the refractive index n_{out}.

2.6.2 Coupled system of radiative transport equations

The coupled system of RTEs for N subdomains with different refractive indices can be written as

$$\left(\frac{\mathrm{i}\omega}{c_k} + \hat{\mathbf{s}} \cdot \nabla + \mu_\mathrm{a}\right) \phi_k(\mathbf{r}, \hat{\mathbf{s}}) = \mu_\mathrm{s} \mathcal{L} \phi_k(\mathbf{r}, \hat{\mathbf{s}}), \quad \mathbf{r} \in \Omega_k \tag{2.46a}$$

$$\phi_k(\mathbf{r}, \hat{\mathbf{s}}) = \phi_{0,k}(\mathbf{r}, \hat{\mathbf{s}}) + R_{k,\text{out}} \phi_k(\mathbf{r}, H_k \hat{\mathbf{s}}), \quad \mathbf{r} \in \partial\Omega_{k,\text{out}}, \quad \hat{\mathbf{s}} \cdot \hat{\mathbf{n}}_k, < 0, \tag{2.46b}$$

$$\phi_k(\mathbf{r}, \hat{\mathbf{s}}) = R_{k,m} \phi_k(\mathbf{r}, H_k \hat{\mathbf{s}}) + T_{m,k} \phi_m(\mathbf{r}, K_{m,k}^{-1}(\hat{\mathbf{s}})), \quad \mathbf{r} \in \Gamma_{k,m}, \quad \hat{\mathbf{s}} \cdot \hat{\mathbf{n}}_k < 0, \tag{2.46c}$$

$m, k = 1, \ldots, N,$

where $c_k = c_0 / n_k$ is the speed of light in the subdomain Ω_k.

3 Numerical methods for light transport models

3.1 REVIEW OF THE NUMERICAL SOLUTION METHODS OF THE LIGHT TRANSPORT MODELS

Analytical solutions of light transport models are typically available only in simple geometries with constant parameters. Therefore, numerical solution methods are often used. For a recent advances in the analytical solution methods of the RTE, see e.g. [138–143]. Another interesting semi-analytical approach is to use the Neumann series for solving of the RTE [144, 145]. The method is applicable also with heterogeneous parameter distributions. However, it is computationally expensive in highly scattering medium since the terms of the Neumann series correspond consecutive orders of scattering events. Therefore, in highly scattering medium, the series converges slowly. For the analytical solution methods of the DA, see e.g. [146,147].

In the numerical solution of light transport models, different methods have been applied for both the spatial and angular parts of the solution. The DA has been numerically solved using a number of ways, see e.g. [148–150]. The most often used numerical solution method of the DA is the FEM which can be considered as a standard tool. The numerical solution of the RTE has been more challenging. For the spatial part, a finite difference method (FDM) [28,151–154], the FEM [115, 153, 155, 156] and a finite volume method (FVM) [157–159] have been the most commonly applied approaches. The standard continuous Galerkin FEM is not well suitable for spatial discretization of convection dominated or hyberbolic problems such as the RTE causing numerical instabilities. Therefore, different modifications of the FEM have been utilized including the discontinuous Galerkin (DG) [160, 161] and the streamline diffusion modification (SDM) (similar to an upwind Petrov-Galerkin) [155, 162, 163]. For the angular part, the discrete ordinate method (DOM) [28,151,152,156,157,159], the FEM [115,120,153,164,165] and the P_n-method [118,119,166,167] have been the most often used approaches. A list of recently used light transport models and their numerical solution methods is given in Table 3.1.

In this thesis, the FEM is utilized in the numerical solution of the light transport models. More precisely, the SDM-FEM is utilized for spatial discretization of the FPE approximations, the hybrid models and the coupled-RTE model while the standard Galerkin FEM is used for the angular discretization and for the spatial discretization of the DA. The FEM was chosen since it can be regarded as a flexible approach when implementing different boundary conditions in complex geometries with inhomogeneous parameter distributions.

Table 3.1: Light transport models and their numerical solution methods.

Model	Author	Year	Numerical method		Contribution
			spatial	angular	
DA	Arridge [148]	1993	FEM	-	2D DA FEM
DA	Sikora [149]	2006	BEM	-	Multilayered geometry with piecewise constant optical properties
DA	Elisee [168]	2010	BEM-FEM	-	Hybrid BEM-FEM
DA	Elisee [169]	2011	BEM	-	Single-level fast multipole method for BEM
DA	Mohan [150]	2011	DG		3D DG for DA
DA	Sikora [170]	2012	BEM	-	Domain decomposition method for BEM
TE	Soloview [77]	2006	FVM	-	FVM for the TE in fluorescence lifetime imaging
TE+ray tracing	Soloview [78]	2011	FVM+ray tracing	-	approximation of the RTE when the medium consists of highly and weakly scattering regions
TE+ray tracing	Soloview [79]	2012	FVM+ray tracing	-	approximation of the RTE for polarized light when the medium consists of highly scattering and weakly scattering regions
Radiosity diffusion model	Arridge [30]	2000	FEM	-	DA FEM coupled with a ray tracing
RTE	Kanschat [155]	1998	SDM-FEM	FEM	SDM-FEM
RTE	Dorn [151]	1998	FDM	DOM	Transport-back transport method
RTE	Hielscher [28]	1998	FDM	DOM	3D FDM/DOM, comparison the DA
RTE	Richling [162]	2001	SDM-FEM	FEM	Angular FEM in 3D
RTE	Klose [171]	2002	FDM	DOM	Upwind FDM/DOM, comparison with measurements
RTE	Aydin [166]	2002	FEM	P_n-FEM	Even-parity 2D P_n-FEM
RTE	Abdoulaev [156]	2003	FEM	DOM	3D FEM/DOM
RTE	Ren [157]	2004	FVM	DOM	FVM/DOM
RTE	Arridge [172]	2006	FEM	FEM	Shape reconstruction using the RTE
RTE	Aydin [173]	2007	FEM	P_n-FEM	Even-parity 3D P_n-FEM
RTE	Gao [153]	2009	FDM/FEM	FEM/DG	Multigrid method both in space and in angle with source iteration
RTE	Montejo [154]	2010	FDM	DOM	3D FM on block-structured Cartesian grids
RTE	Balima [160]	2010	LS-FEM/DG	DOM	Comparison of LS-FEM and DG
RTE	Balima [174]	2010	LS-FEM	DOM	Separation of radiance into collimated and diffuse components
RTE	Mohan [119]	2011	FEM	P_n-FEM	3D variable order P_n
RTE	Balima [161]	2012	DG	DOM	Integral formulation of the cost function and OT reconstructions
RTE	Asllanaj [159]	2012	FVM	FVM	Cell-vertex FVM on unstructured triangular meshes with exponential closure relation
RTE	Balima [175]	2013	DG	DOM	Sobolev filtering of the cost function gradient

Table 3.1: (Continued) Light transport models and their numerical solution methods.

			Numerical method		
Model	Author	Year	spatial	angular	Contribution
SP_n	Klose [71]	2006	FDM	-	SP_n for light propagation
SP_n	Chu [73]	2009	FEM	-	3D FEM-SP_n
Hybrid RTE-DA	Tarvainen [115]	2005	FEM	FEM	Hybrid RTE-DA model
Coupled RTE-DA	Tarvainen [67]	2006	FEM	FEM	Coupled RTE-DA model
Coupled RTE-DA	Tarvainen [163]	2005	SDM-FEM	FEM	SDM-FEM in Coupled RTE-DA model
Coupled RTE-DA	Gorpas [116]	2010	SDM-FEM	FEM	3D Coupled RTE-DA model
FP	Kim [94]	2003	Plane wave	Chebyshev	FP equation for light propagation, 1D half-space or slab
FP	Kim [176]	2004	Plane wave	FDM	2D FP
FP	Kim [177]	2004	Plane wave	FDM	Homogeneous 2D slab
FP	Gonzalez [36]	2008	FDM	FDM	Comparison of forward-peaked scattering approximations
FP	Kim [178]	2008	Plane wave	FDM	Heterogeneous parameters
FP	Phillips [96]	2009	Plane wave + collocation	P_n	Comparison of forward-peaked scattering approximations
gFP	Gonzalez [36]	2008	FDM	FDM	Comparison of forward-peaked scattering approximations
FPE	Gonzalez [36]	2008	FDM	FDM/DOM	Introduced FPE approximation
FPE	Phillips [96]	2009	Plane wave + collocation	P_n	Comparison of forward-peaked scattering approximations
gFPE	Gonzalez [36]	2008	FDM	FDM/DOM	Introduced gFPE approximation
gFPE	Phillips [96]	2009	Plane wave + collocation	P_n	Comparison of forward-peaked scattering approximations
gFPE	Gonzalez [179]	2012	Pseudo-spectral method + FDM	DOM+FDM	Combining DOT with spectroscopy

3.2 NUMERICAL IMPLEMENTATION OF THE CORRECTED DIFFUSION APPROXIMATION

In this section, the numerical implementation of the cDA is described following publication **II** and [34]. The implementation consists of computing the Robin boundary condition coefficients for the DA given by Eqs. (2.23) - (2.25) and the solution of 1D RTE in a half-space (2.19).

Plane wave solutions of 1D RTE in a half space

Since the boundary condition (2.5) is symmetric with respect to $\hat{\mathbf{n}}$ and the scattering phase function (2.3) is rotationally invariant, the boundary value problem (2.19) is rewritten as

$$\begin{aligned}
&\mu\partial_\zeta \Psi_{\mathrm{cDA}}(\zeta,\mu) + \bar{\sigma}_{\mathrm{cDA}}\Psi_{\mathrm{cDA}}(\zeta,\mu) - \\
&\bar{\sigma}_{\mathrm{cDA}}\int_{-1}^{1} h(\mu,\mu')\Psi_{\mathrm{cDA}}(\zeta,\mu')\frac{\mathrm{d}\mu'}{(1-\mu'^2)^{1/2}} = 0, \quad \zeta > 0, \qquad (3.1\mathrm{a})\\
&\Psi_{\mathrm{cDA}}(0,\mu) = \psi(\mu) + R(\mu)\Psi_{\mathrm{cDA}}(0,-\mu), \quad 0 < \mu \le 1, \qquad (3.1\mathrm{b})
\end{aligned}$$

where $\bar{\sigma}_{\mathrm{cDA}}$ is a constant scaled scattering coefficient near $\mathbf{r}_b$ (e.g. the mean of σ_{cDA} near $\mathbf{r}_b$). The redistribution function h is defined as

$$\begin{aligned}
h(\mu,\mu') =& \frac{1}{2\pi}\frac{1-g^2}{1+g^2-2g(\mu\mu'-(1-\mu^2)^{1/2}(1-\mu'^2)^{1/2})}\\
&+\frac{1}{2\pi}\frac{1-g^2}{1+g^2-2g(\mu\mu'+(1-\mu^2)^{1/2}(1-\mu'^2)^{1/2})}. \qquad (3.2)
\end{aligned}$$

To solve the boundary value problem (3.1), plane wave solutions of the form $\Psi_{\mathrm{cDA}}(\zeta,\mu) = e^{\lambda\zeta}V(\mu)$ are employed. Substituting this ansatz into Eq. (3.1a), an eigenvalue problem is obtained

$$\lambda\mu V + \bar{\sigma}_{\mathrm{cDA}}V - \bar{\sigma}_{\mathrm{cDA}}\int_{-1}^{1} h(\mu,\mu')V(\mu')\frac{\mathrm{d}\mu'}{(1-\mu'^2)^{1/2}} = 0. \qquad (3.3)$$

For the properties of such plane wave solutions, see [94,176].

To calculate the plane wave solutions numerically, the DOM is used. In particular, the Gauss-Chebyshev quadrature rule is utilized

$$\int_{-1}^{1} f(\mu)\frac{\mathrm{d}\mu}{(1-\mu^2)^{1/2}} \approx \frac{\pi}{N}\sum_{j=1}^{N} f(\mu_j), \tag{3.4}$$

with

$$\mu_j = \cos\left(\pi\frac{2(N-1-j)-1}{2(N-1)+2}\right), \quad j = 1, \cdots, N, \tag{3.5}$$

where N is the number of quadrature points. Replacing the integral operation in Eq. (3.1a) with the Gauss-Chebyshev quadrature rule and evaluating that result at μ_i, a discrete eigenvalue problem is obtained

$$\lambda\mu_i V(\mu_i) + (\delta_{\mathrm{cDA}} + \bar{\sigma}_{\mathrm{cDA}})V(\mu_i) - \bar{\sigma}_{\mathrm{cDA}}\frac{\pi}{N}\sum_{j=1}^{N} h(\mu_i, \mu_j)V(\mu_j) = 0,$$
$$i = 1, \cdots, N, \tag{3.6}$$

where δ_{cDA} is a small regularization parameter (e.g. $\delta_{\mathrm{cDA}} = 10^{-8}$) equivalent to adding a small amount of absorption. This ensures that the numerically calculated eigenvalues are real and distinct.

Once Eq. (3.6) is solved numerically, N eigenvalues λ_n and eigenvectors $V_n(\mu_i)$ are obtained. For each pair $[\lambda_n, V_n(\mu_i)]$ satisfying Eq. (3.6), the pair $[-\lambda_n, V_n(-\mu_i)]$ satisfies Eq. (3.6) also. As a result, the eigenvalues are ordered and indexed as

$$\lambda_{-N/2} \leq \lambda_{-N/2+1} \leq \cdots \leq \lambda_{-1} \leq \lambda_1 \leq \cdots \leq \lambda_{N/2-1} \leq \lambda_{N/2}. \tag{3.7}$$

Using this indexing the symmetry of the plane wave solutions corresponds to $\lambda_{-n} = -\lambda_n$ and $V_{-n}(\mu_i) = V_n(-\mu_i)$. The eigenvectors are orthogonal according to

$$\frac{\pi}{N}\sum_{i=1}^{N} \mu_i V_m(\mu_i)V_n(\mu_i) = 0, \quad m \neq n. \tag{3.8}$$

The eigenvectors are normalized as

$$\frac{\pi}{N}\sum_{i=1}^{N} \mu_i V_n(\mu_i)V_n(\mu_i) = \begin{cases} -1 & n > 0, \\ +1 & n < 0. \end{cases} \tag{3.9}$$

Boundary condition coefficients

In Eqs. (2.23) - (2.25), the coefficients a_{cDA}, b_{cDA} and f_{cDA} are defined in terms of a projection operator $\mathcal{P}$. This operator is given as an expansion in terms of plane wave solutions derived in [34]. Let the discrete projection operator p_i for $i = N/2+1, \cdots, N$ be defined as

$$p_i = [V_1(\mu_i) - \sum_{n=1}^{N/2} y_{1n} V_n(\mu_i)]\mu_i \tag{3.10}$$

where y_{mn} satisfies the $N/2 \times N/2$ linear system of equations

$$\sum_{m=1}^{N/2} [V_m(-\mu_i) - R(\mu_i)V_m(\mu_i)]y_{mn} = [V_n(\mu_i) - R(\mu_i)V_n(-\mu_i)],$$
$$i = N/2+1, \cdots, N. \tag{3.11}$$

Then, the boundary condition coefficients can be evaluated as

$$a_{\mathrm{cDA}}(\mathbf{r}_b) = \frac{\pi}{N} \sum_{i=N/2+1}^{N} p_i[1 - R(\mu_i)], \tag{3.12}$$

$$b_{\mathrm{cDA}}(\mathbf{r}_b) = d\epsilon\frac{\pi}{N} \sum_{i=N/2+1}^{N} p_i[\mu_i + \mu_i R(\mu_i)], \tag{3.13}$$

$$f_{\mathrm{cDA}}(\mathbf{r}_b) = \frac{\pi}{N} \sum_{i=N/2+1}^{N} p_i \phi_0(\mathbf{r}_b, \mu_i). \tag{3.14}$$

Boundary layer solution

Once the boundary conditions coefficients are computed, Eq. (2.17) subject to boundary condition Eq. (2.22) may be solved either analytically or numerically. In this work, the FEM is used for numerical approximation of the diffusion equation (2.17). Then, the boundary layer solution $\Psi_{\mathrm{cDA}}(\zeta, \mu)$ satisfying boundary value problem

Eq. (2.19) can be computed as an expansion in plane wave solutions [34]. Let H_{ij} be defined as

$$H_{ij} = \sum_{m=1}^{N/2} V_m(-\mu_i) \left[V_m(-\mu_j) - \sum_{n=1}^{N/2} y_{mn} V_n(\mu_j) \right] \mu_j. \tag{3.15}$$

Then, the solution at the boundary $\Psi_{\text{cDA}}(0, \mu_i)$ for the points corresponding to $-1 \leq \mu \leq 1$ is given by

$$\Psi_{\text{cDA}}(0, \mu_i) = \frac{\pi}{N} \sum_{j=N/2+1}^{N} H_{ij} \big[\phi_0(\mathbf{r}_b, \mu_j) - [1 - R(\mu_j)] \Phi_0(\mathbf{r}_b)$$

$$+ \epsilon d \kappa_{\text{cDA}} \mu_j [1 + R(\mu_j)] \hat{\mathbf{n}} \cdot \nabla \Phi_0(\mathbf{r}_b) \big], \quad i = 1, \cdots, N. \tag{3.16}$$

Summary of the algorithm

To summarize, the procedure for a numerical solution of the cDA is given as

1. For a given optical parameters μ_{a} and μ_{s}, compute the asymptotic parameter ϵ using Eq. (2.13) and scaled optical parameters α_{cDA} and σ_{cDA} using Eq. (2.12).
2. Solve the eigenvalue problem (3.6), at the points $\mathbf{r}_b$.
3. Solve the matrix y using Eq. (3.11). Evaluate the discrete projection operator from the Eq. (3.10) and the coefficients of the Robin boundary condition of the DA from Eqs. (3.12)-(3.14).
4. Solve the diffusion equation (2.17) subject to the boundary condition (2.22).
5. Compute the boundary layer correction using Eq. (3.16).
6. Compute the approximation to the radiance $\phi(\mathbf{r}, \hat{\mathbf{s}})$ at the points $\mathbf{r}_b$ using the Eq. (2.26).

3.3 FINITE ELEMENT APPROXIMATION OF THE COUPLED TRANSPORT–DIFFUSION MODEL

First, the finite element (FE) approximation of the coupled transport–diffusion model (2.33) is derived following publication **III** and [67, 115, 163]. The FE approximation of the RTE, the FP equation, the FPE equation, or the DA can be obtained as a special case of the FE approximation of the general model.

In the FEM, a variational formulation of the original problem is derived, and then this infinite dimensional problem is discretized using a suitable set of basis functions. The variational formulation of the hybrid model (2.33) with the SDM [155, 163] can be written as

$$
\begin{aligned}
&\int_{\Omega_\phi}\int_{\mathbb{S}^{d-1}} \frac{\mathrm{i}\omega}{c}\phi(\mathbf{r},\hat{\mathbf{s}})v(\mathbf{r},\hat{\mathbf{s}})\mathrm{d}\hat{\mathbf{s}}\mathrm{d}\mathbf{r} - \int_{\Omega_\phi}\int_{\mathbb{S}^{d-1}} \hat{\mathbf{s}}\cdot\nabla v(\mathbf{r},\hat{\mathbf{s}})\phi(\mathbf{r},\hat{\mathbf{s}})\mathrm{d}\hat{\mathbf{s}}\mathrm{d}\mathbf{r} \\
&+ \int_{\partial\Omega_\phi}\int_{\mathbb{S}^{d-1}} (\hat{\mathbf{s}}\cdot\hat{\mathbf{n}})_+\phi(\mathbf{r},\hat{\mathbf{s}})v(\mathbf{r},\hat{\mathbf{s}})\mathrm{d}\hat{\mathbf{s}}\mathrm{d}S \\
&- \int_{\Gamma}\int_{\mathbb{S}^{d-1}} \frac{1}{|\mathbb{S}^{d-1}|}(\hat{\mathbf{s}}\cdot\hat{\mathbf{n}})_-\Phi(\mathbf{r})v(\mathbf{r},\hat{\mathbf{s}})\mathrm{d}\hat{\mathbf{s}}\mathrm{d}S \\
&+ \int_{\Gamma}\int_{\mathbb{S}^{d-1}} \frac{n}{|\mathbb{S}^{d-1}|}(\hat{\mathbf{s}}\cdot\hat{\mathbf{n}})_-(\hat{\mathbf{s}}\cdot\kappa\nabla\Phi(\mathbf{r}))v(\mathbf{r},\hat{\mathbf{s}})\mathrm{d}\hat{\mathbf{s}}\mathrm{d}S \\
&+ \int_{\Omega_\phi}\int_{\mathbb{S}^{d-1}} \mu_\mathrm{a}\phi(\mathbf{r},\hat{\mathbf{s}})v(\mathbf{r},\hat{\mathbf{s}})\mathrm{d}\hat{\mathbf{s}}\mathrm{d}\mathbf{r} \\
&- \int_{\Omega_\phi}\int_{\mathbb{S}^{d-1}} \mathcal{L}\phi(\mathbf{r},\hat{\mathbf{s}})v(\mathbf{r},\hat{\mathbf{s}})\mathrm{d}\hat{\mathbf{s}}\mathrm{d}\mathbf{r} + \int_{\Omega_\phi}\int_{\mathbb{S}^{d-1}} \delta\frac{\mathrm{i}\omega}{c}\phi(\mathbf{r},\hat{\mathbf{s}})\hat{\mathbf{s}}\cdot\nabla v(\mathbf{r},\hat{\mathbf{s}})\mathrm{d}\hat{\mathbf{s}}\mathrm{d}\mathbf{r} \\
&+ \int_{\Omega_\phi}\int_{\mathbb{S}^{d-1}} \delta(\hat{\mathbf{s}}\cdot\nabla\phi(\mathbf{r},\hat{\mathbf{s}}))(\hat{\mathbf{s}}\cdot\nabla v(\mathbf{r},\hat{\mathbf{s}}))\mathrm{d}\hat{\mathbf{s}}\mathrm{d}\mathbf{r} \\
&+ \int_{\Omega_\phi}\int_{\mathbb{S}^{d-1}} \delta\mu_\mathrm{a}\phi(\mathbf{r},\hat{\mathbf{s}})v(\mathbf{r},\hat{\mathbf{s}})\mathrm{d}\hat{\mathbf{s}}\mathrm{d}\mathbf{r} \\
&- \int_{\Omega_\phi}\delta\int_{\mathbb{S}^{d-1}} \mathcal{L}\phi(\mathbf{r},\hat{\mathbf{s}})(\hat{\mathbf{s}}\cdot\nabla v(\mathbf{r},\hat{\mathbf{s}}))\mathrm{d}\hat{\mathbf{s}}\mathrm{d}\mathbf{r} + \int_{\Omega_\Phi}\kappa\nabla\Phi(\mathbf{r})\cdot\nabla\Psi(\mathbf{r})\mathrm{d}\mathbf{r} \\
&+ \int_{\partial\Omega_{\Phi,\mathrm{out}}} \frac{2\gamma_n}{A}\Phi(\mathbf{r})\Psi(\mathbf{r})\mathrm{d}S - \int_{\Gamma}\kappa\left(\hat{\mathbf{n}}\cdot\nabla\int_{\mathbb{S}^{d-1}}\phi(\mathbf{r},\hat{\mathbf{s}})\mathrm{d}\hat{\mathbf{s}}\right)\Psi(\mathbf{r})\mathrm{d}S \\
&+ \int_{\Omega_\Phi}\mu_\mathrm{a}\Phi(\mathbf{r})\Psi(\mathbf{r})\mathrm{d}\mathbf{r} + \int_{\Omega_\Phi}\frac{\mathrm{i}\omega}{c}\Phi(\mathbf{r})\Psi(\mathbf{r})\mathrm{d}\mathbf{r}
\end{aligned}
$$

$$= \int_{\partial\Omega_{\phi,\text{out}}} \int_{\mathbb{S}^{d-1}} (\hat{\mathbf{s}} \cdot \hat{\mathbf{n}})_{-} \phi_0(\mathbf{r}, \hat{\mathbf{s}}) v(\mathbf{r}, \hat{\mathbf{s}}) \mathrm{d}\hat{\mathbf{s}} \mathrm{d}S + \int_{\partial\Omega_{\Phi,\text{out}}} \frac{2I_s}{A} \Psi(\mathbf{r}) \mathrm{d}S, \tag{3.17}$$

where v and Ψ are test functions in appropriate Sobolev spaces, δ is a SDM parameter, and $(\hat{\mathbf{s}} \cdot \hat{\mathbf{n}})_{+}$ and $(\hat{\mathbf{s}} \cdot \hat{\mathbf{n}})_{-}$ denote the positive and negative parts of the function $(\hat{\mathbf{s}} \cdot \hat{\mathbf{n}})$.

The FE approximation is obtained by approximating the solutions $\phi(\mathbf{r}, \hat{\mathbf{s}})$ and $\Phi(\mathbf{r})$ of the variational formulation (3.17) with a linear combination of the basis functions

$$\phi(\mathbf{r}, \hat{\mathbf{s}})) \approx \sum_{i=1}^{N_s} \sum_{l=1}^{N_a} \alpha_{il} \psi_i(\mathbf{r}) \psi_l(\hat{\mathbf{s}}), \tag{3.18}$$

$$\Phi(\mathbf{r}) \approx \sum_{k=1}^{N_\Phi} a_k \vartheta_k(\mathbf{r}), \tag{3.19}$$

and choosing the test functions

$$v(\mathbf{r}, \hat{\mathbf{s}}) = \psi_j(\mathbf{r}) \psi_m(\hat{\mathbf{s}}), \quad \forall j = 1, ..., N_s,\ m = 1, ..., N_a, \tag{3.20}$$

$$\Psi(\mathbf{r}) = \vartheta_p(\mathbf{r}), \quad \forall p = 1, ..., N, \tag{3.21}$$

where $\psi_i(\mathbf{r})$ and $\psi_l(\hat{\mathbf{s}})$ are the nodal basis functions of the spatial and angular discretizations of $\Omega_\phi \times \mathbb{S}^{d-1}$, α_{il} is the radiance at a spatial node i in an angular direction l, and N_s and N_a are the number of the spatial and angular nodes in subdomain Ω_ϕ, respectively. Further, $\vartheta_k(\mathbf{r})$ is the nodal basis function of the spatial discretization of Ω_Φ, a_k is the fluence at a spatial node k, and N_Φ is the number of spatial nodes in the subdomain Ω_Φ. In this work, a piecewise linear basis is used for both the spatial and angular parts of the approximation. The FE approximation of the coupled model can be written in a matrix form

$$\begin{pmatrix} A_\phi & D \\ F & A_\Phi \end{pmatrix} \begin{pmatrix} \alpha \\ a \end{pmatrix} = \begin{pmatrix} b_\phi \\ b_\Phi \end{pmatrix}. \tag{3.22}$$

where the block-matrices A_ϕ and A_Φ contain the FE approximations of the models to be coupled, and the matrices D and F contain the coupling conditions on the interface Γ. The components of the matrix equation (3.22) are the following. The block A_ϕ is

$$A_\phi = A_0 + A_1 + A_2 + A_3 + A_4, \tag{3.23}$$

where

$$\begin{aligned}
A_0(h,s) =& \frac{\mathrm{i}\omega}{c}\bigg(\int_{\Omega_\phi} \psi_i(\mathbf{r})\psi_j(\mathbf{r})\mathrm{d}r \int_{\mathbb{S}^{d-1}} \psi_l(\hat{\mathbf{s}})\psi_m(\hat{\mathbf{s}})\mathrm{d}\hat{\mathbf{s}} \\
&\quad + \int_{\Omega_\phi} \delta \int_{\mathbb{S}^{d-1}} \hat{\mathbf{s}}\cdot\nabla\psi_j(\mathbf{r})\psi_m(\hat{\mathbf{s}})\psi_l(\hat{\mathbf{s}})\mathrm{d}\hat{\mathbf{s}}\psi_i(\mathbf{r})\mathrm{d}\mathbf{r}\bigg) &\text{(3.24a)}\\
A_1(h,s) =& -\int_{\Omega_\phi}\int_{\mathbb{S}^{d-1}} \hat{\mathbf{s}}\cdot\nabla\psi_j(\mathbf{r})\psi_m(\hat{\mathbf{s}})\psi_l(\hat{\mathbf{s}})\mathrm{d}\hat{\mathbf{s}}\psi_i(\mathbf{r})\mathrm{d}\mathbf{r} \\
&+ \int_{\Omega_\phi} \delta \int_{\mathbb{S}^{d-1}} (\hat{\mathbf{s}}\cdot\nabla\psi_i(\mathbf{r}))(\hat{\mathbf{s}}\cdot\nabla\psi_j(\mathbf{r}))\psi_l(\hat{\mathbf{s}})\psi_m(\hat{\mathbf{s}})\mathrm{d}\hat{\mathbf{s}}\mathrm{d}\mathbf{r} \\
&&\text{(3.24b)}\\
A_2(h,s) =& \int_{\partial\Omega_\phi} \psi_i(\mathbf{r})\psi_j(\mathbf{r})\mathrm{d}S \int_{\mathbb{S}^{d-1}} (\hat{\mathbf{s}}\cdot\hat{\mathbf{n}})_+\psi_l(\hat{\mathbf{s}})\psi_m(\hat{\mathbf{s}})\mathrm{d}\hat{\mathbf{s}} &\text{(3.24c)}\\
A_3(h,s) =& \int_{\Omega_\phi} \mu_{\mathrm{a}}\psi_i(\mathbf{r})\psi_j(\mathbf{r})\mathrm{d}\mathbf{r} \int_{\mathbb{S}^{d-1}} \psi_l(\hat{\mathbf{s}})\psi_m(\hat{\mathbf{s}})\mathrm{d}\hat{\mathbf{s}} \\
&+ \int_{\Omega_\phi} \delta\mu_{\mathrm{a}}\psi_i(\mathbf{r}) \int_{\mathbb{S}^{d-1}} (\hat{\mathbf{s}}\cdot\nabla\psi_j(\mathbf{r}))\psi_m(\hat{\mathbf{s}})\psi_l(\hat{\mathbf{s}})\mathrm{d}\hat{\mathbf{s}}\mathrm{d}\mathbf{r}, &\text{(3.24d)}
\end{aligned}$$

where $h = N_a(j-1)+m$, $s = N_a(i-1)+l$, $j,i = 1,\ldots,N_s$, $m,l = 1,\ldots,N_a$, and $h,s = 1,\ldots,N_sN_a$. The matrix A_4 depends on the chosen scattering operator $\mathcal{L}$. In the case of the RTE, $\mathcal{L} = \mathcal{L}_{\mathrm{RTE}}$, Eq. (2.2), and

$$\begin{aligned}
A_4(h,s) =& \int_{\Omega_\phi} \mu_{\mathrm{s}}\psi_i(\mathbf{r})\psi_j(\mathbf{r})\mathrm{d}\mathbf{r} \int_{\mathbb{S}^{d-1}} \psi_l(\hat{\mathbf{s}})\psi_m(\hat{\mathbf{s}})\mathrm{d}\hat{\mathbf{s}} \\
&+ \int_{\Omega_\phi} \delta\mu_{\mathrm{s}}\psi_i(\mathbf{r}) \int_{\mathbb{S}^{d-1}} (\hat{\mathbf{s}}\cdot\nabla\psi_j(\mathbf{r}))\psi_m(\hat{\mathbf{s}})\psi_l(\hat{\mathbf{s}})\mathrm{d}\hat{\mathbf{s}}\mathrm{d}\mathbf{r} \\
&- \int_{\Omega_\phi} \mu_{\mathrm{s}}\psi_i(\mathbf{r})\psi_j(\mathbf{r})\mathrm{d}\mathbf{r} \int_{\mathbb{S}^{d-1}}\int_{\mathbb{S}^{d-1}} \Theta(\hat{\mathbf{s}}\cdot\hat{\mathbf{s}}')\psi_l(\hat{\mathbf{s}}')\mathrm{d}\hat{\mathbf{s}}'\psi_m(\hat{\mathbf{s}})\mathrm{d}\hat{\mathbf{s}} \\
&- \int_{\Omega_\phi} \delta\mu_{\mathrm{s}} \int_{\mathbb{S}^{d-1}} (\hat{\mathbf{s}}\cdot\nabla\psi_j(\mathbf{r}))\psi_m(\hat{\mathbf{s}}) \int_{s^{d-1}} \Theta(\hat{\mathbf{s}}\cdot\hat{\mathbf{s}}')\psi_l(\hat{\mathbf{s}}')\mathrm{d}\hat{\mathbf{s}}'\mathrm{d}\hat{\mathbf{s}}\psi_i(\mathbf{r})\mathrm{d}\mathbf{r}
\end{aligned} \tag{3.25}$$

In the case of the FP, $\mathcal{L}\phi(\mathbf{r},\hat{\mathbf{s}}) = \mathcal{L}_{\text{FP}}\phi(\mathbf{r},\hat{\mathbf{s}})$, Eq. (2.28), and

$$\begin{aligned} A_4(h,s) = &\int_{\Omega_\phi} a_{1,\text{FP}}\mu_{\text{s}}\psi_i(\mathbf{r})\psi_j(\mathbf{r})\text{d}\mathbf{r}\int_{\mathbb{S}^{d-1}}\nabla_{\hat{\mathbf{s}}}\psi_l(\hat{\mathbf{s}})\cdot\nabla_{\hat{\mathbf{s}}}\psi_m(\hat{\mathbf{s}})\text{d}\hat{\mathbf{s}} \\ &+\int_{\Omega_\phi}\delta a_{1,\text{FP}}\mu_{\text{s}}\psi_i(\mathbf{r})\int_{\mathbb{S}^{d-1}}\left(\nabla_{\hat{\mathbf{s}}}\psi_l(\hat{\mathbf{s}})\cdot\nabla_{\hat{\mathbf{s}}}(\hat{\mathbf{s}}\cdot\nabla\psi_j(\mathbf{r})\psi_m(\hat{\mathbf{s}}))\right)\text{d}\hat{\mathbf{s}}\text{d}\mathbf{r}. \end{aligned} \tag{3.26}$$

In the case of the FPE, $\mathcal{L}\phi(\mathbf{r},\hat{\mathbf{s}}) = \mathcal{L}_{\text{FPE}}\phi(\mathbf{r},\hat{\mathbf{s}})$, Eq. (2.32), and

$$\begin{aligned} A_4(h,s) = &\int_{\Omega_\phi}(1-a_0^{\text{FPE}})\mu_{\text{s}}\psi_i(\mathbf{r})\psi_j(\mathbf{r})\text{d}\mathbf{r}\int_{\mathbb{S}^{d-1}}\psi_l(\hat{\mathbf{s}})\psi_m(\hat{\mathbf{s}})\text{d}\hat{\mathbf{s}} \\ &+\int_{\Omega_\phi}\delta(1-a_0^{\text{FPE}})\mu_{\text{s}}\psi_i(\mathbf{r})\int_{\mathbb{S}^{d-1}}(\hat{\mathbf{s}}\cdot\nabla\psi_j(\mathbf{r}))\psi_m(\hat{\mathbf{s}})\psi_l(\hat{\mathbf{s}})\text{d}\hat{\mathbf{s}}\text{d}\mathbf{r} \\ &+\int_{\Omega_\phi} a_1^{FPE}\mu_{\text{s}}\psi_i(\mathbf{r})\psi_j(\mathbf{r})\text{d}\mathbf{r}\int_{\mathbb{S}^{d-1}}\nabla_{\hat{\mathbf{s}}}\psi_l(\hat{\mathbf{s}})\cdot\nabla_{\hat{\mathbf{s}}}\psi_m(\hat{\mathbf{s}})\text{d}\hat{\mathbf{s}} \\ &+\int_{\Omega_\phi}\delta a_1^{FPE}\mu_{\text{s}}\psi_i(\mathbf{r})\int_{\mathbb{S}^{d-1}}\left(\nabla_{\hat{\mathbf{s}}}\psi_l(\hat{\mathbf{s}})\cdot\nabla_{\hat{\mathbf{s}}}(\hat{\mathbf{s}}\cdot\nabla\psi_j(\mathbf{r})\psi_m(\hat{\mathbf{s}}))\right)\text{d}\hat{\mathbf{s}}\text{d}\mathbf{r}. \\ &-\frac{1}{|\mathbb{S}^{d-1}|}\int_{\Omega_\phi}\mu_{\text{s}}\psi_i(\mathbf{r})\psi_j(\mathbf{r})\text{d}\mathbf{r}\int_{\mathbb{S}^{d-1}}\int_{\mathbb{S}^{d-1}}\left(b_0^{\text{FPE}}P_0(\hat{\mathbf{s}}\cdot\hat{\mathbf{s}}')+db_1^{\text{FPE}}P_1(\hat{\mathbf{s}}\cdot\hat{\mathbf{s}}')\right) \\ &\psi_l(\hat{\mathbf{s}}')\text{d}\hat{\mathbf{s}}'\psi_m(\hat{\mathbf{s}})\text{d}\hat{\mathbf{s}} \\ &-\frac{1}{|\mathbb{S}^{d-1}|}\int_{\Omega_\phi}\delta\mu_{\text{s}}\psi_i(\mathbf{r})\int_{\mathbb{S}^{d-1}}\int_{\mathbb{S}^{d-1}}\left(b_0^{\text{FPE}}P_0(\hat{\mathbf{s}}\cdot\hat{\mathbf{s}}')+db_1^{\text{FPE}}P_1(\hat{\mathbf{s}}\cdot\hat{\mathbf{s}}')\right) \\ &\psi_l(\hat{\mathbf{s}}')\text{d}\hat{\mathbf{s}}'(\hat{\mathbf{s}}\cdot\nabla\psi_j(\mathbf{r}))\psi_m(\hat{\mathbf{s}})\text{d}\hat{\mathbf{s}}\text{d}\mathbf{r}. \end{aligned} \tag{3.27}$$

The DA block A_Φ is

$$A_\Phi = K + C + R + Z, \tag{3.28}$$

where matrices K, C, R, and Z are

$$K(p,k) = \int_{\Omega_\Phi}\kappa\nabla\vartheta_k(\mathbf{r})\cdot\nabla\vartheta_p(\mathbf{r})\text{d}\mathbf{r} \tag{3.29a}$$

$$C(p,k) = \int_{\Omega_\Phi}\mu_{\text{a}}\vartheta_k(\mathbf{r})\vartheta_p(\mathbf{r})\text{d}\mathbf{r} \tag{3.29b}$$

$$R(p,k) = \int_{\partial\Omega_{\Phi,\text{out}}}\frac{2\gamma_n}{A}\vartheta_k(\mathbf{r})\vartheta_p(\mathbf{r})\text{d}S \tag{3.29c}$$

$$Z(p,k) = \frac{\text{i}\omega}{c}\int_{\Omega_\Phi}\vartheta_k(\mathbf{r})\vartheta_p(\mathbf{r})\text{d}\mathbf{r}, \tag{3.29d}$$

where $p, k = 1, ..., N_\Phi$. The elements of the matrices D and F, which correspond to the interface conditions on Γ, are

$$\begin{aligned} D(h,k) = & -\frac{1}{|\mathbb{S}^{d-1}|}\int_\Gamma \vartheta_k(\mathbf{r})\psi_j(\mathbf{r})\mathrm{d}S \int_{\mathbb{S}^{d-1}} (\hat{\mathbf{s}}\cdot\hat{\mathbf{n}})_- \psi_m(\hat{\mathbf{s}})\mathrm{d}\hat{\mathbf{s}} \\ & + \frac{d}{|\mathbb{S}^{d-1}|}\int_\Gamma \kappa \int_{\mathbb{S}^{d-1}} (\hat{\mathbf{s}}\cdot\hat{\mathbf{n}})_- (\hat{\mathbf{s}}\cdot\nabla\vartheta_k(\mathbf{r}))\psi_m(\hat{\mathbf{s}})\mathrm{d}\hat{\mathbf{s}}\psi_j(\mathbf{r})\mathrm{d}S, \end{aligned} \tag{3.30}$$

and

$$F(p,s) = -\int_\Gamma \kappa\,(\hat{\mathbf{n}}\cdot\nabla\psi_i(\mathbf{r}))\,\vartheta_p(\mathbf{r})\mathrm{d}S \int_{\mathbb{S}^{d-1}} \psi_l(\hat{\mathbf{s}})\mathrm{d}\hat{\mathbf{s}}. \tag{3.31}$$

The source vector b_ϕ is

$$b_\phi(h,s) = \int_{\partial\Omega_{\phi,\mathrm{out}}} \psi_j(\mathbf{r})\mathrm{d}S \int_{\mathbb{S}^{d-1}} (\hat{\mathbf{s}}\cdot\hat{\mathbf{n}})_- \phi_0(\mathbf{r},\hat{\mathbf{s}})\psi_m(\hat{\mathbf{s}})\mathrm{d}\hat{\mathbf{s}}, \tag{3.32}$$

and the vector b_Φ is

$$b_\Phi(p) = \int_{\partial\Omega_{\Phi,\mathrm{out}}} \frac{2I_s}{A}\vartheta_p(\mathbf{r})\mathrm{d}S. \tag{3.33}$$

Often the subdomain division is chosen such that the subdomain Ω_ϕ includes the source location and the boundary $\partial\Omega$. Then $\partial\Omega_{\Phi,\mathrm{out}} = \emptyset$, and thus $b_\Phi = 0$. As the solution of the coupled model, the radiance at the nodes of the spatial and angular discretizations in the subdomain Ω_ϕ and the fluence at the spatial nodes of the subdomain Ω_Φ are obtained.

The FE approximation of the FP, FPE, RTE, or DA in the whole domain Ω can be written in the framework of the FE approximation of the coupled model. In the case of the FE approximation of the FP, FPE, or RTE $\Omega_\phi = \Omega$ and $\Omega_\Phi = \emptyset$, and hence $A_\Phi = 0$, $b_\Phi = 0$, $F = 0$, and $D = 0$ in Eq. (3.22). The FE approximation of the DA is obtained by choosing $\Omega_\Phi = \Omega$ and $\Omega_\phi = \emptyset$, and hence $A_\phi = 0$, $b_\phi = 0$, $F = 0$, and $D = 0$ in Eq. (3.22). For more details about the FE approximation of the RTE, FP, and DA see e.g. [115] and publication **I**.

3.4 FINITE ELEMENT APPROXIMATION OF THE RTE WITH PIECEWISE CONSTANT REFRACTIVE INDEX

In this thesis, the solution of the cRTE (2.46) is numerically approximated using the FEM. Next, the variational formulation of the cRTE is derived following a similar procedure as in Section 3.3 and in publication **IV**.

Thus, first each of the equations in (2.46a) are multiplied by a test function v_k and integrated over the domain $\Omega_k \times \mathbb{S}^{d-1}$. Then, by using the Green's theorem [180], separating the resulting boundary integrals over the outer boundary $\partial\Omega_{k,\mathrm{out}}$ and over the interfaces $\Gamma_{k,m}$, and utilizing the boundary conditions (2.46b) and (2.46c), the variational formulation is obtained. The variational formulation of the cRTE (2.46) with the SDM [155, 162, 163] can be written as

$$
\begin{aligned}
&\sum_{k=1}^{N} \Big(\int_{\Omega_k} \int_{\mathbb{S}^{d-1}} \frac{\mathrm{i}\omega}{c_k} \phi_k(\mathbf{r},\hat{\mathbf{s}}) v_k(\mathbf{r},\hat{\mathbf{s}}) \mathrm{d}\hat{\mathbf{s}} \mathrm{d}\mathbf{r} \\
&- \int_{\Omega_k} \int_{\mathbb{S}^{d-1}} \hat{\mathbf{s}} \cdot \nabla v_k(\mathbf{r},\hat{\mathbf{s}}) \phi_k(\mathbf{r},\hat{\mathbf{s}}) \mathrm{d}\hat{\mathbf{s}} \mathrm{d}\mathbf{r} \\
&+ \int_{\partial\Omega_k} \int_{\mathbb{S}^{d-1}} (\hat{\mathbf{s}} \cdot \hat{\mathbf{n}}_k)_+ \phi_k(\mathbf{r},\hat{\mathbf{s}}) v_k(\mathbf{r},\hat{\mathbf{s}}) \mathrm{d}\hat{\mathbf{s}} \mathrm{d}S \\
&- \int_{\partial\Omega_{k,\mathrm{out}}} \int_{\mathbb{S}^{d-1}} (\hat{\mathbf{s}} \cdot \hat{\mathbf{n}}_k)_- R_{k,\mathrm{out}} \phi_k(\mathbf{r}, H_k\hat{\mathbf{s}}) v_k(\mathbf{r},\hat{\mathbf{s}}) \mathrm{d}\hat{\mathbf{s}} \mathrm{d}S \\
&- \sum_{m=1, m\neq k}^{N} \int_{\Gamma_{k,m}} \int_{\mathbb{S}^{d-1}} (\hat{\mathbf{s}} \cdot \hat{\mathbf{n}}_k)_- R_{k,m} \phi_k(\mathbf{r}, H_k\hat{\mathbf{s}}) v_k(\mathbf{r},\hat{\mathbf{s}}) \mathrm{d}\hat{\mathbf{s}} \mathrm{d}S \\
&- \sum_{m=1, m\neq k}^{N} \int_{\Gamma_{k,m}} \int_{\mathbb{S}^{d-1}} (\hat{\mathbf{s}} \cdot \hat{\mathbf{n}}_k)_- T_{m,k} \phi_m(\mathbf{r}, K_{m,k}^{-1}(\hat{\mathbf{s}})) v_k(\mathbf{r},\hat{\mathbf{s}}) \mathrm{d}\hat{\mathbf{s}} \mathrm{d}S \\
&+ \int_{\Omega_k} \int_{\mathbb{S}^{d-1}} \mu_{\mathrm{a}} \phi_k(\mathbf{r},\hat{\mathbf{s}}) v_k(\mathbf{r},\hat{\mathbf{s}}) \mathrm{d}\hat{\mathbf{s}} \mathrm{d}\mathbf{r} \\
&- \int_{\Omega_k} \int_{\mathbb{S}^{d-1}} \mathcal{L} \phi_k(\mathbf{r},\hat{\mathbf{s}}) v_k(\mathbf{r},\hat{\mathbf{s}}) \mathrm{d}\hat{\mathbf{s}} \mathrm{d}\mathbf{r} \\
&+ \int_{\Omega_k} \int_{\mathbb{S}^{d-1}} \delta \frac{\mathrm{i}\omega}{c} \phi_k(\mathbf{r},\hat{\mathbf{s}}) \hat{\mathbf{s}} \cdot \nabla v_k(\mathbf{r},\hat{\mathbf{s}}) \mathrm{d}\hat{\mathbf{s}} \mathrm{d}\mathbf{r} \\
&+ \int_{\Omega_k} \int_{\mathbb{S}^{d-1}} \delta (\hat{\mathbf{s}} \cdot \nabla \phi_k(\mathbf{r},\hat{\mathbf{s}})) (\hat{\mathbf{s}} \cdot \nabla v_k(\mathbf{r},\hat{\mathbf{s}})) \mathrm{d}\hat{\mathbf{s}} \mathrm{d}\mathbf{r}
\end{aligned}
$$

$$
\begin{aligned}
&+ \int_{\Omega_k} \int_{\mathbb{S}^{d-1}} \delta \mu_{\mathrm{a}} \phi_k(\mathbf{r}, \hat{\mathbf{s}}) v_k(\mathbf{r}, \hat{\mathbf{s}}) \mathrm{d}\hat{\mathbf{s}} \mathrm{d}\mathbf{r} \\
&- \int_{\Omega_k} \delta \int_{\mathbb{S}^{d-1}} \mathcal{L}\phi_k(\mathbf{r}, \hat{\mathbf{s}}) (\hat{\mathbf{s}} \cdot \nabla v_k(\mathbf{r}, \hat{\mathbf{s}})) \mathrm{d}\hat{\mathbf{s}} \mathrm{d}\mathbf{r} \\
&- \int_{\partial\Omega_{k,\mathrm{out}}} \int_{\mathbb{S}^{d-1}} (\hat{\mathbf{s}} \cdot \hat{\mathbf{n}}_k)_{-} \phi_{0,k}(\mathbf{r}, \hat{\mathbf{s}}) v_k(\mathbf{r}, \hat{\mathbf{s}}) \mathrm{d}\hat{\mathbf{s}} \mathrm{d}S \Big) = 0 \qquad (3.34)
\end{aligned}
$$

where $R_{k,m}$ and $T_{m,k}$ are given in Eqs. (2.35) and 2.38), respectively.

The FE approximation is obtained by approximating the solutions $\phi_k(\mathbf{r}, \hat{\mathbf{s}})$ of the variational formulation (3.34) with a linear combination of the basis functions

$$
\phi_k(\mathbf{r}, \hat{\mathbf{s}}) \approx \sum_{i=1}^{N_{s,k}} \sum_{l=1}^{N_{a,k}} \alpha_{il}^{k} \psi_{i,k}(\mathbf{r}) \psi_{l,k}(\hat{\mathbf{s}}), \qquad (3.35)
$$

and choosing the test functions

$$
v_k(\mathbf{r}, \hat{\mathbf{s}}) = \psi_{j,k}(\mathbf{r}) \psi_{m,k}(\hat{\mathbf{s}}), \quad \forall j = 1, ..., N_{s,k}, \ m = 1, ..., N_{a,k}, \qquad (3.36)
$$

where $\psi_{i,k}(\mathbf{r})$ and $\psi_{l,k}(\hat{\mathbf{s}})$ are the nodal basis functions of the spatial and angular discretizations of $\Omega_k \times \mathbb{S}^{d-1}$, α_{il}^{k} is the radiance in spatial nodal point i into angular direction l in the subdomain Ω_k, and $N_{s,k}$ and $N_{a,k}$ are the number of spatial and angular nodes in the subdomain Ω_k, respectively. Therefore, different number of angular directions can be used in different subdomains if that is feasible. In this work, we use a piecewise linear basis for both spatial and angular parts of the solution. The FE approximation of the coupled model can be written in a matrix form as

$$
\begin{pmatrix}
A_1 & C_{1,2} & \cdots & \cdots & C_{1,N} \\
C_{2,1} & A_2 & \ddots & \ddots & \vdots \\
\vdots & \ddots & \ddots & \ddots & \vdots \\
C_{N-1,1} & \ddots & \ddots & A_{N-1} & C_{N-1,N} \\
C_{N,1} & \cdots & \cdots & C_{N,N-1} & A_N
\end{pmatrix}
\begin{pmatrix} \alpha_1 \\ \vdots \\ \alpha_N \end{pmatrix}
=
\begin{pmatrix} b_1 \\ \vdots \\ b_N \end{pmatrix}, \qquad (3.37)
$$

where the vector of radiances in the different subdomains is $\alpha = (\alpha_1, \dots, \alpha_N) = (\alpha_{1,1}^{1}, ..., \alpha_{1,N_{a,1}}^{1}, ..., \alpha_{N_{s,1},N_{a,1}}^{1}, ..., \alpha_{N_{s,N},N_{a,N}}^{N})^T \in \mathbb{C}^{\sum_{k=1}^{N} N_{s,k} N_{a,k}}$.

The matrix $A_k \in \mathbb{C}^{N_{s,k}N_{a,k} \times N_{s,k}N_{a,k}}$ contains the FE approximation of the RTE in the subdomain Ω_k

$$A_k = A_{0,k} + A_{1,k} + A_{2,k} + A_{3,k} + A_{4,k}, \tag{3.38}$$

where

$$\begin{aligned}
A_{0,k}(h,s) =& \frac{\mathrm{i}\omega}{c_k}\left(\int_{\Omega_k} \psi_i(\mathbf{r})\psi_j(\mathbf{r})\mathrm{d}r \int_{\mathbb{S}^{d-1}} \psi_l(\hat{\mathbf{s}})\psi_m(\hat{\mathbf{s}})\mathrm{d}\hat{\mathbf{s}}\right. \\
&\left. + \int_{\Omega_k} \delta \int_{\mathbb{S}^{d-1}} \hat{\mathbf{s}} \cdot \nabla\psi_j(\mathbf{r})\psi_m(\hat{\mathbf{s}})\psi_l(\hat{\mathbf{s}})\mathrm{d}\hat{\mathbf{s}}\psi_i(\mathbf{r})\mathrm{d}\mathbf{r}\right), \qquad (3.39\mathrm{a}) \\
A_{1,k}(h,s) =& -\int_{\Omega_k}\int_{\mathbb{S}^{d-1}} \hat{\mathbf{s}} \cdot \nabla\psi_j(\mathbf{r})\psi_m(\hat{\mathbf{s}})\psi_l(\hat{\mathbf{s}})\mathrm{d}\hat{\mathbf{s}}\psi_i(\mathbf{r})\mathrm{d}\mathbf{r} \\
&+ \int_{\Omega_k} \delta \int_{\mathbb{S}^{d-1}} (\hat{\mathbf{s}} \cdot \nabla\psi_i(\mathbf{r}))(\hat{\mathbf{s}} \cdot \nabla\psi_j(\mathbf{r}))\psi_l(\hat{\mathbf{s}})\psi_m(\hat{\mathbf{s}})\mathrm{d}\hat{\mathbf{s}}\mathrm{d}\mathbf{r}, \\
&\qquad (3.39\mathrm{b}) \\
A_{2,k}(h,s) =& \int_{\partial\Omega_k} \psi_i(\mathbf{r})\psi_j(\mathbf{r})\mathrm{d}S \int_{\mathbb{S}^{d-1}} (\hat{\mathbf{s}} \cdot \hat{\mathbf{n}}_k)_+ \psi_l(\hat{\mathbf{s}})\psi_m(\hat{\mathbf{s}})\mathrm{d}\hat{\mathbf{s}} \\
&- \int_{\partial\Omega_{k,\mathrm{out}}} \psi_i(\mathbf{r})\psi_j(\mathbf{r})\mathrm{d}S \int_{\mathbb{S}^{d-1}} (\hat{\mathbf{s}} \cdot \hat{\mathbf{n}}_k)_- R_{k,\mathrm{out}}\psi_l(H_k\hat{\mathbf{s}})\psi_m(\hat{\mathbf{s}})\mathrm{d}\hat{\mathbf{s}} \\
&- \int_{\Gamma_{k,m}} \psi_i(\mathbf{r})\psi_j(\mathbf{r})\mathrm{d}S \int_{\mathbb{S}^{d-1}} (\hat{\mathbf{s}} \cdot \hat{\mathbf{n}}_k)_- R_{k,m}\psi_l(H_k\hat{\mathbf{s}})\psi_m(\hat{\mathbf{s}})\mathrm{d}\hat{\mathbf{s}}, \\
&\qquad (3.39\mathrm{c}) \\
A_{3,k}(h,s) =& \int_{\Omega_k} \mu_\mathrm{a}\psi_i(\mathbf{r})\psi_j(\mathbf{r})\mathrm{d}\mathbf{r} \int_{\mathbb{S}^{d-1}} \psi_l(\hat{\mathbf{s}})\psi_m(\hat{\mathbf{s}})\mathrm{d}\hat{\mathbf{s}} \\
&+ \int_{\Omega_k} \delta\mu_\mathrm{a}\psi_i(\mathbf{r}) \int_{\mathbb{S}^{d-1}} (\hat{\mathbf{s}} \cdot \nabla\psi_j(\mathbf{r}))\psi_m(\hat{\mathbf{s}})\psi_l(\hat{\mathbf{s}})\mathrm{d}\hat{\mathbf{s}}\mathrm{d}\mathbf{r}, \qquad (3.39\mathrm{d}) \\
A_{4,k}(h,s) =& \int_{\Omega_k} \mu_\mathrm{s}\psi_i(\mathbf{r})\psi_j(\mathbf{r})\mathrm{d}\mathbf{r} \int_{\mathbb{S}^{d-1}} \psi_l(\hat{\mathbf{s}})\psi_m(\hat{\mathbf{s}})\mathrm{d}\hat{\mathbf{s}} \\
&+ \int_{\Omega_k} \delta\mu_\mathrm{s}\psi_i(\mathbf{r}) \int_{\mathbb{S}^{d-1}} (\hat{\mathbf{s}} \cdot \nabla\psi_j(\mathbf{r}))\psi_m(\hat{\mathbf{s}})\psi_l(\hat{\mathbf{s}})\mathrm{d}\hat{\mathbf{s}}\mathrm{d}\mathbf{r} \\
&- \int_{\Omega_k} \mu_\mathrm{s}\psi_i(\mathbf{r})\psi_j(\mathbf{r})\mathrm{d}\mathbf{r} \int_{\mathbb{S}^{d-1}}\int_{\mathbb{S}^{d-1}} \Theta(\hat{\mathbf{s}} \cdot \hat{\mathbf{s}}')\psi_l(\hat{\mathbf{s}}')\mathrm{d}\hat{\mathbf{s}}'\psi_m(\hat{\mathbf{s}})\mathrm{d}\hat{\mathbf{s}} \\
&- \int_{\Omega_k} \delta\mu_\mathrm{s} \int_{\mathbb{S}^{d-1}} (\hat{\mathbf{s}} \cdot \nabla\psi_j(\mathbf{r}))\psi_m(\hat{\mathbf{s}}) \int_{\mathbb{S}^{d-1}} \Theta(\hat{\mathbf{s}} \cdot \hat{\mathbf{s}}')\psi_l(\hat{\mathbf{s}}')\mathrm{d}\hat{\mathbf{s}}'\mathrm{d}\hat{\mathbf{s}}\psi_i(\mathbf{r})\mathrm{d}\mathbf{r}, \\
&\qquad (3.39\mathrm{e})
\end{aligned}$$

where $h = N_{a,k}(j-1) + m$, $s = N_{a,k}(i-1) + l$ ($j, i = 1, \ldots, N_{s,k}$, $m, l = 1, \ldots, N_{a,k}$, and $h, s = 1, \ldots, N_{s,k}N_{a,k}$). Further, the matrix

$C_{m,k} \in \mathbb{R}^{N_{s,n}N_{a,n} \times N_{s,k}N_{a,k}}$ contains the coupling conditions on the interface $\Gamma_{k,m}$ due to the radiance transmitted from the subdomain Ω_m into the subdomain Ω_k. Note that the matrix $C_{m,k}$ is non-zero only if Ω_m and Ω_k share an interface $\Gamma_{k,m}$. The elements of the matrix $C_{m,k}$ can be written as

$$C_{m,k}(p,s) = -\int_{\Gamma_{k,m}} \psi_i(\mathbf{r})\psi_e(\mathbf{r})\mathrm{d}S \int_{\mathbb{S}^{d-1}} (\hat{\mathbf{s}} \cdot \hat{\mathbf{n}}_k)_{-} T_{m,k} \psi_l(K_{m,k}^{-1}(\hat{\mathbf{s}}))\psi_u(\hat{\mathbf{s}})\mathrm{d}\hat{\mathbf{s}}, \tag{3.40}$$

where $p = N_{a,n}(e-1) + u$, ($e = 1, \ldots, N_{s,n}$, $u = 1, \ldots, N_{a,n}$, and $p = 1, \ldots, N_{s,n}N_{a,n}$). The source vector in the subdomain Ω_k is

$$b_k(h) = \int_{\partial\Omega_{k,\mathrm{out}}} \psi_j(\mathbf{r})\mathrm{d}S \int_{\mathbb{S}^{d-1}} (\hat{\mathbf{s}} \cdot \hat{\mathbf{n}}_k)_{-} \phi_{0,k}(\mathbf{r},\hat{\mathbf{s}})\psi_m(\hat{\mathbf{s}})\mathrm{d}\hat{\mathbf{s}}. \tag{3.41}$$

4 Numerical results

In this chapter, the numerical results based on publications **I–IV** are reviewed and discussed. The results for the cDA based on publication **II** are presented and discussed in Section 4.1. In Section 4.2, the results for the forward-peaked scattering approximations and the hybrid models are reviewed and discussed. The results are primarily based on publications **I** and **III**, and [181]. The section also contains some unpublished results. In Section 4.3, the results for the coupled RTE model with piecewise constant refractive index are presented and discussed based on publication **IV**.

4.1 CORRECTED DIFFUSION APPROXIMATION

The cDA was derived and implemented in a 1D case in [34]. The numerical implementation of the cDA in a 2D case was introduced in publication **II**. In this approach, the goal was to utilize the FEM for the solution of the DA such that the implementation would be applicable in complex geometries with spatially inhomogeneous parameter distributions. Moreover, the goal was to derive the method in a dimension independent form and to describe the method such that it could be easily implemented in the existing numerical solvers of the DA which are widely used in the biomedical optics community.

In **II**, the performance of the cDA was tested with 2D simulations. Simulation domain Ω was a circle with radius of 20 mm. Two types of test cases were considered: a homogeneous medium with matched refractive indices inside and outside the domain for three different values of scattering coefficient μ_s and the same cases with mismatched refractive indices. Since the cDA was derived for the steady state case the modulation frequency was $f = 0$. The results of the cDA were compared to the FE approximations of the DA and the RTE.

The FE mesh for the spatial discretization of the domain contained 4687 nodal points and 9196 triangular elements. For the angular discretization of the RTE, 64 equally spaced angular directions were used. The same FE mesh was used for all of the models. The number of spatial and angular nodes was chosen by monitoring the convergence of the errors of the FE approximations as a function of number of nodal points. Earlier, the FE approximation of the RTE has been evaluated against the Monte Carlo method. Therefore, the FE approximation of the RTE can be considered as a good reference model and the numerical errors caused by the spatial and angular discretization are significantly smaller than the errors between the models.

4.1.1 Matched refractive indices

As the first case, a medium with matched refractive indices on the boundary was considered. The refractive indices inside and outside the medium were $n_{\text{in}} = 1$ and $n_{\text{out}} = 1$, respectively. The scattering coefficient was given three different values $\mu_s = 50$, 5 and 0.5 mm^{-1}. The absorption coefficient and the anisotropy parameter were constants, $\mu_a = 0.01$ mm^{-1} and $g = 0.8$, respectively.

The radiances on the boundary $(x, y) = (0, -20)$ mm for $\mu_s =$ 5 mm^{-1} computed using the cDA, the DA and the RTE are shown in left image of Figure 4.1. In the case of the DA, the radiance was approximated using Eq. (2.8). The exitances, computed using Eq. (2.7) from the cDA, the DA and the RTE solutions, are shown in Figure 4.2. Furthermore, the relative errors of the exitances of the cDA and the DA against the RTE are shown in Figure 4.3. The computation times of the models are given in Table 4.1.

As it can be seen from Figure 4.1, the radiance computed using the cDA agree relatively well with the RTE and satisfies the vacuum boundary condition in inward direction. Note that the RTE may give small negative or positive values in inward direction due to numerical reasons. The approximation to the radiance given by the DA gives negative radiance in inward direction which is unre-

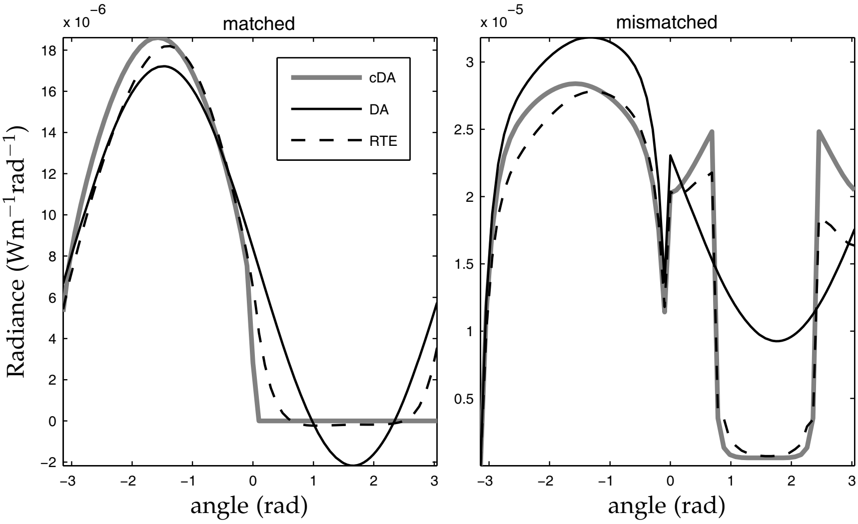

Figure 4.1: The radiance on the boundary $(x, y) = (0, -20)$ *mm computed using the cDA, the DA and the RTE for* $\mu_s = 5$ *mm*$^{-1}$ *with matched (left) and mismatched refractive indices (right).*

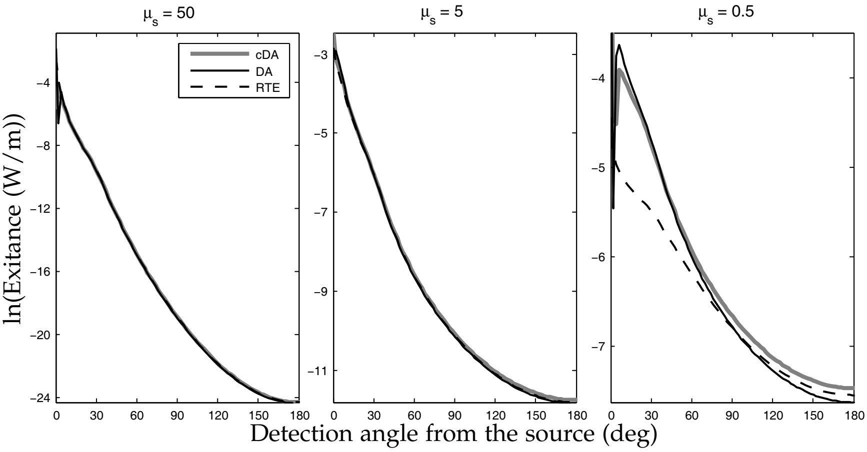

Figure 4.2: Logarithm of the exitance on the boundary of the domain computed using the cDA, the DA and the RTE for different values of μ_s *with matched refractive indices.*

alistic. The results show that as scattering becomes large compared to absorption, the relative error of exitance decreases for the cDA as

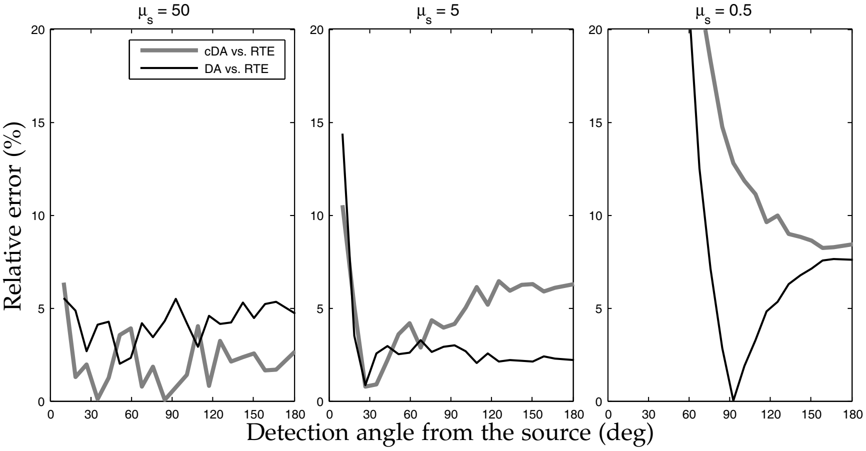

Figure 4.3: Relative error (%) of the exitance on the boundary of the domain computed using the cDA and the DA for different values of μ_s with matched refractive indices.

Table 4.1: The computation times of the models for different values of μ_s.

	Computation time (s)			Relative computation time	
μ_s (mm^{-1})	cDA	DA	RTE	cDA/RTE	DA/RTE
50	8.9	3.3	144.4	0.062	0.023
5	8.8	3.2	134.9	0.065	0.024
0.5	8.6	3.3	135.2	0.064	0.025

the asymptotic theory predicts. The computation times in Table 4.1 show that solving the cDA is comparable with the DA. In addition, solving either the cDA and the DA is much faster than solving the RTE. Thus, the cDA models light propagation more accurately than the standard DA without significant increase in computation time.

4.1.2 Mismatched refractive indices

For the second case, a medium with mismatched refractive indices on the boundary was considered. The refractive indices inside and outside the medium were $n_{\text{in}} = 1.33$ and $n_{\text{out}} = 1$, respectively.

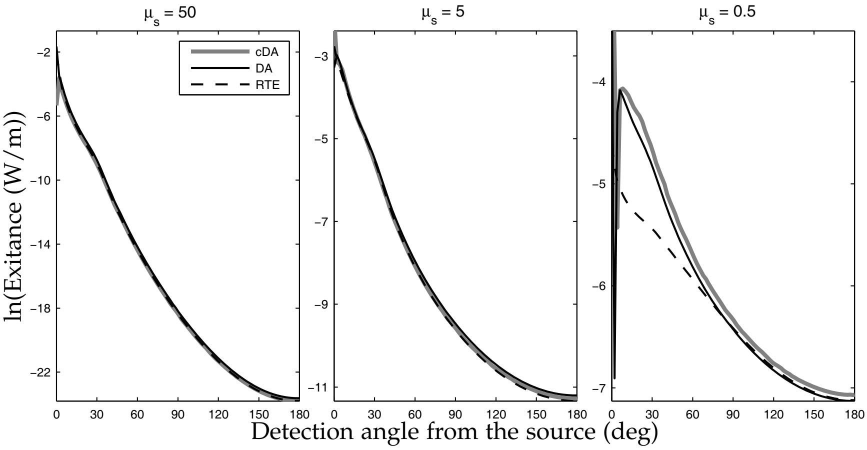

Figure 4.4: Logarithm of the exitance on the boundary of the domain computed using the cDA, the DA and the RTE for different values of μ_s with mismatched refractive indices.

Other optical parameters were the same as before. The radiances on the boundary $(x, y) = (0, -20)$ mm for $\mu_s = 5$ mm^{-1} computed using the cDA, the DA and the RTE are shown in right image of Figure 4.1. The exitances computed using different models are shown in Figure 4.4 and the relative error of the exitance is shown in Figure 4.5.

As it can be seen from Figure 4.1, the approximation to the radiance given by the cDA agrees better with the RTE than the approximation given by the DA. The results in Figure 4.5 show that the relative error of exitance decreases for the cDA when the ratio of absorption and scattering decreases due to the asymptotic theory behind the model. For the DA, the relative error can be large close to the boundary while giving satisfactory results inside the domain. In addition, decrease in ratio of absorption and scattering does not ensure decrease in relative error for the DA.

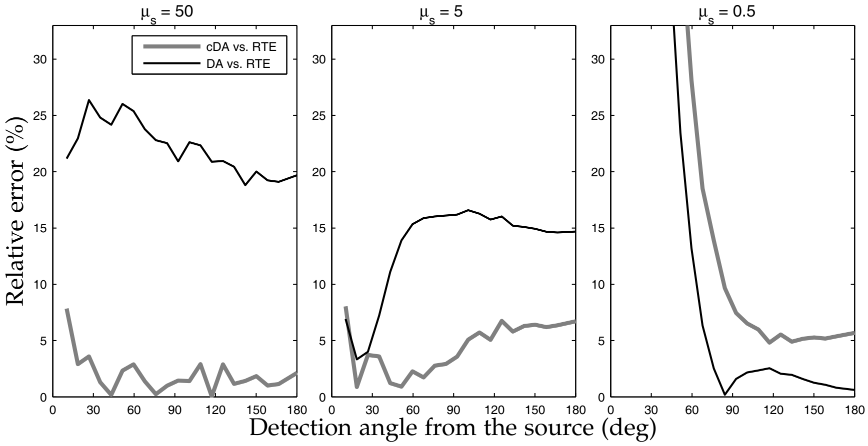

Figure 4.5: Relative error (%) of the exitance on the boundary of the domain computed using the cDA and the DA for different values of μ_s with mismatched refractive indices.

4.2 FORWARD-PEAKED SCATTERING APPROXIMATIONS

In this section, the results for the FP and FPE equations, and the hybrid models are reviewed and discussed based on publication **I** and **III**, and [181]. First, the accuracy of the FP and the FPE equations is evaluated in a homogeneous medium with various optical properties. Then, the performance of the hybrid models is discussed including the effect of the coupling interface location and the computational load compared to the RTE.

4.2.1 Homogeneous medium with different optical properties

The effect of the scattering coefficient and the anisotropy parameter to the accuracy of the forward-peaked scattering approximations against the RTE is investigated below. The solution of the RTE served as a reference for the FP and the FPE. All the models were solved using the FEM as described in Section 3.3.

The simulation domain Ω was a circle with a radius of 20 mm. Total of six cases were considered. In the first three cases (cases 1a–1c), the scattering coefficient was given three values $\mu_s = 0.5\ \mathrm{mm}^{-1}$,

Table 4.2: The scattering coefficient $\mu_{\rm s}$, the absorption coefficient $\mu_{\rm a}$, the anisotropy parameter g, and the reduced scattering coefficient $\mu'_{\rm s}$ of the simulation cases in a homogeneous medium.

	$\mu_{\rm s}(\text{mm}^{-1})$	$\mu_{\rm a}(\text{mm}^{-1})$	g	$\mu'_{\rm s}(\text{mm}^{-1})$
Case 1a	0.5	0.01	0.9	0.05
Case 1b	5	0.01	0.9	0.5
Case 1c	50	0.01	0.9	5
Case 2a	5	0.01	0.3	3.5
Case 2b	5	0.01	0.6	2
Case 2c	5	0.01	0.8	1

$\mu_{\rm s} = 5\ \text{mm}^{-1}$, and $\mu_{\rm s} = 50\ \text{mm}^{-1}$, respectively. The anisotropy parameter and the absorption coefficient were constants in these cases $g = 0.9$ and $\mu_{\rm a} = 0.01\ \text{mm}^{-1}$. These values correspond to a low-scattering, moderate scattering, and highly scattering (diffuse) medium, respectively. In the last three cases (cases 2a–2c), the anisotropy parameter was varied $g = 0.3$, $g = 0.6$, and $g = 0.8$, and the other parameters were constants $\mu_{\rm s} = 5$ and $\mu_{\rm a} = 0.01\ \text{mm}^{-1}$. These values correspond to a nearly uniform scattering, forward dominated scattering, and forward-peaked scattering, respectively. The optical parameters used in simulations are given in Table 4.2. The modulation frequency of the input signal was $f = 100$ MHz. The source was a highly collimated beam with a Gaussian angular dependence.

The FE mesh for the spatial discretization of the domain Ω contained 7169 nodes and 14 058 triangular elements. The same spatial FE mesh was used for all of the models. In the case 1a, the angular discretization consisted of 32 equally spaced angular directions for the FP and the FPE equations, and 64 angular directions for the RTE. In the cases 1b–1c, 16 directions were used for the FP and the FPE equations, and 32 directions were used for the RTE, respectively. The number of the angular directions was chosen by monitoring the convergence of the error of the FE approximations

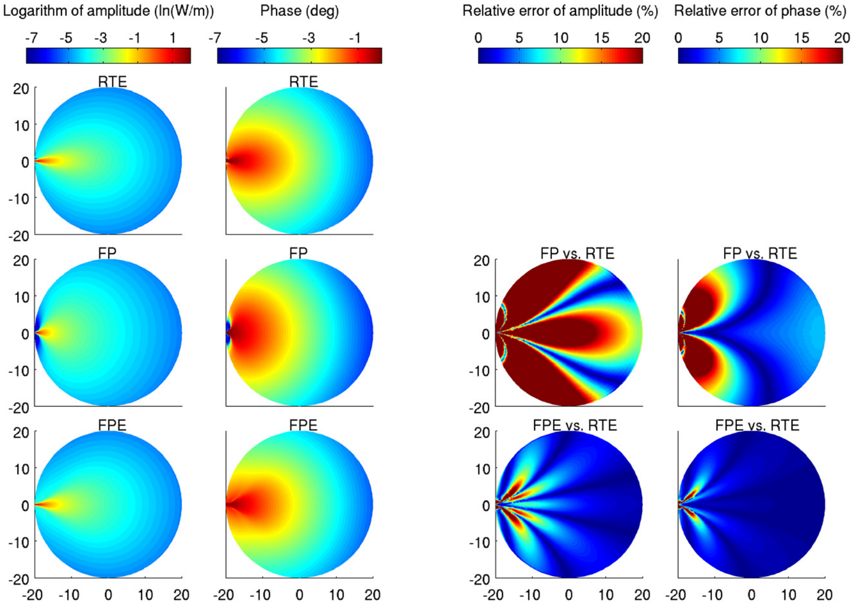

Figure 4.6: Logarithm of the amplitude (first column) and the phase shift (second column) of the fluence computed using the RTE (first row), the FP equation (second row) and the FPE equation (third row) for the case 1a ($\mu_s = 0.5\ mm^{-1}$). The relative errors of the amplitude and the phase shift for the FP and the FPE equations against the RTE are shown in the third and fourth columns.

as a function of the number of angular directions.

The fluences computed using the RTE, the FP equation, and the FPE equation with the different scattering coefficients are shown in Figures 4.6, 4.7, and 4.8 corresponding to the cases 1a–1c, respectively. Moreover, the fluences computed using the different anisotropy parameters are shown in Figures 4.9, 4.10, and 4.11. In addition, the relative errors of the fluences against the RTE are shown.

When scattering is weak (case 1a, Figure 4.6), the FP equation gives large errors close to the source since scattering can not be modeled using an angular diffusion as assumed in the FP equation. For the angular diffusion to take place, several consecutive

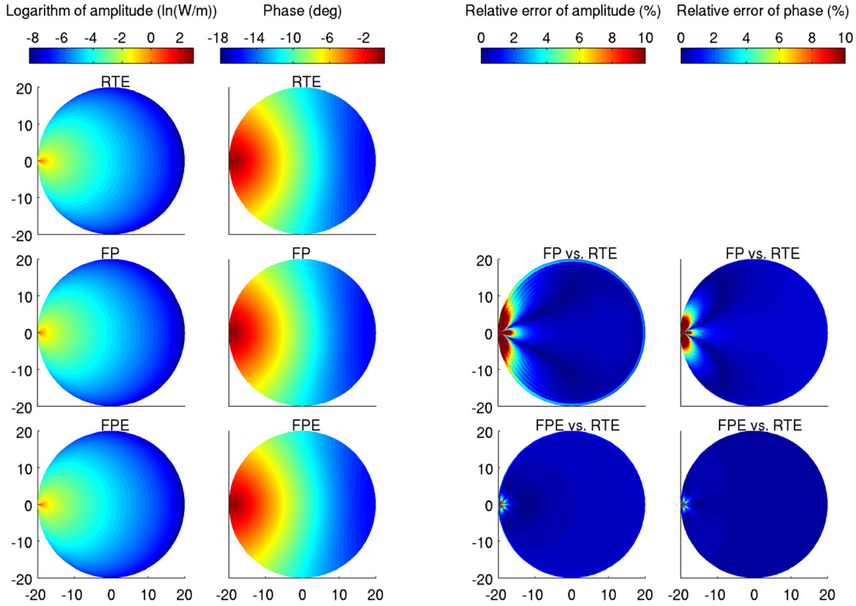

Figure 4.7: Logarithm of the amplitude (first column) and the phase shift (second column) of the fluence computed using the RTE (first row), the FP equation (second row) and the FPE equation (third row) for the case 1b ($\mu_s = 5\ mm^{-1}$). The relative errors of the amplitude and the phase shift for the FP and the FPE equations against the RTE are shown in the third and fourth columns.

forward-peaked scattering events are needed. This length scale is characterized by the transport mean free path l^*, which is in this case $l^* = 20$ mm. As a result, the FP equation gives too smooth solution in the front of the source and underestimates the fluence next to the source since it does not allow back-scattering. On the other hand, the FPE equation agrees relatively well with the RTE expect next to the collimated Gaussian source. This is due to different scattering models used in the RTE and the FPE. This difference occurs at distances less than one transport mean free path l^*. When scattering is moderate (case 1b, Figure 4.7), or strong (case 1c, Figure 4.8), the area next to source where the FP underestimates the fluence becomes smaller. In these cases, the FPE equation gives al-

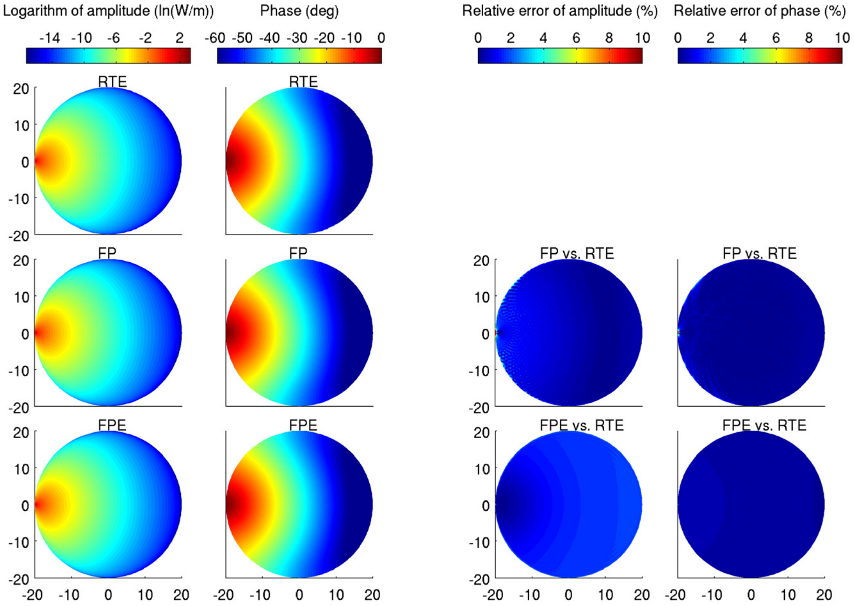

Figure 4.8: Logarithm of the amplitude (first column) and the phase shift (second column) of the fluence computed using the RTE (first row), the FP equation (second row) and the FPE equation (third row) for the case 1c ($\mu_s = 50\ mm^{-1}$). The relative errors of the amplitude and the phase shift for the FP and the FPE equations against the RTE are shown in the third and fourth columns.

most the same results as the RTE in the whole domain with the relative error of less than one per cent.

The results with nearly uniform scattering in Figure 4.9 show that when the assumption of the forward-peaked scattering is violated, the FP equation does not approximate the RTE accurately, as expected. When the anisotropy parameter approaches to unity, the FP equation agrees increasingly well with the RTE. This is in agreement with the earlier studies [177]. In this case, the transport mean free path l^* becomes large compared to the scattering mean free path l_s which is the asymptotic limit used to the derive the FP equation [93]. In contrast to the FP equation, the FPE equation allows back-scattering and is applicable also to the cases with nearly

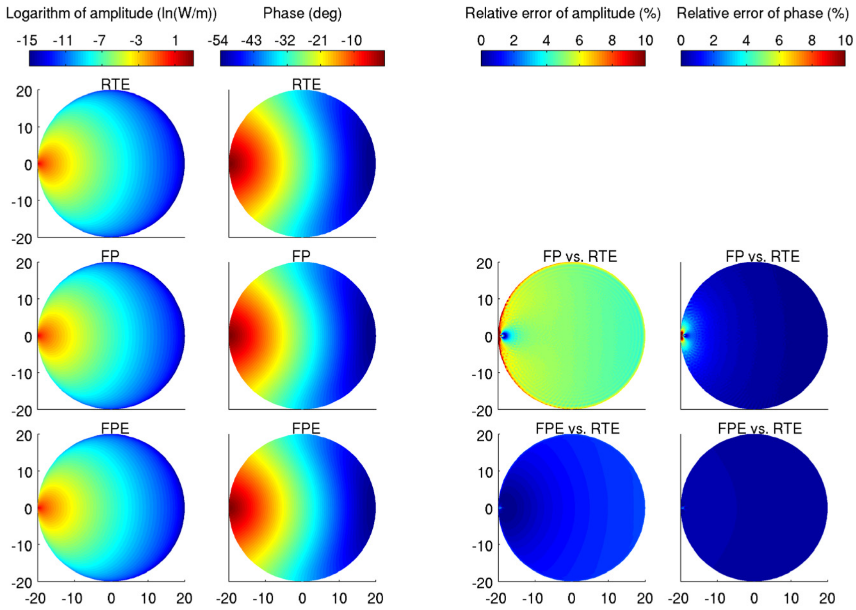

Figure 4.9: Logarithm of the amplitude (first column) and the phase shift (second column) of the fluence computed using the RTE (first row), the FP equation (second row) and the FPE equation (third row) for the case 2a ($g = 0.3$). The relative errors of the amplitude and the phase shift for the FP and the FPE equations against the RTE are shown in the third and fourth columns.

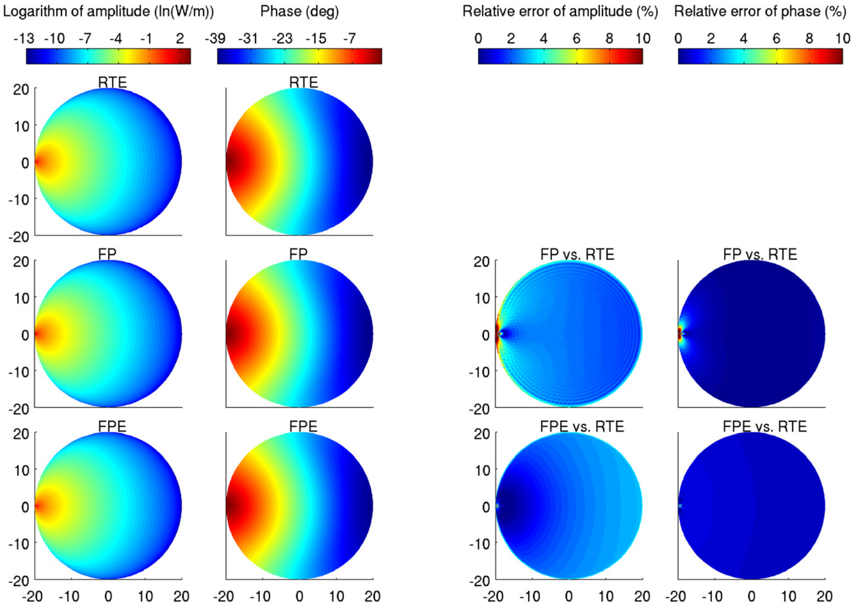

Figure 4.10: Logarithm of the amplitude (first column) and the phase shift (second column) of the fluence computed using the RTE (first row), the FP equation (second row) and the FPE equation (third row) for the case 2b ($g = 0.6$). The relative errors of the amplitude and the phase shift for the FP and the FPE equations against the RTE are shown in the third and fourth columns.

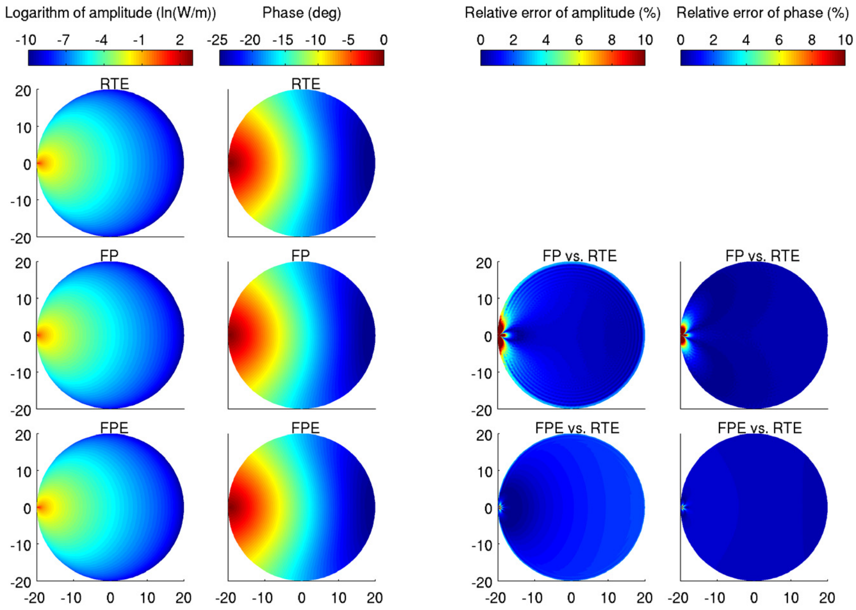

Figure 4.11: Logarithm of the amplitude (first column) and the phase shift (second column) of the fluence computed using the RTE (top row) and the FPE (bottom row) for the case 2c ($g = 0.8$). The relative errors of the amplitude and the phase shift for the FP and the FPE equations against the RTE are shown in the third and fourth columns.

uniform scattering and forward dominated scattering. Hence, the accuracy of the FPE equation does not depend on the anisotropy parameter.

4.2.2 Hybrid forward-peaked-scattering–diffusion approximations

The performance of the proposed coupled models was tested with 2D simulations. The solutions of the cFP-DA and cFPE-DA were compared to the solution of the previously developed cRTE-DA and the solutions of the FP equation, FPE equation, DA, and RTE. The solution of the RTE served as a reference for other methods. All the models were solved using the FEM. The FE approximations of the coupled models were computed using Eq. (3.22) with the corresponding discretized scattering operator Eq. (3.25), (3.26), or (3.27). The quantity of interest was the fluence inside the domain and on the boundary which was computed from the radiance using Eq. (2.6).

Effect of the coupling interface location

First, the effect of the distance between the coupling interface and the source to the accuracy of the solutions was investigated. The simulation domain Ω was a disk with a radius of 20 mm. The optical properties were: the scattering coefficient $\mu_{\mathrm{s}} = 3\ \mathrm{mm}^{-1}$, the absorption coefficient $\mu_{\mathrm{a}} = 0.01\ \mathrm{mm}^{-1}$, and the scattering shape parameter $g = 0.8$. The optical properties were chosen such that, according to theory, light becomes diffuse after propagating a few millimeters from the source. The modulation frequency of the input signal was 100 MHz. Refractive indices inside and outside of the domain were $n_{\mathrm{in}} = n_{\mathrm{out}} = 1$, and thus the reflection parameter $A = 1$ in Eq. (2.11).

In the coupled models, the spatial domain Ω was divided into two different subdomains Ω_{ϕ} and Ω_{Φ}. The subdomain Ω_{ϕ} contained elements within 2.5 mm from the boundary and within a fixed distance from the source. These distances were chosen as 3,

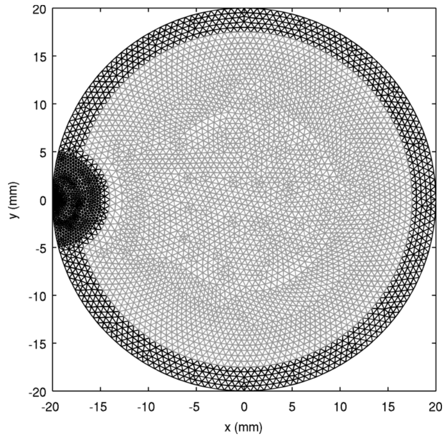

Figure 4.12: Mesh for the coupled model with 6 mm distance between the coupling interface and the source. The FP, FPE or RTE subdomain Ω_ϕ is marked with black and the DA subdomain Ω_Φ with gray.

4, 5, 6, 7, and 10 mm. The subdomain Ω_Φ covered the remaining region. Then, the FE mesh corresponding to each case was created. The FE meshes for the spatial discretization of different cases consisted of 4780-4910 nodes and 9350-9590 triangular elements depending on the location of the interface. The FE mesh with 6 mm distance between the coupling interface and the source is shown in Figure 4.12. For the angular discretization of the FP equation and FPE equation, 16 equally spaced angular directions were used, and for the RTE 64 directions were used.

The fluences were computed using the models as described in Section 3.3. Figure 4.13 shows the fluence computed using the coupled models and the corresponding nodal-wise relative errors against the RTE with 3 mm distance between the coupling interface and the source. The fluences and the relative errors computed with 6 mm distance between the coupling interface and the source are shown in Figure 4.14.

To compare the accuracy of the solutions, the norms of the relative errors of the fluences were computed. Therefore, 10 232 uniformly distributed points inside the domain were taken and the

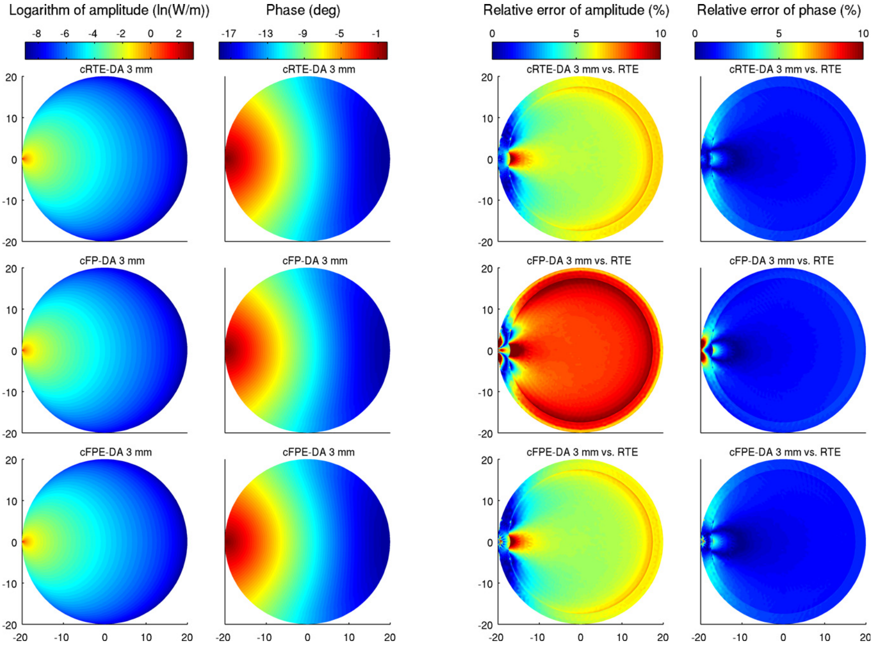

Figure 4.13: Logarithm of amplitudes (first column) and phase shifts (second column) of fluences computed using the cRTE-DA, cFP-DA, and cFPE-DA (rows from top to bottom in the respective order) with 3 mm distance between the coupling interface and the source. Relative errors of amplitudes and phase shifts against the RTE are shown in third and fourth columns.

norm of the relative error was computed

$$\Delta_{\Phi}(\%) = \int_{\Omega} \frac{\Phi - \Phi_{\mathrm{RTE}}}{\Phi_{\mathrm{RTE}}} \mathrm{d}\mathbf{r} \times 100\%. \tag{4.1}$$

The results are shown in Figure 4.15 as a function of distance between the coupling interface and the source. In addition, the norms of the relative errors of the FP, FPE, and DA are shown with vertical lines.

The results for the coupled models show that when the coupling of the models is done too close to the source, when the radiance is not smooth as a function of direction, the relative error is large not only on the coupling interface but in the whole domain. On the other hand, when the coupling is made far enough, after

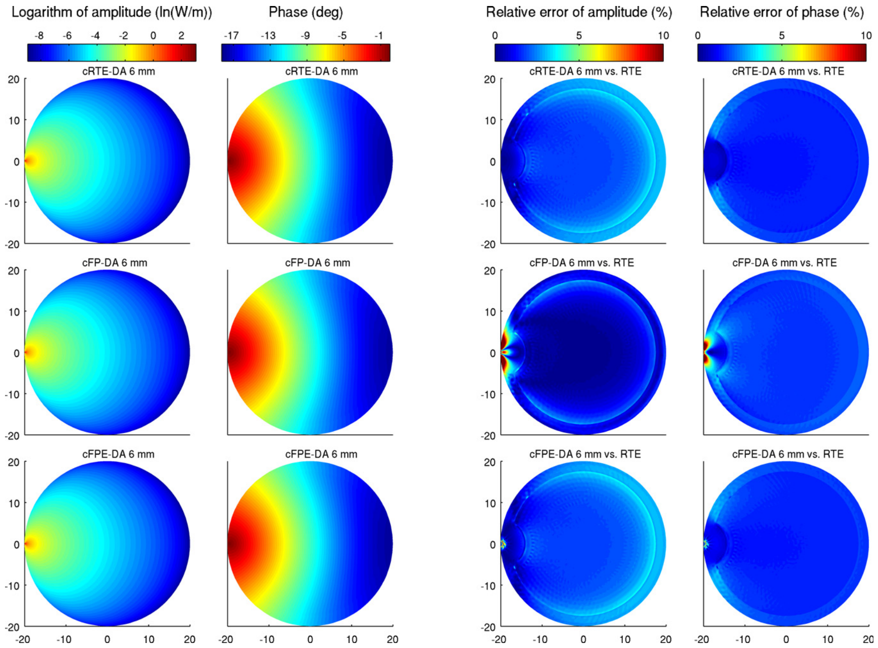

Figure 4.14: Logarithm of amplitudes (first column) and phase shifts (second column) of fluences computed using the cRTE-DA, cFP-DA, and cFPE-DA (rows from top to bottom in the respective order) with 6 mm distance between the coupling interface and the source. Relative errors of amplitudes and phase shifts against the RTE are shown in third and fourth columns.

light has become diffuse, the norm of the relative error decreases for all of the coupled models going under the error level of the DA. Thus, the coupling should be done such that the coupling conditions, Eqs. (2.33c) and (2.33f), are valid. If this is not the case and the DA is used too close to the boundary, or near or inside the low-scattering regions, significant modeling errors can yield [181]. These modeling errors may be amplified even more in the solution of the inverse problem resulting large errors in the reconstructed tomographic images. When the coupling conditions are valid on the coupling interface, the coupled models give almost as good results as using the corresponding FP, FPE, or RTE in the whole domain.

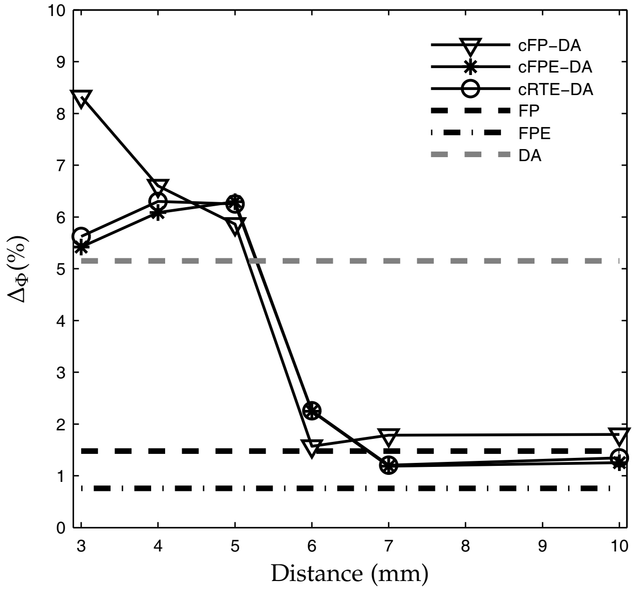

Figure 4.15: Norm of the relative error of the fluence $\Delta_\Phi(\%)$ against the distance between the coupling interface and the source.

Computational load

Next, the computational load of the models was compared. For the coupled models, the distance between the coupling interface and the source was 6 mm. The FE matrix sizes, the number of nonzero elements, and the (sparse) matrix filling ratios were computed, and the FE matrix assembling times and the FE matrix equation solution times were recorded. The results are given in Table 4.3. The computations were done on a workstation with two Intel Xeon quadracore processors clocked at 2.27 GHz and 48 GB of RAM using MATLAB® version 7.10 (R2010a), (The MathWorks, Inc.). The matrix equation was solved using MATLAB's function "mldivide", which implements the appropriate solver for (complex sparse) matrices using LAPACK.

The FPE approximations have a few advantages in the assembling of the FE matrices over the RTE. In the case of the FP, the

Table 4.3: The FE matrix sizes, number of non-zero elements, matrix filling ratios, FE matrix assembling times t_{mat}, relative FE matrix assembling times, FE matrix equation solution times t_{sol}, and relative FE matrix equation solution times.

	Matrix size	Non-zeros	Filling ratio (%)	t_{mat}(min)	$t_{\mathrm{mat}}/t_{\mathrm{mat,RTE}}$(%)	t_{sol}(min)	$t_{\mathrm{sol}}/t_{\mathrm{sol,RTE}}$(%)
RTE	306 112×306 112	135 327 744	0.144	8.389	-	6.363	-
DA	4783×4783	33 039	0.144	0.060	0.72	0.001	0.02
FP	76 528×76 528	1 585 872	0.027	0.466	5.56	0.208	3.27
FPE	76 528×76 528	8 457 984	0.144	0.851	10.17	0.220	3.45
cRTE-DA	116 266×116 266	47 651 710	0.353	2.087	24.88	0.879	13.82
cFP-DA	31 450×31 450	600 180	0.061	0.209	2.50	0.039	0.61
cFPE-DA	31 450×31 450	3 014 852	0.305	0.278	3.32	0.045	0.70

blocks related to the angular part of the FE matrix are sparse due to the angular differential operator in contrast to the FPE and RTE in which the blocks are full. Hence, the assembling of the FE matrices is fast and the amount of required memory is smaller. Moreover, the smooth integral operator in the FPE can be computed efficiently using the matrix outer products of one-dimensional integrals. This is not the case for the RTE. Since smaller amount of angular directions are needed for the FP and FPE, the computation times and the amount of required memory are much smaller compared to the RTE. This feature is important especially in 3D. In addition, using the coupled models reduces the computation time even more. The computation times of the coupled FP-DA and FPE-DA are almost ten times lower for the matrix assembling and almost twenty times lower for the matrix equation solution than that of the coupled RTE-DA. Thus, using the coupled models leads to reduction in computational load compared to the RTE while preserving sufficient accuracy.

4.3 RTE WITH PIECEWISE CONSTANT REFRACTIVE INDEX

The FE approximation of coupled RTE model with piecewise constant refractive index was introduced in publication **IV**. The motivation was to develop a model which would allow different refractive indices, for instance for each tissue type, inside the medium and would be applicable in arbitrary geometries with complex interfaces between the subdomains.

The performance of the proposed cRTE was tested with 2D simulations. The simulation domain Ω was a square $[-20, 20]$ mm $\times[-20, 20]$ mm. The solution of the cRTE was compared to the solution of the Monte Carlo simulation. In the MC simulations, a photon packet method, originally developed in [182] was modified to allow computation in complex inhomogeneous geometries represented by FE meshes with piece-wise constant refractive indices [33]. The number of simulated photons in each simulation was 500×10^6 with the average statistical relative error less than 5×10^{-4}. The effect of refractive index variations on the boundary measurements was investigated.

4.3.1 Effect of refractive index contrast deep inside the target

First, a square inclusion with different refractive index located deep inside the target was investigated as shown in Figure 4.16. The domain was divided into two disjoint subdomains Ω_1 and Ω_2 corresponding to the regions with different refractive indices. The FE mesh for the spatial discretization of the subdomain Ω_1 is marked with dark gray and the subdomain Ω_2 is marked with light gray in Figure 4.16. The FE meshes consisted of 4015 and 241 nodes and 7749 and 428 triangular elements for the subdomains Ω_1 and Ω_2, respectively. For the angular discretization, 64 equally spaced angular directions were used for the both subdomains.

The scattering and absorption properties were the same in the both subdomains: $\mu_\mathrm{s} = 1$ mm^{-1}, $\mu_\mathrm{a} = 0.01$ mm^{-1}, $g = 0.8$. The refractive index of the subdomain Ω_1 was $n_1 = 1.4$ and the refractive index of the subdomain Ω_2 was varied using values $n_2 = 1, 1.05, ..., 2$. The refractive index of the exterior was $n_\mathrm{out} = 1$.

The fluences computed using the cRTE and the MC are shown in Figure 4.17. In addition, per cent relative error of the fluence computed using the cRTE against the MC is shown. Figure 4.18 shows the fluence on the boundary computed using the cRTE as a function of distance along the boundary. In addition, per cent rel-

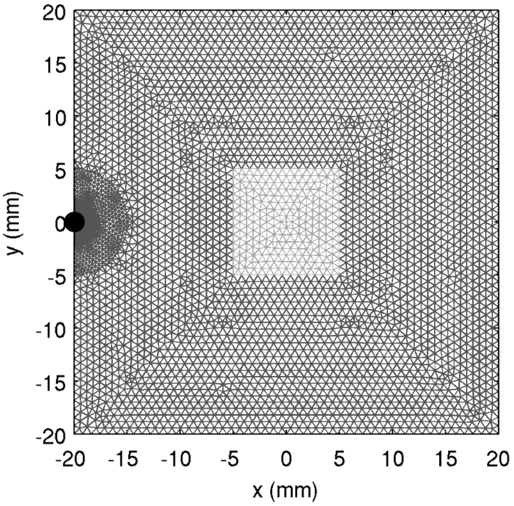

Figure 4.16: Mesh for the domain with a square inclusion inside the target. The subdomain Ω_1 *is marked with dark gray and the subdomain* Ω_2 *with light gray. The source is marked with a black circle.*

ative difference against the case with $n_2 = 1.4$ (matched refractive indices) is shown. The mean of the relative difference of the boundary measurements against the case with $n_2 = 1.4$ was computed for the amplitude and for the phase as

$$\Delta_{|\Phi|}(\%) = \text{mean}\left(\left|\frac{|\Phi(\mathbf{r})| - |\Phi_{\text{ref}}(\mathbf{r})|}{|\Phi_{\text{ref}}(\mathbf{r})|}\right|\right) \times 100\%, \tag{4.2}$$

$$\Delta_{\arg(\Phi)}(\%) = \text{mean}\left(\left|\frac{\arg(\Phi(\mathbf{r})) - \arg(\Phi_{\text{ref}}(\mathbf{r}))}{\arg(\Phi_{\text{ref}}(\mathbf{r}))}\right|\right) \times 100\%, \tag{4.3}$$

where $\Phi_{\text{ref}}(\mathbf{r})$ is the solution with $n_2 = 1.4$, $|\cdot|$ is the absolute value and $\arg(\cdot)$ is the phase angle. These are shown in Figure 4.19.

The results in Figure 4.17 show that when the refractive index of the inclusion is lower ($n_2 = 1$) than the refractive index of the background ($n_1 = 1.4$) strong reflection occurs when light enters the inclusion. In contrast, when the refractive index is larger ($n_2 = 2$) than the background, more light is transmitted into the inclusion and total internal reflection takes place when light exits the inclusion, as expected. When the cRTE and the MC solutions are com-

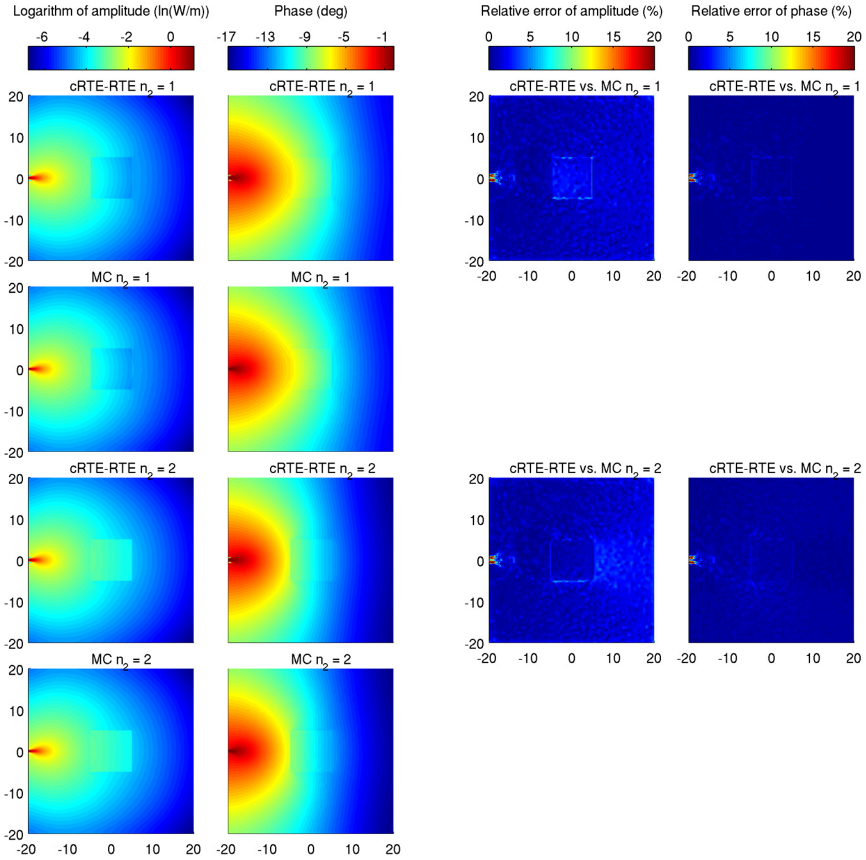

Figure 4.17: Logarithm of the amplitude (first column) and the phase shift (second column) of the fluence computed using the cRTE model (first and third row) and using the MC (second and fourth row) in a medium with a square inclusion. Refractive index of the inclusion is $n_2 = 1$ (first and second row) and $n_2 = 2$ (third and fourth row). Per cent relative error of the amplitude and the phase shift against the MC are shown in third and fourth columns.

pared, a very good agreement is found and the relative error is under three per cent for both the amplitude and the phase further from the source.

The results show that the fluence on the boundary is changed significantly when the refractive index is not constant within the target. When the refractive index of the inclusion is lower ($n_2 = 1$)

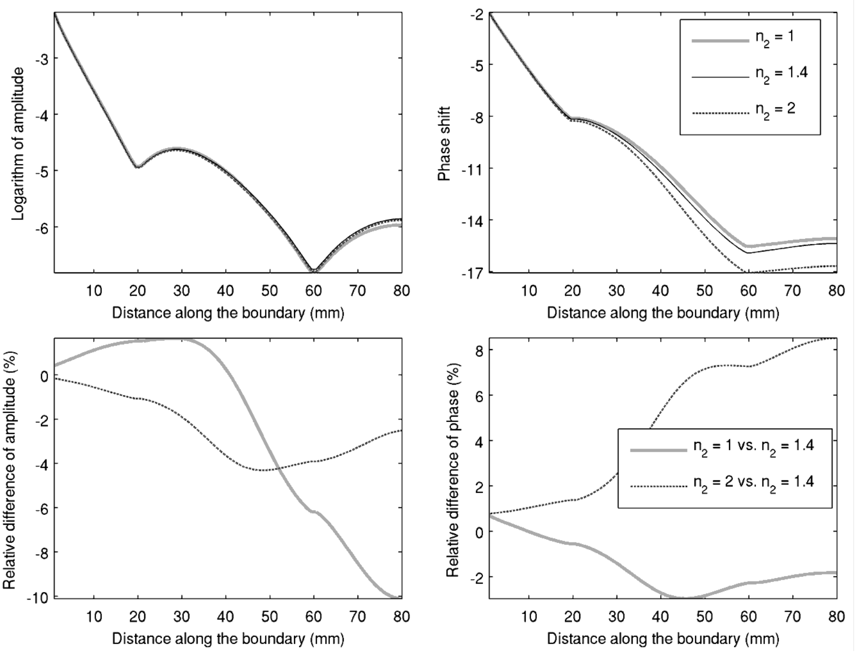

Figure 4.18: Top row: Logarithm of the amplitude (left) and the phase shift (right) of the fluence computed using the cRTE model for $n_2 = 1$ *(gray line),* $n_2 = 1.4$ *(black line) and* $n_2 = 2$ *(dashed line) as a function of distance along the boundary. Bottom row: Per cent relative difference of the amplitude (bottom left) and the phase shift (bottom right) against the case* $n_2 = 1.4$.

than the background, the model predicts increase in the amplitude next to the source due to the reflection from the inclusion. At the opposite side of the target, the amplitude is up to 10 % lower compared to the fluence without the inclusion. For the phase, smaller values are predicted by the model next to the source since photons can arrive earlier to the boundary due to the possible reflection. If the refractive index is larger ($n_2 = 2$) than the background, the amplitude is one to four per cent lower compared to the fluence obtained without the inclusion. For the phase, up to 8 % larger values are obtained since photons can arrive later to the boundary due to the internal reflection inside the inclusion. These contrasts in the boundary data are larger than the typical measurement er-

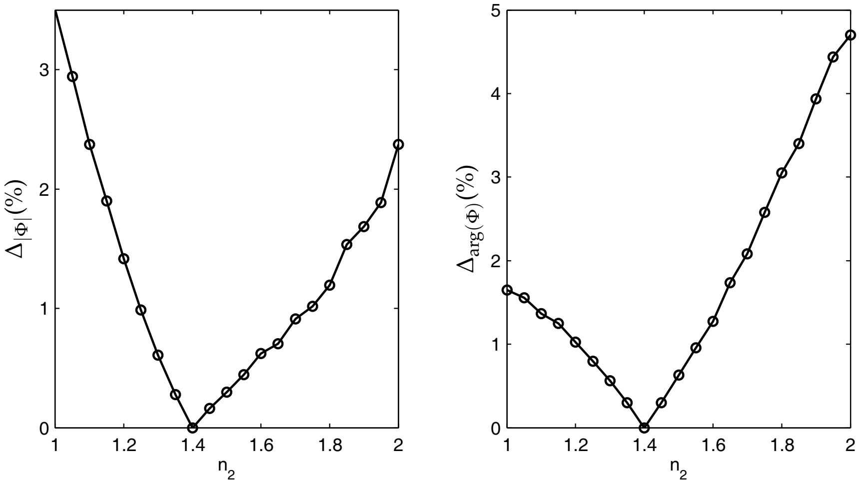

Figure 4.19: Mean per cent relative difference of the amplitude $\Delta_{|\Phi|}$ (left) and the phase shift $\Delta_{\arg(\Phi)}$ (right) of the fluence on the boundary as a function of refractive index of the inclusion n_2.

rors [3]. Therefore, these contrasts can be important in the image reconstruction problem since even small, both modeling and measurement, errors are amplified when solving the inverse problem.

4.3.2 Effect of refractive index contrast close to the boundary

In the second case, the inclusion located close to the boundary of the target as shown in Figure 4.20. The FE meshes consisted of 3476 and 1051 nodes and 6398 and 1779 triangular elements for the subdomains Ω_1 and Ω_2, respectively. The number of angular directions was the same as before. In addition, the scattering and absorption properties were the same as in the first case in Section 4.3.1. Again, the refractive index of the background was set to $n_1 = 1.4$ and the refractive index of the layer n_2 was varied.

The fluences computed using the cRTE and the MC are shown in Figure 4.21 for $n_2 = 1$ and for $n_2 = 2$. In addition, the relative error of the fluence computed using the cRTE is shown. Figure 4.22 shows the fluence on the boundary for $n_2 = 1$, $n_2 = 1.4$ and

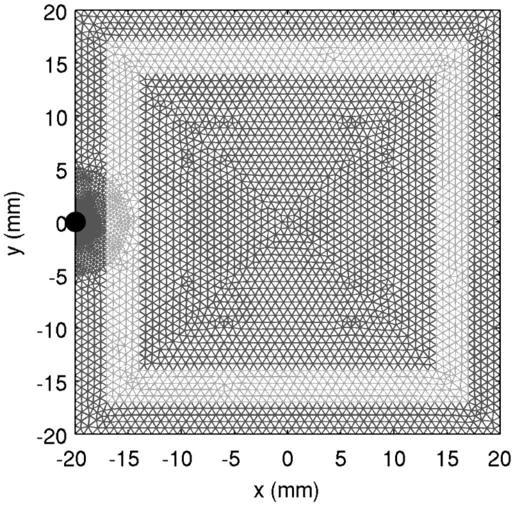

Figure 4.20: Mesh for the domain with a layer inclusion close to the boundary of the domain. The subdomain Ω_1 is marked with dark gray and the subdomain Ω_2 with light gray. The source is marked with a black circle.

for $n_2 = 2$. The mean of the relative difference of the boundary measurements against the case with $n_2 = 1.4$ (matched refractive indices) is shown in Figure 4.23.

The results in Figure 4.21 show that for a smaller refractive index value ($n_2 = 1$) strong reflection occurs in front of the source when light enters the layer, as expected. As a result, a major portion of light remains between the layer and the boundary of the target. In addition, the part of the light which is transmitted through the layer in the front of the source gets reflected at the opposite side of the layer. Hence, some part of the light remains trapped inside the inner boundary of the layer. In contrast, for a larger refractive index ($n_2 = 2$) more light is transmitted into the layer, which acts as a waveguide, and light propagates along the layer. This is due to the total internal reflection. The cRTE and the MC solutions agree relative well even though some differences can be seen at the right-hand side of the target between the layer and the boundary of the target.

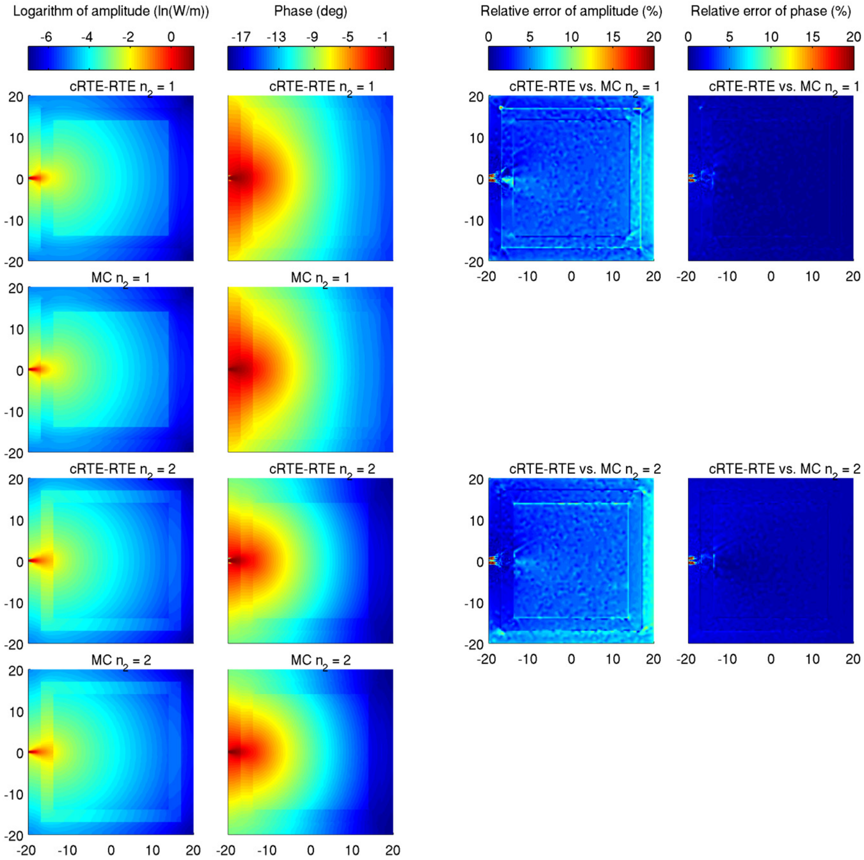

Figure 4.21: Logarithm of the amplitude (first column) and the phase shift (second column) of the fluence computed using the cRTE model (first and third row) and using the MC (second and fourth row) in a medium with a layer inclusion. Refractive index of the inclusion is $n_2 = 1$ (first and second row) and $n_2 = 2$ (third and fourth row). Per cent relative error of the amplitude and the phase shift against the MC are shown in third and fourth columns.

The results in Figure 4.22 show that up to 15 % larger and 25 % smaller values can be measured for the amplitude next to the source and at the opposite side of the target, respectively, when the refractive index n_2 is smaller than the background in comparison to the fluences computed without the inclusion. For the phase, up to 15 % difference can be obtained. Based on the results it can be con-

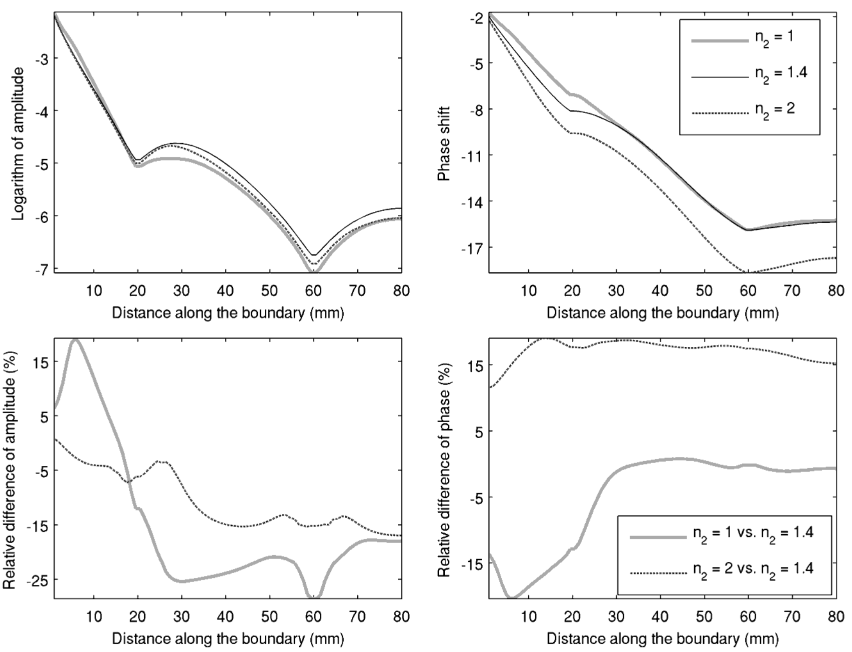

Figure 4.22: Top row: Logarithm of the amplitude (left) and the phase shift (right) of the fluence computed using the cRTE model for $n_2 = 1$ (gray line), $n_2 = 1.4$ (black line) and $n_2 = 2$ (dashed line) as a function of distance along the boundary. Bottom row: Per cent relative difference of the amplitude (bottom left) and the phase shift (bottom right) against the case $n_2 = 1.4$.

cluded that if the internal refractive index change occurs close to the boundary, significant changes in the boundary measurements can be obtained.

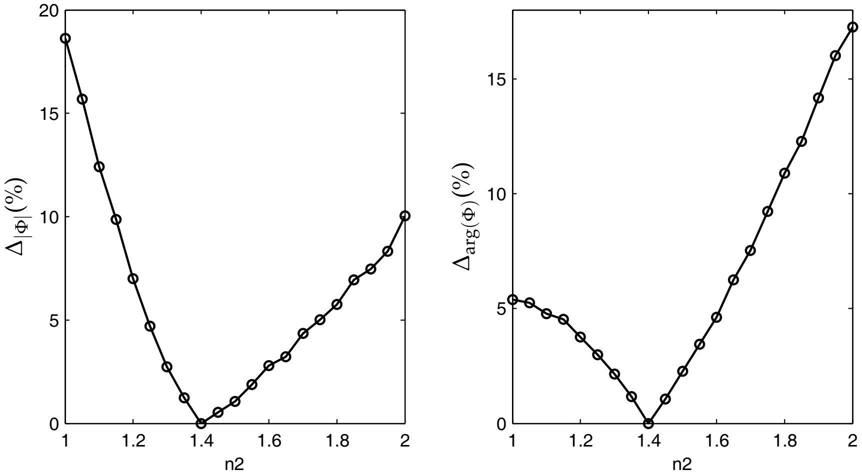

Figure 4.23: Mean per cent relative difference of the amplitude $\Delta_{|\Phi|}$ *(left) and the phase shift* $\Delta_{\arg(\Phi)}$ *(right) of the fluence on the boundary as a function of refractive index of the layer* n_2*.*

5 Summary and conclusions

In this thesis, computational methods based on forward-peaked scattering approximations and hybrid models for modeling light propagation in biological tissues were developed. The gold standard model for light propagation in tissue-like media is the radiative transport equation. However, solving the RTE is computationally expensive and therefore it is typically approximated using the diffusion approximation due to strong scattering of NIR light in tissues. The DA does not model light propagation accurately near the boundaries and sources, and in low-scattering regions such as the cerebrospinal fluid surrounding the brain and in the ventricles. The goal of this thesis was to develop methods which are computationally less expensive to solve than the RTE but still more accurate than the DA. The developed methods were based on four approaches.

As the first approach, the corrected diffusion approximation, which corrects for the error made by the DA near the boundaries, was numerically implemented. The cDA is based on an asymptotic analysis of the RTE when scattering is much stronger than absorption. The analysis yields an additive correction term for the DA near the boundary which satisfies 1D RTE. The numerical implementation included solving the DA using the FEM and plane wave solution of the 1D RTE in a half space. The cDA can be used in complex geometries with spatially varying parameter distributions and it can be utilized in existing numerical or analytical solution methods of the DA. The results show that the cDA can correct the error made by the DA near the boundary. Moreover, computing the correction term does not increase the computation time significantly compared to the DA.

As the second approach, Fokker-Planck-Eddington type approximations, which take into account forward-peaked and large angle scattering analytically when approximating the RTE, were utilized. More precisely, the Fokker-Planck and the Fokker-Planck-

Eddington equations were used as light transport models. Since these approximations take into account forward-peaked scattering analytically, coarser angular discretization can be used compared with the RTE leading to reduction in computational load. As the third approach, hybrid models which utilize the FPE and the DA as light transport models in different subdomains were developed. The FPE approximations were used in those parts of the domain in which the DA is not valid, such as in low-scattering regions and near the boundaries, and the DA was used elsewhere. The models were coupled on the interfaces between the subdomains and the resulting system of equations was solved simultaneously. The FPE approximations and the hybrid models were numerically solved using the FEM.

The proposed FPE approximations and the hybrid models were tested using numerical simulations and the results were compared to the RTE and the DA. The results show that the accuracy of the FP equation increases as the anisotropy parameter g approaches to unity. On the other hand, the FPE, which takes into account both forward-peaked and large angle scattering, is applicable over a wide range of anisotropy parameters. In general, the results show that FPE approximates the RTE with good accuracy in biological tissues. In addition, the results show that the hybrid models describe light propagation well when the coupling of the models is done such that the assumptions of the DA are valid on the coupling interfaces. These assumptions are typically fulfilled in highly scattering media away from the boundaries, sources, and low-scattering regions. Moreover, using the hybrid models can reduce the computation time significantly over the RTE depending on the size of the domain, the optical properties and the subdomain divisions.

The fourth approach included developing a RTE based coupled model which is applicable when the refractive index is piece-wise constant within the domain. In the cRTE model, light propagation in each subdomain with constant refractive index is modeled using the RTE and the equations are coupled using boundary conditions describing Fresnel reflection and transmission on the interfaces between the subdomains. The resulting coupled system of RTEs was numerically solved using the FEM. The results show that the cRTE describes light propagation accurately in comparison with the Monte Carlo method. In addition, the results show that neglecting internal refractive index changes can lead to significant errors in the boundary measurements of scattered light.

Biomedical optics provides a unique opportunity for functional imaging. The information given by different imaging modalities ranges from molecular environment to changes in blood volume and oxygenation. The reconstruction of 3D tomographic images of these quantities requires an accurate and computationally feasible mathematical model for light propagation inside the tissues. By combining the methods developed in this thesis it may possible to use hybrid models and forward-peaked scattering approximations to reduce computational load and to take into account the refractive index variations between different tissues types. This combined model could provide a computationally feasible way to model light propagation in 3D with sufficient accuracy.

In the future, the developed methods will be applied to image reconstruction problem of DOT, fDOT and QPAT. In addition, the methods can be applicable also in other areas of science in which the RTE describes propagation particles such as in radiation therapy treatment planning of cancer and radiative heat transfer.

Bibliography

[1] S. Arridge, "Optical tomography in medical imaging," *Inverse Problems* **15,** 41–41 (1999).

[2] A. Gibson, J. Hebden, and S. R. Arridge, "Recent advances in diffuse optical imaging," *Physics in medicine and biology* **50,** R1 (2005).

[3] I. Nissilä, T. Noponen, K. Kotilahti, T. Katila, L. Lipiäinen, T. Tarvainen, M. Schweiger, and S. Arridge, "Instrumentation and calibration methods for the multichannel measurement of phase and amplitude in optical tomography," *Review of Scientific Instruments* **76,** 044302 (2005).

[4] I. Nissilä, K. Kotilahti, K. Fallström, and T. Katila, "Instrumentation for the accurate measurement of phase and amplitude in optical tomography," *Review of Scientific Instruments* **73,** 3306 (2002).

[5] D. Piao, H. Dehghani, S. Jiang, S. Srinivasan, and B. W. Pogue, "Instrumentation for video-rate near-infrared diffuse optical tomography," *Review of Scientific Instruments* **76,** – (2005).

[6] D. J. Cuccia, F. Bevilacqua, A. J. Durkin, and B. J. Tromberg, "Modulated imaging: quantitative analysis and tomography of turbid media in the spatial-frequency domain," *Optics Letters* **30,** 1354–1356 (2005).

[7] V. Lukic, V. A. Markel, and J. C. Schotland, "Optical tomography with structured illumination," *Optics Letters* **34,** 983–985 (2009).

[8] N. Ducros, C. D'Andrea, G. Valentini, T. Rudge, S. Arridge, and A. Bassi, "Full-wavelet approach for fluorescence diffuse

optical tomography with structured illumination," *Optics Letters* **35,** 3676–3678 (2010).

[9] C. D'Andrea, N. Ducros, A. Bassi, S. Arridge, and G. Valentini, "Fast 3D optical reconstruction in turbid media using spatially modulated light," *Biomedical Optics Express* **1,** 471–481 (2010).

[10] J. Ripoll, R. B. Schulz, and V. Ntziachristos, "Free-Space Propagation of Diffuse Light: Theory and Experiments," *Physical Review Letters* **91,** 103901 (2003).

[11] R. B. Schulz, J. Ripoll, and V. Ntziachristos, "Noncontact optical tomography of turbid media," *Optics Letters* **28,** 1701–1703 (2003).

[12] S. Arridge and J. Schotland, "Optical tomography: forward and inverse problems," *Inverse Problems* **25,** 123010 (2009).

[13] F. E. W. Schmidt, M. E. Fry, E. M. C. Hillman, J. C. Hebden, and D. T. Delpy, "A 32-channel time-resolved instrument for medical optical tomography," *Review of Scientific Instruments* **71,** 256–265 (2000).

[14] C. H. Schmitz, M. Lcker, J. M. Lasker, A. H. Hielscher, and R. L. Barbour, "Instrumentation for fast functional optical tomography," *Review of Scientific Instruments* **73,** 429–439 (2002).

[15] J. M. Lasker, J. M. Masciotti, M. Schoenecker, C. H. Schmitz, and A. H. Hielscher, "Digital-signal-processor-based dynamic imaging system for optical tomography," *Review of Scientific Instruments* **78,** – (2007).

[16] A. Yodh and B. Chance, "Spectroscopy and imaging with diffusing light," *Physics Today* **48,** 34–41 (1995).

[17] D. Boas, D. Brooks, E. Miller, C. DiMarzio, M. Kilmer, R. Gaudette, and Q. Zhang, "Imaging the body with diffuse optical tomography," *Signal Processing Magazine, IEEE* **18,** 57–75 (2001).

[18] A. Hielscher, A. Bluestone, G. Abdoulaev, A. Klose, J. Lasker, M. Stewart, U. Netz, and J. Beuthan, "Near-infrared diffuse optical tomography," *Disease markers* **18,** 313–337 (2002).

[19] S. Diamond, T. Huppert, V. Kolehmainen, M. Franceschini, J. Kaipio, S. Arridge, and D. Boas, "Dynamic physiological modeling for functional diffuse optical tomography," *Neuroimage* **30,** 88–101 (2006).

[20] A. Bluestone, G. Abdoulaev, C. Schmitz, R. Barbour, and A. Hielscher, "Three-dimensional optical tomography of hemodynamics in the human head," *Optics Express* **9,** 272–286 (2001).

[21] A. Corlu, R. Choe, T. Durduran, M. A. Rosen, M. Schweiger, S. R. Arridge, M. D. Schnall, and A. G. Yodh, "Three-dimensional in vivo fluorescence diffuse optical tomography of breast cancer in humans," *Optics Express* **15,** 6696–6716 (2007).

[22] B. Cox, J. G. Laufer, S. R. Arridge, and P. C. Beard, "Quantitative spectroscopic photoacoustic imaging: a review," *Journal of Biomedical Optics* **17,** 061202–1–061202–22 (2012).

[23] J. Kaipio and E. Somersalo, *Statistical and computational inverse problems* (Springer Science+ Business Media, Inc., 2005).

[24] K. Ren, "Recent Developments in Numerical Techniques for Transport-Based Medical Imaging Methods," *Communications in Computational Physics* **8,** 1–50 (2010).

[25] G. Bal, "Inverse transport theory and applications," *Inverse Problems* **25,** 053001 (48pp) (2009).

[26] L. Wang and H. Wu, *Biomedical optics: principles and imaging* (Wiley-Blackwell, 2007).

[27] A. Ishimaru, *Wave Propagation and Scattering in Random Media (Academic, New York)* (IEEE Press, 1978).

[28] A. Hielscher, R. Alcouffe, and R. Barbour, "Comparison of finite-difference transport and diffusion calculations for photon migration in homogeneous and heterogeneous tissues," *Physics in Medicine and Biology* **43,** 1285–1302 (1998).

[29] L. Wang and S. Jacques, "Hybrid model of Monte Carlo simulation and diffusion theory for light reflectance by turbid media," *Journal of Optical Society of America A* **10,** 1746–1752 (1993).

[30] S. Arridge, H. Dehghani, M. Schweiger, and E. Okada, "The finite element model for the propagation of light in scattering media: a direct method for domains with nonscattering regions," *Medical Physics* **27,** 252–264 (2000).

[31] S. Arridge, J. Kaipio, V. Kolehmainen, M. Schweiger, E. Somersalo, T. Tarvainen, and M. Vauhkonen, "Approximation errors and model reduction with an application in optical diffusion tomography," *Inverse Problems* **22,** 175 (2006).

[32] V. Kolehmainen, M. Schweiger, I. Nissilä, T. Tarvainen, S. Arridge, and J. Kaipio, "Approximation errors and model reduction in three-dimensional diffuse optical tomography," *Journal of Optical Society of America A* **26,** 2257–2268 (2009).

[33] T. Tarvainen, V. Kolehmainen, A. Pulkkinen, M. Vauhkonen, M. Schweiger, S. Arridge, and J. Kaipio, "An approximation error approach for compensating for modelling errors in DOT," *Inverse Problems* **26,** 015005 (2010).

[34] A. Kim, "Correcting the diffusion approximation at the boundary," *Journal of Optical Society of America A* **28,** 1007–1015 (2011).

[35] C. Leakeas and E. Larsen, "Generalized Fokker-Planck approximations of particle transport with highly forward-peaked scattering," *Nuclear Science and Engineering* **137,** 236–250 (2001).

[36] P. González-Rodríguez and A. Kim, "Light propagation in tissues with forward-peaked and large-angle scattering," *Applied Optics* **47,** 2599–2609 (2008).

[37] G. Bal, "Radiative transfer equations with varying refractive index: a mathematical perspective," *Journal of Optical Society of America A* **23,** 1639–1644 (2006).

[38] K. Case and P. Zweifel, *Linear transport theory* (Addison-Wesley Educational Publishers Inc., US, 1967).

[39] S. Chandrasekhar, *Radiative transfer* (Oxford University Press, London, 1950).

[40] J. J. Duderstadt and W. R. Martin, *Transport theory* (John Wiley & Sons, 1979).

[41] M. I. Mishchenko, "Vector Radiative Transfer Equation for Arbitrarily Shaped and Arbitrarily Oriented Particles: a Microphysical Derivation from Statistical Electromagnetics," *Applied Optics* **41,** 7114–7134 (2002).

[42] M. I. Mishchenko, "Poynting–Stokes tensor and radiative transfer in discrete random media: the microphysical paradigm," *Optics Express* **18,** 19770–19791 (2010).

[43] J. Ripoll, "Derivation of the scalar radiative transfer equation from energy conservation of Maxwell's equations in the far field," *Journal of the Optical Society of America A* **28,** 1765–1775 (2011).

[44] L. Ryzhik, G. Papanicolaou, and J. B. Keller, "Transport equations for elastic and other waves in random media," *Wave Motion* **24,** 327 – 370 (1996).

[45] G. Bal, "Kinetics of scalar wave fields in random media," *Wave Motion* **43,** 132 – 157 (2005).

[46] G. E. Thomas and K. Stamnes, *Radiative transfer in the atmosphere and ocean* (Cambridge University Press, 2002).

[47] G. B. Rybicki and A. P. Lightman, *Radiative processes in astrophysics* (John Wiley & Sons, 2008).

[48] E. E. Lewis and W. F. Miller, *Computational methods of neutron transport* (John Wiley and Sons, Inc., New York, NY, 1984).

[49] S. R. Arridge and J. C. Hebden, "Optical imaging in medicine: II. Modelling and reconstruction," *Physics in Medicine and Biology* **42,** 841 (1997).

[50] M. H. Kalos and P. A. Whitlock, *Monte carlo methods* (John Wiley & Sons, 2008).

[51] S. R. Arridge, M. Hiraoka, and M. Schweiger, "Statistical basis for the determination of optical pathlength in tissue," *Physics in Medicine and Biology* **40,** 1539 (1995).

[52] L. Wang, S. L. Jacques, and L. Zheng, "MCML–Monte Carlo modeling of light transport in multi-layered tissues," *Computer Methods and Programs in Biomedicine* **47,** 131 – 146 (1995).

[53] D. Boas, J. Culver, J. Stott, and A. Dunn, "Three dimensional Monte Carlo code for photon migration through complex heterogeneous media including the adult human head," *Optics Express* **10,** 159–170 (2002).

[54] Y. Fukui, Y. Ajichi, and E. Okada, "Monte Carlo Prediction of Near-Infrared Light Propagation in Realistic Adult and Neonatal Head Models," *Applied Optics* **42,** 2881–2887 (2003).

[55] J. Heiskala, I. Nissilä, T. Neuvonen, S. Järvenpää, and E. Somersalo, "Modeling anisotropic light propagation in a realistic model of the human head," *Applied Optics* **44,** 2049–2057 (2005).

[56] E. Alerstam, T. Svensson, and S. Andersson-Engels, "Parallel computing with graphics processing units for high-speed Monte Carlo simulation of photon migration," *Journal of Biomedical Optics* **13,** 060504–060504–3 (2008).

[57] Q. Fang and D. A. Boas, "Monte Carlo simulation of photon migration in 3D turbid media accelerated by graphics processing units," *Optics Express* **17,** 20178–20190 (2009).

[58] Q. Fang, "Mesh-based Monte Carlo method using fast ray-tracing in Plücker coordinates," *Biomedical Optics Express* **1,** 165–175 (2010).

[59] N. Ren, J. Liang, X. Qu, J. Li, B. Lu, and J. Tian, "GPU-based Monte Carlo simulation for light propagation in complex heterogeneous tissues," *Optics Express* **18,** 6811–6823 (2010).

[60] H. Shen and G. Wang, "A tetrahedron-based inhomogeneous Monte Carlo optical simulator," *Physics in Medicine and Biology* **55,** 947 (2010).

[61] L. Henyey and J. Greenstein, "Diffuse radiation in the Galaxy," *The Astrophysics Journal* **93,** 70–83 (1941).

[62] W. Cheong, S. Prahl, A. Welch, et al., "A review of the optical properties of biological tissues," *IEEE Journal of Quantum Electronics* **26,** 2166–2185 (1990).

[63] J. R. Mourant, J. P. Freyer, A. H. Hielscher, A. A. Eick, D. Shen, and T. M. Johnson, "Mechanisms of light scattering from biological cells relevant to noninvasive optical-tissue diagnostics," *Applied Optics* **37,** 3586–3593 (1998).

[64] M. Canpolat and J. R. Mourant, "High-angle scattering events strongly affect light collection in clinically relevant measurement geometries for light transport through tissue," *Physics in Medicine and Biology* **45,** 1127 (2000).

[65] E. Larsen and J. Keller, "Asymptotic solution of neutron transport problems for small mean free paths," *Journal of Mathematical Physics* **15,** 75–82 (1974).

[66] G. J. Habetler and B. J. Matkowsky, "Uniform asymptotic expansions in transport theory with small mean free paths, and

the diffusion approximation," *Journal of Mathematical Physics* **16,** 846–854 (1975).

[67] T. Tarvainen, M. Vauhkonen, V. Kolehmainen, and J. Kaipio, "Finite element model for the coupled radiative transfer equation and diffusion approximation," *International Journal for Numerical Methods in Engineering* **65,** 383–405 (2006).

[68] J. Heino and E. Somersalo, "Estimation of optical absorption in anisotropic background," *Inverse Problems* **18,** 559–573 (2002).

[69] M. Schweiger, S. Arridge, M. Hiraoka, and D. Delpy, "The finite element method for the propagation of light in scattering media: boundary and source conditions," *Medical Physics* **22,** 1779 (1995).

[70] M. Keijzer, W. Star, and P. Storchi, "Optical diffusion in layered media," *Applied Optics* **27,** 1820–1824 (1988).

[71] A. D. Klose and E. W. Larsen, "Light transport in biological tissue based on the simplified spherical harmonics equations," *Journal of Computational Physics* **220,** 441 – 470 (2006).

[72] M. Frank, A. Klar, E. W. Larsen, and S. Yasuda, "Time-dependent simplified P_N approximation to the equations of radiative transfer," *Journal of Computational Physics* **226,** 2289 – 2305 (2007).

[73] M. Chu, K. Vishwanath, A. D. Klose, and H. Dehghani, "Light transport in biological tissue using three-dimensional frequency-domain simplified spherical harmonics equations," *Physics in Medicine and Biology* **54,** 2493 (2009).

[74] M. Chu and H. Dehghani, "Image reconstruction in diffuse optical tomography based on simplified spherical harmonics approximation," *Optics Express* **17,** 24208–24223 (2009).

[75] Y. Lu, A. Douraghy, H. B. Machado, D. Stout, J. Tian, H. Herschman, and A. F. Chatziioannou, "Spectrally resolved bioluminescence tomography with the third-order simplified spherical harmonics approximation," *Physics in Medicine and Biology* **54,** 6477 (2009).

[76] J. Tian, K. Liu, Y. Lu, C. Qin, X. Yang, S. Zhu, D. Han, J. Feng, X. Ma, and Z. Chang, "Evaluation of the simplified spherical harmonics approximation in bioluminescence tomography through heterogeneous mouse models," *Optics Express* **18,** 20988–21002 (2010).

[77] V. Y. Soloviev, "Mesh adaptation technique for Fourier-domain fluorescence lifetime imaging," *Medical Physics* **33,** 4176–4183 (2006).

[78] V. Y. Soloviev and S. R. Arridge, "Optical Tomography in weakly scattering media in the presence of highly scattering inclusions," *Biomedical Optics Express* **2,** 440–451 (2011).

[79] V. Y. Soloviev, G. Zacharakis, G. Spiliopoulos, R. Favicchio, T. Correia, S. R. Arridge, and J. Ripoll, "Tomographic imaging with polarized light," *Journal of the Optical Society of America A* **29,** 980–988 (2012).

[80] R. Aronson, "Extrapolation distance for diffusion of light," *Proc. SPIE* **1888,** 297–305 (1993).

[81] R. Haskell, L. Svaasand, T. Tsay, T. Feng, M. McAdams, and B. Tromberg, "Boundary conditions for the diffusion equation in radiative transfer," *Journal of Optical Society of America A* **11,** 2727–2741 (1994).

[82] R. Aronson, "Boundary conditions for diffusion of light," *Journal of the Optical Society of America A* **12,** 2532–2539 (1995).

[83] R. Aronson and N. Corngold, "Photon diffusion coefficient in an absorbing medium," *Journal of the Optical Society of America A* **16,** 1066–1071 (1999).

[84] J. Ripoll and M. Nieto-Vesperinas, "Index mismatch for diffuse photon density waves at both flat and rough diffuse–diffuse interfaces," *Journal of the Optical Society of America A* **16,** 1947–1957 (1999).

[85] G. W. Faris, "Diffusion equation boundary conditions for the interface between turbid media: a comment," *Journal of the Optical Society of America A* **19,** 519–520 (2002).

[86] S. Fantini, M. A. Franceschini, and E. Gratton, "Effective source term in the diffusion equation for photon transport in turbid media," *Applied Optics* **36,** 156–163 (1997).

[87] X. Intes, B. Le Jeune, F. Pellen, Y. Guern, J. Cariou, , and J. Lotrian, "Localization of the virtual point source used in the diffusion approximation to model a collimated beam source," *Waves in Random Media* **9,** 489–499 (1999).

[88] T. Spott and L. O. Svaasand, "Collimated Light Sources in the Diffusion Approximation," *Applied Optics* **39,** 6453–6465 (2000).

[89] G. Pomraning and B. Ganapol, "Asymptotically consistent reflection boundary conditions for diffusion theory," *Annals of Nuclear Energy* **22,** 787–817 (1995).

[90] S. B. Rohde and A. D. Kim, "Modeling the diffuse reflectance due to a narrow beam incident on a turbid medium," *Journal of the Optical Society of America A* **29,** 231–238 (2012).

[91] S. B. Rohde and A. D. Kim, "Convolution model of the diffuse reflectance for layered tissues," *Optics Letters* **39,** 154–157 (2014).

[92] A. Kim and M. Moscoso, "Diffusion of Polarized Light," *Multiscale Modeling & Simulation* **9,** 1624–1645 (2011).

[93] G. Pomraning, "The Fokker-Planck operator as an asymptotic limit," *Mathematical Models and Methods in Applied Sciences* **2,** 21–36 (1992).

[94] A. Kim and J. Keller, "Light propagation in biological tissue," *Journal of Optical Society of America A* **20,** 92–98 (2003).

[95] P. González-Rodríguez and A. Kim, "Comparison of light scattering models for diffuse optical tomography," *Optics Express* **17,** 8756–8774 (2009).

[96] K. Phillips and C. Lancellotti, "On the accuracy of generalized Fokker-Planck transport equations in tissue optics," *Applied Optics* **48,** 229–241 (2009).

[97] E. Olbrant and M. Frank, "Generalized Fokker-Planck theory for electron and photon transport in biological tissues: application to radiotherapy," *Computational and Mathematical Methods in Medicine* **11,** 313–339 (2010).

[98] W. Han, J. Eichholz, and G. Wang, "On a family of differential approximations of the radiative transfer equation," *Journal of Mathematical Chemistry* **50,** 689–702 (2012).

[99] W. Han, J. Eichholz, and Q. Sheng, "Theory of Differential Approximations of Radiative Transfer Equation," in *Advances in Applied Mathematics and Approximation Theory*, Vol. 41, G. A. Anastassiou and O. Duman, eds. (Springer New York, 2013), pp. 121-148.

[100] W. Han, Y. Li, Q. Sheng, and J. Tang, "A numerical method for generalized Fokker-Planck equations," in *Recent Advances in Scientific Computing and Applications*, Vol. 586, Contemporary Mathematics (2013), pp. 171–179.

[101] Q. Sheng and W. Han, "Well-posedness of the Fokker–Planck equation in a scattering process," *Journal of Mathematical Analysis and Applications* **406,** 531 – 536 (2013).

[102] E. Larsen and L. Liang, "The Atomic Mix Approximation for Charged Particle Transport," *SIAM Journal on Applied Mathematics* **68,** 43–58 (2007).

[103] J. Joseph, W. Wiscombe, and J. Weinman, "The delta-Eddington approximation for radiative flux transfer," *Journal of the Atmospheric Sciences* **33,** 2452–2459 (1976).

[104] S. Prahl, *Light transport in tissue,* PhD thesis (University of Texas at Austin, 1988).

[105] V. Venugopalan, J. S. You, and B. J. Tromberg, "Radiative transport in the diffusion approximation: An extension for highly absorbing media and small source-detector separations," *Physical Review E* **58,** 2395–2407 (1998).

[106] C. K. Hayakawa, B. Y. Hill, J. S. You, F. Bevilacqua, J. Spanier, and V. Venugopalan, "Use of the δ-P1 Approximation for Recovery of Optical Absorption, Scattering, and Asymmetry Coefficients in Turbid Media," *Applied Optics* **43,** 4677–4684 (2004).

[107] T. Saratoon, T. Tarvainen, S. R. Arridge, and B. T. Cox, "3D quantitative photoacoustic tomography using the δ-Eddington approximation," in *Proc. SPIE,* Vol. 8581 (2013), pp. 85810V–85810V–12.

[108] G. Pomraning, "Higher order fokker-planck operators," *Nuclear Science and Engineering* **124,** 390–397 (1996).

[109] A. K. Prinja and G. Pomraning, "A generalized Fokker-Planck model for transport of collimated beams," *Nuclear Science and Engineering* **137,** 227–235 (2001).

[110] H. Dehghani, S. Arridge, M. Schweiger, and D. Delpy, "Optical tomography in the presence of void regions," *Journal of Optical Society of America A* **17,** 1659–1670 (2000).

[111] T. Hayashi, Y. Kashio, and E. Okada, "Hybrid Monte Carlo-diffusion method for light propagation in tissue with a low-scattering region," *Applied Optics* **42,** 2888–2896 (2003).

[112] G. Alexandrakis, T. Farrell, and M. Patterson, "Monte Carlo diffusion hybrid model for photon migration in a two-layer turbid medium in the frequency domain," *Applied Optics* **39,** 2235–2244 (2000).

[113] G. Alexandrakis, D. Busch, G. Faris, and M. Patterson, "Determination of the optical properties of two-layer turbid media by use of a frequency-domain hybrid Monte Carlo diffusion model," *Applied Optics* **40,** 3810–3821 (2001).

[114] G. Bal and Y. Maday, "Coupling of transport and diffusion models in linear transport theory," *Mathematical Modelling and Numerical Analysis* **36,** 69–86 (2002).

[115] T. Tarvainen, M. Vauhkonen, V. Kolehmainen, and J. Kaipio, "Hybrid radiative-transfer-diffusion model for optical tomography," *Applied Optics* **44,** 876–886 (2005).

[116] D. Gorpas, D. Yova, and K. Politopoulos, "A three-dimensional finite elements approach for the coupled radiative transfer equation and diffusion approximation modeling in fluorescence imaging," *Journal of Quantitative Spectroscopy and Radiative Transfer* **111,** 553–568 (2010).

[117] D. Gorpas and S. Andersson-Engels, "Evaluation of a radiative transfer equation and diffusion approximation hybrid forward solver for fluorescence molecular imaging," *Journal of Biomedical Optics* **17,** 126010–126010 (2012).

[118] S. Wright, M. Schweiger, and S. Arridge, "Reconstruction in optical tomography using the PN approximations," *Measurement Science and Technology* **18,** 79–86 (2007).

[119] P. S. Mohan, T. Tarvainen, M. Schweiger, A. Pulkkinen, and S. R. Arridge, "Variable order spherical harmonic expansion scheme for the radiative transport equation using finite elements," *Journal of Computational Physics* **230,** 7364–7383 (2011).

[120] T. Tarvainen, V. Kolehmainen, S. R. Arridge, and J. P. Kaipio, "Image reconstruction in diffuse optical tomography using the coupled radiative transport-diffusion model," *Journal of Quantitative Spectroscopy and Radiative Transfer* **112,** 2600–2608 (2011).

[121] G. C. Pomraning, *The equations of radiation hydrodynamics* (Courier Dover Publications, 1973).

[122] H. Ferwerda, "The radiative transfer equation for scattering media with a spatially varying refractive index," *Journal of Optics A: Pure and Applied Optics* **1,** L1–L2 (1999).

[123] J.-M. Tualle and E. Tinet, "Derivation of the radiative transfer equation for scattering media with a spatially varying refractive index," *Optics Communications* **228,** 33–38 (2003).

[124] L. Martí-López, J. Bouza-Domínguez, J. Hebden, S. Arridge, and R. Martín, "Validity conditions for the radiative transfer equation," *Journal of the Optical Society of America A* **20,** 2046–2056 (2003).

[125] M. L. Shendeleva, "Radiative transfer in a turbid medium with a varying refractive index: comment," *Journal of the Optical Society of America A* **21,** 2464–2467 (2004).

[126] M. Premaratne, E. Premaratne, and A. J. Lowery, "The photon transport equation for turbid biological media with spatially varying isotropic refractive index," *Optics Express* **13,** 389–399 (2005).

[127] L. Martí-López, J. Bouza-Domínguez, R. Martínez-Celorio, and J. Hebden, "An investigation of the ability of modified radiative transfer equations to accommodate laws of geometrical optics," *Optics Communications* **266,** 44 – 49 (2006).

[128] G. Bal, "Radiative transfer equations with varying refractive index: a mathematical perspective," *Journal of the Optical Society of America A* **23,** 1639–1644 (2006).

[129] J.-M. Tualle, "Link between the laws of geometrical optics and the radiative transfer equation in media with a spatially varying refractive index," *Optics Communications* **281,** 3631 – 3635 (2008).

[130] J. Boulanger, O. Balima, and A. Charette, "Refractive index imaging from radiative transfer equation-based reconstruction algorithm: Fundamentals," *Journal of Quantitative Spectroscopy and Radiative Transfer* **112,** 1222–1228 (2011).

[131] J. Cassell and M. Williams, "Radiation transport and internal reflection in a sphere," *Journal of Quantitative Spectroscopy and Radiative Transfer* **101,** 16 – 28 (2006).

[132] J. Cassell and M. Williams, "Radiation transport and internal reflection in a two region, turbid sphere," *Journal of Quantitative Spectroscopy and Radiative Transfer* **104,** 400 – 427 (2007).

[133] Z. Jin and K. Stamnes, "Radiative transfer in nonuniformly refracting layered media: atmosphere-ocean system," *Applied Optics* **33,** 431–442 (1994).

[134] R. Elaloufi, S. Arridge, R. Pierrat, and R. Carminati, "Light propagation in multilayered scattering media beyond the diffusive regime," *Applied Optics* **46,** 2528–2539 (2007).

[135] R. Garcia, C. Siewert, and A. Yacout, "On the use of Fresnel boundary and interface conditions in radiative-transfer calculations for multilayered media," *Journal of Quantitative Spectroscopy and Radiative Transfer* **109,** 752 – 769 (2008).

[136] B. Bulgarelli, V. B. Kisselev, and L. Roberti, "Radiative transfer in the atmosphere-ocean system: the finite-element method," *Applied Optics* **38,** 1530–1542 (1999).

[137] K. G. Phillips and S. L. Jacques, "Solution of transport equations in layered media with refractive index mismatch using the P_N-method," *Journal of the Optical Society of America A* **26,** 2147–2162 (2009).

[138] G. Panasyuk, J. C. Schotland, and V. A. Markel, "Radiative transport equation in rotated reference frames," *Journal of Physics A: Mathematical and General* **39,** 115 (2006).

[139] M. Machida, G. Y. Panasyuk, J. C. Schotland, and V. A. Markel, "The Green's function for the radiative transport equation in the slab geometry," *Journal of Physics A: Mathematical and Theoretical* **43,** 065402 (2010).

[140] A. Liemert and A. Kienle, "Radiative transfer in two-dimensional infinitely extended scattering media," *Journal of Physics A: Mathematical and Theoretical* **44,** 505206 (2011).

[141] A. Liemert and A. Kienle, "Infinite space Green's function of the time-dependent radiative transfer equation," *Biomedical Optics Express* **3,** 543–551 (2012).

[142] A. Liemert and A. Kienle, "Green's functions for the two-dimensional radiative transfer equation in bounded media," *Journal of Physics A: Mathematical and Theoretical* **45,** 175201 (2012).

[143] A. Liemert and A. Kienle, "Analytical approach for solving the radiative transfer equation in two-dimensional layered media," *Journal of Quantitative Spectroscopy and Radiative Transfer* **113,** 559 – 564 (2012).

[144] A. K. Jha, M. A. Kupinski, T. Masumura, E. Clarkson, A. V. Maslov, and H. H. Barrett, "Simulating photon-transport in uniform media using the radiative transport equation: a study using the Neumann-series approach," *Journal of the Optical Society of America A* **29,** 1741–1757 (2012).

[145] A. K. Jha, M. A. Kupinski, H. H. Barrett, E. Clarkson, and J. H. Hartman, "Three-dimensional Neumann-series approach to model light transport in nonuniform media," *Journal of the Optical Society of America A* **29,** 1885–1899 (2012).

[146] M. S. Patterson, B. Chance, and B. C. Wilson, "Time resolved reflectance and transmittance for the noninvasive measurement of tissue optical properties," *Applied Optics* **28,** 2331–2336 (1989).

[147] S. Arridge, M. Cope, and D. Delpy, "The theoretical basis for the determination of optical pathlengths in tissue: temporal and frequency analysis Phys," *Physics in Medicine and Biology* **37,** 1531–60 (1992).

[148] S. Arridge, M. Schweiger, M. Hiraoka, and D. Delpy, "A finite element approach for modeling photon transport in tissue," *Medical Physics* **20,** 299–299 (1993).

[149] J. Sikora, A. Zacharopoulos, A. Douiri, M. Schweiger, L. Horesh, S. R. Arridge, and J. Ripoll, "Diffuse photon propagation in multilayered geometries," *Physics in Medicine and Biology* **51,** 497–516 (2006).

[150] P. S. Mohan, V. Y. Soloviev, and S. R. Arridge, "Discontinuous Galerkin method for the forward modelling in optical diffusion tomography," *International Journal for Numerical Methods in Engineering* **85,** 562–574 (2011).

[151] O. Dorn, "A transport-backtransport method for optical tomography," *Inverse Problems* **14,** 1107–1130 (1998).

[152] J. Boulanger and A. Charette, "Reconstruction optical spectroscopy using transient radiative transfer equation and pulsed laser: a numerical study," *Journal of Quantitative Spectroscopy and Radiative Transfer* **93,** 325–336 (2005).

[153] H. Gao and H. Zhao, "A fast-forward solver of radiative transfer equation," *Transport Theory and Statistical Physics* **38,** 149–192 (2009).

[154] L. D. Montejo, A. D. Klose, and A. H. Hielscher, "Implementation of the equation of radiative transfer on block-structured

grids for modeling light propagation in tissue," *Biomedical Optics Express* **1,** 861–878 (2010).

[155] G. Kanschat, "A robust finite element discretization for radiative transfer problems with scattering," *East West Journal of Numerical Mathematics* **6,** 265–272 (1998).

[156] G. Abdoulaev and A. Hielscher, "Three-dimensional optical tomography with the equation of radiative transfer," *Journal of Electronic Imaging* **12,** 594 (2003).

[157] K. Ren, G. Abdoulaev, G. Bal, and A. Hielscher, "Algorithm for solving the equation of radiative transfer in the frequency domain," *Optics Letters* **29,** 578–580 (2004).

[158] K. Ren, G. Bal, and A. Hielscher, "Frequency Domain Optical Tomography Based on the Equation of Radiative Transfer," *SIAM Journal on Scientific Computing* **28,** 1463–1489 (2006).

[159] F. Asllanaj and S. Fumeron, "Applying a new computational method for biological tissue optics based on the time-dependent two-dimensional radiative transfer equation," *Journal of Biomedical Optics* **17,** 075007–1–075007–11 (2012).

[160] O. Balima, A. Charette, and D. Marceau, "Comparison of light transport models based on finite element and the discrete ordinates methods in view of optical tomography applications," *Journal of Computational and Applied Mathematics* **234,** 2259 – 2271 (2010).

[161] O. Balima, Y. Favennec, J. Boulanger, and A. Charette, "Optical tomography with the discontinuous Galerkin formulation of the radiative transfer equation in frequency domain," *Journal of Quantitative Spectroscopy and Radiative Transfer* 805–814 (2012).

[162] S. Richling, E. Meinköhn, N. Kryzhevoi, and G. Kanschat, "Radiative transfer with finite elements," *Astronomy and Astrophysics* **380,** 776–788 (2001).

[163] T. Tarvainen, M. Vauhkonen, V. Kolehmainen, S. Arridge, and J. Kaipio, "Coupled radiative transfer equation and diffusion approximation model for photon migration in turbid medium with low-scattering and non-scattering regions," *Physics in Medicine and Biology* **50,** 4913–4930 (2005).

[164] J. Tervo, P. Kolmonen, M. Vauhkonen, L. M. Heikkinen, and J. P. Kaipio, "A finite-element model of electron transport in radiation therapy and a related inverse problem," *Inverse Problems* **15,** 1345 (1999).

[165] E. Boman, J. Tervo, and M. Vauhkonen, "Modelling the transport of ionizing radiation using the finite element method," *Physics in Medicine and Biology* **50,** 265–280 (2005).

[166] E. Aydin, C. De Oliveira, and A. Goddard, "A comparison between transport and diffusion calculations using a finite element-spherical harmonics radiation transport method," *Medical Physics* **29,** 2013 (2002).

[167] K. Grella and C. Schwab, "Sparse tensor spherical harmonics approximation in radiative transfer," *Journal of Computational Physics* **230,** 8452 – 8473 (2011).

[168] J. Elisee, A. Gibson, and S. Arridge, "Combination of Boundary Element Method and Finite Element Method in Diffuse Optical Tomography," *IEEE Transactions on Biomedical Engineering* **57,** 2737–2745 (2010).

[169] J. Elisee, M. Bonnet, and S. Arridge, "Accelerated boundary element method for diffuse optical imaging," *Optics Letters* **36,** 4101–4103 (2011).

[170] J. Sikora and T. Grzywacz, "Domain Decomposition Method for Diffuse Optical Tomography problems," *Engineering Analysis with Boundary Elements* **36,** 1005–1013 (2012).

[171] A. D. Klose, U. Netz, J. Beuthan, and A. H. Hielscher, "Optical tomography using the time-independent equation of radiative transfer–Part 1: forward model," *Journal of Quantitative Spectroscopy and Radiative Transfer* **72,** 691–713 (2002).

[172] S. R. Arridge, O. Dorn, J. P. Kaipio, V. Kolehmainen, M. Schweiger, T. Tarvainen, M. Vauhkonen, and A. Zacharopoulos, "Reconstruction of subdomain boundaries of piecewise constant coefficients of the radiative transfer equation from optical tomography data," *Inverse Problems* **22,** 2175 (2006).

[173] E. D. Aydin, "Three-dimensional photon migration through voidlike regions and channels," *Applied Optics* **46,** 8272–8277 (2007).

[174] O. Balima, T. Pierre, A. Charette, and D. Marceau, "A least square finite element formulation of the collimated irradiation in frequency domain for optical tomography applications," *Journal of Quantitative Spectroscopy and Radiative Transfer* **111,** 280 – 286 (2010).

[175] O. Balima, Y. Favennec, and D. Rousse, "Optical tomography reconstruction algorithm with the finite element method: An optimal approach with regularization tools," *Journal of Computational Physics* **251,** 461 – 479 (2013).

[176] A. Kim, "Transport theory for light propagation in biological tissue," *Journal of Optical Society of America A* **21,** 820–827 (2004).

[177] A. D. Kim and M. Moscoso, "Beam propagation in sharply peaked forward scattering media," *Journal of the Optical Society of America A* **21,** 797–803 (2004).

[178] A. D. Kim and P. Tranquilli, "Numerical solution of the Fokker-Planck equation with variable coefficients," *Journal of Quantitative Spectroscopy and Radiative Transfer* **109,** 727 – 740 (2008).

[179] P. González-Rodríguez, D. Álvarez, A. D. Kim, and M. Moscoso, "Combining diffuse optical tomography and spectroscopy to detect and characterize lesions in two-layered tissues," *Journal of the Optical Society of America A* **29,** 450–456 (2012).

[180] G. Arfken, H. Weber, and H. Weber, *Mathematical methods for physicists* (Academic press New York, 1985).

[181] O. Lehtikangas and T. Tarvainen, "Utilizing Fokker-Planck-Eddington approximation in modeling light transport in tissues-like media," in *Proc. SPIE*, Vol. 8799 (2013), p. 879908.

[182] S. Prahl, M. Keijzer, S. Jacques, and A. Welch, "A Monte Carlo model of light propagation in tissue," in *SPIE Proceedings of Dosimetry of Laser Radiation in Medicine and Biology* (1989), pp. 102–111.

Paper **I**

O. Lehtikangas, T. Tarvainen,
V. Kolehmainen, A. Pulkkinen,
S.R. Arridge, J.P. Kaipio,
"Finite element approximation
of the Fokker–Planck equation
for diffuse optical tomography,"
*Journal of Quantitative Spectroscopy
and Radiative Transfer*,
111, pp. 1406–1417, 2010.

Journal of Quantitative Spectroscopy & Radiative Transfer 111 (2010) 1406–1417

Contents lists available at ScienceDirect

Journal of Quantitative Spectroscopy & Radiative Transfer

journal homepage: www.elsevier.com/locate/jqsrt

Finite element approximation of the Fokker–Planck equation for diffuse optical tomography

O. Lehtikangas [a], T. Tarvainen [a,b,*], V. Kolehmainen [a], A. Pulkkinen [a,c], S.R. Arridge [b], J.P. Kaipio [a,d]

[a] Department of Physics and Mathematics, University of Eastern Finland, P.O. Box 1627, 70211 Kuopio, Finland
[b] Department of Computer Science, University College London, Gower Street, London WC1E 6BT, UK
[c] Sunnybrook Research Institute, Sunnybrook Health Sciences Centre, 2075 Bayview Ave., Toronto, ON, Canada M4N 3M5
[d] Department of Mathematics, University of Auckland, Private Bag 92019, Auckland Mail Centre, Auckland 1142, New Zealand

ARTICLE INFO

Article history:
Received 23 November 2009
Received in revised form
5 March 2010
Accepted 8 March 2010

Keywords:
Diffuse optical tomography
Finite element method
Fokker–Planck equation
Inverse problems

ABSTRACT

In diffuse optical tomography, light transport theory is used to describe photon propagation inside turbid medium. A commonly used simplification for the radiative transport equation is the diffusion approximation due to computational feasibility. However, it is known that the diffusion approximation is not valid close to the sources and boundary and in low-scattering regions. Fokker–Planck equation describes light propagation when scattering is forward-peaked. In this article a numerical solution of the Fokker–Planck equation using finite element method is developed. Approach is validated against Monte Carlo simulation and compared with the diffusion approximation. The results show that the Fokker–Planck equation gives equal or better results than the diffusion approximation on the boundary of a homogeneous medium and in turbid medium containing a low-scattering region when scattering is forward-peaked.

1. Introduction

In diffuse optical tomography (DOT), the goal is to reconstruct the optical properties of tissues using boundary measurements of scattered near infrared light. The imaging modality has potential applications for example in detection of breast cancer, neonatal brain imaging and functional brain activation studies [1,2]. In the measurement set-up, a set of optical fibers, optodes, are attached on the boundary of the object in measurement and source positions. Near infrared light is guided into the object at one source position at a time and transmitted light is measured from all the measurement positions using light sensitive detectors. Then, this measurement process is repeated for all source positions.

The image reconstruction in DOT is a nonlinear ill-posed inverse problem. The iterative solution of this problem requires several solutions of the forward problem. Moreover, due to ill-posedness of the reconstruction problem, even small errors in the modelling can produce large errors in reconstructions. Therefore, an accurate and computationally feasible forward model is needed.

Light propagation in biological tissues is governed by the transport theory [3,4]. This leads to describing the multiple scattering phenomenon in biological tissues using the radiative transport equation (RTE). Due to computational complexity of the RTE, different approximations have been developed to ease up the computation of the forward problem. A common approximation is the P_n approximation where the solution of the RTE is expanded into series of spherical harmonics.

---

[*] Corresponding author at: Department of Physics and Mathematics, University of Eastern Finland, P.O. Box 1627, 70211 Kuopio, Finland. Tel.: +358 40 3552310; fax: +358 17 162585.
E-mail address: Tanja.Tarvainen@uef.fi (T. Tarvainen).

0022-4073/$ - see front matter © 2010 Elsevier Ltd. All rights reserved.
doi:10.1016/j.jqsrt.2010.03.003

The most often used model for the solution of the forward problem in DOT is the diffusion approximation (DA) which is a special case of the P_1 approximation. The DA is computationally feasible but it has limitations in accuracy; it fails to describe light propagation accurately in low-scattering regions as well as in the proximity of the light source and boundaries [1,5].

Recently there has been a growing interest in using other approximations of the RTE as a forward model. The idea of using the Fokker–Planck equation as the forward model in DOT was introduced in [6]. The Fokker–Planck equation can be used to describe light propagation accurately when scattering is strongly forward dominated [7]. This is the case in biological tissues [8,6].

The derivation of the Fokker–Planck equation for light transport can be found in [9] and for particle transport in [10]. In the derivation of the Fokker–Planck equation for light transport, the scattering probability distribution is approximated by a sum of delta function and a second order correction [9]. This approximation explains the limits of the Fokker–Planck equation. It cannot describe the light propagation accurately when the scattering is not forward dominated, but on the other hand when it is the Fokker–Planck equation offers a good model for light propagation.

There are few numerical solutions to the Fokker–Planck equation. A numerical solution for the Fokker–Planck equation using discrete ordinates method was developed for particle transport in [11]. In [12], a method for computing Green's function for the Fokker–Planck equation as an expansion in plane wave modes was developed. The plane wave modes for the Fokker–Planck equation were calculated using finite difference approximation. The DOT reconstruction of the scattering and absorption coefficients using the Fokker–Planck equation as a forward model was presented in [13]. The forward problem was solved numerically using the finite difference method and the inverse problem was solved using a transport–backtransport method developed in [14].

In this paper, a finite element solution of the Fokker–Planck equation is introduced. The finite element method (FEM) is a flexible approach when implementing different boundary conditions and handling complex geometries. It has successfully been used in numerical solution of the light transport problems [15–17]. In this paper both spatial and angular variables are discretized using the FEM when solving the Fokker–Planck equation. A similar approach has earlier been used in solution of the RTE and the radiative transfer problem of ionizing radiation [17,18]. To the authors knowledge the Fokker–Planck equation has not yet been solved using the finite element method.

In the numerical solution of the RTE, dense angular dicretization is needed in order to describe light propagation accurately in strongly scattering medium [13]. Therefore, large computational resources are needed in the solutions of the RTE. The Fokker–Planck equation, on the other hand, assumes that the scattering is forward peaked. Thus, coarser angular discretization can be used in the numerical computation compared to the RTE, leading to smaller amount of computation load and time [13].

The rest of the paper is organized as follows. In Section 2, we give a short review of the RTE, the DA, and the Fokker–Planck equation. In Section 3, we derive a finite element solution for the Fokker–Planck equation. In Section 4, we test the proposed FE-model with simulations. In Section 5, conclusions are given.

2. Light transport models

Let $\Omega \subset \mathbb{R}^n$ be the physical domain and n=2,3 be the dimension of the domain. In addition, let $\hat{s} \in S^{n-1}$ denote a unit vector in the direction of interest.

The frequency domain version of the RTE is of the form

$$\frac{\mathrm{i}\omega}{c}\phi(r,\hat{s})+\hat{s}\cdot\nabla\phi(r,\hat{s})+\mu_{\mathrm{a}}\phi(r,\hat{s})=\mu_{\mathrm{s}}L\phi(r,\hat{s})+q(r,\hat{s}), \tag{1}$$

where i is the imaginary unit, c is the speed of light in medium, ω is the angular modulation frequency of the input signal, $q(r,\hat{s})$ is the source inside Ω, $\phi(r,\hat{s})$ is the radiance, $\mu_{\mathrm{s}}=\mu_{\mathrm{s}}(r)$ and $\mu_{\mathrm{a}}=\mu_{\mathrm{a}}(r)$ are the scattering and absorption parameters of the medium and L is the scattering operator defined as

$$L\phi(r,\hat{s})=-\phi(r,\hat{s})+\int_{S^{n-1}}\Theta(\hat{s},\hat{s}')\phi(r,\hat{s}')\,\mathrm{d}\hat{s}'. \tag{2}$$

The scattering phase function $\Theta(\hat{s},\hat{s}')$ describes the probability density for a photon to scatter from direction $\hat{s}'$ to direction $\hat{s}$. In this study the domain is assumed to be isotropic in the sense that probability of scattering depends only on the relative angle, not on the absolute angles, i.e. $\Theta(\hat{s},\hat{s}')=\Theta(\hat{s}\cdot\hat{s}')$. An often used phase function for isotropic materia is the Henyey–Greenstein scattering function [19] which is of the form

$$\Theta(\hat{s}\cdot\hat{s}')=\begin{cases}\dfrac{1}{2\pi}\dfrac{1-g^2}{(1+g^2-2g\hat{s}\cdot\hat{s}')} & n=2,\\[2ex] \dfrac{1}{4\pi}\dfrac{1-g^2}{(1+g^2-2g\hat{s}\cdot\hat{s}')^{3/2}} & n=3,\end{cases} \tag{3}$$

where parameter g defines the shape of the probability distribution. Values of g are in the range from -1 to 1, for $g<0$ scattering is backward dominated and for $g>0$ scattering is forward dominated. When g=0, scattering phase function is a uniform distribution. In biological tissues, g is typically close to 1.

In DOT, a natural boundary condition for the RTE is the so-called vacuum boundary condition which assumes that no photons travel in an inward direction at the boundary $\partial\Omega$, thus

$$\phi(r,\hat{s})=0,\quad r\in\partial\Omega,\quad \hat{s}\cdot\hat{n}<0, \tag{4}$$

where $\hat{n}$ denotes the outward unit normal on $\partial\Omega$ [1]. The vacuum boundary condition can be modified to take into account a boundary source $\phi_0(r,\hat{s})$ at source position $\varepsilon_i \subset \partial\Omega$,

$$\phi(r,\hat{s})=\begin{cases}\phi_0(r,\hat{s}), & r\in\bigcup_j\varepsilon_j, \quad \hat{s}\cdot\hat{n}<0,\\ 0, & r\in\partial\Omega\backslash\bigcup_j\varepsilon_j, \quad \hat{s}\cdot\hat{n}<0.\end{cases} \tag{5}$$

Photon density is defined as an integral of the radiance over angular directions

$$\Phi(r)=\int_{S^{n-1}}\phi(r,\hat{s})\,\mathrm{d}\hat{s}. \tag{6}$$

2.1. Diffusion approximation

The diffusion approximation for the RTE has been derived in numerous references, e.g. [1,4,3,20]. In the frequency domain the DA is of the form

$$-\nabla\cdot\kappa\nabla\Phi(r)+\mu_{\mathrm{a}}\Phi(r)+\frac{\mathrm{i}\omega}{c}\Phi(r)=q_0(r), \tag{7}$$

where $q_0(r)$ is the isotropic source inside Ω. The diffusion coefficient κ is defined as

$$\kappa=\frac{1}{n(\mu_{\mathrm{a}}+\mu_{\mathrm{s}}')}, \tag{8}$$

where n is the dimension of the domain and μ_{s}' is the reduced scattering coefficient

$$\mu_{\mathrm{s}}'=(1-g_1)\mu_{\mathrm{s}}, \tag{9}$$

and g_1 is the mean of cosine of the scattering function

$$g_1=\int_{S^{n-1}}(\hat{s}\cdot\hat{s}')\Theta(\hat{s}\cdot\hat{s}')\,\mathrm{d}\hat{s}. \tag{10}$$

In the case of Henyey–Greenstein phase function g_1=g. The DA cannot satisfy the boundary condition (4) exactly. Typically, the boundary condition is approximated with a Robin-type boundary condition

$$\Phi(r)+\frac{1}{2\gamma_n}\kappa A\frac{\partial\Phi(r)}{\partial\hat{n}}=\begin{cases}\dfrac{I_s}{\gamma_n}, & r\in\bigcup_j\varepsilon_j,\\ 0, & r\in\partial\Omega\backslash\bigcup_j\varepsilon_j,\end{cases} \tag{11}$$

where γ_n is dimension dependent constant ($\gamma_2=1/\pi,\gamma_3=1/4$) [20], A=(1 + R)/(1−R) and R is the reflection coefficient on the boundary [21] and I_s is an inward directed diffuse boundary current [21]

2.2. Fokker–Planck equation

In the case of forward-peaked scattering, one can approximate the RTE by using the Fokker–Planck approximation. In the approximation, the scattering phase function is approximated as

$$\Theta(\hat{s}\cdot\hat{s}')\approx a_0\delta(\hat{s}-\hat{s}')+a_1\delta''(\hat{s}-\hat{s}'), \tag{12}$$

where δ is a delta function, δ'' is a second order derivative of delta function and a_0 and a_1 are constants. Inserting this approximation into the RTE (1) and by examining the eigenvalues of the scattering operator the Fokker–Planck approximation is obtained. The scattering operator L is approximated as

$$L\phi(r,\hat{s})\approx\xi_n(1-g_1)\Delta_{\hat{s}}\phi(r,\hat{s}), \tag{13}$$

where $\Delta_{\hat{s}}$ denotes the Laplacian operator in spherical coordinates and ξ_n is dimension dependent constant. In dimension n=2,3 constant ξ_n is [13]

$$\xi_n=\begin{cases}1 & n=2,\\ 1/2 & n=3.\end{cases} \tag{14}$$

In case of the Henyey–Greenstein scattering function, the resulting Fokker–Planck equation in the frequency domain is

$$\frac{\mathrm{i}\omega}{c}\phi(r,\hat{s})+\hat{s}\cdot\nabla\phi(r,\hat{s})+\mu_{\mathrm{a}}\phi(r,\hat{s})=\xi_n\mu_{\mathrm{s}}(1-g)\Delta_{\hat{s}}\phi(r,\hat{s})+q(r,\hat{s}). \tag{15}$$

Unlike the DA, the Fokker–Planck equation can satisfy the same boundary condition (5) as the RTE. As a solution of the Fokker–Planck equation the radiance $\phi(r,\hat{s})$ at spatial point r into angular direction $\hat{s}$ is obtained. The photon density $\Phi(r)$ can be calculated from the radiance by using Eq. (6).

3. Finite element implementations

In this section, the finite element approximation for the Fokker–Planck equation is derived. In the finite element method a variational formulation, also known as a weak formulation, for the problem is derived, and this infinite dimensional problem is discretized using a suitable basis for the solution. The finite element approximation for the Fokker–Planck equation derived here follows the same kind of procedure as the FE model for the RTE derived in [17].

3.1. Variational formulation

To obtain a variational formulation of the Fokker–Planck equation (15), it is multiplied by test function $v(r,\hat{s})$ and integrated over domain $G=\Omega\times S^{n-1}$. In DOT there are no internal sources and thus the source term in Eq. (15) is $q(r,\hat{s})=0$. After some manipulation and using boundary condition (5), the resulting weak formulation is obtained. It is of the form

$$\begin{aligned}&\int_\Omega\int_{S^{n-1}}\frac{\mathrm{i}\omega}{c}\phi(r,\hat{s})v(r,\hat{s})\,\mathrm{d}\hat{s}\,\mathrm{d}r-\int_\Omega\int_{S^{n-1}}\hat{s}\cdot\nabla v(r,\hat{s})\phi(r,\hat{s})\,\mathrm{d}\hat{s}\,\mathrm{d}r\\&\quad+\int_{\partial\Omega}\int_{S^{n-1}}(\hat{s}\cdot\hat{n})_+\phi(r,\hat{s})v(r,\hat{s})\,\mathrm{d}\hat{s}\,\mathrm{d}S\\&\quad+\int_\Omega\int_{S^{n-1}}\mu_{\mathrm{a}}\phi(r,\hat{s})v(r,\hat{s})\,\mathrm{d}\hat{s}\,\mathrm{d}r\\&\quad+\int_\Omega\int_{S^{n-1}}\xi_n\mu_{\mathrm{s}}(1-g)\frac{1}{\sin^2\varphi}\frac{\partial\phi(r,\theta)}{\partial\theta}\frac{\partial v(r,\theta)}{\partial\theta}\,\mathrm{d}\theta\,\mathrm{d}r\\&\quad-\int_\Omega\int_{S^{n-1}}\xi_n\mu_{\mathrm{s}}(1-g)\frac{1}{\sin\varphi}\frac{\partial}{\partial\varphi}\left(\sin\varphi\frac{\partial\phi(r,\hat{s})}{\partial\varphi}\right)v(r,\hat{s})\,\mathrm{d}\hat{s}\,\mathrm{d}r\\&=\int_{\partial\Omega}\int_{S^{n-1}}(\hat{s}\cdot\hat{n})_-\phi_0(r,\hat{s})v(r,\hat{s})\,\mathrm{d}\hat{s}\,\mathrm{d}S,\end{aligned} \tag{16}$$

where $(\hat{s}\cdot\hat{n})_+$ and $(\hat{s}\cdot\hat{n})_-$ denote the positive and negative parts of $(\hat{s}\cdot\hat{n})$ and $\phi_0(r,\hat{s})$ is the boundary source. The derivation of the variational formulation is explained in more detail in Appendix A.

3.2. Finite element approximation

In the FE-approximation of the Fokker–Planck equation, the solution of the variational formulation equation (16) is approximated with a linear combination of the basis functions

$$\phi(r,\hat{s})\approx\phi^h(r,\hat{s})=\sum_{i=1}^{N_n}\sum_{l=1}^{N_a}\alpha_{il}\psi_i(r)\psi_l(\hat{s}), \tag{17}$$

where $\psi(r)$ and $\psi(\hat{s})$ are the nodal basis functions of the spatial and angular discretizations, respectively, and α_{il} is the radiance in spatial nodal point i into angular direction l. In this paper we use a piecewise linear basis for both the spatial and angular parts of the solution. Using the chosen finite dimensional basis and choosing basis functions $\psi_j(r)$ and $\psi_m(\hat{s})$ as test functions, a finite dimensional approximation for the variational formulation in Eq. (16) is obtained. A more detailed derivation of the FE-approximation is given in Appendix B. The FE-approximation of the Fokker–Planck equation is of the form

$$(A_0+A_1+A_2+A_3+A_4+A_5)\alpha = b_1\psi^0, \tag{18}$$

where $\alpha = (\alpha_{1,1},\ldots,\alpha_{1,N_a},\ldots,\alpha_{N_n,1},\ldots,\alpha_{N_n,N_a})^T \in \mathbb{C}^{N_nN_a}$ is the radiance at the nodes of the spatial and angular grids. The source intensity vector $\psi^0 = (\psi^0_{1,1},\ldots,\psi^0_{N_n,N_a}) \in \mathbb{R}^{N_nN_a}$ includes nonzero elements at the spatial nodes $r_i \in \varepsilon_j \subset \partial\Omega$ s.t. ψ^0_{il} is the source intensity at the node i to the angular direction l. Further, the components of the matrices in Eq. (18) are

$$A_0(h,s) = \frac{\mathrm{i}\omega}{c}\int_\Omega \psi_i(r)\psi_j(r)\,\mathrm{d}r\int_{S^{n-1}}\psi_l(\hat{s})\psi_m(\hat{s})\,\mathrm{d}\hat{s}, \tag{19}$$

$$A_1(h,s) = -\int_\Omega\int_{S^{n-1}}\hat{s}\cdot\nabla\psi_j(r)\psi_m(\hat{s})\psi_l(\hat{s})\,\mathrm{d}\hat{s}\psi_i(r)\,\mathrm{d}r, \tag{20}$$

$$A_2(h,s) = \int_{\partial\Omega}\psi_i(r)\psi_j(r)\,\mathrm{d}S\int_{S^{n-1}}(\hat{s}\cdot\hat{n})_+\psi_l(\hat{s})\psi_m(\hat{s})\,\mathrm{d}\hat{s}, \tag{21}$$

$$A_3(h,s) = \int_\Omega \mu_\mathrm{a}\psi_i(r)\psi_j(r)\,\mathrm{d}r\int_{S^{n-1}}\psi_l(\hat{s})\psi_m(\hat{s})\,\mathrm{d}\hat{s}, \tag{22}$$

$$A_4(h,s) = \int_\Omega \xi_n\mu_\mathrm{s}(1-g)\psi_i(r)\psi_j(r)\,\mathrm{d}r\int_{S^{n-1}}\frac{1}{\sin^2\varphi}\frac{\partial\psi_l(\hat{s})}{\partial\theta}\frac{\partial\psi_m(\hat{s})}{\partial\theta}\,\mathrm{d}\hat{s}, \tag{23}$$

$$A_5(h,s) = -\int_\Omega \xi_n\mu_\mathrm{s}(1-g)\psi_i(r)\psi_j(r)\,\mathrm{d}r \int_{S^{n-1}}\frac{1}{\sin\varphi}\frac{\partial}{\partial\varphi}\left(\sin\varphi\frac{\partial\psi_l(\hat{s})}{\partial\varphi}\right)\psi_m(\hat{s})\,\mathrm{d}\hat{s}, \tag{24}$$

$$b_1(h) = \int_{\partial\Omega}\psi_i(r)\psi_j(r)\,\mathrm{d}S\int_{S^{n-1}}(\hat{s}\cdot\hat{n})_-\psi_l(\hat{s})\psi_m(\hat{s})\,\mathrm{d}\hat{s}, \tag{25}$$

where $h=N_a(j-1)+m$, $s=N_a(i-1)+l$, $j,i=1,\ldots,N_n$, $m,l=1,\ldots,N_a$ and $h,s=1,\ldots,N_nN_a$.

4. Results and discussion

The finite element solution of the Fokker–Planck equation was tested with 2D simulations. In 2D the zenith angle is $\varphi = 0$ and therefore $A_5=0$ in matrix equation (18). The simulations were carried out in a circular domain Ω centered at the origin and with radius 20 mm. The light source was located at $(-20,0)$ with direction perpendicular to $\partial\Omega$. The frequency of the input signal was 100 MHz. The refractive indices of the object and the surrounding medium were $n=1$.

The results were compared with the finite element solution of the DA and with Monte Carlo (MC) simulations. The finite element solution of the DA was obtained as in [17,22]. The diffuse source model was used. For the spatial discretization of the DA and the Fokker–Planck equation, the same spatial grid was used. In the Monte Carlo simulation, a photon packet method, developed in [23] and extended in [24], was modified to allow computation in complex inhomogeneous geometries. This was achieved by depicting the computational domain with triangular elements. A more detailed description of the Monte Carlo method can be found in [25].

4.1. Homogeneous medium

First the performance of the finite element solution of the Fokker–Planck equation was tested in homogeneous medium with different scattering properties. The finite element mesh for the spatial discretization contained 4687 nodal points and 9196 elements. For the angular discretization 32 equally spaced angular directions were used. The number of angular directions was chosen by inspecting the convergence of the FE-solution against the Monte Carlo solution on the boundary of the object.

4.1.1. Constant scattering coefficient, varying scattering shape parameter g

The optical properties of the medium used for the first two simulations are given in Table 1 (cases 1A and 1B). In the simulations, the absorption and scattering coefficients were constants $\mu_\mathrm{a} = 0.01\,\mathrm{mm}^{-1}$ and $\mu_\mathrm{s} = 1\,\mathrm{mm}^{-1}$, and scattering shape parameter got two values g=0.6 (case 1A) and g=0.9 (case 1B).

The photon densities on the boundary of the domain calculated with Fokker–Planck equation, using Eqs. (17) and (6), the DA and MC are shown in Fig. 1. The logarithms of the amplitudes on the boundary of the object along the detection angle, which is the angle between the source and detector, are shown the first column and the phase shifts are shown the second column.

On the first row the scattering shape parameter g=0.6 (case 1A) and on the second row g=0.9 (case 1B). All results are in same scale and they are scaled with respect to the source strength.

The relative errors of the photon densities of the Fokker–Planck equation and the DA were calculated by comparing them against the solution of MC. The results are shown in Fig. 2. To give a quantitative estimate of the errors, the squared norm of the relative errors was computed. The results are given in Table 2 (cases 1A and 1B).

Table 1
The scattering coefficient μ_s, absorption coefficient μ_a, scattering shape parameter g and reduced scattering coefficient μ'_s for the simulations in homogeneous medium.

	μ_s (mm^{-1})	μ_a (mm^{-1})	g	μ'_s (mm^{-1})
1A	1	0.01	0.6	0.4
1B	1	0.01	0.9	0.1
2A	0.5	0.01	0.8	0.1
2B	5	0.01	0.8	1.0

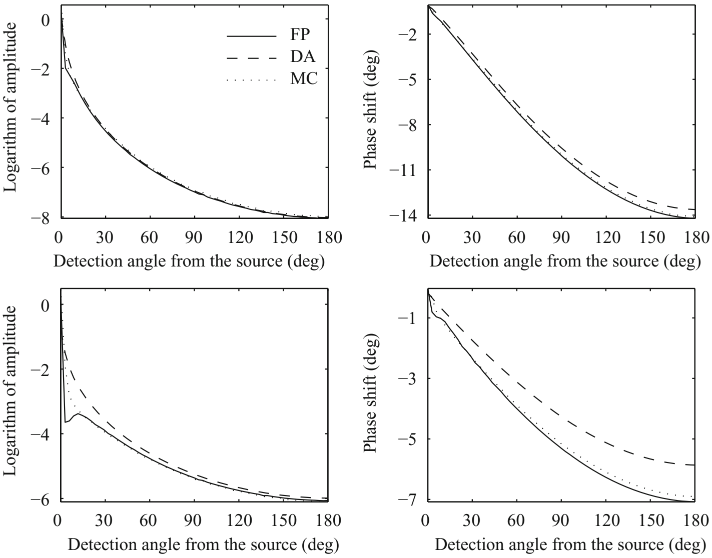

Fig. 1. The logarithms of the amplitudes (left column) and the phase shifts (right column) of the photon densities on the boundary of the object calculated with Fokker–Planck equation (solid line), DA (dashed line) and Monte Carlo (dotted line). On the top row $g=0.6$ (case 1A) and the bottom row $g=0.9$ (case 1B).

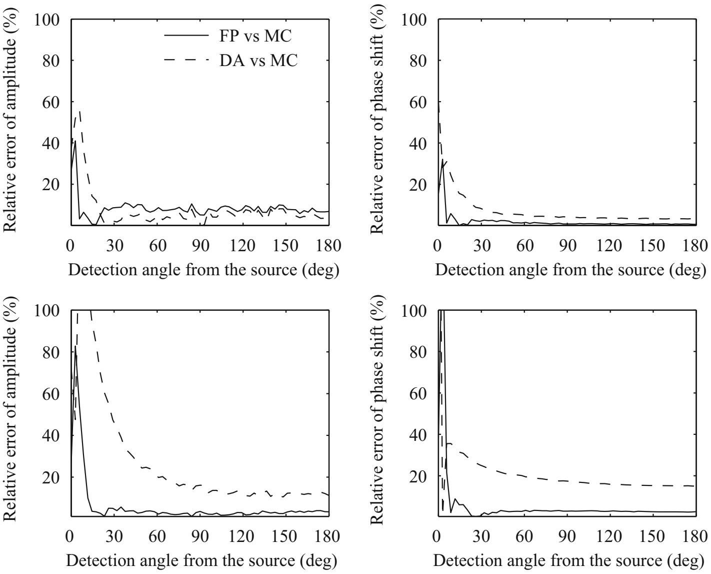

Fig. 2. The relative errors of the amplitudes (left column) and the phase shifts (right column) of the photon densities on the boundary of the object calculated with the Fokker–Planck equation (solid line) and the DA (dashed line). On the top row $g=0.6$ (case 1A) and the bottom row $g=0.9$ (case 1B).

The results show that the finite element solution of the Fokker–Planck equation gives almost the same result as Monte Carlo excluding a drop close to the source in the highly forward-peaked case ($g=0.9$). We expect that this drop, which can be seen in some extent in all of the results, is due to the differences between the radiative transport and Fokker–Planck models. All three models give almost the same results far from the source in amplitude data. However, in the phase shift the DA differs from the results of the Fokker–Planck equation and MC especially in the highly forward-peaked case. The relative errors show that the Fokker–Planck equation gives equal or better results than the DA when compared to MC.

4.1.2. *Constant scattering shape parameter, varying scattering coefficient* μ_s

The proposed model was tested in the homogeneous medium also with two different scattering coefficients. The optical parameters that were used in the simulations are given in Table 1 (cases 2A and 2B). Now the scattering shape parameter was constant g=0.8. The scattering coefficient μ_s was given two values $\mu_s = 0.5\,\text{mm}^{-1}$ (case 2A) and $\mu_s = 5\,\text{mm}^{-1}$ (case 2B).

The photon densities calculated with the Fokker–Planck, the DA and MC are shown in Fig. 3. The figures are in respective order as in Fig. 1. On the first row the scattering coefficient was $\mu_s = 0.5\,\text{mm}^{-1}$ (case 2A) and on the second row it was $\mu_s = 5\,\text{mm}^{-1}$ (case 2B). The relative errors of the photon densities are shown in Fig. 4 and the squared norm of the relative errors is given in Table 2 (cases 2A and 2B).

In the case 2A where $\mu_s = 0.5\,\text{mm}^{-1}$, the FE-solution of the Fokker–Planck equation gives almost equal results as MC apart from a drop close to the source. The solution of the DA differs from the other approaches clearly. In the highly scattering case 2B ($\mu_s = 5\,\text{mm}^{-1}$), the Fokker–Planck, the DA and MC give almost the same results. In this case, the squared norm of the relative error is larger for the solution of the Fokker–Planck equation than for the solution of the DA. However, both of them are smaller than the norms of the other cases.

4.2. *Comparison of the FE-solutions of the Fokker–Planck equation and RTE*

The computational load of the FE-solution of the Fokker–Planck equation was compared with the FE-solution of the RTE. The finite element solution of the RTE was obtained as in [17]. In the FE-solution of the RTE, the same spatial discretization was used as for the Fokker–Planck equation. Furthermore, the angular discretization was chosen similarly as for the Fokker–Planck equation. The sizes of the FE-matrices, number of nonzero elements and matrix filling ratios are given in Table 3. The

Table 2
The squared norm of the relative errors for Fokker–Planck ε_{FP} (%) and DA ε_{DA}(%).

	ε_{FP} (amplitude) (%)	ε_{DA} (amplitude) (%)	ε_{FP} (phase shift) (%)	ε_{DA} (phase shift) (%)
1A	7.19	14.18	0.010	0.157
1B	7.77	51.77	0.094	2.79
2A	7.82	51.80	0.086	2.83
2B	4.36	0.33	0.005	0.012

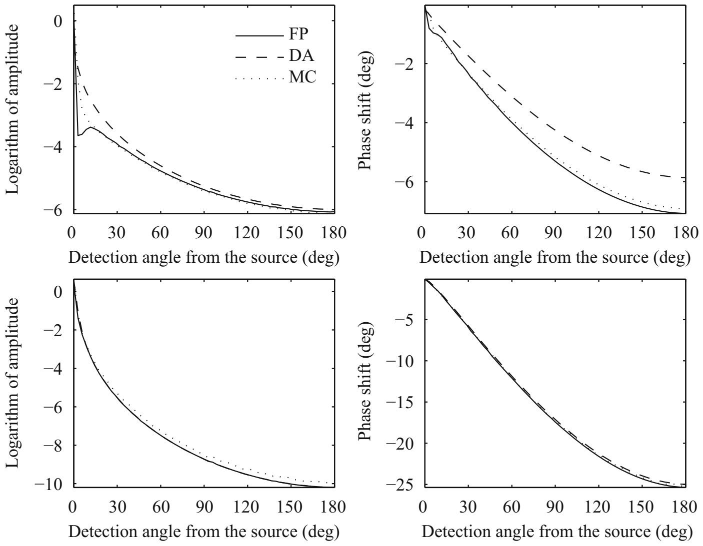

Fig. 3. The logarithms of the amplitudes (left column) and the phase shifts (right column) of the photon densities on boundary of the object calculated with Fokker–Planck equation (solid line), DA (dashed line) and Monte Carlo (dotted line). On the top row scattering coefficient $\mu_s = 0.5\,\text{mm}^{-1}$ (case 2A) and in the bottom row $\mu_s = 5\,\text{mm}^{-1}$ (case 2B).

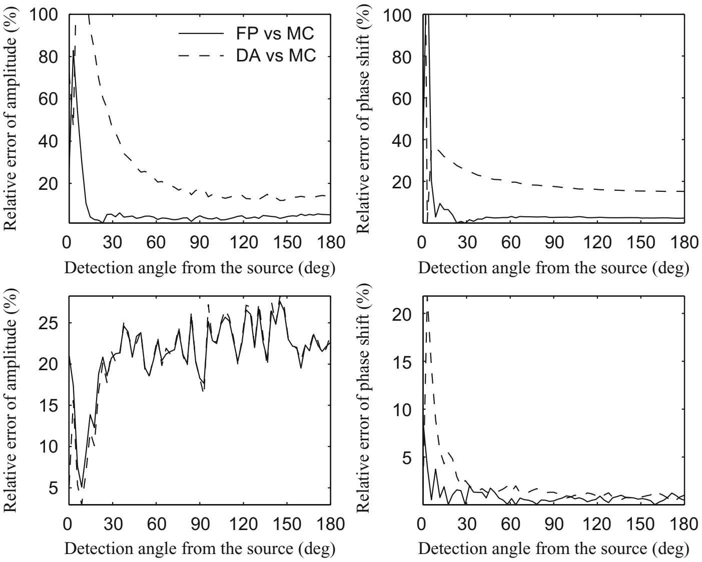

Fig. 4. The relative errors of the amplitudes (left column) and the phase shifts (right column) of the photon densities on the boundary of the object calculated with the Fokker–Planck equation (solid line) and the DA (dashed line). On the top row scattering coefficient $\mu_s = 0.5\,\mathrm{mm}^{-1}$ (case 2A) and in the bottom row $\mu_s = 5\,\mathrm{mm}^{-1}$ (case 2B).

Table 3
The number of angular directions N_a, matrix sizes, number of the nonzeros and matrix filling ratios in the FE-discretizations of the Fokker–Planck (FP) equation and the RTE.

	FP	RTE	
N_a	32	32	64
Matrix size	149 984 × 149 984	149 984 × 149 984	299 968 × 299 968
Nonzeros	3 115 296	33 229 824	132 919 296
Filling ratio (%)	0.014	0.15	0.15

Table 4
The number of angular directions N_a of the FE-discretizations and relative CPU-times $t_{\mathrm{RTE}}/t_{\mathrm{FP}}$ of the Fokker–Planck (FP) equation and RTE for the homogeneous test cases.

	$N_{a,\mathrm{FP}}$	$N_{a,\mathrm{RTE}}$	$t_{\mathrm{RTE}}/t_{\mathrm{FP}}$
1A	32	32	3.58
1B	32	64	26.66
2A	32	32	11.63
2B	32	64	8.39

FE-solution of the RTE contains discretization of the scattering phase function which leads to full angular matrices. In contrast, the FE-solution of the Fokker–Planck equation contains derivatives of a basis functions with respect to angular variables. Thereby, angular matrices are sparse when piecewise basis functions are used.

CPU-times of the FE-solutions were computed for all homogeneous test cases. The relative CPU-times $t_{\mathrm{RTE}}/t_{\mathrm{FP}}$ and the number of angular direction N_a are given in Table 4. The results show that the CPU-times of the FE-solution of the Fokker–Planck equation are smaller than the CPU-times of the FE-solution of the RTE even when the sizes of the matrices are equal. Most of the relative CPU-times are order of magnitude smaller for the Fokker–Planck equation when compared to the RTE. Thus, significant computational savings can be obtained by using the Fokker–Planck equation compared to the RTE when scattering is forward-peaked.

4.3. Inhomogeneous medium

Next the proposed FE-model was tested in inhomogeneous medium including a low-scattering void-like region. The geometry of the domain was the same as earlier, but now the medium included a low-scattering void-like region. The geometry for the simulations is shown in Fig. 5. In the first simulation the void-like region was a low-scattering layer 2 mm inside the boundary of the circle (left figure). The width of the layer was 2 mm, and thus the inner radius of the low-scattering gap was 16 mm. In the second simulation the void region was a low-scattering inclusion inside the domain (right figure). The center of the low-scattering circular inclusion was located at $(-5,5)$ and its radius was 6 mm.

The scattering coefficients of the background and the void were $\mu_s = 1\,\mathrm{mm}^{-1}$ and $\mu_s = 0.001\,\mathrm{mm}^{-1}$, respectively. The absorption coefficient and the scattering shape parameters were constants in the whole domain, $\mu_a = 0.01\,\mathrm{mm}^{-1}$ and g=0.8, respectively.

The finite element mesh for the spatial discretization of the inhomogeneous medium including a low-scattering layer contained 3791 nodal points and 7300 elements. For the angular discretization 64 equally spaced angular directions were used. The discretization of the circular domain with inclusion contained 2923 nodal points and 5698 elements for the spatial part and 32 equally spaced angular directions for the angular part.

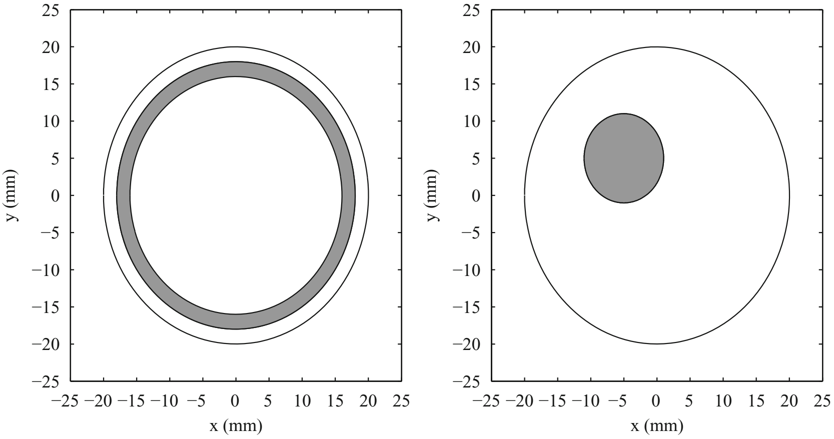

Fig. 5. The inhomogeneous medium including a low-scattering void-like region. On the left void-like region is a low-scattering layer and on the right it is a low-scattering inclusion inside the domain.

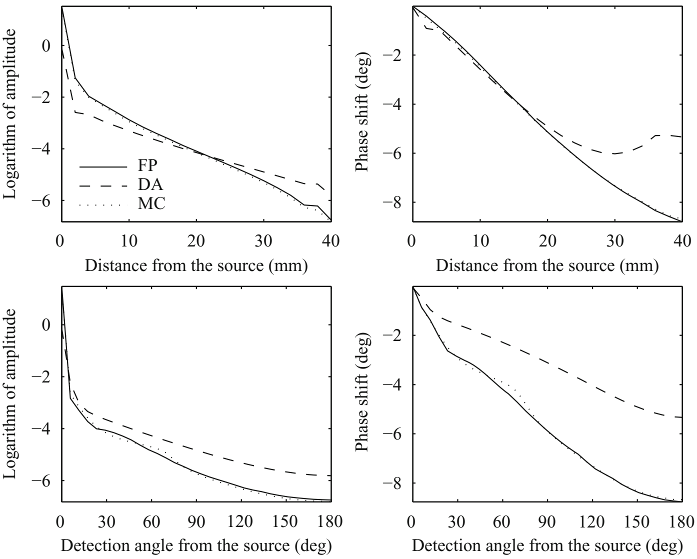

Fig. 6. The logarithms of amplitudes (left column) and the phase shifts (right column) of the photon densities calculated with the Fokker–Planck equation (solid line), DA (dashed line) and Monte Carlo (dotted line) inside the circular medium including a low-scattering layer. The photon densities along the source direction are on the top row and the photon densities on the boundary of the object along the detection angle are on the bottom row.

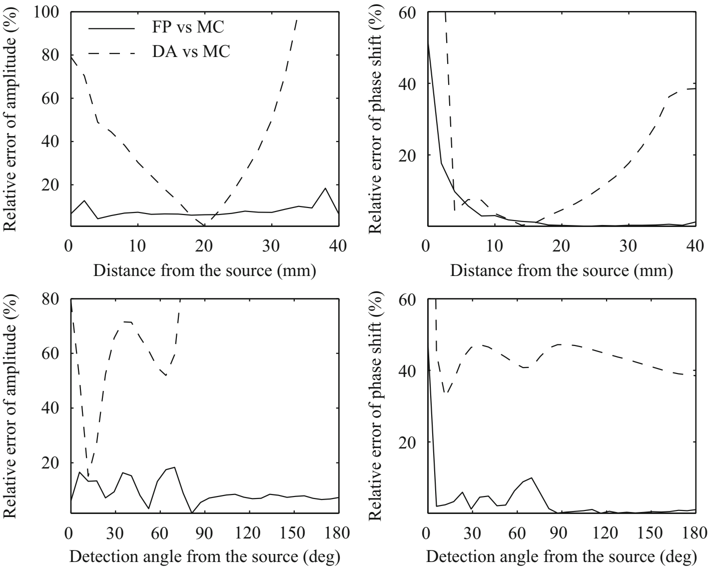

Fig. 7. The relative errors of the amplitudes (left column) and the phase shifts (right column) of the photon densities calculated with the Fokker–Planck equation (solid line) and the DA (dashed line) in the circular medium including a low-scattering layer. The relative errors along the source direction are on the top row and the relative errors on the boundary of the object along the detection angle are on the bottom row.

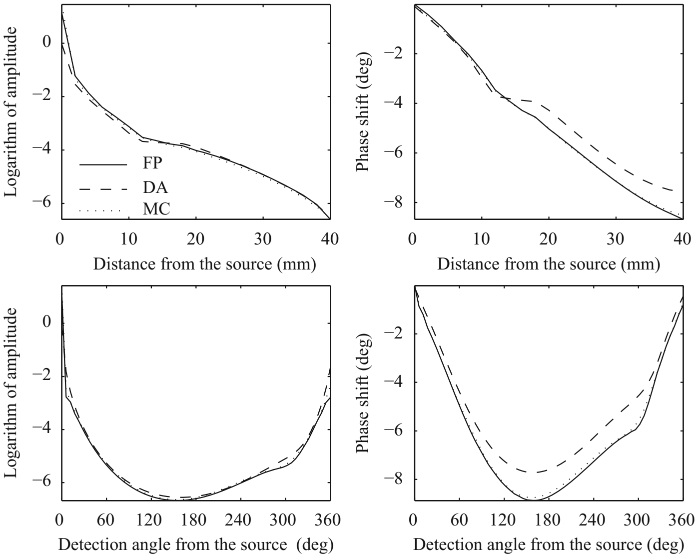

Fig. 8. The logarithms of amplitudes (left column) and the phase shifts (right column)of the photon densities calculated with the Fokker–Planck equation (solid line), DA (dashed line) and Monte Carlo (dotted line) in the circular medium including a low-scattering inclusion. The photon densities along the source direction are on the top row and the photon densities on the boundary of the object along the detection angle are on the bottom row.

4.3.1. Low-scattering layer

The photon densities were calculated with the Fokker–Planck equation, the DA and MC. The results are shown in Fig. 6. The logarithms of the amplitudes are shown the first column and the phase shifts are shown the second column. The photon densities as a function of the distance

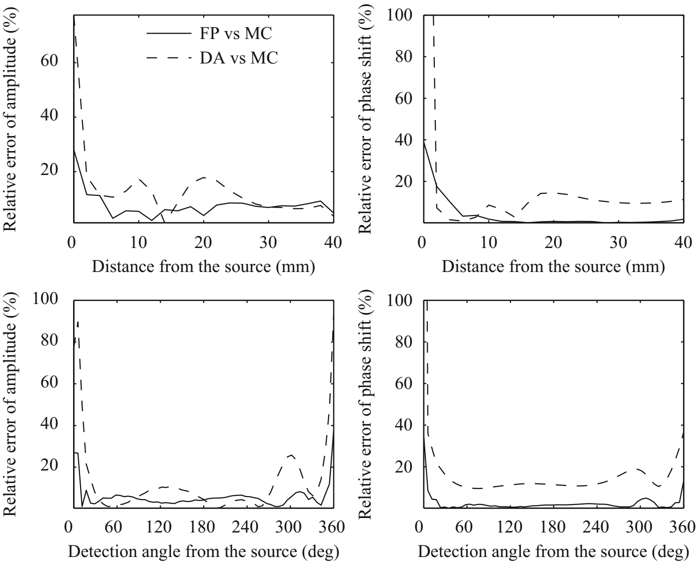

Fig. 9. The relative errors of the amplitudes (left column) and the phase shifts (right column) of the photon densities calculated with the Fokker–Planck equation (solid line) and the DA (dashed line) in the circular medium including a low-scattering inclusion. The relative errors along the source direction are on the top row and the relative errors on the boundary of the object along the detection angle are on the bottom row.

from the source are on the top row and the photon densities as a function of the detection angle are on the bottom row. The relative errors of the photon densities are shown in Fig. 7. The figures are in respective order as in Fig. 6.

The results of the DA differ clearly from the results of the Fokker–Planck equation when compared to MC. The Fokker–Planck equation describes the light propagation more accurately than the DA on the center axis and on the boundary. Especially on the phase shift the Fokker–Planck equation predicts the light propagation with good precision.

4.3.2. *Low-scattering inclusion*

The photon densities were computed as earlier. The results are shown in Fig. 8. Furthermore, the relative errors of the photon densities are shown in Fig. 9. Because the case was not symmetric, the results are shown over full circle instead of semi-circle.

The results show that the Fokker–Planck equation gives more accurate results both on the center axis and on the boundary. All three models give similar results on the amplitude, but still the Fokker–Planck equation is more accurate than the DA. In addition, in the phase shift the Fokker–Planck is clearly more accurate than the DA.

5. Conclusions

In this paper, a finite element solution of the Fokker–Planck equation was introduced. The Fokker–Planck equation is an approximation to the radiative transfer equation that is applicable when the scattering is forward-peaked. Due to angular dependence the Fokker–Planck equation is computationally more expensive than the diffusion approximation, but still less demanding to solve than the full transport equation [13].

The finite element solution of the Fokker–Planck equation was tested with simulations with different optical properties. The results of the proposed FE-model were compared with the finite element solution of the DA and Monte Carlo simulations. The results show that the Fokker–Planck equation can describe light propagation accurately when the scattering is forward-peaked. The relative errors indicate that the accuracy of the Fokker–Planck equation is equal or better compared to the DA when the scattering is forward dominated which is the usual situation in DOT.

The FE-solution of the Fokker–Planck equation has a good accuracy also in cases in which turbid medium includes a low-scattering void-like region. Thus the Fokker–Planck equation could also be utilized in this demanding case where the DA fails.

Acknowledgments

This work was supported by the Academy of Finland (Projects 122499, 119270 and 213476, Finnish Center of Excellence in Inverse Problems Research), Vilho, Yrjö and Kalle Väisälä foundation and by EPSRC Grant EP/E034950/1.

Appendix A. Variational formulation of the Fokker–Planck equation

To derive variational formulation for Eq. (15), it is multiplied by test function $v(r,\hat{s})$ and integrated over domain $G=\Omega\times S^{n-1}$

$$\int_G \frac{\mathrm{i}\omega}{c}\phi(r,\hat{s})v(r,\hat{s})\,\mathrm{d}V+\int_G(\hat{s}\cdot\nabla)\phi(r,\hat{s})v(r,\hat{s})\,\mathrm{d}V \\ +\int_G \mu_\mathrm{a}\phi(r,\hat{s})v(r,\hat{s})\,\mathrm{d}V \\ -\int_G \xi_n\mu_\mathrm{s}(1-g)\Delta_{\hat{s}}\phi(r,\hat{s})v(r,\hat{s})\,\mathrm{d}V=0 \quad \forall v(r,\hat{s}). \tag{26}$$

Using Green's theorem [26] and boundary condition (5), the second term of Eq. (26) can be written as

$$\int_\Omega\int_{S^{n-1}} v(r,\hat{s})(\hat{s}\cdot\nabla\phi(r,\hat{s}))\,\mathrm{d}\hat{s}\,\mathrm{d}r \\ =-\int_\Omega\int_{S^{n-1}}\hat{s}\cdot\nabla v(r,\hat{s})\phi(r,\hat{s})\,\mathrm{d}\hat{s}\,\mathrm{d}r \\ +\int_{\partial\Omega}\int_{S^{n-1}}(\hat{s}\cdot\hat{n})\phi(r,\hat{s})v(r,\hat{s})\,\mathrm{d}\hat{s}\,\mathrm{d}r \\ =-\int_\Omega\int_{S^{n-1}}\hat{s}\cdot\nabla v(r,\hat{s})\phi(r,\hat{s})\,\mathrm{d}\hat{s}\,\mathrm{d}r \\ +\int_{\partial\Omega}\int_{S^{n-1}}(\hat{s}\cdot\hat{n})_+\phi(r,\hat{s})v(r,\hat{s})\,\mathrm{d}\hat{s}\,\mathrm{d}r \\ +\int_{\partial\Omega}\int_{S^{n-1}}(\hat{s}\cdot\hat{n})_-\phi_0(r,\hat{s})v(r,\hat{s})\,\mathrm{d}\hat{s}\,\mathrm{d}S, \tag{27}$$

where $(\hat{s}\cdot\hat{n})_+$ and $(\hat{s}\cdot\hat{n})_-$ denote the positive and negative parts of $(\hat{s}\cdot\hat{n})$ defined as

$$(\hat{s}\cdot\hat{n})_+=\begin{cases}(\hat{s}\cdot\hat{n}) & \hat{s}\cdot\hat{n}\geq 0,\\ 0 & \hat{s}\cdot\hat{n}<0,\end{cases} \tag{28}$$

$$(\hat{s}\cdot\hat{n})_-=\begin{cases}0 & \hat{s}\cdot\hat{n}\geq 0,\\ -(\hat{s}\cdot\hat{n}) & \hat{s}\cdot\hat{n}<0.\end{cases} \tag{29}$$

The fourth term of Eq. (26) can be written as

$$\int_\Omega\int_{S^{n-1}}\xi_n\mu_\mathrm{s}(1-g)\Delta_{\hat{s}}\phi(r,\hat{s})v(r,\hat{s})\,\mathrm{d}\hat{s}\,\mathrm{d}r \\ =\int_\Omega\int_{S^{n-1}}\xi_n\mu_\mathrm{s}(1-g)\frac{1}{\sin\varphi}\frac{\partial}{\partial\varphi}\left(\sin\varphi\frac{\partial\phi(r,\hat{s})}{\partial\varphi}\right)v(r,\hat{s})\,\mathrm{d}\hat{s}\,\mathrm{d}r \\ -\int_\Omega\int_{S^{n-1}}\xi_n\mu_\mathrm{s}(1-g)\frac{1}{\sin^2\varphi}\frac{\partial\phi(r,\hat{s})}{\partial\theta}\frac{\partial v(r,\hat{s})}{\partial\theta}\,\mathrm{d}\hat{s}\,\mathrm{d}r \\ +\underbrace{\int_\Omega\int_{\partial S^{n-1}}\xi_n\mu_\mathrm{s}\frac{1}{\sin^2\varphi}\frac{\partial\phi(r,\hat{s})}{\partial\theta}v(r,\hat{s})\,\mathrm{d}A\,\mathrm{d}r}_{=0}. \tag{30}$$

Using Eqs. (28) and (31), we can write Eq. (26) as

$$\int_\Omega\int_{S^{n-1}}\frac{\mathrm{i}\omega}{c}\phi(r,\hat{s})v(r,\hat{s})\,\mathrm{d}\hat{s}\,\mathrm{d}r-\int_\Omega\int_{S^{n-1}}\hat{s}\cdot\nabla v(r,\hat{s})\phi(r,\hat{s})\,\mathrm{d}\hat{s}\,\mathrm{d}r \\ +\int_{\partial\Omega}\int_{S^{n-1}}(\hat{s}\cdot\hat{n})_+\phi(r,\hat{s})v(r,\hat{s})\,\mathrm{d}\hat{s}\,\mathrm{d}S \\ +\int_\Omega\int_{S^{n-1}}\mu_\mathrm{a}\phi(r,\hat{s})v(r,\hat{s})\,\mathrm{d}\hat{s}\,\mathrm{d}r \\ +\int_\Omega\int_{S^{n-1}}\xi_n\mu_\mathrm{s}(1-g)\frac{1}{\sin^2\varphi}\frac{\partial\phi(r,\hat{s})}{\partial\theta}\frac{\partial v(r,\hat{s})}{\partial\theta}\,\mathrm{d}\hat{s}\,\mathrm{d}r \\ -\int_\Omega\int_{S^{n-1}}\xi_n\mu_\mathrm{s}(1-g)\frac{1}{\sin\varphi}\frac{\partial}{\partial\varphi}\left(\sin\varphi\frac{\partial\phi(r,\hat{s})}{\partial\varphi}\right)v(r,\hat{s})\,\mathrm{d}\hat{s}\,\mathrm{d}r \\ =\int_{\partial\Omega}\int_{S^{n-1}}(\hat{s}\cdot\hat{n})_-\phi_0(r,\hat{s})v(r,\hat{s})\,\mathrm{d}\hat{s}\,\mathrm{d}S. \tag{31}$$

Eq. (31) is the variational formulation of the Fokker–Planck Eq. (15).

Appendix B. Finite element approximation of the Fokker–Planck equation

Solution $\phi(r,\hat{s})$ of the variational formulation is approximated with a linear combination of the basis functions, Eq. (17). Using the chosen basis and choosing basis functions $\psi_l(r)$ and $\psi_m(\hat{s})$ as test functions and inserting them into variational formulation (31), we arrive at system of equations

$$\int_\Omega\int_{S^{n-1}}\frac{\mathrm{i}\omega}{c}\sum_{i=1}^{N_n}\sum_{l=1}^{N_a}\alpha_{il}\psi_i(r)\psi_l(\hat{s})\psi_j(r)\psi_m(\hat{s})\,\mathrm{d}\hat{s}\,\mathrm{d}r \\ -\int_\Omega\int_{S^{n-1}}\hat{s}\cdot\nabla\psi_j(r)\psi_m(\hat{s})\sum_{i=1}^{N_n}\sum_{l=1}^{N_a}\alpha_{il}\psi_i(r)\psi_l(\hat{s})\,\mathrm{d}\hat{s}\,\mathrm{d}r \\ +\int_{\partial\Omega}\int_{S^{n-1}}(\hat{s}\cdot\hat{n})_+\sum_{i=1}^{N_n}\sum_{l=1}^{N_a}\alpha_{il}\psi_i(r)\psi_l(\hat{s})\psi_j(r)\psi_m(\hat{s})\,\mathrm{d}\hat{s}\,\mathrm{d}S \\ +\int_\Omega\int_{S^{n-1}}\mu_\mathrm{a}\sum_{i=1}^{N_n}\sum_{l=1}^{N_a}\alpha_{il}\psi_i(r)\psi_l(\hat{s})\psi_j(r)\psi_m(\hat{s})\,\mathrm{d}\hat{s}\,\mathrm{d}r \\ +\int_\Omega\int_{S^{n-1}}\xi_n\mu_\mathrm{s}(1-g)\sum_{i=1}^{N_n}\sum_{l=1}^{N_a}\alpha_{il}\frac{1}{\sin^2\varphi} \\ \frac{\partial\psi_i(r)\psi_l(\hat{s})}{\partial\theta}\frac{\partial\psi_j(r)\psi_m(\hat{s})}{\partial\theta}\,\mathrm{d}\hat{s}\,\mathrm{d}r \\ -\int_\Omega\int_{S^{n-1}}\xi_n\mu_\mathrm{s}(1-g)\sum_{i=1}^{N_n}\sum_{l=1}^{N_a}\alpha_{il}\frac{1}{\sin\varphi} \\ \frac{\partial}{\partial\varphi}\left(\sin\varphi\frac{\partial\psi_i(r)\psi_l(\hat{s})}{\partial\varphi}\right)\psi_j(r)\psi_m(\hat{s})\,\mathrm{d}\hat{s}\,\mathrm{d}r \\ =\int_{\partial\Omega}\int_{S^{n-1}}(\hat{s}\cdot\hat{n})_-\phi_0\psi_j(r)\psi_m(\hat{s})\,\mathrm{d}\hat{s}\,\mathrm{d}S. \tag{32}$$

The boundary source $\phi_0(r,\hat{s})$ can be represented in the same basis as the solution

$$\phi_0(r,\hat{s})\approx\sum_{i=1}^{N_n}\sum_{l=1}^{N_a}\psi_{il}^0\psi_i(r)\psi_l(\hat{s}), \tag{33}$$

where ψ_{il}^0 is source intensity in the spatial node i into the angular direction l. Inserting this into Eq. (32) and by changing the order of integration and summation, the following system of equations is obtained:

$$\frac{\mathrm{i}\omega}{c}\sum_{i=1}^{N_n}\sum_{l=1}^{N_a}\alpha_{il}\int_\Omega\psi_i(r)\psi_j(r)\,\mathrm{d}r\int_{S^{n-1}}\psi_l(\hat{s})\psi_m(\hat{s})\,\mathrm{d}\hat{s} \\ -\sum_{i=1}^{N_n}\sum_{l=1}^{N_a}\alpha_{il}\int_\Omega\int_{S^{n-1}}\hat{s}\cdot\nabla\psi_j(r)\psi_m(\hat{s})\psi_i(r)\psi_l(\hat{s})\,\mathrm{d}\hat{s}\,\mathrm{d}r \\ +\sum_{i=1}^{N_n}\sum_{l=1}^{N_a}\alpha_{il}\int_{\partial\Omega}\psi_i(r)\psi_j(r)\,\mathrm{d}S\int_{S^{n-1}}(\hat{s}\cdot\hat{n})_+\psi_l(\hat{s})\psi_m(\hat{s})\,\mathrm{d}\hat{s} \\ +\sum_{i=1}^{N_n}\sum_{l=1}^{N_a}\alpha_{il}\int_\Omega\mu_\mathrm{a}\psi_i(r)\psi_j(r)\,\mathrm{d}r\int_{S^{n-1}}\psi_l(\hat{s})\psi_m(\hat{s})\,\mathrm{d}\hat{s} \\ +\sum_{i=1}^{N_n}\sum_{l=1}^{N_a}\alpha_{il}\int_\Omega\xi_n\mu_\mathrm{s}(1-g)\psi_i(r)\psi_j(r)\,\mathrm{d}r$$

$$\int_{S^{n-1}} \frac{1}{\sin^2\varphi}\frac{\partial\psi_l(\hat{s})}{\partial\theta}\frac{\partial\psi_m(\hat{s})}{\partial\theta}\,\mathrm{d}\hat{s} - \sum_{i=1}^{N_n}\sum_{l=1}^{N_a}\alpha_{il}$$

$$\int_{\Omega}\xi_n\mu_s(1-g)\psi_i(r)\psi_j(r)\,\mathrm{d}r\int_{S^{n-1}}\frac{1}{\sin\varphi}\frac{\partial}{\partial\varphi}\left(\sin\varphi\frac{\partial\psi_l(\hat{s})}{\partial\varphi}\right)\psi_m(\hat{s})\,\mathrm{d}\hat{s}$$

$$= \sum_{i=1}^{N_n}\sum_{l=1}^{N_a}\psi_{il}^{0}\int_{\partial\Omega}\psi_i(r)\psi_j(r)\,\mathrm{d}S\int_{S^{n-1}}(\hat{s}\cdot\hat{n})_{-}\psi_l(\hat{s})\psi_m(\hat{s})\,\mathrm{d}\hat{s}. \tag{34}$$

This is the FE-approximation of the Fokker–Planck equation. It can further be written in the matrix form (18).

References

[1] Arridge S. Optical tomography in medical imaging. Inverse Problems 1999;15:41.

[2] Gibson A, Hebden J, Arridge S. Recent advances in diffuse optical imaging. Physics in Medicine and Biology 2005;50(4):1–43.

[3] Case K, Zweifel P. Linear transport theory. USA: Addison-Wesley Educational Publishers Inc.; 1967.

[4] Ishimaru A. Wave propagation and scattering in random media. New York: Academic; 1978.

[5] Hielscher A, Alcouffe R, Barbour R. Comparison of finite-difference transport and diffusion calculations for photon migration in homogeneous and heterogeneous tissues. Physics in Medicine and Biology 1998;43(5):1285–302.

[6] Kim A, Keller J. Light propagation in biological tissue. Journal of the Optical Society of America A 2003;20(1):92–8.

[7] Bal G. Inverse transport theory and applications. Inverse Problems 2009;25:053001.

[8] Cheong W, Prahl S, Welch A, et al. A review of the optical properties of biological tissues. IEEE Journal of Quantum Electronics 1990;26(12):2166–85.

[9] González-Rodríguez P, Kim A. Light propagation in tissues with forward-peaked and large-angle scattering. Applied Optics 2008;47(14):2599–609.

[10] Pomraning G. The Fokker–Planck operator as an asymptotic limit. Mathematical Models and Methods in Applied Sciences 1992;2: 21–36.

[11] Morel J. Fokker–Planck calculations using standard discrete ordinates transport codes. Nuclear Science and Engineering 1981;79:340–56.

[12] Kim A. Transport theory for light propagation in biological tissue. Journal of the Optical Society of America A 2004;21(5):820–7.

[13] González-Rodríguez P, Kim A. Comparison of light scattering models for diffuse optical tomography. Optics Express 2009;17(11):8756–74.

[14] Dorn O. A transport–backtransport method for optical tomography. Inverse Problems 1998;14:1107–30.

[15] Abdoulaev G, Hielscher A. Three-dimensional optical tomography with the equation of radiative transfer. Journal of Electronic Imaging 2003;12:594.

[16] Aydin E, De Oliveira C, Goddard A. A comparison between transport and diffusion calculations using a finite element-spherical harmonics radiation transport method. Medical Physics 2002;29:2013.

[17] Tarvainen T, Vauhkonen M, Kolehmainen V, Kaipio JP. Hybrid radiative-transfer-diffusion model for optical tomography. Applied Optics 2005;44(6):876–86.

[18] Boman E, Tervo J, Vauhkonen M. Modelling the transport of ionizing radiation using the finite element method. Physics in Medicine and Biology 2005;50(2):265–80.

[19] Henyey L, Greenstein J. Diffuse radiation in the Galaxy, Astrophys. J. 1941;93.

[20] Heino J, Somersalo E. Estimation of optical absorption in anisotropic background. Inverse Problems 2002;18:559–73.

[21] Schweiger M, Arridge S, Hiraoka M, Delpy D. The finite element method for the propagation of light in scattering media: boundary and source conditions. Medical Physics 1995;22:1779.

[22] Kolehmainen V, Vauhkonen M, Kaipio J, Arridge S. Recovery of piecewise constant coefficients in optical diffusion tomography. Inverse Problems 1999;15:1375–91.

[23] Prahl S, Keijzer M, Jacques S, Welch A. A Monte Carlo model of light propagation in tissue. In: SPIE proceedings of dosimetry of laser radiation in medicine and biology, 1989. p. 102–11.

[24] Heiskala J, Nissilä I, Neuvonen T, Järvenpää S, Somersalo E. Modeling anisotropic light propagation in a realistic model of the human head. Applied Optics 2005;44(11):2049–57.

[25] Tarvainen T, Kolehmainen V, Pulkkinen A, Vauhkonen M, Schweiger M, Arridge SR, et al. Approximation error approach for compensating modelling errors between the radiative transfer equation and the diffusion approximation in diffuse optical tomography. Inverse Problems 2010;26:015005 [18pp.].

[26] Arfken G, Weber H, Weber H. Mathematical methods for physicists. New York: Academic Press; 1985.

Paper **II**

O. Lehtikangas, T. Tarvainen,
A.D. Kim,
"Modeling boundary measurements of scattered light using the corrected diffusion approximation",
Biomedical Optics Express,
3, pp. 552–571, 2012.

Modeling boundary measurements of scattered light using the corrected diffusion approximation

Ossi Lehtikangas,[1,*] **Tanja Tarvainen,**[1,2] **and Arnold D. Kim**[3]

[1] *Department of Applied Physics, University of Eastern Finland, P.O. Box 1627, 70211 Kuopio, Finland*

[2] *Department of Computer Science, University College London, Gower Street, London WC1E 6BT, United Kingdom*

[3] *School of Natural Sciences, University of California, Merced, 5200 North Lake Road, Merced, CA 95343, USA*

[*] *Ossi.Lehtikangas@uef.fi*

Abstract: We study the modeling and simulation of steady-state measurements of light scattered by a turbid medium taken at the boundary. In particular, we implement the recently introduced corrected diffusion approximation in two spatial dimensions to model these boundary measurements. This implementation uses expansions in plane wave solutions to compute boundary conditions and the additive boundary layer correction, and a finite element method to solve the diffusion equation. We show that this corrected diffusion approximation models boundary measurements substantially better than the standard diffusion approximation in comparison to numerical solutions of the radiative transport equation.

OCIS codes: (170.7050) Turbid media; (030.5620) Radiative transfer; (290.1990) Diffusion; (170.3660) Light propagation in tissues; (000.3860) Mathematical methods in physics.

References and links

1. A. Ishimaru, *Wave Propagation and Scattering in Random Media* (IEEE, New York, 1997).
2. L.V. Wang and H. Wu, *Biomedical Optics: Principles and Imaging* (Wiley, Hoboken, NJ, 2007).
3. S.R. Arridge, “Optical tomography in medical imaging,” Inv. Prob. **15**, R41–R93 (1999).
4. S.R. Arridge and J.C. Schotland, “Optical tomography: forward and inverse problems,” Inv. Prob. **25** 123010 (2009).
5. A.P. Gibson, J.C. Hebden, S.R. Arridge, “Recent advances in diffuse optical imaging,” Phys. Med. Biol. **50** R1–R43 (2005).
6. B.T. Cox, S.R. Arridge, K.P. Köstli, P.C. Beard, “Two-dimensional quantitative photoacoustic image reconstruction of absorption distributions in scattering media by use of a simple iterative method,” Appl. Opt. **45**, 1866–1875 (2006).
7. G. Bal and K. Ren, “Multi-source quantitative photoacoustic tomography in a diffusive regime,” Inv. Prob. **27**, 075003 (2011).
8. A.Q. Bauer, R.E. Nothdurft, T.N. Erpelding, L.V. Wang, J.P. Culver, “Quantitative photoacoustic imaging: correcting for heterogeneous light fluence distributions using diffuse optical tomography,” J. Biomed. Opt. **16**, 096016 (2011).
9. R. Aronson, “Extrapolation distance for diffusion of light,” Proc. SPIE **1888**, 297–304 (1993).
10. R. C. Haskell, L. O. Svaasand, T.-T. Tsay, T.-C. Feng, M. S. McAdams and B. J. Tromberg, “Boundary conditions for the diffusion equation in radiative transfer,” J. Opt. Soc. Am. A **11**, 2727–2741 (1994).
11. R. Aronson, “Boundary conditions for the diffusion of light,” J. Opt. Soc. Am. A **12**, 2532–2539 (1995).
12. R. Aronson and N. Corngold, “Photon diffusion coefficient in an absorbing medium,” J. Opt. Soc. Am. A **16**, 1066–1071 (1999).

#160854 - $15.00 USD Received 5 Jan 2012; revised 9 Feb 2012; accepted 9 Feb 2012; published 21 Feb 2012

13. J. Ripoll and M. Nieto-Vesperinas, “Index mismatch for diffuse photon density waves at both flat and rough diffuse-diffuse interfaces,” J. Opt. Soc. Am. A **16**, 1947–1957 (1999).
14. S. Fantini, M. A. Franceschini and E. Gratton, “Effective source term in the diffusion equation for photon transport in turbid media,” Appl. Opt. **36**, 156–163 (1997).
15. X. Intes, B. Le Jeune, F. Pellen, Y. Guern, J. Cariou and J. Lotrian, “Localization of the virtual point source used in the diffusion approximation to model a collimated beam source,” Waves Random Media **9**, 489–499 (1999).
16. T. Spott and L. O. Svaasand, “Collimated light sources in the diffusion approximation,” Appl. Opt. **39**, 6453–6465 (2000).
17. L.-H. Wang and S. L. Jacques, “Hybrid model of Monte Carlo simulation and diffusion theory for light reflectance by turbid media,” J. Opt. Soc. Am. A **10**, 1746–1752 (1993).
18. T. Tarvainen, M. Vauhkonen, V. Kolehmainen and J. P. Kaipio, “Finite element model for the coupled radiative transfer equation and diffusion approximation,” Int. J. Num. Math. Eng. **65**, 383–405 (2006).
19. H. Gao and H. Zhao, “A fast forward solver of radiative transfer equation,” Transp. Theory Stat. Phys **38**, 149–192 (2009).
20. A.D. Kim, “Correcting the diffusion approximation at the boundary,” J. Opt. Soc. Am. A **28**, 1007–1015 (2011).
21. E.W. Larsen and J. B. Keller, “Asymptotic solution of neutron transport problems for small mean free paths,” J. Math. Phys. **15**, 75–81 (1974).
22. G.J. Habetler and B. J. Matkowsky, “Uniform asymptotic expansions in transport theory with small mean free paths, and the diffusion approximation,” J. Math. Phys. **16**, 846–854 (1975).
23. G.C. Pomraning and B. D. Ganapol, “Asymptotically consistent reflection boundary conditions for diffusion theory,” Ann. Nucl. Energy **22**, 787–817 (1995).
24. L.G. Henyey and J.L. Greenstein, “Diffuse radiation in the Galaxy,” Astrophys. J. **93**, 70–83 (1941).
25. J. Heino, S.R. Arridge, J. Sikora and E. Somersalo, “Anisotropic effects in highly scattering media,” Phys. Rev. E **68**, 031908 (2003).
26. A.D. Kim and J. B. Keller, “Light propagation in biological tissue,” J. Opt. Soc. Am. A **20**, 92–98 (2003).
27. A.D. Kim, “Transport theory for light propagation in biological tissue,” J. Opt. Soc. Am. A **21**, 820–827 (2004).
28. S.R. Arridge, M. Schweiger, M. Hiraoka and D. T. Delpy, “A finite element approach for modeling photon transport in tissue,” Med. Phys. **20**, 299–299 (1993).
29. K.D. Paulsen and H. Jiang, “Spatially varying optical property reconstruction using a finite element diffusion equation approximation,” Med. Phys. **22**, 691–702 (1995).
30. M. Schweiger and S.R. Arridge, “The finite-element method for the propagation of light in scattering media: frequency domain case,” Med. Phys. **24**, 895–902 (1997).
31. V. Kolehmainen, S.R. Arridge, W.R.B Lionheart, M. Vauhkonen and J.P. Kaipio, “Recovery of region boundaries of piecewise constant coefficients of an elliptic PDE from boundary data,” Inv. Prob. **15**, 1375–1391 (1999).
32. T. Tarvainen, M. Vauhkonen, V. Kolehmainen and J.P. Kaipio, “Hybrid radiative-transfer-diffusion model for optical tomography,” Appl. Opt. **44**, 876–886 (2005).
33. T. Tarvainen, M. Vauhkonen, V. Kolehmainen, S.R. Arridge and J.P. Kaipio, “Coupled radiative transfer equation and diffusion approximation model for photon migration in turbid medium with low-scattering and non-scattering regions,” Phys. Med. Biol, **50**, 4913–4930 (2005).
34. A.D. Kim and M. Moscoso, “Diffusion of polarized light,” Multiscale Model. Simul. **9**, 1624–1645 (2011).
35. T. Tarvainen, V. Kolehmainen, S.R. Arridge and J.P. Kaipio, “Image reconstruction in diffuse optical tomography using the coupled radiative transport-diffusion model,” J. Quant. Spect. Rad. Trans. **112** 2600–2608 (2011).
36. M. Schweiger, S.R. Arridge, M. Hiraoka, D.T. Delpy, “The finite element method for the propagation of light in scattering media: boundary and source conditions,” Med. Phys. **22**, 1779–1792 (1995).
37. M. Keijzer, W.M. Star, P.R.M. Storchi, “Optical diffusion in layered media,” Appl. Opt. **27**, 1820–1824 (1988).
38. G. Kanschat, “A robust finite element discretization for radiative transfer problems with scattering,” East West J. Num. Math. **6**, 265–272 (1998).
39. S. Richling, E. Meinköhn, N. Kryzhevoi and G. Kanschat, “Radiative transfer with finite elements,” Astron. Astrophys. **380**, 776–788 (2001).

---

1. Introduction

Non-invasive boundary measurements of light scattered by tissues are important for biomedical applications [1, 2]. By extracting information from these measurements regarding the optical properties of tissues (*e.g.* absorption and scattering), one may gain valuable insight into tissue health. For example, in diffuse optical tomography (DOT) and fluorescence diffuse optical tomography (fDOT), one seeks to reconstruct the optical properties of tissues from measurements of light at the boundary of the domain. The applications include, for example, detection and classification of breast cancer, monitoring of infant brain tissue oxygenation level and functional brain activation studies, for reviews see e.g. [3–5]. In quantitative photoacoustic tomog-

#160854 - $15.00 USD Received 5 Jan 2012; revised 9 Feb 2012; accepted 9 Feb 2012; published 21 Feb 2012

raphy (QPAT) one seeks to estimate concentration of chromophores, such as hemoglobin and melanin, inside tissues by combining the optical contrast and ultrasound propagation [6–8].

Image reconstruction problems in DOT, fDOT and QPAT are non-linear ill-posed inverse problems. There are no direct methods for the solution of these problems, and thus they are typically stated as minimization problems such as regularized output least squares. The iterative solution of this problem requires repetitive solutions of the forward model. Therefore, it is essential to have a computationally feasible forward model that describes light propagation in tissues accurately.

The theory of radiative transport governs light propagation in tissues [1,2]. This theory takes into account absorption and scattering due to inhomogeneities in the medium. The major challenge in using radiative transport theory to study light propagation in tissues is that it is mathematically complicated due mostly to the large number of variables in the radiative transport equation (RTE). The large dimensionality of the RTE makes even computational methods challenging.

Tissues typically scatter light strongly and absorb light weakly. For that reason, one often replaces the RTE by the diffusion approximation (DA) [1–4]. In the DA, one assumes that the light becomes nearly isotropic due to strong multiple scattering. The DA is much simpler to solve than the RTE. However, applying the DA to model boundary measurements is problematic. It is well known that the DA is not valid near sources or boundaries. This is because the assumption that light is nearly isotropic is too restrictive to take into account sources and boundary conditions. Nonetheless, the DA has been used to model boundary measurements with some success despite these limitations. Regardless, there still exists a need for more accurate models of boundary measurements. Consequently, the prescription of “correct” boundary conditions [9–13] and source terms [14–16] for the DA has been a long-standing issue.

There have been some works that have taken into account sources and boundaries correctly by combining the solutions of the RTE and the DA to form a hybrid method. Wang and Jacques [17] used Monte Carlo simulations for the RTE in combination with the DA. Tarvainen *et al* [18] developed a coupled method combining solutions of the RTE and DA both within a finite element framework for both space and angle. This coupled method can take into account correctly boundaries, sources as well as low-scattering regions in the interior of the domain. Recently, Gao and Zhao [19] developed a sophisticated numerical method to solve the RTE. This method employs multigrid methods in both space and angle where the coarsest grid level is consistent with the DA when scattering is strong and absorption is weak.

Recently, Kim [20] presented an asymptotic analysis of the RTE leading to the so-called corrected diffusion approximation (cDA). The additive correction to the DA is given by a boundary layer solution. This boundary layer solution corrects for the error made by the DA near the boundary. It vanishes rapidly away from the boundary (on the order of one scattering mean free path) so that the standard DA approximates the solution deep within the interior of the domain. The asymptotic analysis used to derive this boundary layer solution was established in the early 1970’s in the neutron transport community [21,22]. In fact, Pomraning and Ganapol [23] used this asymptotic analysis to study boundary conditions for the DA in detail.

In this paper, we use the cDA to model boundary measurements. Using a finite element method (FEM) to solve the DA, we are able to consider general spatial domains. By computing the boundary layer solution only for boundary points where we are modeling measurements, we show that the cDA provides a superior approximation to the solution of the RTE requiring only a small amount of more work than solving the DA itself. In particular, we consider a spatial domain $\Omega \subset \mathbb{R}^2$ with boundary $\partial\Omega$. Although the simulations presented here are limited to two-dimensional (2D) case, the theory derived in [20] and reviewed here is represented in dimensional independent form allowing for the realization of the method both in two and three

#160854 - $15.00 USD Received 5 Jan 2012; revised 9 Feb 2012; accepted 9 Feb 2012; published 21 Feb 2012

dimensions (3D). In 3D, the cDA consist of solving 3D diffusion equation and one-dimensional radiative transport equation for each of the measurements locations. Thus, the extension of method to 3D is straightforward.

The remainder of the paper is as follows. In Section 2, we give an overview of the asymptotic analysis of the RTE leading to the cDA. In Section 3 we give details of the calculations needed to compute the boundary condition coefficients for the diffusion equation and the boundary layer solution. In addition, we give details of the numerical method used to solve the diffusion equation. In Section 4 we show results from our computational simulations. Section 5 is the conclusions.

2. Asymptotic analysis of the radiative transport equation

The steady-state radiative transport equation

$$\hat{\mathbf{s}} \cdot \nabla \phi + \mu_a \phi + \mu_s \mathscr{L} \phi = 0 \tag{1}$$

governs continuous light propagation in an absorbing and scattering medium. The radiance $\phi := \phi(\mathrm{r}, \hat{\mathbf{s}})$ gives the power at position $\mathrm{r} \in \Omega \subset \mathbb{R}^n$ flowing in direction $\hat{\mathbf{s}} \in S^{n-1}$ with n denoting the number of spatial dimensions and S^{n-1} denoting the unit sphere. The absorption and scattering coefficients are denoted by $\mu_a := \mu_a(\mathrm{r})$ and $\mu_s := \mu_s(r)$, respectively. The scattering operator $\mathscr{L}$ is defined as

$$\mathscr{L}\phi = \phi - \int_{S^{n-1}} \Theta(\hat{\mathbf{s}} \cdot \hat{\mathbf{s}}')\phi(\mathrm{r}, \hat{\mathbf{s}}')\mathrm{d}\hat{\mathbf{s}}'. \tag{2}$$

The scattering phase function Θ gives the fraction of light scattered in direction $\hat{\mathbf{s}}$ due to light incident in direction $\hat{\mathbf{s}}'$. We assume that scattering is rotationally invariant so that the scattering phase function Θ depends only $\hat{\mathbf{s}} \cdot \hat{\mathbf{s}}'$.

To solve Eq. (1) in $\Omega \times S^{n-1}$, we must supplement boundary conditions of the form

$$\phi = \phi_0 + \mathscr{R}\phi \quad \text{on } \Gamma_{\text{in}} = \{(\mathrm{r}, \hat{\mathbf{s}}) \in \partial\Omega \times S^{n-1}, \hat{\mathbf{s}} \cdot \hat{\mathbf{n}} < 0\} \tag{3}$$

where ϕ_0 is the source, $\partial\Omega$ the boundary of domain Ω and $\hat{\mathbf{n}}$ denotes the unit *outward* normal on $\partial\Omega$. Here, $\mathscr{R}\phi$ denotes the reflection of light due to a mismatch in the refractive index at the boundary (see Appendix B, Eq. (B.4)). Boundary condition Eq. (3) prescribes the radiance over only the directions pointing into the domain.

Boundary measurements are given by the exitance $\Gamma(\mathrm{r}_b)$ defined as

$$\Gamma(\mathrm{r}_b) = \int_{\hat{\mathbf{s}} \cdot \hat{n} > 0} T(\hat{\mathbf{s}} \cdot \hat{n})\phi(\mathrm{r}_b, K(\hat{\mathbf{s}}))\mathrm{d}\hat{\mathbf{s}}, \quad \mathrm{r}_b \in \partial\Omega, \tag{4}$$

where $T = 1 - R$ is the Fresnel transmission coefficient in the case of mismatched refractive indices at the boundary and mapping K implements the Snell's law in a vector form (see Appendix B, Eq. (B.15)). Furthermore, other quantity of interest is the fluence rate $\Upsilon(\mathrm{r})$, defined as an integral of the radiance over angular directions

$$\Upsilon(\mathrm{r}) = \int_{S^{n-1}} \phi(\mathrm{r}, \hat{\mathbf{s}})\mathrm{d}\hat{\mathbf{s}}, \quad \mathrm{r} \in \Omega. \tag{5}$$

We consider the case in which scattering is strong and absorption is weak. To make this assumption explicit, we introduce a small, dimensionless parameter $0 < \varepsilon \ll 1$ according to

$$\mu_a = \varepsilon\alpha, \quad \mu_s = \varepsilon^{-1}\sigma. \tag{6}$$

By substituting Eq. (6) into Eq. (1), we obtain

$$\varepsilon\hat{\mathbf{s}} \cdot \nabla\phi + \varepsilon^2\alpha\phi + \sigma\mathscr{L}\phi = 0. \tag{7}$$

We seek an asymptotic solution of Eq. (7) in the limit as $\varepsilon \to 0^+$ of the form

$$\phi = \Phi + \Psi. \tag{8}$$

Here, Φ denotes the interior solution and Ψ denotes the boundary layer solution. This asymptotic analysis was done recently in [20]. In what follows, we summarize the results from that work.

Seeking the interior solution Φ in the form

$$\Phi = \Phi_0 + \varepsilon \Phi_1 + O(\varepsilon^2), \tag{9}$$

we find that $\Phi_0 = \Phi_0(\mathrm{r})$ and $\Phi_1 = -n\kappa \hat{\mathbf{s}} \cdot \nabla \Phi_0$ with Φ_0 satisfying the diffusion equation

$$\nabla \cdot (\kappa \nabla \Phi_0) - \alpha \Phi_0 = 0. \tag{10}$$

The diffusion coefficient κ is defined as

$$\kappa = [n\sigma(1-g)]^{-1}, \tag{11}$$

with g denoting the anisotropy factor defined as the mean of the cosine of the scattering phase function

$$g = \int_{S^{n-1}} (\hat{\mathbf{s}} \cdot \hat{\mathbf{s}}') \Theta(\hat{\mathbf{s}} \cdot \hat{\mathbf{s}}') \mathrm{d}\hat{\mathbf{s}}'. \tag{12}$$

The leading order behavior of the interior solution $\Phi \sim \Phi_0(\mathrm{r}) - \varepsilon n\kappa \hat{\mathbf{s}} \cdot \nabla \Phi_0(\mathrm{r})$ is a weakly linear function of $\hat{\mathbf{s}}$. In general, a weakly linear function of $\hat{\mathbf{s}}$ is not sufficient to satisfy boundary condition Eq. (3). For that reason, we add a boundary layer solution Ψ to correct the interior solution near the boundary. This boundary layer solution decays rapidly away from the boundary on a length scale that is $O(\varepsilon)$. Thus, $\phi \sim \Phi_0 - \varepsilon n\kappa \hat{\mathbf{s}} \cdot \nabla \Phi_0$ deep in the interior of Ω far away from the boundary $\partial\Omega$.

To compute Ψ near a particular boundary point $\mathrm{r}_b \in \partial\Omega$, consider a coordinate system (ρ, z) where ρ is a vector parallel to the tangent plane at r_b and z is the coordinate along $-\hat{\mathbf{n}}$. Let $z = \varepsilon\zeta$, $\mu = \hat{\mathbf{s}} \cdot (-\hat{\mathbf{n}})$ and $\hat{\mathbf{s}}_\perp = \hat{\mathbf{s}} + \mu \hat{\mathbf{n}}$. Then, each of the terms in the boundary layer solution $\Psi(\rho, \zeta, \hat{\mathbf{s}}) = \Psi_0(\rho, \zeta, \hat{\mathbf{s}}) + \varepsilon \Psi_1(\rho, \zeta, \hat{\mathbf{s}}) + O(\varepsilon^2)$ satisfies boundary value problems for the one-dimensional radiative transport equations of the form

$$\mu \partial_\zeta \Psi_0 + \bar{\sigma} \mathscr{L} \Psi_0 = 0, \quad \text{in } \zeta > 0, \tag{13a}$$

$$\Psi_0 \big|_{\zeta=0} = \phi_0 + \mathscr{R} \Psi_0 - \Phi_0 + \mathscr{R} \Phi_0, \quad \text{on } 0 < \mu \leq 1. \tag{13b}$$

and

$$\mu \partial_\zeta \Psi_1 + \bar{\sigma} \mathscr{L} \Psi_1 = -\hat{\mathbf{s}}_\perp \cdot \nabla_\perp \Psi_0, \quad \text{in } \zeta > 0, \tag{14a}$$

$$\Psi_1 \big|_{\zeta=0} = \mathscr{R} \Psi_1 - \Phi_1 + \mathscr{R} \Phi_1, \quad \text{on } 0 < \mu \leq 1. \tag{14b}$$

with $\bar{\sigma} = \sigma(\mathrm{r}_b)$ and $\nabla_\perp$ denoting the gradient with respect to ρ. Both Ψ_0 and Ψ_1 must satisfy the asymptotic matching condition

$$\Psi_0, \Psi_1 \to 0, \quad \zeta \to \infty. \tag{15}$$

To ensure asymptotic matching condition Eq. (15) is satisfied, one must set

$$\mathscr{P} [\Phi_0 - \mathscr{R} \Phi_0 + \Phi_1 - \mathscr{R} \Phi_1 - \phi_0] = 0. \tag{16}$$

Received 5 Jan 2012; revised 9 Feb 2012; accepted 9 Feb 2012; published 21 Feb 2012

Here, $\mathscr{P}$ is the operator that projects boundary sources for the one-dimensional half space problem onto the mode of the solution that does not decay as $\zeta \to 0$. We give more details about $\mathscr{P}$ in Section 3.

For the special case in which the boundary source is axisymmetric about $\hat{\mathbf{n}}$ so that $\phi_0 = \phi_0(\mathrm{r}_b, \mu)$, the right-hand side of Eq. (14a) vanishes identically and Eq. (16) reduces to the familiar Robin boundary condition

$$a\Phi_0 + b\kappa\hat{\mathbf{n}} \cdot \nabla\Phi_0 = f, \quad \text{on } \partial\Omega, \tag{17}$$

with

$$a = \mathscr{P}[1 - R(\mu)], \tag{18}$$
$$b = \varepsilon n \mathscr{P}[\mu(1 + R(\mu))], \tag{19}$$
$$f = \mathscr{P}[\phi_0(\mathrm{r}_b, \mu)]. \tag{20}$$

The function $R(\mu)$ is the Fresnel reflection coefficient defined with respect to μ which is defined on the local coordinate system with respect to r_b. Equation (10) together with the boundary condition Eq. (17) is known as the diffusion approximation to the RTE. The standard diffusion approximation, which is derived from the spherical harmonics expansion of the RTE, is shown in Appendix A.

Upon solution of Eq. (10) subject to boundary condition Eq. (17), the boundary layer solution in axisymmetric case $\Psi(\zeta, \mu) = \Psi_0 + \varepsilon\Psi_1$ satisfies

$$\mu\partial_\zeta\Psi + \bar{\sigma}\mathscr{L}\Psi = 0, \quad \text{in } \zeta > 0, \tag{21a}$$

$$\begin{aligned}\Psi(0, \mu) = \phi_0(\mathrm{r}_b, \mu) + R(\mu)\Psi(0, -\mu) - [1 - R(\mu)]\Phi_0(\mathrm{r}_b)\\ + \varepsilon n\kappa\mu[1 + R(\mu)]\hat{\mathbf{n}} \cdot \nabla\Phi_0(\mathrm{r}_b), \quad \text{on } 0 < \mu \leq 1.\end{aligned} \tag{21b}$$

Upon solution of boundary value problem Eq. (21), the corrected diffusion approximation evaluated at $\mathrm{r}_b \in \partial\Omega$ is then given by

$$\phi(\mathrm{r}, \hat{\mathbf{s}}_b) \sim \Phi_0(\mathrm{r}_b) - \varepsilon n\kappa\hat{\mathbf{s}} \cdot \nabla\Phi_0(\mathrm{r}_b) + \Psi(0, \mu). \tag{22}$$

Equation (22) gives the asymptotic solution up to $O(\varepsilon^2)$.

3. Numerical implementations

In this section, we give a method used to compute the boundary condition coefficients given by Eqs. (18) - (20) and the solution of the boundary value problem Eq. (21) given the diffusion approximation. Furthermore, we describe briefly a finite element method to solve Eq. (10) subject to boundary condition Eq. (17).

3.1. Computing boundary condition coefficients and boundary layer solutions

To compute the coefficients of the boundary conditions for the diffusion approximation and the boundary layer solution for $\Omega \subset \mathbb{R}^2$, we need to study the canonical half space problem:

$$\cos\theta\partial_\zeta\Psi + \bar{\sigma}\Psi - \bar{\sigma}\int_{-\pi}^{\pi}\Theta(\theta - \theta')\Psi(\zeta, \theta')\mathrm{d}\theta' = 0, \quad \text{in } \zeta > 0, \tag{23a}$$

$$\Psi\big|_{\zeta=0} = \psi + \mathscr{R}\Psi, \quad \text{on } -\pi/2 < \theta < \pi/2. \tag{23b}$$

Received 5 Jan 2012; revised 9 Feb 2012; accepted 9 Feb 2012; published 21 Feb 2012

Here, θ parameterizes S^1 and $\cos\theta = \hat{\mathbf{s}}\cdot(-\hat{\mathbf{n}})$. The boundary source ψ is assumed to be even so that $\psi(\theta) = \psi(-\theta)$ which corresponds to a boundary source that is axisymmetric with respect to $\hat{\mathbf{n}}$. We use the Henyey-Greenstein scattering phase function [24, 25]

$$\Theta(\theta-\theta') = \frac{1}{2\pi}\frac{1-g^2}{1+g^2-2g\cos(\theta-\theta')}. \tag{24}$$

Since boundary condition Eq. (23b) prescribes an even function of θ at $\zeta = 0$ and because the scattering phase function given in Eq. (24) is rotationally invariant, the solution is an even function of θ:

$$\Psi(\zeta,\theta) = \Psi(\zeta,-\theta). \tag{25}$$

For that case, we have

$$\int_{-\pi}^{\pi}\Theta(\theta-\theta')\Psi(\zeta,\theta')\mathrm{d}\theta' = \int_0^{\pi}\left[\Theta(\theta+\theta')+\Theta(\theta-\theta')\right]\Psi(\zeta,\theta')\mathrm{d}\theta'. \tag{26}$$

Let $\mu = \cos\theta$. Then, we can rewrite boundary value problem Eq. (23) as

$$\mu\partial_\zeta\Psi + \bar{\sigma}\Psi - \bar{\sigma}\int_{-1}^{1}h(\mu,\mu')\Psi(\zeta,\mu')\frac{\mathrm{d}\mu'}{(1-\mu'^2)^{1/2}} = 0, \quad \text{in } \zeta > 0, \tag{27a}$$

$$\Psi(0,\mu) = \psi(\mu) + R(\mu)\Psi(0,-\mu), \quad \text{on } 0 < \mu \le 1. \tag{27b}$$

Here, the redistribution function h is defined as

$$\begin{aligned} h(\mu,\mu') =& \frac{1}{2\pi}\frac{1-g^2}{1+g^2-2g(\mu\mu'-(1-\mu^2)^{1/2}(1-\mu'^2)^{1/2})} \\ &+\frac{1}{2\pi}\frac{1-g^2}{1+g^2-2g(\mu\mu'+(1-\mu^2)^{1/2}(1-\mu'^2)^{1/2})}. \end{aligned} \tag{28}$$

3.1.1. Plane wave solutions

We use plane wave solutions to solve boundary value problem Eq. (27). Plane wave solutions are special solutions of Eq. (27a) of the form $\Psi = e^{\lambda\zeta}V(\mu)$. Substituting this ansatz into Eq. (27a), we obtain the eigenvalue problem

$$\lambda\mu V + \bar{\sigma}V - \bar{\sigma}\int_{-1}^{1}h(\mu,\mu')V(\mu')\frac{\mathrm{d}\mu'}{(1-\mu'^2)^{1/2}} = 0. \tag{29}$$

There are several properties of plane wave solutions that are useful for computing solutions of the radiative transport equation [26, 27].

To calculate plane wave solutions numerically, we use the discrete ordinate method. In particular, we use the Gauss-Chebyshev quadrature rule

$$\int_{-1}^{1}f(\mu)\frac{\mathrm{d}\mu}{(1-\mu^2)^{1/2}} \approx \frac{\pi}{N}\sum_{j=1}^{N}f(\mu_j), \tag{30}$$

with

$$\mu_j = \cos\left(\pi\frac{2(N-j)-1}{2(N-1)+2}\right), \quad j = 1,\cdots,N. \tag{31}$$

Replacing the integral operation in Eq. (27a) with the Gauss-Chebyshev quadrature rule and evaluating that result at μ_i, we obtain

$$\lambda\mu_i V(\mu_i) + (\delta+\bar{\sigma})V(\mu_i) - \bar{\sigma}\frac{\pi}{N}\sum_{j=1}^{N}h(\mu,\mu_j)V(\mu_j) = 0, \quad i = 1,\cdots,N. \tag{32}$$

#160854 - $15.00 USD Received 5 Jan 2012; revised 9 Feb 2012; accepted 9 Feb 2012; published 21 Feb 2012

Equation (32) is a discrete eigenvalue problem suitable for numerical computations. Notice that in Eq. (32) we have added a small regularization parameter $0 < \delta \ll 1$ which is equivalent to adding a small amount of absorption. This ensures that the eigenvalues we calculate numerically are real and distinct. The numerical error incurred by introducing δ is exponentially small. For our numerical calculations, we typically have chosen $\delta = 10^{-8}$.

Suppose we solve numerically Eq. (32). We will obtain N eigenvalues λ_n and eigenvectors $V_n(\mu_i)$. For each pair $[\lambda_n, V_n(\mu_i)]$ satisfying Eq. (32), the pair $[-\lambda_n, V_n(-\mu_i)]$ satisfies Eq. (32) also. As a result, we order and index the eigenvalues according to

$$\lambda_{-N/2} \le \lambda_{-N/2+1} \le \cdots \le \lambda_{-1} \le \lambda_1 \le \cdots \le \lambda_{N/2-1} \le \lambda_{N/2}. \tag{33}$$

Using this indexing the symmetry of the plane wave solutions corresponds to $\lambda_{-n} = -\lambda_n$ and $V_{-n}(\mu_i) = V_n(-\mu_i)$. The eigenvectors are orthogonal according to

$$\frac{\pi}{N}\sum_{i=1}^{N} \mu_i V_m(\mu_i) V_n(\mu_i) = 0, \quad m \neq n. \tag{34}$$

We normalize the eigenvectors according to

$$\frac{\pi}{N}\sum_{i=1}^{N} \mu_i V_n(\mu_i) V_n(\mu_i) = \begin{cases} -1 & n > 0, \\ +1 & n < 0. \end{cases} \tag{35}$$

3.1.2. Boundary condition coefficients

In Eqs. (18) - (20), the coefficients a, b and f are defined in terms of a projection operator $\mathscr{P}$. This operator is given as an expansion in plane wave solutions derived in [20]. Here, we state the result. Let p_i for $i = N/2+1, \cdots, N$ be defined as

$$p_i = [V_1(\mu_i) - \sum_{n=1}^{N/2} y_{1n} V_n(\mu_i)]\mu_i \tag{36}$$

where y_{mn} satisfies the $N/2 \times N/2$ linear system of equations

$$\sum_{m=1}^{N/2} [V_m(-\mu_i) - R(\mu_i) V_m(\mu_i)] y_{mn} = [V_n(\mu_i) - R(\mu_i) V_n(-\mu_i)], \quad i = N/2+1, \cdots, N. \tag{37}$$

Then, we compute the boundary condition coefficients through evaluation of

$$a(\mathrm{r}_b) = \frac{\pi}{N} \sum_{i=N/2+1}^{N} p_i [1 - R(\mu_i)], \tag{38}$$

$$b(\mathrm{r}_b) = n\varepsilon \frac{\pi}{N} \sum_{i=N/2+1}^{N} p_i [\mu_i + \mu_i R(\mu_i)], \tag{39}$$

$$f(\mathrm{r}_b) = \frac{\pi}{N} \sum_{i=N/2+1}^{N} p_i \phi_0(\mathrm{r}_b, \mu_i). \tag{40}$$

3.1.3. Boundary layer solution

Now that we have computed the boundary condition coefficients in boundary condition Eq. (17), let us suppose that we have solved Eq. (10) subject to boundary condition Eq. (17). We show how we solve this boundary value problem numerically in Section 3.2. Then, the boundary

Received 5 Jan 2012; revised 9 Feb 2012; accepted 9 Feb 2012; published 21 Feb 2012

layer solution Ψ satisfying boundary value problem Eq. (21) can be computed as an expansion in plane wave solutions. This expansion is derived in [20]. Here, we give the result for $\Psi(0,\mu_i)$ for $-1 \le \mu \le 1$ which is what we need to correct the DA at the boundary. Let H_{ij} be defined as

$$H_{ij} = \sum_{m=1}^{N/2} V_m(-\mu_i)\left[V_m(-\mu_j) - \sum_{n=1}^{N/2} y_{mn} V_n(\mu_j)\right]\mu_j. \tag{41}$$

Then $\Psi(0,\mu_i)$ for the points corresponding to $-1 \le \mu \le 1$ is given by

$$\begin{aligned}\Psi(0,\mu_i) = \frac{\pi}{N} \sum_{j=N/2+1}^{N} & H_{ij}\left[\phi_0(\mathrm{r}_b,\mu_j) - [1-R(\mu_j)]\Phi_0(\mathrm{r}_b)\right. \\ & \left. +\varepsilon n\kappa\mu_j[1+R(\mu_j)]\hat{\mathbf{n}}\cdot\nabla\Phi_0(\mathrm{r}_b)\right], \quad i = 1,\cdots,N. \end{aligned}\tag{42}$$

3.2. Computing the diffusion approximation

In this work, the FEM is used to solve the DA, Eq. (10) subject to Eq. (17). We follow the same procedure as in the case of the standard DA, see e.g. [28–32]. The variational formulation of the DA is

$$\int_\Omega \kappa\nabla\Phi_0\cdot\nabla \mathrm{d}r + \int_\Omega \alpha\Phi_0 v \mathrm{d}r + \int_{\partial\Omega} \frac{a}{b}\Phi_0 v \mathrm{d}S = \int_{\partial\Omega} \frac{f}{b} v \mathrm{d}S, \tag{43}$$

where v is a test function. By representing Φ_0 in a finite dimensional basis the problem is discretized. The FE-approximation of the DA can be written in the form

$$(K + C + D)\,\mathrm{c} = G, \tag{44}$$

where

$$K(p,k) = \int_\Omega \kappa\nabla\vartheta_k(\mathrm{r})\cdot\nabla\vartheta_p(\mathrm{r})\mathrm{d}r \tag{45}$$

$$C(p,k) = \int_\Omega \alpha\vartheta_k(\mathrm{r})\vartheta_p(\mathrm{r})\mathrm{d}r \tag{46}$$

$$D(p,k) = \int_{\partial\Omega} \frac{a}{b}\vartheta_k(\mathrm{r})\vartheta_p(\mathrm{r})\mathrm{d}S \tag{47}$$

where $k, p = 1,\cdots,N$, $\vartheta(\mathrm{r})$ is the nodal basis function and N is the number of spatial nodes. The source vector is

$$G(p) = \int_{\partial\Omega} \frac{f}{b}\vartheta_p(\mathrm{r})\mathrm{d}S. \tag{48}$$

Vector $\mathrm{c} = (\mathrm{c}_1,\cdots,\mathrm{c}_N)^T \in \mathbb{R}^N$ is the solution of the DA at the nodes of the spatial grid.

3.3. Summary of the algorithm

To summarize, the procedure for a numerical solution of the cDA is given as

1. For a given optical parameters μ_a and μ_s, compute the asymptotic parameter ε using Eq. (50) and scaled optical parameters α and σ using Eq. (6).
2. Solve the eigenvalue problem, Eq. (32), at the measurement points r_b.
3. Solve the matrix y using Eq. (37). Evaluate the discrete projection operator from the Eq. (36) and the coefficients of the Robin boundary condition of the DA from Eqs. (38)-(40).

4. Solve the DA Eq. (10) subject to the boundary condition Eq. (17) using the FEM, Eq. (44). Evaluate the solution and the gradient at the measurement points r_b.
5. Compute the boundary layer correction using Eq. (42).
6. Compute the approximation to the radiance ϕ at the measurement points r_b using the Eq. (22).

4. Numerical results

The performance of the cDA was tested with 2D simulations. Simulation domain Ω was a circle with radius of 20 mm centered at the origin. The source $\phi_0(\mathrm{r},\hat{\mathbf{s}})$ was located at $(x,y)=(-20,0)$ mm with cosine shape giving the largest value in inward direction and value zero in direction of tangent to the boundary

$$\phi_0(\mathrm{r}_b,\hat{\mathbf{s}}) = -\hat{\mathbf{s}}\cdot\hat{\mathbf{n}}, \quad \hat{\mathbf{s}}\cdot\hat{\mathbf{n}} < 0. \tag{49}$$

Three types of test cases were considered: a homogeneous medium with matched refractive indices inside and outside the domain for three different values of scattering coefficient μ_s, the same cases with mismatched refractive indices, and a heterogeneous medium.

The results of the cDA were compared with the results of the standard DA (see Appendix A) and the RTE. The cDA was solved as explained above in Section 3.3. The standard DA was solved with the FEM similarly as in [32]. The FE-approximation of the RTE was implemented similarly as in [32, 33] in the case of matched refractive indices. The implementation is explained in more detail in Appendix B.

The FE-mesh for the spatial discretization of the domain contained approximately 4687 nodal points and 9196 triangular elements for the homogeneous test cases and 6114 nodal points and 11 988 elements for the heterogeneous test case. For the angular discretization of the RTE 64 equally spaced angular directions were used. Parameter ε was chosen as the ratio of the total mean free path $l = (\mu_s+\mu_a)^{-1}$ to the size of the domain L [34]

$$\varepsilon = \frac{(\mu_s+\mu_a)^{-1}}{L}. \tag{50}$$

4.1. *Matched refractive indices*

For the first case, we consider a medium with matched refractive indices at the boundary. The refractive indices inside and outside the medium were $n_{\mathrm{in}} = 1$ and $n_{\mathrm{out}} = 1$, respectively. The scattering coefficient was given three value $\mu_s = 50$, 5 and 0.5 mm^{-1}. The absorption coefficient and the anisotropy factor were constants, $\mu_a = 0.01$ mm^{-1} and $g = 0.8$, respectively.

Radiances at the boundary point $(x,y)=(0,-20)$ for $\mu_s = 5$ mm^{-1} computed using the cDA, the DA and the RTE are shown in left image of Fig. 1. To compare the performance of the cDA against the DA, two different quantities were investigated. First, the fluence rate inside the domain was computed using Eq. (5), and secondly the exitance at the boundary was computed using Eq. (4). The exitances computed using the cDA, the DA and the RTE are shown in Fig. 2. In addition, the relative errors of fluence rates computed using the cDA (top row) and the DA (bottom row) against the RTE for different values of μ_s are shown in Fig. 3. Furthermore, the relative errors of exitances are shown in Fig. 4. To give a quantitative estimate of the errors, the means of the relative errors of fluence rates Δ_{Φ_0} and the exitances Δ_Γ were computed. The results are given in Table 1. We also recorded the computation times of the different models. These are given in Table 2.

As it can be seen from Fig. 1, the radiance computed using the cDA agree relatively well with the RTE and satisfy the zero boundary condition in inward direction. Note that the RTE may

#160854 - $15.00 USD Received 5 Jan 2012; revised 9 Feb 2012; accepted 9 Feb 2012; published 21 Feb 2012

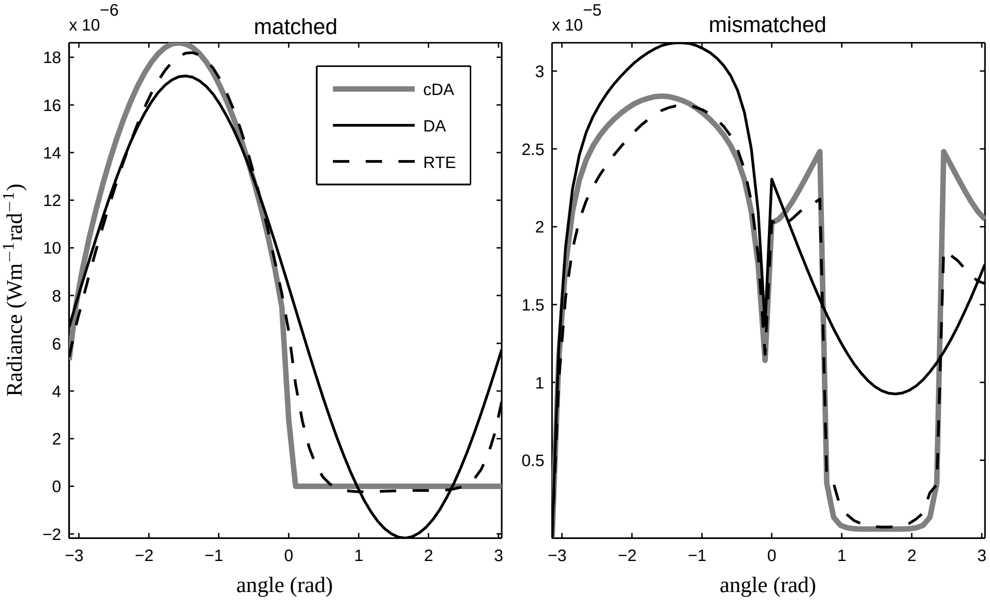

Fig. 1. Radiance at the boundary point $(x,y) = (0,-20)$ computed using the cDA, the DA and the RTE for μ_s = 5 mm^{-1} with matched (left) and mismatched refractive indices (right).

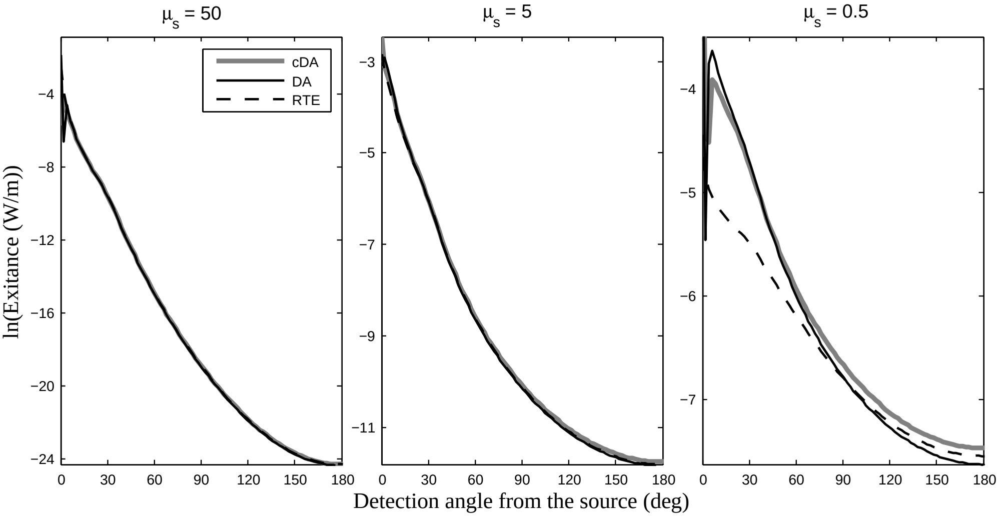

Fig. 2. Logarithm of exitance at the boundary of the domain computed using the cDA, the DA and the RTE for different values of μ_s with matched refractive indices at the boundary.

#160854 - $15.00 USD Received 5 Jan 2012; revised 9 Feb 2012; accepted 9 Feb 2012; published 21 Feb 2012

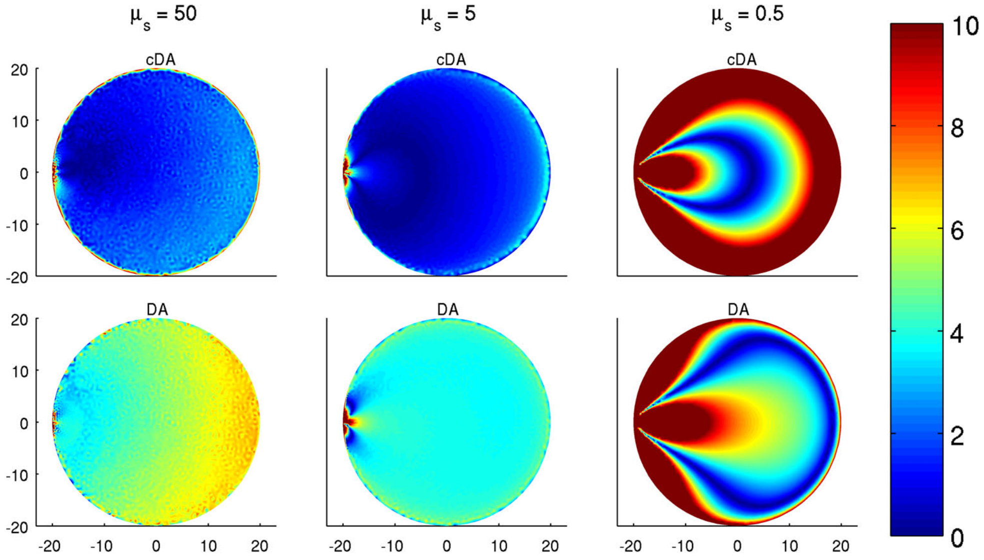

Fig. 3. Percent relative error of fluence rate computed using the cDA (top row) and the DA (bottom row) for different values of μ_s with matched refractive indices at the boundary. The values are cut at 10%.

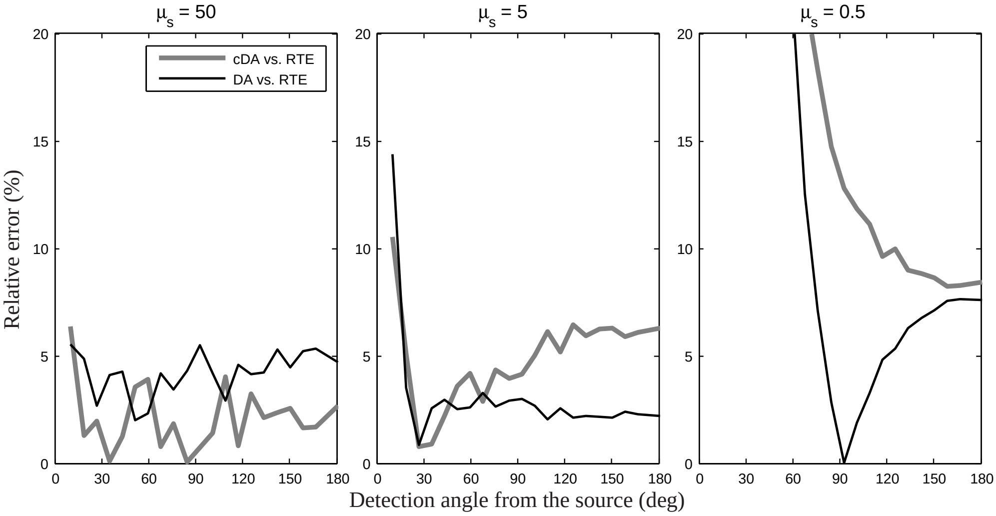

Fig. 4. Percent relative error of exitance at the boundary computed using the cDA and the DA for different values of μ_s with matched refractive indices.

#160854 - $15.00 USD Received 5 Jan 2012; revised 9 Feb 2012; accepted 9 Feb 2012; published 21 Feb 2012

give small negative or positive values in inward direction due to numerical reasons. The DA gives negative radiance in inward direction which are unphysical. The relative error of fluence rate is approximately 2 % for the cDA and between 4-6 % for the standard DA when scattering coefficient is $\mu_s = 50$ and $\mu_s = 5$ mm^{-1} as it can be seen from Fig. 3 and Table 1. For $\mu_s = 0.5$ mm^{-1} both the cDA and the standard DA give large errors since the assumptions of the DA are not valid anymore. Figure 4 shows that as scattering becomes large compared to absorption, the relative error of exitance decreases for the cDA just as the asymptotic theory predicts.

The computation times in Table 2 show that solving the cDA is feasible when compared with the standard DA. In addition, solving both the cDA and the DA are much faster than solving the RTE. Thus, the cDA models light propagation more accurately than the standard DA and requires only a small amount of more work.

Table 1. The mean of the relative error of fluence rate $\Delta_{\Phi_0}(\%)$ and exitance $\Delta_\Gamma(\%)$ computed using the cDA and the DA for different values of $\mu_s(\text{mm}^{-1})$ and asymptotic parameter ε with matched refractive indices.

		Δ_{Φ_0}		Δ_Γ	
μ_s	ε	cDA	DA	cDA	DA
50	0.001	2.10	5.21	2.11	4.21
5	0.01	1.43	4.19	4.86	3.04
0.5	0.1	17.32	14.10	42.31	42.54

Table 2. The computation times of the models for different values of μ_s.

	Computation time			Relative computation time	
μ_s	cDA	DA	RTE	cDA/RTE	DA/RTE
50	8.9 s	3.3 s	2.4 min	6.2 %	2.3 %
5	8.8 s	3.2 s	2.2 min	6.5 %	2.4 %
0.5	8.6 s	3.3 s	2.3 min	6.4 %	2.5 %

4.2. *Mismatched refractive indices*

For the second case, we consider a medium with mismatched refractive indices at the boundary. The refractive indices inside and outside the medium were $n_{\text{in}} = 1.33$ and $n_{\text{out}} = 1$, respectively. Other optical parameters were the same as before. Radiances at the boundary point $(x,y) = (0,-20)$ for $\mu_s = 5$ mm^{-1} computed using the cDA, the DA and the RTE are shown in right image of Fig. 1. Again, the quantities of interest were the fluence rate inside the domain and the exitance at the boundary. The exitances computed using different models are shown in Fig. 5. In addition, the relative errors of fluence rates and exitances are shown in Figs. 6 and 7, respectively. As before, the means of the relative errors of fluence rates and exitances were computed and the results are given in Table 3.

As it can be seen Fig. 1, the approximation to the radiance given by the cDA agrees better with the RTE than the approximation given by the DA. Furthermore, the results in Fig. 6 and Table 3 show the relative error of fluence rate is between 2-3 % for the cDA when $\mu_s = 50$ mm^{-1} and $\mu_s = 5$ mm^{-1}. For the DA the relative error is larger giving the largest errors at the boundary. For the case $\mu_s = 0.5$ mm^{-1} neither of the approximations are valid. Figure 7 shows that the relative error of exitance decreases for the cDA when the ratio of absorption

#160854 - $15.00 USD Received 5 Jan 2012; revised 9 Feb 2012; accepted 9 Feb 2012; published 21 Feb 2012

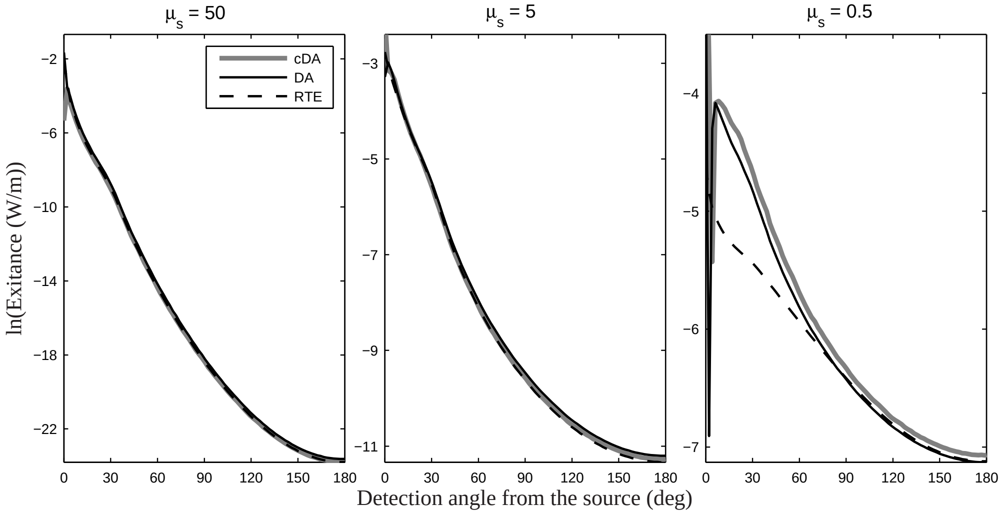

Fig. 5. Logarithm of exitance at the boundary of the domain computed using the cDA, the DA and the RTE for different values of μ_s with mismatched refractive indices.

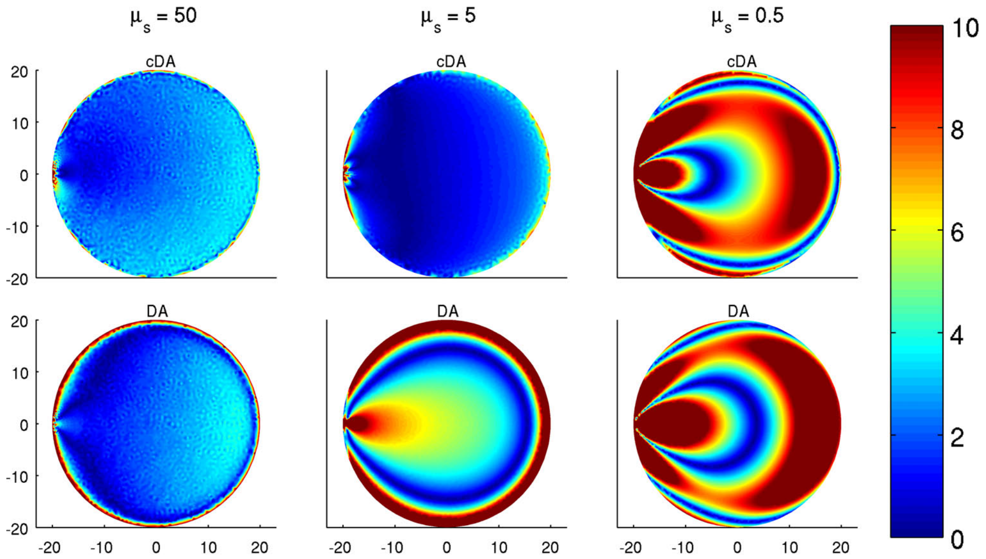

Fig. 6. Percent relative error of fluence rate computed using the cDA (top row) and the DA (bottom row) for different values of μ_s with mismatched refractive indices. The values are cut at 10%.

#160854 - $15.00 USD Received 5 Jan 2012; revised 9 Feb 2012; accepted 9 Feb 2012; published 21 Feb 2012

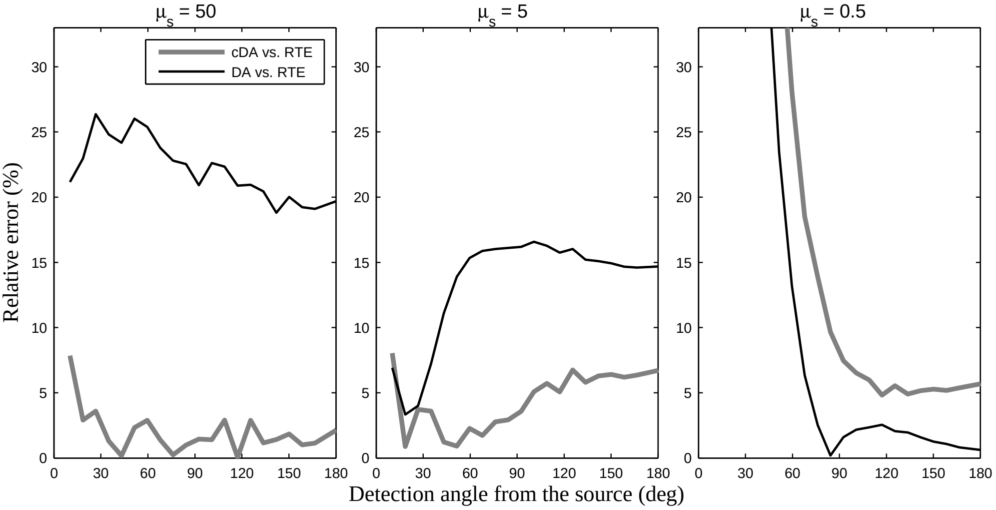

Fig. 7. Percent relative error of exitance computed using the cDA and the DA for different values of μ_s with mismatched refractive indices.

and scattering decreases due to the asymptotic theory behind the model. In contrast, the relative error of the standard DA may not have a global error bound over the whole domain. In that case, the relative error might be large close to the boundary while giving satisfactory results inside the domain. In addition, decrease in ratio of absorption and scattering does not ensure decrease in relative error for the DA. Thus, the cDA models light propagation more accurately than the standard DA when compared with the RTE.

Table 3. The mean of the relative error of fluence rate $\Delta_{\Phi_0}(\%)$ and exitance $\Delta_{\Gamma}(\%)$ computed using the cDA and the DA for different values of μ_s and asymptotic parameter ε with mismatched refractive indices .

		Δ_{Φ_0}		Δ_{Γ}	
μ_s	ε	cDA	DA	cDA	DA
50	0.001	2.63	3.73	1.96	22.14
5	0.01	1.59	6.31	4.38	13.33
0.5	0.1	11.18	11.74	39.20	26.26

4.3. Heterogeneous medium

For the third case, we consider a medium with heterogeneous optical properties. Simulated optical parameters of the medium are shown in Fig. 8. The scattering and absorption coefficients of the background were $(\mu_s, \mu_a) = (10, 0.01)$ mm^{-1}. Furthermore, optical parameters of scattering and absorbing inclusions were $(\mu_s, \mu_a) = (20, 0.01)$ mm^{-1} and $(\mu_s, \mu_a) = (10, 0.02)$ mm^{-1}, respectively. The anisotropy factor in the whole domain was $g = 0.8$. The refractive indices inside and outside the medium were $n_{\text{in}} = 1.33$ and $n_{\text{out}} = 1$, respectively. Asymptotic parameter $\varepsilon = 0.005$ was computed from Eq. (50) using the optical parameters of the background. The exitances are shown in Fig. 9. The relative errors of fluence rates computed using the cDA and the DA are shown in Fig. 10. Furthermore, the relative errors of exitances are

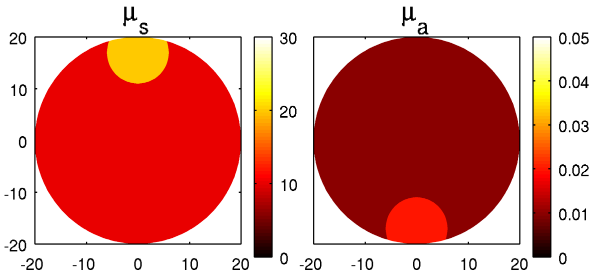

Fig. 8. Optical parameters for the heterogeneous test case.

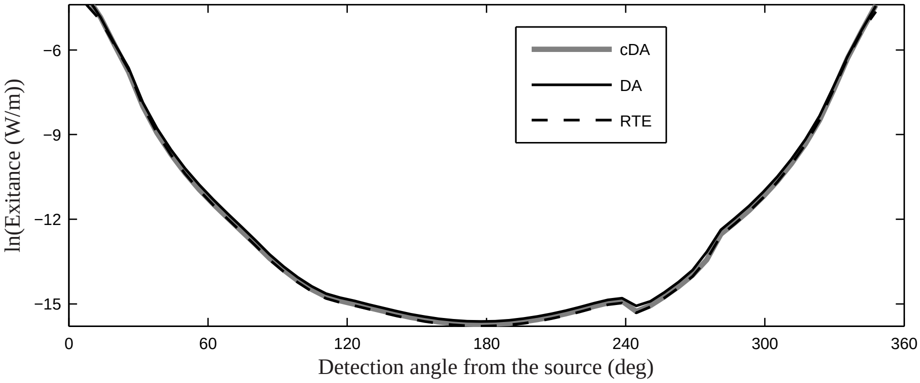

Fig. 9. Logarithm of exitance at the boundary of the domain computed using the cDA, the DA and the RTE for the heterogeneous test case.

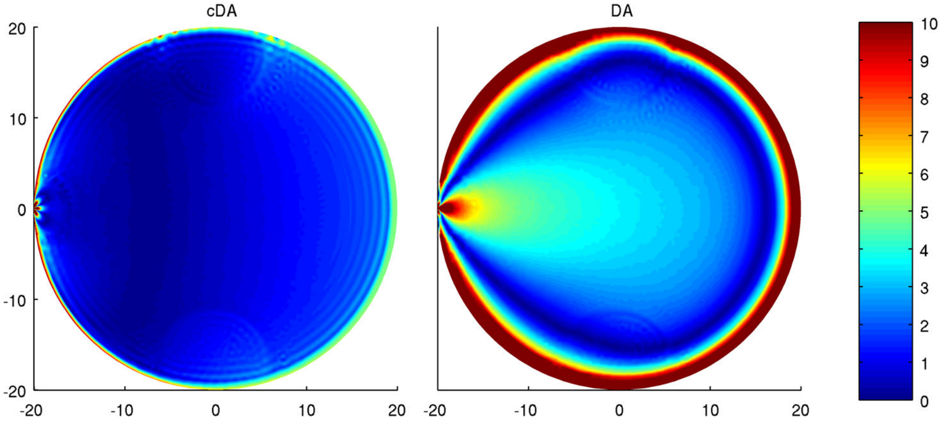

Fig. 10. Percent relative error of fluence rate computed using the cDA (left) and the DA (right) for the heterogeneous test case. The values are cut at 10%.

#160854 - $15.00 USD Received 5 Jan 2012; revised 9 Feb 2012; accepted 9 Feb 2012; published 21 Feb 2012

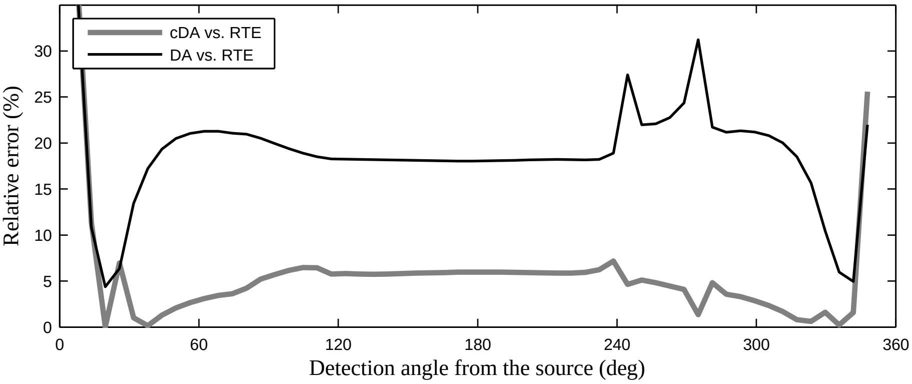

Fig. 11. Percent relative error of exitance for the heterogeneous test case.

shown in Fig. 11.

The mean of the relative error of fluence rate is 1.69 % for the cDA over whole domain. In contrast, the mean of the relative error of fluence rate is 5.07 % for the DA. In addition, the DA gives larger errors close to the boundary than inside the domain as it can be seen from Fig. 10. Furthermore, the relative error of exitance is smaller for the cDA (mean 5.38 %) than that of for the DA (mean 18.73 %). Thus, the cDA gives more accurate results over whole domain than the standard DA due to a global error bound given by the asymptotic theory.

5. Conclusions

In this work, recently introduced corrected diffusion approximation was numerically implemented. In the cDA, an additive correction term is computed for the DA at the boundary based on asymptotic analysis of the RTE. The procedure for computing the cDA requires only small modifications to the existing solvers for the DA. In particular, one only needs to modify the spatial coefficients of the DA and the Robin boundary condition. In addition, an additive correction term, which satisfies a one-dimensional radiative transport equation, is readily solved using the plane wave solutions.

The performance of the cDA was tested with 2D simulations. The results were compared with the results of the DA and the RTE. The results show that the cDA models boundary measurements of scattered light more accurately than the standard DA with only a small increase in computation time.

Appendix A. The standard diffusion approximation

The most typical approach to derive the standard DA from the RTE is expand the radiance, the source term, and the phase function into series using the spherical harmonics and truncate the series [1,3]. The standard DA can be regarded as a special case of the first order approximation. In the standard DA framework, the approximation that is used for the radiance is of the form [1, 3, 35]

$$\phi(\mathrm{r},\hat{\mathbf{s}}) \approx \frac{1}{|S^{n-1}|}\Phi_0(\mathrm{r}) - \frac{n}{|S^{n-1}|}(\hat{\mathbf{s}}\cdot\kappa_{\mathrm{DA}}\nabla\Phi_0(\mathrm{r})), \tag{A.1}$$

where $|S^{n-1}|$ is the surface measure of S^{n-1} and κ_{DA} is the diffusion coefficient defined as

$$\kappa_{\mathrm{DA}} = (n(\mu_a+\mu_s(1-g)))^{-1}. \tag{A.2}$$

The standard diffusion approximation consists of diffusion equation of the form

$$-\nabla \cdot \kappa_{\mathrm{DA}} \nabla \Phi_0(\mathrm{r}) + \mu_a \Phi_0(\mathrm{r}) = 0, \tag{A.3}$$

and the Robin boundary condition is of the form

$$\Phi_0(\mathrm{r}) + \frac{1}{2\gamma_n} \kappa_{\mathrm{DA}} A \frac{\partial \Phi_0(\mathrm{r})}{\partial \hat{\mathbf{n}}} = \frac{I_s}{\gamma_n}, \tag{A.4}$$

where γ_n is a dimension dependent constant ($\gamma_2 = 1/\pi$, $\gamma_3 = 1/4$) and I_s is an inward directed diffuse boundary current at the source position [36]. The parameters A takes into account a mismatch in refractive indices inside and outside the domain and it can be derived from the Fresnel's law [36, 37]

$$A = \frac{2/(1-R_0) - 1 + |\cos(\theta_c)|^3}{1 - |\cos(\theta_c)|^2}, \tag{A.5}$$

where $\theta_c = \arcsin(n_{\mathrm{out}}/n_{\mathrm{in}})$ is the critical angle and $R_0 = (n_{\mathrm{in}}/n_{\mathrm{out}} - 1)^2/(n_{\mathrm{in}}/n_{\mathrm{out}} + 1)^2$.

Appendix B. FE-approximation of the RTE with reflection boundary condition

Let us consider the steady-state RTE Eq. (1). Let $\hat{\mathbf{s}}_i$ and $\hat{\mathbf{s}}_r$ be the directions of incident and reflected light, respectively, at the boundary with a mismatch in refractive indices. Furthermore, let $\hat{\mathbf{s}}_t$ be the direction refracted light. We write the boundary condition for the radiance pointing inward into the domain (i.e. for the directions $\hat{\mathbf{s}}_r \cdot \hat{\mathbf{n}} < 0$) in terms of the incident radiance pointing outward ($\hat{\mathbf{s}}_i \cdot \hat{\mathbf{n}} > 0$). Mapping from direction $\hat{\mathbf{s}}_i$ to direction $\hat{\mathbf{s}}_r$ is given by $H : \hat{\mathbf{s}}_i \rightarrow \hat{\mathbf{s}}_r$

$$\hat{\mathbf{s}}_r = H \hat{\mathbf{s}}_i, \tag{B.1}$$

$$H = \left(-2\hat{\mathbf{n}}\hat{\mathbf{n}}^T + \mathbf{I}\right), \tag{B.2}$$

where $\mathbf{I}$ is an identity matrix. The matrix H is a Householder transformation, and thus $H^{-1} = H^T = H$. Therefore, the inverse mapping $H^{-1} : \hat{\mathbf{s}}_r \rightarrow \hat{\mathbf{s}}_i$ is given by

$$\hat{\mathbf{s}}_i = H^{-1} \hat{\mathbf{s}}_r = H \hat{\mathbf{s}}_r. \tag{B.3}$$

Now, the boundary condition Eq. (3) can be written as follows

$$\phi(\mathrm{r}, \hat{\mathbf{s}}) = \phi_0(\mathrm{r}, \hat{\mathbf{s}}) + R\phi(\mathrm{r}, H\hat{\mathbf{s}}), \quad \hat{\mathbf{s}} \cdot \hat{\mathbf{n}} < 0, \tag{B.4}$$

where R is the Fresnel reflection coefficient defined as

$$R = \frac{1}{2}\left(\frac{n_{\mathrm{in}} \cos\varphi_i - n_{\mathrm{out}} \cos\varphi_t}{n_{\mathrm{in}} \cos\varphi_i + n_{\mathrm{out}} \cos\varphi_t}\right)^2 + \frac{1}{2}\left(\frac{n_{\mathrm{in}} \cos\varphi_t - n_{\mathrm{out}} \cos\varphi_i}{n_{\mathrm{in}} \cos\varphi_t + n_{\mathrm{out}} \cos\varphi_i}\right)^2, \tag{B.5}$$

where

$$\cos\varphi_i = \hat{\mathbf{n}} \cdot \hat{\mathbf{s}}_i, \tag{B.6}$$

$$\cos\varphi_t = \sqrt{1 - \left(\frac{n_{\mathrm{in}}}{n_{\mathrm{out}}}\right)^2 (1 - (\cos\varphi_i)^2)} \tag{B.7}$$

and n_{in}, n_{out} are the refractive indices inside and outside of the object, respectively.

Utilizing the streamline-diffusion modification [33,38,39], the variational formulation of the RTE Eq. (1) subject to the boundary condition Eq. (B.4) is obtained as

$$\begin{aligned}
&-\int_{\Omega}\int_{S^{n-1}} \hat{\mathbf{s}}\cdot\nabla v(\mathrm{r},\hat{\mathbf{s}})\phi(\mathrm{r},\hat{\mathbf{s}})\mathrm{d}\hat{\mathbf{s}}\mathrm{d}\mathrm{r} + \int_{\Omega}\delta\int_{S^{n-1}}(\hat{\mathbf{s}}\cdot\nabla\phi(\mathrm{r},\hat{\mathbf{s}}))(\hat{\mathbf{s}}\cdot\nabla v(\mathrm{r},\hat{\mathbf{s}}))\mathrm{d}\hat{\mathbf{s}}\mathrm{d}\mathrm{r}\\
&+\int_{\partial\Omega}\int_{S^{n-1}}(\hat{\mathbf{s}}\cdot\hat{n})_{+}\phi(\mathrm{r},\hat{\mathbf{s}})v(\mathrm{r},\hat{\mathbf{s}})\mathrm{d}\hat{\mathbf{s}}\mathrm{d}S - \int_{\partial\Omega}\int_{S^{n-1}}(\hat{\mathbf{s}}\cdot\hat{n})_{-}r\phi(\mathrm{r},H\hat{\mathbf{s}})v(\mathrm{r},\hat{\mathbf{s}})\mathrm{d}\hat{\mathbf{s}}\mathrm{d}S\\
&+\int_{\Omega}\int_{S^{n-1}}(\mu_s+\mu_a)\phi(\mathrm{r},\hat{\mathbf{s}})v(\mathrm{r},\hat{\mathbf{s}})\mathrm{d}\hat{\mathbf{s}}\mathrm{d}\mathrm{r} + \int_{\Omega}\int_{S^{n-1}}\delta(\mu_s+\mu_a)\phi(\mathrm{r},\hat{\mathbf{s}})(\hat{\mathbf{s}}\cdot\nabla v(\mathrm{r},\hat{\mathbf{s}}))\mathrm{d}\hat{\mathbf{s}}\mathrm{d}\mathrm{r}\\
&-\int_{\Omega}\int_{S^{n-1}}\mu_s\int_{s^{n-1}}\Theta(\hat{\mathbf{s}}\cdot\hat{\mathbf{s}}')\phi(\mathrm{r},\hat{\mathbf{s}}')\mathrm{d}\hat{\mathbf{s}}'v(\mathrm{r},\hat{\mathbf{s}})\mathrm{d}\hat{\mathbf{s}}\mathrm{d}\mathrm{r}\\
&-\int_{\Omega}\int_{S^{n-1}}\delta\mu_s\int_{s^{n-1}}\Theta(\hat{\mathbf{s}}\cdot\hat{\mathbf{s}}')\phi(\mathrm{r},\hat{\mathbf{s}}')\mathrm{d}\hat{\mathbf{s}}'(\hat{\mathbf{s}}\cdot\nabla v(\mathrm{r},\hat{\mathbf{s}}))\mathrm{d}\hat{\mathbf{s}}\mathrm{d}\mathrm{r}\\
&=\int_{\partial\Omega}\int_{S^{n-1}}(\hat{\mathbf{s}}\cdot\hat{n})_{-}\phi_0(r,\hat{\mathbf{s}})v(\mathrm{r},\hat{\mathbf{s}})\mathrm{d}\hat{\mathbf{s}}\mathrm{d}S, \qquad \text{(B.8)}
\end{aligned}$$

where δ is element-wise stabilization parameter in the streamline-diffusion modification which depends on local the absorption and scattering and $(\hat{\mathbf{s}}\cdot\hat{\mathbf{n}})_{+}$ and $(\hat{\mathbf{s}}\cdot\hat{\mathbf{n}})_{-}$ denote the positive and negative parts of the function $\hat{\mathbf{s}}\cdot\hat{\mathbf{n}}$. The finite element approximation of the RTE is of the form

$$(A_1+A_2+A_3+A_4)\beta = b_1\upsilon^0, \qquad \text{(B.9)}$$

where $\beta = (\beta_{1,1},\cdots,\beta_{1,N_a},\cdots,\beta_{N_n,1},\cdots,\beta_{N_n,N_a})^T \in \mathbb{R}^{N_nN_a}$ is the radiance at the nodes of the spatial and angular grid and $\upsilon^0(\upsilon^0_{1,1},\cdots,\upsilon^0_{1,N_a},\cdots,\upsilon^0_{N_n,N_a})^T \in \mathbb{R}^{N_nN_a}$ is the source intensity at the nodes of the angular and spatial discretizations. Further, the components of the matrices in Eq. (B.9) are

$$\begin{aligned}
A_1(h,s) &= -\int_{\Omega}\int_{S^{n-1}}\hat{\mathbf{s}}\cdot\nabla\upsilon_j(\mathrm{r})\upsilon_m(\hat{\mathbf{s}})\upsilon_l(\hat{\mathbf{s}})\mathrm{d}\hat{\mathbf{s}}\upsilon_i(\mathrm{r})\mathrm{d}\mathrm{r}\\
&\quad+\int_{\Omega}\delta\int_{S^{n-1}}(\hat{\mathbf{s}}\cdot\nabla\upsilon_i(\mathrm{r}))(\hat{\mathbf{s}}\cdot\nabla\upsilon_j(\mathrm{r}))\upsilon_l(\hat{\mathbf{s}})\upsilon_m(\hat{\mathbf{s}})\mathrm{d}\hat{\mathbf{s}}\mathrm{d}\mathrm{r} && \text{(B.10)}\\
A_2(h,s) &= \int_{\partial\Omega}\upsilon_i(\mathrm{r})\upsilon_j(\mathrm{r})\mathrm{d}S\int_{S^{n-1}}(\hat{\mathbf{s}}\cdot\hat{n})_{+}\upsilon_l(\hat{\mathbf{s}})\upsilon_m(\hat{\mathbf{s}})\mathrm{d}\hat{\mathbf{s}}\\
&\quad-\int_{\partial\Omega}\upsilon_i(\mathrm{r})\upsilon_j(\mathrm{r})\mathrm{d}S\int_{S^{n-1}}(\hat{\mathbf{s}}\cdot\hat{n})_{-}r\upsilon_l(H\hat{\mathbf{s}})\upsilon_m(\hat{\mathbf{s}})\mathrm{d}\hat{\mathbf{s}} && \text{(B.11)}\\
A_3(h,s) &= \int_{\Omega}(\mu_s+\mu_a)\upsilon_i(\mathrm{r})\upsilon_j(\mathrm{r})\mathrm{d}\mathrm{r}\int_{S^{n-1}}\upsilon_l(\hat{\mathbf{s}})\upsilon_m(\hat{\mathbf{s}})\mathrm{d}\hat{\mathbf{s}}\\
&\quad+\int_{\Omega}\delta(\mu_s+\mu_a)\upsilon_i(\mathrm{r})\int_{S^{n-1}}(\hat{\mathbf{s}}\cdot\nabla\upsilon_j(\mathrm{r}))\upsilon_m(\hat{\mathbf{s}})\upsilon_l(\hat{\mathbf{s}})\mathrm{d}\hat{\mathbf{s}}\mathrm{d}\mathrm{r} && \text{(B.12)}\\
A_4(h,s) &= -\int_{\Omega}\mu_s\upsilon_i(\mathrm{r})\upsilon_j(\mathrm{r})\mathrm{d}\mathrm{r}\int_{S^{n-1}}\int_{S^{n-1}}\Theta(\hat{\mathbf{s}}\cdot\hat{\mathbf{s}}')\upsilon_l(\hat{\mathbf{s}}')\mathrm{d}\hat{\mathbf{s}}'\upsilon_m(\hat{\mathbf{s}})\mathrm{d}\hat{\mathbf{s}}\\
&\quad-\int_{\Omega}\delta\mu_s\int_{S^{n-1}}(\hat{\mathbf{s}}\cdot\nabla\upsilon_j(\mathrm{r}))\upsilon_m(\hat{\mathbf{s}})\int_{s^{n-1}}\Theta(\hat{\mathbf{s}}\cdot\hat{\mathbf{s}}')\upsilon_l(\hat{\mathbf{s}}')\mathrm{d}\hat{\mathbf{s}}'\mathrm{d}\hat{\mathbf{s}}\upsilon_i(\mathrm{r})\mathrm{d}\mathrm{r} && \text{(B.13)}\\
b_1(h,s) &= \int_{\partial\Omega}\upsilon_i(\mathrm{r})\upsilon_j(\mathrm{r})\mathrm{d}S\int_{S^{n-1}}(\hat{\mathbf{s}}\cdot\hat{n})_{-}\upsilon_l(\hat{\mathbf{s}})\upsilon_m(\hat{\mathbf{s}})\mathrm{d}\hat{\mathbf{s}}, && \text{(B.14)}
\end{aligned}$$

where $h = N_a(j-1)+m$, $s = N_a(i-1)+l$, $j,i = 1,\cdots,N_n$, $m,l = 1,\cdots,N_a$, $h,s = 1,\cdots,N_nN_a$ and $\upsilon_i(\mathrm{r})$, $\upsilon_j(\mathrm{r})$ and $\upsilon_l(\hat{\mathbf{s}})$, $\upsilon_m(\hat{\mathbf{s}})$ are the nodal spatial and angular basis functions, respectively. The indices i, l refer to the basis functions, j, m to the test functions and N_n and N_a are the number of nodes in the spatial and angular discretizations, respectively.

After the RTE is solved using Eq. (B.9), the direction $\hat{\mathbf{s}}_t$ of the refracted radiance at the boundary exiting the domain can be computed from Snell's law which is in vector form K :

$(\hat{\mathbf{s}}_i, \hat{\mathbf{n}}, n_{\text{in}}, n_{\text{out}}) \rightarrow \hat{\mathbf{s}}_t$

$$\hat{\mathbf{s}}_t = \frac{n_{\text{in}}}{n_{\text{out}}}\hat{\mathbf{s}}_i + \left(\cos\varphi_t - \frac{n_{\text{in}}}{n_{\text{out}}}\cos\varphi_i\right)\hat{n}. \tag{B.15}$$

Moreover, the inverse mapping $K^{-1} : (\hat{\mathbf{s}}_t, \hat{\mathbf{n}}, n_{\text{in}}, n_{\text{out}}) \rightarrow \hat{\mathbf{s}}_i$ is given by $K : (-\hat{\mathbf{s}}_t, -\hat{\mathbf{n}}, n_{\text{out}}, n_{\text{in}}) \rightarrow -\hat{\mathbf{s}}_i$ due to reciprocity of light propagation. Note the change of signs and order of normal vectors.

Thus, the final form of the radiance after applying the Snell's law is of the form

$$\phi_t(r, \hat{\mathbf{s}}) = \begin{cases} T\phi(\mathrm{r}, K(\hat{\mathbf{s}})) & r \in \partial\Omega \qquad \hat{\mathbf{s}} \cdot \hat{n} \geq 0, \\ \phi(\mathrm{r}, \hat{\mathbf{s}}) & r \in \partial\Omega \qquad \hat{\mathbf{s}} \cdot \hat{n} < 0 \\ \phi(\mathrm{r}, \hat{\mathbf{s}}) & r \in \Omega \setminus \partial\Omega, \end{cases} \tag{B.16}$$

where $T = 1 - R$ is the Fresnel transmission coefficient.

Acknowledgments

The authors would like to thank professor Simon Arridge from useful discussions. The work of O. Lehtikangas and T. Tarvainen has been supported by the Academy of Finland (projects 136220, 140984, and 213476, 250215 Finnish Centre of Excellence in Inverse Problems Research), Finnish Doctoral Programme in Computational Sciences (FICS), Magnus Ehrnrooth foundation and by the strategic funding of the University of Eastern Finland. A. D. Kim acknowledges support from the National Science Foundation (grant DMS-0806039).

Paper **III**

O. Lehtikangas, T. Tarvainen,
“Hybrid forward-peaked-scattering-diffusion approximations for light propagation in turbid media with low-scattering regions”,
Journal of Quantitative Spectroscopy and Radiative Transfer,
116, pp. 132–144, 2013.

Journal of Quantitative Spectroscopy & Radiative Transfer 116 (2013) 132–144

Contents lists available at SciVerse ScienceDirect

Journal of Quantitative Spectroscopy & Radiative Transfer

journal homepage: www.elsevier.com/locate/jqsrt

Hybrid forward-peaked-scattering-diffusion approximations for light propagation in turbid media with low-scattering regions

O. Lehtikangas [a,*], T. Tarvainen [a,b]

[a] Department of Applied Physics, University of Eastern Finland, P.O. Box 1627, 70211 Kuopio, Finland
[b] Department of Computer Science, University College London, Gower Street, London WC1E 6BT, United Kingdom

ARTICLE INFO

Article history:
Received 20 August 2012
Received in revised form
9 October 2012
Accepted 24 October 2012
Available online 3 November 2012

Keywords:
Diffuse optical tomography
Hybrid light transport models
Radiative transport equation
Fokker–Planck–Eddington approximations
Diffusion approximation
Finite element method

ABSTRACT

Coupled light transport models which use forward-peaked scattering approximations of the radiative transport equation and the diffusion approximation to model light propagation in tissues are introduced. The forward-peaked Fokker–Planck–Eddington approximations are used in those parts of the domain in which the diffusion approximation is not valid, such as close to the source and boundary, and in low-scattering regions. The diffusion approximation is used elsewhere. The models are coupled through boundary conditions and the resulting system of equations is solved using a finite element method. The proposed coupled Fokker–Planck-diffusion and Fokker–Planck–Eddington-diffusion models are tested with simulations, and compared with the radiative transport equation, diffusion approximation and coupled radiative transport-diffusion model. The results show that the new coupled models give almost as accurate results as the radiative transport equation with reduced computational load.

1. Introduction

Non-invasive optical imaging modalities provide useful information about tissue health. By measuring light propagation through tissues one can derive images of the optical properties of the medium. These imaging modalities include, for example, diffuse optical tomography (DOT) in which the optical properties of tissues are reconstructed on the basis of the transmission measurements of scattered near-infrared light on the surface of the object. Medical applications of DOT include breast cancer detection, monitoring of infant brain oxygenation level and functional brain activation studies, for reviews see e.g. [1–5].

Image reconstruction problem in DOT is a non-linear ill-posed inverse problem. Thus, even small errors in measurements or modelling can cause large errors in the reconstructed images. Moreover, the iterative solution of the non-linear problem requires several solutions of the corresponding forward model. Therefore, an accurate and computationally feasible forward model is needed.

Light propagation in tissues is governed by the radiative transport equation (RTE) [1,4,6,7]. The RTE takes into account absorption and multiple scattering due to inhomogeneities in the medium. The RTE does not have an analytical solution in arbitrary geometry and numerical methods are computationally expensive due to a large number of variables in the RTE. Therefore, the RTE is often approximated by some computationally less demanding model.

The most often used approximation to the RTE is the diffusion approximation (DA). In the DA, one assumes that light becomes almost isotropic due to strong scattering. In addition, scattering must be much stronger than absorption. Due to these limitations, the DA fails to describe light propagation accurately close to the boundary, sources, and in low-scattering and non-scattering regions [1,8–10]. A typical low-scattering region encountered in optical imaging

---

[*] Corresponding author. Tel.: +358 40 3553913; fax: +358 17 162585.
E-mail address: Ossi.Lehtikangas@uef.fi (O. Lehtikangas).

0022-4073/$ - see front matter © 2012 Elsevier Ltd. All rights reserved.
http://dx.doi.org/10.1016/j.jqsrt.2012.10.017

of the brain is the cerebrospinal fluid around the brain and in the ventricles.

To overcome the limitations of the diffusion approximation, different hybrid models have been introduced. The hybrid models include the radiosity diffusion model [10,11], hybrid Monte Carlo-diffusion models [9,12–14], hybrid radiative transport-diffusion models [15–18], and the variable order spherical harmonics (P_n) approximation to the RTE [19,20]. The radiosity diffusion model combines the diffusion theory with a ray-tracing algorithm and is applicable in highly scattering medium with non-scattering regions. The hybrid Monte Carlo-diffusion models can be used in complex heterogeneous media but suffer from a time-consuming nature of Monte Carlo simulations and often require an iterative mapping between the models in order to take into account backscattering between the sub-domains leading to computationally excessive problems. In the hybrid radiative transport-diffusion models, light propagation is modeled using the RTE in sub-domains in which the DA is not valid. The DA is used in the rest of the domain and the models are coupled with boundary conditions at the interfaces between the sub-domains . The variable order spherical harmonics approximation uses different orders of the P_n-approximation in each sub-domain depending on local scattering and absorption properties.

In tissues, scattering is typically forward-peaked, indicating that the direction of photons changes only a little in scattering events. The numerical solution of the RTE with forward-peaked scattering is challenging due to dense angular discretization needed to describe scattering accurately. Motivated by that, Fokker–Planck–Eddington-approximations have been proposed to approximate the RTE [21–29]. These approximations include, for example, the Fokker–Planck (FP) and Fokker–Planck–Eddington (FPE) equations. These approximations take into account forward-peaked and large-angle scattering analytically by approximating the scattering probability distribution using a linear combination of delta functions and Legendre polynomials. As a result, forward-peaked scattering probability distribution is replaced by an angular differential operator together with a smooth integral operator. Thus, coarser angular discretization can be used compared with the RTE leading to computational savings [24,27].

In this paper, we use the Fokker–Planck–Eddington-approximations to approximate the RTE. We introduce coupled Fokker–Planck-diffusion (cFP-DA) and coupled Fokker–Planck–Eddington-diffusion (cFPE-DA) models for modelling light propagation in tissues. The coupled models are solved with a finite element method (FEM). We compare the results of the coupled models with the solutions of the RTE, FP, FPE, and DA, and with the previously developed [17] coupled RTE-DA (cRTE-DA).

The rest of the paper is organized as follows. The light transport models including the forward-peaked scattering approximations are reviewed and the coupled models are introduced in Section 2. The numerical solutions of the coupled models using the FEM are described in Section 3. In Section 4 we test the proposed coupled models with simulations. Section 5 gives the conclusions.

2. Light transport models

2.1. The radiative transport equation

A widely accepted model for light propagation in tissues is the radiative transport equation [7]. The RTE is a one-speed approximation of the Boltzmann transport equation, and thus energy is assumed to be preserved in scattering events. In addition, the refractive index is assumed to be constant within the medium. The RTE neglects wave phenomena such as diffraction and interference, and treats photons as particles which propagate along straight lines between scattering and absorption events.

Let $\Omega \subset \mathbb{R}^n$ be the physical domain, and $n = 2,3$ be the dimension of the domain. In addition, let $\hat{\mathbf{s}} \in \mathbb{S}^{n-1}$ denote a unit vector in the direction of interest on the unit sphere $\mathbb{S}^{n-1}$. The frequency domain version of the RTE without internal sources is

$$\frac{\mathrm{i}\omega}{c}\phi(\mathbf{r},\hat{\mathbf{s}})+\hat{\mathbf{s}}\cdot\nabla\phi(\mathbf{r},\hat{\mathbf{s}})+\mu_{\mathrm{a}}\phi(\mathbf{r},\hat{\mathbf{s}})=\mu_{\mathrm{s}}\mathcal{L}\phi(\mathbf{r},\hat{\mathbf{s}}), \tag{1}$$

where i is the imaginary unit, ω is the angular modulation frequency of the input signal (the units of Hz), c is the speed of light in the medium (the units of m/s), $\phi(\mathbf{r},\hat{\mathbf{s}})$ is the radiance (the units of $\mathrm{W\,m^{-2}\,sr^{-1}}$ in 3D and $\mathrm{W\,m^{-1}\,rad^{-1}}$ in 2D), and $\mu_{\mathrm{s}} = \mu_{\mathrm{s}}(\mathbf{r})$ and $\mu_{\mathrm{a}} = \mu_{\mathrm{a}}(\mathbf{r})$ are the scattering and absorption coefficients of the medium (the units of m^{-1}), respectively [1,30,31].

The scattering operator $\mathcal{L}_{\mathrm{RTE}}$ is

$$\begin{aligned}\mathcal{L}\phi(\mathbf{r},\hat{\mathbf{s}}) &= \mathcal{L}_{\mathrm{RTE}}\phi(\mathbf{r},\hat{\mathbf{s}}) \\ &= -\phi(\mathbf{r},\hat{\mathbf{s}})+\int_{\mathbb{S}^{n-1}}\Theta(\hat{\mathbf{s}}\cdot\hat{\mathbf{s}}')\phi(r,\hat{\mathbf{s}}')\,\mathrm{d}\hat{\mathbf{s}}',\end{aligned} \tag{2}$$

where the scattering phase function $\Theta(\hat{\mathbf{s}}\cdot\hat{\mathbf{s}}')$ describes the probability for a photon to scatter from direction $\hat{\mathbf{s}}'$ in direction $\hat{\mathbf{s}}$. An often used phase function is the Henyey–Greenstein scattering function [32]

$$\Theta(\hat{\mathbf{s}}\cdot\hat{\mathbf{s}}')=\frac{1}{|\mathbb{S}^{n-1}|}\frac{1-g^2}{(1+g^2-2\,g\hat{\mathbf{s}}\cdot\hat{\mathbf{s}}')^{n/2}}, \tag{3}$$

where scattering shape parameter g defines the shape of the probability distribution, and $|\mathbb{S}^{n-1}|$ is the surface measure of $\mathbb{S}^{n-1}|\mathbb{S}^1| = 2\pi$ and $|\mathbb{S}^2| = 4\pi$). The angular moments of the scattering phase function are

$$g_m=\int_{\mathbb{S}^{n-1}}(\hat{\mathbf{s}}\cdot\hat{\mathbf{s}}')^m\Theta(\hat{\mathbf{s}}\cdot\hat{\mathbf{s}}')\,\mathrm{d}\hat{\mathbf{s}}. \tag{4}$$

In the case of the Henyey–Greenstein phase function angular moments are $g_m = g^m$. In biological tissues, the first moment is typically close to 1 indicating that scattering is forward-peaked [33]. Thus, the direction of photons is most likely to change only a little in scattering events.

In this paper, it is assumed that no photons travel in an inward direction at the boundary $\partial\Omega$ except at the source location $\varepsilon_t \subset \partial\Omega$

$$\phi(\mathbf{r},\hat{\mathbf{s}})=\begin{cases}\phi_0(\mathbf{r},\hat{\mathbf{s}}), & \mathbf{r}\in\varepsilon_t, \quad \hat{\mathbf{s}}\cdot\hat{\mathbf{n}}<0,\\ 0, & \mathbf{r}\in\partial\Omega\backslash\varepsilon_t, \quad \hat{\mathbf{s}}\cdot\hat{\mathbf{n}}<0,\end{cases} \tag{5}$$

where $\hat{\mathbf{n}}$ is an outward unit normal and $\phi_0(\mathbf{r},\hat{\mathbf{s}})$ is the source. Quantities of interest include photon density defined as an integral of the radiance over angular directions [1]

$$\Phi(\mathbf{r}) = \int_{\mathbb{S}^{n-1}} \phi(\mathbf{r},\hat{\mathbf{s}})\, \mathrm{d}\hat{\mathbf{s}}. \tag{6}$$

2.2. Fokker–Planck approximation

The Fokker–Planck equation can be derived either using the Taylor expansion of the scattering operator $\mathcal{L}$ at $\hat{\mathbf{s}} \approx \hat{\mathbf{s}}'$ [23], using asymptotic analysis when the scattering mean free path $l_s = \mu_s^{-1}$ is small while the transport mean free path $l^* = (\mu_s(1-g_1))^{-1}$ is necessarily not small [21,4], or by approximating the scattering operator eigenvalues [22,24]. In the following, we shortly review the third approach.

When scattering is forward-peaked, one can approximate the scattering phase function $\Theta(\hat{\mathbf{s}} \cdot \hat{\mathbf{s}}')$ using a linear combination of the delta function and its even derivatives [24]. The Fokker–Planck approximation to the scattering phase function $\Theta(\hat{\mathbf{s}} \cdot \hat{\mathbf{s}}')$ is

$$\Theta(\hat{\mathbf{s}} \cdot \hat{\mathbf{s}}') \approx \Theta_{\mathrm{FP}}(\hat{\mathbf{s}} \cdot \hat{\mathbf{s}}') = a_0^{\mathrm{FP}} \delta(\hat{\mathbf{s}} - \hat{\mathbf{s}}') + a_1^{\mathrm{FP}} \delta^{(2)}(\hat{\mathbf{s}} - \hat{\mathbf{s}}'), \tag{7}$$

where coefficients $a_0^{\mathrm{FP}} = 1$ and $a_1^{\mathrm{FP}} = (n-1)^{-1}(1-g_1)$ can be determined from the eigenvalues of the original scattering operator $\mathcal{L}$ [24,25], δ is the delta function, and $\delta^{(2)}$ is the second-order derivative of the delta function. The resulting approximative scattering operator $\mathcal{L}_{\mathrm{FP}}$ is

$$\mathcal{L}\phi(\mathbf{r},\hat{\mathbf{s}}) \approx \mathcal{L}_{\mathrm{FP}}\phi(\mathbf{r},\hat{\mathbf{s}}) = \frac{1}{n-1}(1-g_1)\Delta_{\hat{\mathbf{s}}}\phi(\mathbf{r},\hat{\mathbf{s}}), \tag{8}$$

where $\Delta_{\hat{\mathbf{s}}}$ is the Laplacian operator in spherical coordinates (or Laplace–Beltrami operator) on the unit sphere $\mathbb{S}^{n-1}$. The Fokker–Planck equation is obtained by substituting Eq. (8) into Eq. (1).

2.3. Fokker–Planck–Eddington approximation

In the presence of both forward-peaked and large-angle scattering, smoothly varying Legendre polynomials can be used to approximate the scattering phase function in addition to the delta function and its even derivatives [24]. The Fokker–Planck–Eddington approximation is

$$\Theta(\hat{\mathbf{s}} \cdot \hat{\mathbf{s}}') \approx \Theta_{\mathrm{FPE}}(\hat{\mathbf{s}} \cdot \hat{\mathbf{s}}') = a_0^{\mathrm{FPE}} \delta(\hat{\mathbf{s}} - \hat{\mathbf{s}}') + a_1^{\mathrm{FPE}} \delta^{(2)}(\hat{\mathbf{s}} - \hat{\mathbf{s}}') + \frac{1}{|\mathbb{S}^{n-1}|}\left(b_0^{\mathrm{FPE}} P_0(\hat{\mathbf{s}} \cdot \hat{\mathbf{s}}') + n b_1^{\mathrm{FPE}} P_1(\hat{\mathbf{s}} \cdot \hat{\mathbf{s}}')\right), \tag{9}$$

where P_k is the Legendre polynomial of order k and the coefficients a_0^{FPE}, a_1^{FPE}, b_0^{FPE}, and b_1^{FPE} can be determined from the eigenvalues of the original scattering operator [24,25]. As a result, we obtain

$$a_0^{\mathrm{FPE}} = \frac{g_2}{5}(9-4g_1), \tag{10a}$$

$$a_1^{\mathrm{FPE}} = \frac{g_2}{5}(1-g_1), \tag{10b}$$

$$b_0^{\mathrm{FPE}} = 1 - \frac{9}{5}g_2 + \frac{4}{5}g_3, \tag{10c}$$

$$b_1^{\mathrm{FPE}} = g_1 - \frac{8}{5}g_2 + \frac{3}{5}g_3, \tag{10d}$$

when $n=2$, and

$$a_0^{\mathrm{FPE}} = 2g_2 - g_3, \tag{11a}$$

$$a_1^{\mathrm{FPE}} = \frac{g_2 - g_3}{6}, \tag{11b}$$

$$b_0^{\mathrm{FPE}} = 1 - 2g_2 + g_3, \tag{11c}$$

$$b_1^{\mathrm{FPE}} = g_1 - \frac{5g_2}{3} + \frac{2g_3}{3}, \tag{11d}$$

when $n=3$. Fig. 1 shows the Henyey–Greenstein scattering phase function $\Theta(\hat{\mathbf{s}} \cdot \hat{\mathbf{s}}')$, and the approximative phase functions $\Theta_{\mathrm{FP}}(\hat{\mathbf{s}} \cdot \hat{\mathbf{s}}')$ and $\Theta_{\mathrm{FPE}}(\hat{\mathbf{s}} \cdot \hat{\mathbf{s}}')$ with scattering shape parameter $g=0.8$. The delta function was numerically approximated as $\delta(x) \approx (a\sqrt{\pi})^{-1}\exp(-x^2 a^{-2})$ with $a=0.1$. The resulting approximative scattering operator is

$$\mathcal{L}\phi(\mathbf{r},\hat{\mathbf{s}}) \approx \mathcal{L}_{\mathrm{FPE}}\phi(\mathbf{r},\hat{\mathbf{s}}) = -(1-a_0^{\mathrm{FPE}})\phi(\mathbf{r},\hat{\mathbf{s}}) + a_1^{\mathrm{FPE}}\Delta_{\hat{\mathbf{s}}}\phi(\mathbf{r},\hat{\mathbf{s}}) + \frac{1}{|\mathbb{S}^{n-1}|}\int_{\mathbb{S}^{n-1}} \left(b_0^{\mathrm{FPE}} P_0(\hat{\mathbf{s}} \cdot \hat{\mathbf{s}}') + n b_1^{\mathrm{FPE}} P_1(\hat{\mathbf{s}} \cdot \hat{\mathbf{s}}')\right)\phi(\mathbf{r},\hat{\mathbf{s}}')\, \mathrm{d}\hat{\mathbf{s}}'. \tag{12}$$

The Fokker–Planck–Eddington equation is obtained by substituting Eq. (12) into Eq. (1).

2.4. Diffusion approximation

The diffusion approximation to the RTE can be derived, for example, by expanding the radiance, the source term, and the phase function into series using the spherical harmonics and truncating the series to the first order [7,1], or by using asymptotic techniques when scattering is strong and absorption is weak [34–36]. In the DA framework, the approximation that is used for the radiance

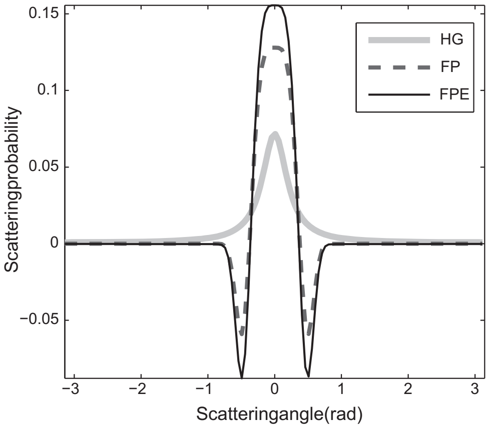

Fig. 1. Henyey–Greenstein scattering phase function $\Theta(\hat{\mathbf{s}} \cdot \hat{\mathbf{s}}')$ and the approximations $\Theta_{\mathrm{FP}}(\hat{\mathbf{s}} \cdot \hat{\mathbf{s}}')$ and $\Theta_{\mathrm{FPE}}(\hat{\mathbf{s}} \cdot \hat{\mathbf{s}}')$ with scattering shape parameter $g=0.8$.

is [1,7,17]

$$\phi(\mathbf{r},\hat{\mathbf{s}}) \approx \frac{1}{|S^{n-1}|}\Phi(\mathbf{r}) - \frac{n}{|S^{n-1}|}(\hat{\mathbf{s}}\cdot\kappa\nabla\Phi(\mathbf{r})), \tag{13}$$

where κ is the diffusion coefficient

$$\kappa = (n(\mu_a+\mu_s(1-g_1)))^{-1}. \tag{14}$$

In the frequency domain, the DA without internal sources is of the form [1]

$$-\nabla\cdot\kappa\nabla\Phi(\mathbf{r}) + \mu_a\Phi(\mathbf{r}) + \frac{i\omega}{c}\Phi(\mathbf{r}) = 0. \tag{15}$$

The DA cannot satisfy the boundary condition (5) exactly. Typically, the boundary condition is approximated with a Robin-type boundary condition

$$\Phi(\mathbf{r}) + \frac{1}{2\gamma_n}\kappa A\frac{\partial\Phi(\mathbf{r})}{\partial\hat{\mathbf{n}}} = \begin{cases} \frac{I_s}{\gamma_n}, & \mathbf{r}\in\varepsilon_t, \\ 0, & \mathbf{r}\in\partial\Omega\backslash\varepsilon_t, \end{cases} \tag{16}$$

where γ_n is a dimension dependent constant ($\gamma_2 = 1/\pi$, $\gamma_3 = 1/4$), and I_s is an inward directed diffuse boundary current at the source position [37,38]. The parameter A takes into account a mismatch in refractive indices at the boundary and it can be derived from the Fresnel's law.

2.5. Coupled model

We write the coupled model [17,39,40] in a general form allowing the use of any scattering operator $\mathcal{L}$. In the coupled model, the domain Ω is divided into two disjoint subsets Ω_ϕ and Ω_Φ. The sub-domain Ω_ϕ covers the regions in which the DA is not valid such as the vicinity of the source and the boundaries, and regions with low-scattering . Light propagation in sub-domain Ω_ϕ is modeled using either the FP, FPE, or RTE depending on the chosen scattering operator. The DA is used in the sub-domain $\Omega_\Phi = \Omega\backslash\Omega_\phi$ which covers the rest of the domain. The boundaries of the sub-domains are denoted by $\partial\Omega_\phi$ and $\partial\Omega_\Phi$. Furthermore, the interface of sub-domains is denoted by $\Gamma = \partial\Omega_\phi\cap\partial\Omega_\Phi$. The external boundaries are denoted by $\partial\Omega_{\phi,\text{out}} = \partial\Omega_\phi\backslash\Gamma$ and $\partial\Omega_{\Phi,\text{out}} = \partial\Omega_\Phi\backslash\Gamma$.

The models are coupled through boundary conditions at the interface Γ. The location of the interface Γ should be chosen such that the radiance is almost isotropic. Then, the DA is a valid approximation and the coupling between the models is applicable. Usually, this criterion can be fulfilled in diffuse media with distances greater than three transport mean free paths l^* from the boundaries, sources and low-scattering regions. The coupled model is of the form

$$\frac{i\omega}{c}\phi(\mathbf{r},\hat{\mathbf{s}}) + \hat{\mathbf{s}}\cdot\nabla\phi(\mathbf{r},\hat{\mathbf{s}}) + \mu_a\phi(\mathbf{r},\hat{\mathbf{s}}) = \mu_s\mathcal{L}\phi(\mathbf{r},\hat{\mathbf{s}}), \quad \mathbf{r}\in\Omega_\phi \tag{17a}$$

$$\phi(\mathbf{r},\hat{\mathbf{s}}) = \begin{cases} \phi_0(\mathbf{r},\hat{\mathbf{s}}), & \mathbf{r}\in\varepsilon_t, \quad \hat{\mathbf{s}}\cdot\hat{\mathbf{n}}<0, \\ 0, & \mathbf{r}\in\partial\Omega_{\phi,\text{out}}\backslash\varepsilon_t, \quad \hat{\mathbf{s}}\cdot\hat{\mathbf{n}}<0, \end{cases} \tag{17b}$$

$$\phi(\mathbf{r},\hat{\mathbf{s}}) = \frac{1}{|\mathbb{S}^{n-1}|}\Phi(\mathbf{r}) - \frac{n}{|\mathbb{S}^{n-1}|}\hat{\mathbf{s}}\cdot(\kappa\nabla\Phi(\mathbf{r})), \quad \mathbf{r}\in\Gamma \tag{17c}$$

$$-\nabla\cdot\kappa\nabla\Phi(\mathbf{r}) + \mu_a\Phi(\mathbf{r}) + \frac{i\omega}{c}\Phi(\mathbf{r}) = 0, \quad \mathbf{r}\in\Omega_\Phi \tag{17d}$$

$$\Phi(\mathbf{r}) + \frac{1}{2\gamma_n}\kappa A\frac{\partial\Phi(\mathbf{r})}{\partial\hat{\mathbf{n}}} = \begin{cases} \frac{I_s}{\gamma_n}, & \mathbf{r}\in\varepsilon_t, \\ 0, & \mathbf{r}\in\partial\Omega_{\Phi,\text{out}}\backslash\varepsilon_t, \end{cases} \tag{17e}$$

$$\Phi(\mathbf{r}) = \int_{\mathbb{S}^{n-1}}\phi(\mathbf{r},\hat{\mathbf{s}})\,d\hat{\mathbf{s}}, \quad \mathbf{r}\in\Gamma, \tag{17f}$$

where the coupled RTE-DA, FP-DA, and FPE-DA models are obtained by using the corresponding scattering operator Eq. (2), (8), or (12), respectively.

3. Finite element approximation of the coupled model

In this work, the solution of the coupled model (17) is approximated numerically using the FEM. In the FEM, a variational formulation of the original problem is derived, and then this infinite dimensional problem is discretized using a suitable set of basis functions.

The variational formulation of the coupled model (17) with a streamline diffusion modification [41,39] can be written as

$$\begin{aligned}
&\int_{\Omega_\phi}\int_{\mathbb{S}^{n-1}}\frac{i\omega}{c}\phi(\mathbf{r},\hat{\mathbf{s}})v(\mathbf{r},\hat{\mathbf{s}})\,d\hat{\mathbf{s}}\,d\mathbf{r} - \int_{\Omega_\phi}\int_{\mathbb{S}^{n-1}}\hat{\mathbf{s}}\cdot\nabla v(\mathbf{r},\hat{\mathbf{s}}) \\
&\quad \phi(\mathbf{r},\hat{\mathbf{s}})\,d\hat{\mathbf{s}}\,d\mathbf{r} \\
&\quad + \int_{\partial\Omega_\phi}\int_{\mathbb{S}^{n-1}}(\hat{\mathbf{s}}\cdot\hat{\mathbf{n}})_+\phi(\mathbf{r},\hat{\mathbf{s}})v(\mathbf{r},\hat{\mathbf{s}})\,d\hat{\mathbf{s}}\,dS \\
&\quad - \int_\Gamma\int_{\mathbb{S}^{n-1}}\frac{1}{|\mathbb{S}^{n-1}|}(\hat{\mathbf{s}}\cdot\hat{\mathbf{n}})_-\Phi(\mathbf{r})v(\mathbf{r},\hat{\mathbf{s}})\,d\hat{\mathbf{s}}\,dS \\
&\quad + \int_\Gamma\int_{\mathbb{S}^{n-1}}\frac{n}{|\mathbb{S}^{n-1}|}(\hat{\mathbf{s}}\cdot\hat{\mathbf{n}})_-(\hat{\mathbf{s}}\cdot\kappa\nabla\Phi(\mathbf{r}))v(\mathbf{r},\hat{\mathbf{s}})\,d\hat{\mathbf{s}}\,dS \\
&\quad + \int_{\Omega_\phi}\int_{\mathbb{S}^{n-1}}\mu_a\phi(\mathbf{r},\hat{\mathbf{s}})v(\mathbf{r},\hat{\mathbf{s}})\,d\hat{\mathbf{s}}\,d\mathbf{r} \\
&\quad - \int_{\Omega_\phi}\int_{\mathbb{S}^{n-1}}\mathcal{L}\phi(\mathbf{r},\hat{\mathbf{s}})v(\mathbf{r},\hat{\mathbf{s}})\,d\hat{\mathbf{s}}\,d\mathbf{r} + \int_{\Omega_\phi}\int_{\mathbb{S}^{n-1}}\delta\frac{i\omega}{c}\phi(\mathbf{r},\hat{\mathbf{s}})\hat{\mathbf{s}} \\
&\quad \cdot\nabla v(\mathbf{r},\hat{\mathbf{s}})\,d\hat{\mathbf{s}}\,d\mathbf{r} \\
&\quad + \int_{\Omega_\phi}\int_{\mathbb{S}^{n-1}}\delta(\hat{\mathbf{s}}\cdot\nabla\phi(\mathbf{r},\hat{\mathbf{s}}))(\hat{\mathbf{s}}\cdot\nabla v(\mathbf{r},\hat{\mathbf{s}}))\,d\hat{\mathbf{s}}\,d\mathbf{r} \\
&\quad + \int_{\Omega_\phi}\int_{\mathbb{S}^{n-1}}\delta\mu_a\phi(\mathbf{r},\hat{\mathbf{s}})v(\mathbf{r},\hat{\mathbf{s}})\,d\hat{\mathbf{s}}\,d\mathbf{r} \\
&\quad - \int_{\Omega_\phi}\delta\int_{\mathbb{S}^{n-1}}\mathcal{L}\phi(\mathbf{r},\hat{\mathbf{s}})(\hat{\mathbf{s}}\cdot\nabla v(\mathbf{r},\hat{\mathbf{s}}))\,d\hat{\mathbf{s}}\,d\mathbf{r} + \int_{\Omega_\Phi}\kappa\nabla\Phi(\mathbf{r}) \\
&\quad \cdot\nabla\Psi(\mathbf{r})\,d\mathbf{r} \\
&\quad + \int_{\partial\Omega_{\Phi,\text{out}}}\frac{2\gamma_n}{A}\Phi(\mathbf{r})\Psi(\mathbf{r})\,dS - \int_\Gamma\kappa\left(\hat{\mathbf{n}}\cdot\nabla\int_{\mathbb{S}^{n-1}}\phi(\mathbf{r},\hat{\mathbf{s}})\,d\hat{\mathbf{s}}\right)\Psi(\mathbf{r})\,dS \\
&\quad + \int_{\Omega_\Phi}\mu_a\Phi(\mathbf{r})\Psi(\mathbf{r})\,d\mathbf{r} + \int_{\Omega_\Phi}\frac{i\omega}{c}\Phi(\mathbf{r})\Psi(\mathbf{r})\,d\mathbf{r} \\
&\quad = \int_{\partial\Omega_{\phi,\text{out}}}\int_{\mathbb{S}^{n-1}}(\hat{\mathbf{s}}\cdot\hat{\mathbf{n}})_-\phi_0(\mathbf{r},\hat{\mathbf{s}})v(\mathbf{r},\hat{\mathbf{s}})\,d\hat{\mathbf{s}}\,dS + \int_{\partial\Omega_{\Phi,\text{out}}}\frac{2I_s}{A}\Psi(\mathbf{r})\,dS,
\end{aligned} \tag{18}$$

where v and Ψ are test functions, and δ is a streamline-diffusion modification parameter.

The FE-approximation is obtained by approximating the solutions $\phi(\mathbf{r},\hat{\mathbf{s}})$ and $\Phi(\mathbf{r})$ of the variational formulation

(18) with a linear combination of the basis functions

$$\phi(\mathbf{r},\hat{\mathbf{s}}) \approx \sum_{i=1}^{N_n} \sum_{l=1}^{N_a} \alpha_{il} \psi_i(\mathbf{r}) \psi_l(\hat{\mathbf{s}}), \tag{19}$$

$$\Phi(\mathbf{r}) \approx \sum_{k=1}^{N} a_k \vartheta_k(\mathbf{r}), \tag{20}$$

where $\psi_i(\mathbf{r})$ and $\psi_l(\hat{\mathbf{s}})$ are the nodal basis functions of the spatial and angular discretizations of $\Omega_\phi \times \mathbb{S}^{n-1}$, α_{il} is the radiance at a spatial node i in an angular direction l, and N_n and N_a are the number of the spatial and angular nodes in sub-domain Ω_ϕ, respectively. Further, $\vartheta_k(\mathbf{r})$ is the nodal basis function of the spatial discretization of Ω_Φ, a_k is the photon density at a spatial node k, and N is the number of spatial nodes in the sub-domain Ω_Φ. In this work, we use a piecewise linear basis for both the spatial and angular parts of the approximation. The FE-approximation of the coupled model can be written in a matrix form as

$$\begin{pmatrix} A_\phi & D \\ F & A_\Phi \end{pmatrix} \begin{pmatrix} \alpha \\ a \end{pmatrix} = \begin{pmatrix} b_\phi \\ b_\Phi \end{pmatrix}, \tag{21}$$

where the block-matrices A_ϕ and A_Φ contain the FE-approximations of the models to be coupled, and the matrices D and F contain the coupling conditions on the interface Γ. The components of the matrix equation (21) are the following. The block A_ϕ is

$$A_\phi = A_0 + A_1 + A_2 + A_3 + A_4, \tag{22}$$

where

$$\begin{aligned} A_0(h,s) = \frac{\mathrm{i}\omega}{c} \Bigg(& \int_{\Omega_\phi} \psi_i(\mathbf{r}) \psi_j(\mathbf{r})\, \mathrm{d}r \int_{\mathbb{S}^{n-1}} \psi_l(\hat{\mathbf{s}}) \psi_m(\hat{\mathbf{s}})\, \mathrm{d}\hat{\mathbf{s}} \\ & + \int_{\Omega_\phi} \delta \int_{\mathbb{S}^{n-1}} \hat{\mathbf{s}} \cdot \nabla \psi_j(\mathbf{r}) \psi_m(\hat{\mathbf{s}}) \psi_l(\hat{\mathbf{s}})\, \mathrm{d}\hat{\mathbf{s}} \psi_i(\mathbf{r})\, \mathrm{d}\mathbf{r} \Bigg), \end{aligned} \tag{23a}$$

$$\begin{aligned} A_1(h,s) = & -\int_{\Omega_\phi} \int_{\mathbb{S}^{n-1}} \hat{\mathbf{s}} \cdot \nabla \psi_j(\mathbf{r}) \psi_m(\hat{\mathbf{s}}) \psi_l(\hat{\mathbf{s}})\, \mathrm{d}\hat{\mathbf{s}} \psi_i(\mathbf{r})\, \mathrm{d}\mathbf{r} \\ & + \int_{\Omega_\phi} \delta \int_{\mathbb{S}^{n-1}} (\hat{\mathbf{s}} \cdot \nabla \psi_i(\mathbf{r}))(\hat{\mathbf{s}} \cdot \nabla \psi_j(\mathbf{r})) \psi_l(\hat{\mathbf{s}}) \psi_m(\hat{\mathbf{s}})\, \mathrm{d}\hat{\mathbf{s}}\, \mathrm{d}\mathbf{r}, \end{aligned} \tag{23b}$$

$$A_2(h,s) = \int_{\partial\Omega_\phi} \psi_i(\mathbf{r}) \psi_j(\mathbf{r})\, \mathrm{d}S \int_{\mathbb{S}^{n-1}} (\hat{\mathbf{s}} \cdot \hat{\mathbf{n}})_+ \psi_l(\hat{\mathbf{s}}) \psi_m(\hat{\mathbf{s}})\, \mathrm{d}\hat{\mathbf{s}}, \tag{23c}$$

$$\begin{aligned} A_3(h,s) = & \int_{\Omega_\phi} \mu_a \psi_i(\mathbf{r}) \psi_j(\mathbf{r})\, \mathrm{d}\mathbf{r} \int_{\mathbb{S}^{n-1}} \psi_l(\hat{\mathbf{s}}) \psi_m(\hat{\mathbf{s}})\, \mathrm{d}\hat{\mathbf{s}} \\ & + \int_{\Omega_\phi} \delta \mu_a \psi_i(\mathbf{r}) \int_{\mathbb{S}^{n-1}} (\hat{\mathbf{s}} \cdot \nabla \psi_j(\mathbf{r})) \psi_m(\hat{\mathbf{s}}) \psi_l(\hat{\mathbf{s}})\, \mathrm{d}\hat{\mathbf{s}}\, \mathrm{d}\mathbf{r}, \end{aligned} \tag{23d}$$

where $h = N_a(j-1) + m$, $s = N_a(i-1) + l$, $j,i = 1, \ldots, N_n$, $m, l = 1, \ldots, N_a$, and $h,s = 1, \ldots, N_n N_a$. The matrix A_4 depends on the chosen scattering operator $\mathcal{L}$. In the case of the RTE, $\mathcal{L} = \mathcal{L}_{\mathrm{RTE}}$ and

$$\begin{aligned} A_4(h,s) = & \int_{\Omega_\phi} \mu_s \psi_i(\mathbf{r}) \psi_j(\mathbf{r})\, \mathrm{d}\mathbf{r} \int_{\mathbb{S}^{n-1}} \psi_l(\hat{\mathbf{s}}) \psi_m(\hat{\mathbf{s}})\, \mathrm{d}\hat{\mathbf{s}} \\ & + \int_{\Omega_\phi} \delta \mu_s \psi_i(\mathbf{r}) \int_{\mathbb{S}^{n-1}} (\hat{\mathbf{s}} \cdot \nabla \psi_j(\mathbf{r})) \psi_m(\hat{\mathbf{s}}) \psi_l(\hat{\mathbf{s}})\, \mathrm{d}\hat{\mathbf{s}}\, \mathrm{d}\mathbf{r} \\ & - \int_{\Omega_\phi} \mu_s \psi_i(\mathbf{r}) \psi_j(\mathbf{r})\, \mathrm{d}\mathbf{r} \int_{\mathbb{S}^{n-1}} \int_{\mathbb{S}^{n-1}} \Theta(\hat{\mathbf{s}} \cdot \hat{\mathbf{s}}') \psi_l(\hat{\mathbf{s}}')\, \mathrm{d}\hat{\mathbf{s}}' \psi_m(\hat{\mathbf{s}})\, \mathrm{d}\hat{\mathbf{s}} \\ & - \int_{\Omega_\phi} \delta \mu_s \int_{\mathbb{S}^{n-1}} (\hat{\mathbf{s}} \cdot \nabla \psi_j(\mathbf{r})) \psi_m(\hat{\mathbf{s}}) \\ & \int_{S^{n-1}} \Theta(\hat{\mathbf{s}} \cdot \hat{\mathbf{s}}') \psi_l(\hat{\mathbf{s}}')\, \mathrm{d}\hat{\mathbf{s}}'\, \mathrm{d}\hat{\mathbf{s}} \psi_i(\mathbf{r})\, \mathrm{d}\mathbf{r} \end{aligned} \tag{24}$$

In the case of the FP, $\mathcal{L}\phi(\mathbf{r},\hat{\mathbf{s}}) = \mathcal{L}_{\mathrm{FP}}\phi(\mathbf{r},\hat{\mathbf{s}})$ and

$$\begin{aligned} A_4(h,s) = & \int_{\Omega_\phi} a_{1,\mathrm{FP}} \mu_s \psi_i(\mathbf{r}) \psi_j(\mathbf{r})\, \mathrm{d}\mathbf{r} \int_{\mathbb{S}^{n-1}} \nabla_{\hat{\mathbf{s}}} \psi_l(\hat{\mathbf{s}}) \cdot \nabla_{\hat{\mathbf{s}}} \psi_m(\hat{\mathbf{s}})\, \mathrm{d}\hat{\mathbf{s}} \\ & + \int_{\Omega_\phi} \delta a_{1,\mathrm{FP}} \mu_s \psi_i(\mathbf{r}) \int_{\mathbb{S}^{n-1}} (\nabla_{\hat{\mathbf{s}}} \psi_l(\hat{\mathbf{s}}) \cdot \nabla_{\hat{\mathbf{s}}} (\hat{\mathbf{s}} \cdot \nabla \psi_j(\mathbf{r}) \psi_m(\hat{\mathbf{s}})))\, \mathrm{d}\hat{\mathbf{s}}\, \mathrm{d}\mathbf{r}. \end{aligned} \tag{25}$$

In the case of the FPE, $\mathcal{L}\phi(\mathbf{r},\hat{\mathbf{s}}) = \mathcal{L}_{\mathrm{FPE}}\phi(\mathbf{r},\hat{\mathbf{s}})$ and

$$\begin{aligned} A_4(h,s) = & \int_{\Omega_\phi} (1 - a_0^{\mathrm{FPE}}) \mu_s \psi_i(\mathbf{r}) \psi_j(\mathbf{r})\, \mathrm{d}\mathbf{r} \int_{\mathbb{S}^{n-1}} \psi_l(\hat{\mathbf{s}}) \psi_m(\hat{\mathbf{s}})\, \mathrm{d}\hat{\mathbf{s}} \\ & + \int_{\Omega_\phi} \delta (1 - a_0^{\mathrm{FPE}}) \mu_s \psi_i(\mathbf{r}) \int_{\mathbb{S}^{n-1}} (\hat{\mathbf{s}} \cdot \nabla \psi_j(\mathbf{r})) \psi_m(\hat{\mathbf{s}}) \psi_l(\hat{\mathbf{s}})\, \mathrm{d}\hat{\mathbf{s}}\, \mathrm{d}\mathbf{r} \\ & - \int_{\Omega_\phi} a_1^{FPE} \mu_s \psi_i(\mathbf{r}) \psi_j(\mathbf{r})\, \mathrm{d}\mathbf{r} \int_{\mathbb{S}^{n-1}} \nabla_{\hat{\mathbf{s}}} \psi_l(\hat{\mathbf{s}}) \cdot \nabla_{\hat{\mathbf{s}}} \psi_m(\hat{\mathbf{s}})\, \mathrm{d}\hat{\mathbf{s}} \\ & - \int_{\Omega_\phi} \delta a_1^{FPE} \mu_s \psi_i(\mathbf{r}) \int_{\mathbb{S}^{n-1}} (\nabla_{\hat{\mathbf{s}}} \psi_l(\hat{\mathbf{s}}) \cdot \nabla_{\hat{\mathbf{s}}} (\hat{\mathbf{s}} \cdot \nabla \psi_j(\mathbf{r}) \psi_m(\hat{\mathbf{s}})))\, \mathrm{d}\hat{\mathbf{s}}\, \mathrm{d}\mathbf{r} \\ & - \frac{1}{|\mathbb{S}^{n-1}|} \int_{\Omega_\phi} \mu_s \psi_i(\mathbf{r}) \psi_j(\mathbf{r})\, \mathrm{d}\mathbf{r} \int_{\mathbb{S}^{n-1}} \int_{\mathbb{S}^{n-1}} (b_0^{\mathrm{FPE}} P_0(\hat{\mathbf{s}} \cdot \hat{\mathbf{s}}') \\ & + n b_1^{\mathrm{FPE}} P_1(\hat{\mathbf{s}} \cdot \hat{\mathbf{s}}')) \psi_l(\hat{\mathbf{s}}')\, \mathrm{d}\hat{\mathbf{s}}' \psi_m(\hat{\mathbf{s}})\, \mathrm{d}\hat{\mathbf{s}} \\ & - \frac{1}{|\mathbb{S}^{n-1}|} \int_{\Omega_\phi} \delta \mu_s \psi_i(\mathbf{r}) \int_{\mathbb{S}^{n-1}} \int_{\mathbb{S}^{n-1}} (b_0^{\mathrm{FPE}} P_0(\hat{\mathbf{s}} \cdot \hat{\mathbf{s}}') \\ & + n b_1^{\mathrm{FPE}} P_1(\hat{\mathbf{s}} \cdot \hat{\mathbf{s}}')) \psi_l(\hat{\mathbf{s}}')\, \mathrm{d}\hat{\mathbf{s}}' (\hat{\mathbf{s}} \cdot \nabla \psi_j(\mathbf{r})) \psi_m(\hat{\mathbf{s}})\, \mathrm{d}\hat{\mathbf{s}}\, \mathrm{d}\mathbf{r}. \end{aligned} \tag{26}$$

The DA block A_Φ is

$$A_\Phi = K + C + R + Z, \tag{27}$$

where matrices K, C, R, and Z are

$$K(p,k) = \int_{\Omega_\Phi} \kappa \nabla \vartheta_k(\mathbf{r}) \cdot \nabla \vartheta_p(\mathbf{r})\, \mathrm{d}\mathbf{r}, \tag{28a}$$

$$C(p,k) = \int_{\Omega_\Phi} \mu_a \vartheta_k(\mathbf{r}) \vartheta_p(\mathbf{r})\, \mathrm{d}\mathbf{r}, \tag{28b}$$

$$R(p,k) = \int_{\partial\Omega_{\Phi,\mathrm{out}}} \frac{2\gamma_n}{A} \vartheta_k(\mathbf{r}) \vartheta_p(\mathbf{r})\, \mathrm{d}S, \tag{28c}$$

$$Z(p,k) = \frac{\mathrm{i}\omega}{c} \int_{\Omega_\Phi} \vartheta_k(\mathbf{r}) \vartheta_p(\mathbf{r})\, \mathrm{d}\mathbf{r}, \tag{28d}$$

where $p, k = 1, \ldots, N$. The elements of the matrices D and F, which implement the interface conditions on Γ, are

$$\begin{aligned} D(h,k) = & -\frac{1}{|\mathbb{S}^{n-1}|} \int_\Gamma \vartheta_k(\mathbf{r}) \psi_j(\mathbf{r})\, \mathrm{d}S \int_{\mathbb{S}^{n-1}} (\hat{\mathbf{s}} \cdot \hat{\mathbf{n}})_- \psi_m(\hat{\mathbf{s}})\, \mathrm{d}\hat{\mathbf{s}} \\ & + \frac{n}{|\mathbb{S}^{n-1}|} \int_\Gamma \kappa \int_{\mathbb{S}^{n-1}} (\hat{\mathbf{s}} \cdot \hat{\mathbf{n}})_- (\hat{\mathbf{s}} \cdot \nabla \vartheta_k(\mathbf{r})) \psi_m(\hat{\mathbf{s}})\, \mathrm{d}\hat{\mathbf{s}} \psi_j(\mathbf{r})\, \mathrm{d}S, \end{aligned} \tag{29}$$

and

$$F(p,s) = -\int_\Gamma \kappa (\hat{\mathbf{n}} \cdot \nabla \psi_i(\mathbf{r})) \vartheta_p(\mathbf{r})\, \mathrm{d}S \int_{\mathbb{S}^{n-1}} \psi_l(\hat{\mathbf{s}})\, \mathrm{d}\hat{\mathbf{s}}. \tag{30}$$

The vector b_ϕ is of the form

$$b_\phi = b_1 \psi^0, \tag{31}$$

where $\psi^0 = (\psi^0_{1,1}, \ldots, \psi^0_{N_n,N_a}) \in \mathbb{R}^{N_n N_a}$ is the source intensity vector and

$$b_1(h,s) = \int_{\partial\Omega_{\phi,\mathrm{out}}} \psi_i(\mathbf{r})\psi_j(\mathbf{r})\,\mathrm{d}S \int_{\mathbb{S}^{n-1}} (\hat{\mathbf{s}}\cdot\hat{\mathbf{n}})_{-}\psi_l(\hat{\mathbf{s}})\psi_m(\hat{\mathbf{s}})\,\mathrm{d}\hat{\mathbf{s}}. \tag{32}$$

The vector b_Φ is

$$b_\Phi(p) = \int_{\partial\Omega_{\Phi,\mathrm{out}}} \frac{2I_s}{A} \vartheta_p(\mathbf{r})\,\mathrm{d}S. \tag{33}$$

Often the sub-domain division is chosen such that the sub-domain Ω_ϕ includes the source location and the boundary $\partial\Omega$. Then $\partial\Omega_{\Phi,\mathrm{out}} = \emptyset$, and thus $b_\Phi = 0$. As a solution of the coupled model, the radiance at the nodes of the spatial and angular discretizations in the sub-domain Ω_ϕ, and the photon density at the spatial nodes of the sub-domain Ω_Φ are obtained.

The FE-approximation of the FP, FPE, RTE, or DA in the whole domain Ω can be written in the framework of the FE-approximation of the coupled model. In the case of the FE-approximation of the FP, FPE, or RTE $\Omega_\phi = \Omega$ and $\Omega_\Phi = \emptyset$, and hence $A_\Phi = 0$, $b_\Phi = 0$, $F=0$, and $D=0$ in Eq. (21). The FE-approximation of the DA is obtained by choosing $\Omega_\Phi = \Omega$ and $\Omega_\phi = \emptyset$, and hence $A_\phi = 0$, $b_\phi = 0$, $F=0$, and $D=0$ in Eq. (21). For more details about the finite element approximation of the RTE, FP, and DA see e.g. [16,27].

4. Results

The performances of the proposed coupled models were tested with 2D simulations. The solutions of the cFP-DA and cFPE-DA were compared with the solution of the previously developed cRTE-DA and the solutions of the FP, FPE, DA, and RTE. The solution of the RTE served as a reference for other methods. All the models were solved using the FEM. The FE-approximations of the coupled models were computed using Eq. (21) with the corresponding discretized scattering operator Eq. (24), (25), or (26). The quantity of interest was the photon density inside the domain and at the boundary which was computed from the radiance using Eq. (6).

4.1. Effect of the coupling interface location

First, the effect of the distance between the coupling interface and the source to the accuracy of the solutions of the coupled models was investigated. The simulation domain Ω was a circle with a radius of 20 mm. The optical properties were: the scattering coefficient $\mu_s = 3\ \mathrm{mm}^{-1}$, the absorption coefficient $\mu_a = 0.01\ \mathrm{mm}^{-1}$, and the scattering shape parameter $g=0.8$. The optical properties were chosen such that, according to the theory, light becomes diffusive after propagating a few millimeters from the source. The modulation frequency of the input signal was 100 MHz. Refractive indices inside and outside of the domain were $n_{\mathrm{in}} = n_{\mathrm{out}} = 1$, and thus parameter $A=1$ in Eq. (16).

In the coupled models, the spatial domain Ω was divided into two different sub-domains Ω_ϕ and Ω_Φ. The sub-domain Ω_ϕ contained elements within 2.5 mm from the boundary and within chosen distance from the source. The chosen distances were 3, 4, 5, 6, 7, and 10 mm. The sub-domain Ω_Φ covered the remaining region. Then, the FE-mesh corresponding to each case was created. The FE-meshes for the spatial discretization of different cases consisted of 4780–4910 nodes and 9350–9590 triangular elements depending on the location of the interface. The FE-mesh with 6 mm distance between the coupling interface and the source is shown in Fig. 2. The sub-domain Ω_ϕ is marked with black and the DA sub-domain Ω_Φ is marked with grey. For the angular discretization of the FP and FPE, 16 equally spaced angular directions were used, and for the RTE 64 directions were used. The number of the angular directions was chosen by comparing the FE-approximations against the FE-approximation of the RTE with 128 angular directions. Since the FP and FPE take into account forward-peaked scattering analytically, a coarser angular discretization can be used compared with the RTE.

The photon densities were computed using the models as described in Section 3. Fig. 3 shows the logarithm of the amplitude and the phase shift of the photon density computed using the RTE, FP, FPE, and DA. The corresponding nodal-wise relative errors of the amplitudes and the phase shifts against the RTE are also shown. Fig. 4 shows the photon densities computed using the coupled models and the corresponding relative errors with 3 mm distance between the coupling interface and the source. The photon densities and the relative errors computed with 6 mm distance between the coupling interface and the source are shown in Fig. 5.

To compare the accuracy of the solutions, the norms of the relative errors of the photon densities were computed.

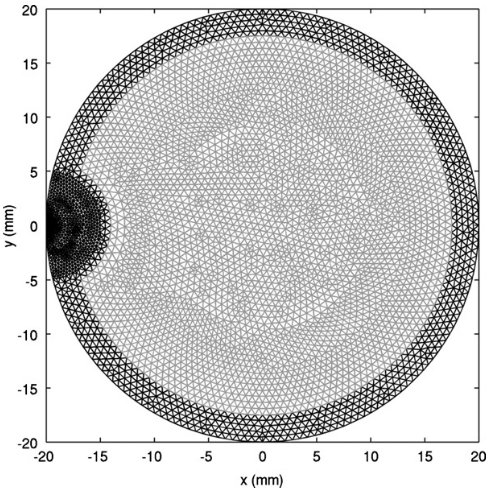

Fig. 2. Mesh for the coupled model with 6 mm distance between the coupling interface and the source. The FP, FPE or RTE sub-domain Ω_ϕ is marked with black and the DA sub-domain Ω_Φ with grey.

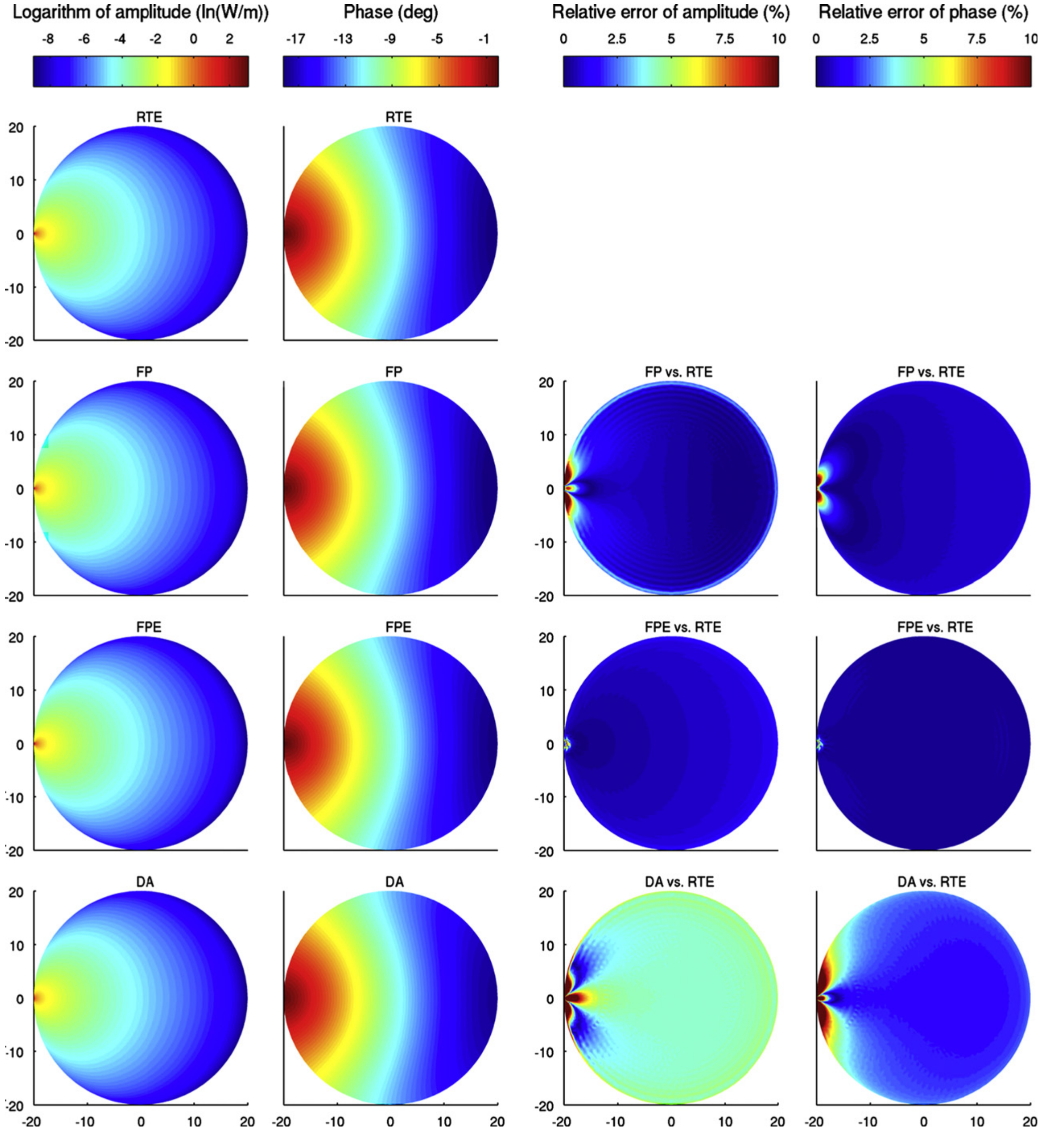

Fig. 3. Logarithm of amplitudes (first column) and phase shifts (second column) of photon densities computed using the RTE, FP, FPE, and DA (rows from top to bottom in the respective order). Relative errors of amplitudes and phase shifts against the RTE are shown in third and fourth columns.

Therefore, we took 10,232 uniformly distributed points inside the domain and computed the norm of the relative error as

$$\Delta_{\Phi} = \left\| \frac{\Phi - \Phi_{\mathrm{RTE}}}{\Phi_{\mathrm{RTE}}} \right\|. \tag{34}$$

The results are shown in Fig. 6 as a function of distance between the coupling interface and the source.

In addition, the norms of the relative errors of the FP, FPE, and DA are shown with vertical lines.

The results show that the RTE and FPE give almost the same results. The relative error of the FPE is under 1% both in the amplitude and the phase. The FP and DA give larger errors than the FPE especially close to the source. The FP does not allow photons to scatter next to the source. As a result, the FP underestimates the photon density next to the source [42] which can be seen as an increase in the relative error in Fig. 3. The FP and the DA give satisfactory results further from the source.

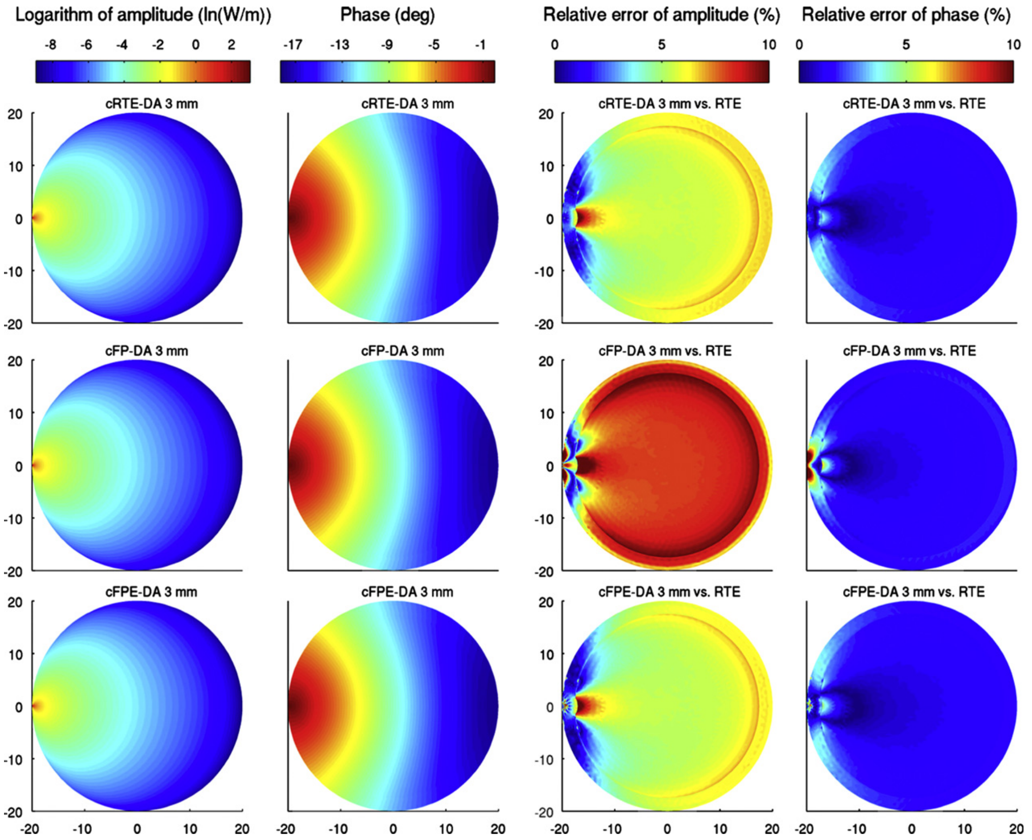

Fig. 4. Logarithm of amplitudes (first column) and phase shifts (second column) of photon densities computed using the cRTE-DA, cFP-DA, and cFPE-DA (rows from top to bottom in the respective order) with 3 mm distance between the coupling interface and the source. Relative errors of amplitudes and phase shifts against the RTE are shown in third and fourth columns.

The results for the coupled models show that when the coupling of the models is done too close to the source, when the radiance is not smooth as a function of direction, the solution is erroneous in the whole domain. As a result, the norm of the relative error is large. On the other hand, when the coupling is made far enough, after light has become diffuse, the norm decreases for all of the coupled models going under the error level of the DA. Thus, the coupling should be done such that the coupling conditions, Eqs. (17c) and (17f), are valid. In that case, the coupled models give almost as good results as using the corresponding FP, FPE, or RTE in the whole domain. Thus, using the coupled models is applicable compared with using the RTE.

4.2. Computational load

Next, the computational load of the models was compared. For the coupled models, the distance between the coupling interface and the source was 6 mm. The FE-matrix sizes, the number of non-zero elements, and the matrix filling ratios were computed, and the FE-matrix assembling times and the FE-matrix equation solution times were recorded. The results are given in Table 1. The computations were done on a workstation with two Intel Xeon quadracore processors clocked at 2.27 GHz and 48 GiB of memory using MATLAB® version 7.10 (R2010a), (The MathWorks, Inc.). The matrix equation was solved using MATLAB's function "mldivide".

The FPE-approximations have a few advantages in the assembling of the FE-matrices over the RTE. In the case of the FP, the resulting FE-matrix is sparse due to the angular differential operator in contrary to the FPE and RTE in which the matrices are block-diagonal . Hence, the assembling of the FE-matrices is fast and the amount of required memory is smaller. Moreover, the smooth integral operator in the FPE can be computed efficiently using the tensor products of one-dimensional integrals. This is not the case for the RTE. Since smaller amount of angular directions are needed for the FP and FPE, the computation

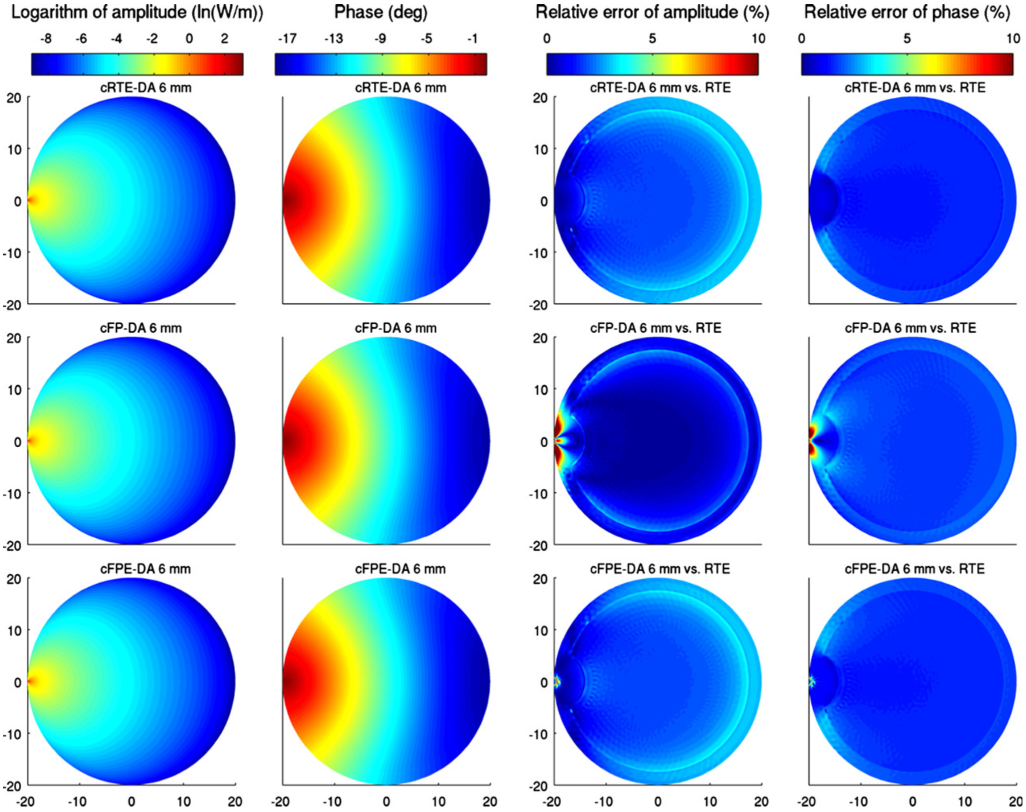

Fig. 5. Logarithm of amplitudes (first column) and phase shifts (second column) of photon densities computed using the cRTE-DA, cFP-DA, and cFPE-DA (rows from top to bottom in the respective order) with 6 mm distance between the coupling interface and the source. Relative errors of amplitudes and phase shifts against the RTE are shown in third and fourth columns.

times and the amount of required memory are much smaller compared with the RTE. This feature can be important especially in 3D. In addition, using the coupled models reduce the computation time even more. The computation times of the coupled FP-DA and FPE-DA are almost 10 times smaller for the matrix assembling and almost 20 times smaller for the matrix equation solution than that of the coupled RTE-DA. Thus, using the coupled models leads to computational savings compared with the RTE while preserving sufficient accuracy.

4.3. Realistic head geometry

The coupled models were tested in a realistic head geometry with tissue-like optical properties. The simulation domain was a 2D slice of a segmented image from a magnetic resonance image of a new-born infant head. The head slice is shown in the left image of Fig. 7. The image was segmented into six different regions: scalp, skull, grey mater, white mater, cerebrospinal fluid (CSF) around the brain, and CSF in the ventricles. The optical properties of different regions used in the simulations are given in Table 2. Other parameters were the same as before.

The computational domain was divided into sub-domains Ω_ϕ and Ω_Φ such that the sub-domain Ω_ϕ covered all the low-scattering regions as well as regions close to the source and the boundary. The sub-domain division between the models is shown in the right image of Fig. 7. The sub-domain Ω_ϕ is marked with light grey and the sub-domain Ω_Φ with white color. The CSF-regions are marked with dark grey. The location of the source was at the bottom of the domain and it is marked with a triangle.

The FE-mesh for the spatial discretization of the whole domain Ω contained 10,970 nodes and 21,607 triangular elements. For the coupled models the FE-mesh contained 6141 and 5490 nodes, and 11,270 and 10,337 triangular elements for the spatial discretization of the sub-domains Ω_ϕ and Ω_Φ, respectively. For the angular discretization of the FP and FPE 16 and for the RTE 32 equally spaced angular directions were used.

The photon densities inside the head slice computed using the RTE, FP, FPE, and DA are shown in first and second columns of Fig. 8. The photon densities computed using the cRTE-DA, cFP-DA, and cFPE-DA are shown in third and fourth columns of Fig. 8. The logarithms of the amplitudes are shown in first and third columns and the phase shifts are shown in second and fourth columns. Fig. 9 shows the photon density at the boundary.

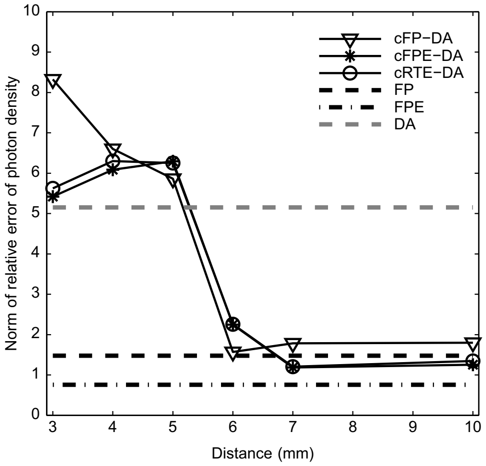

Fig. 6. Norm of the relative error of photon density against the distance between the coupling interface and the source.

As it can be seen from Fig. 8, the RTE, FP, FPE, and the coupled models give similar results. The solution of the DA differs from the solution of the other models. This is due to the low-scattering CSF regions in which the diffusion theory breaks down. The photon densities at the boundary in Fig. 9 indicate that the FPE, cFPE-DA, and cRTE-DA give the most accurate results compared with the RTE. Thus, the coupled models provide a useful approximation to the RTE with almost the same accuracy.

Table 2
The absorption coefficient μ_a, the scattering coefficient μ_s, and the scattering shape parameter g of different regions.

	μ_a (mm^{-1})	μ_s (mm^{-1})	g
Scalp	0.018	4.75	0.6
Skull	0.016	4	0.6
Grey mater	0.048	1.25	0.6
White mater	0.036	2.5	0.6
CSF around the brain	0.0048	0.16	0.8
CSF in the ventricles	0.0048	0.006	0.8

Table 1
The FE-matrix sizes, number of non-zero elements, matrix filling ratios, FE-matrix assembling times t_{mat}, relative FE-matrix assembling times, FE-matrix equation solution times t_{sol}, and relative FE-matrix equation solution times.

	Matrix size	Non-zeros	Filling ratio (%)	t_{mat} (min)	$t_{\mathrm{mat}}/t_{\mathrm{mat,RTE}}$ (%)	t_{sol} (min)	$t_{\mathrm{sol}}/t_{\mathrm{sol,RTE}}$ (%)
RTE	306,112 × 306,112	135,327,744	0.144	8.389	–	6.363	–
DA	4783 × 4783	33,039	0.144	0.060	0.72	0.001	0.02
FP	76,528 × 76,528	1,585,872	0.027	0.466	5.56	0.208	3.27
FPE	76,528 × 76,528	8,457,984	0.144	0.851	10.17	0.220	3.45
cRTE-DA	116,266 × 116,266	47,651,710	0.353	2.087	24.88	0.879	13.82
cFP-DA	31,450 × 31,450	600,180	0.061	0.209	2.50	0.039	0.61
cFPE-DA	31,450 × 31,450	3,014,852	0.305	0.278	3.32	0.045	0.70

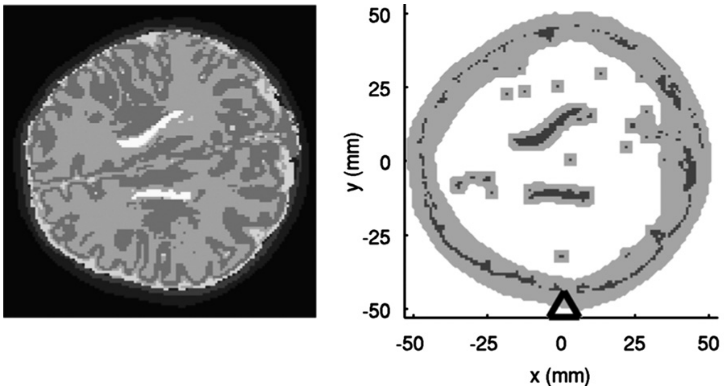

Fig. 7. Segmented image from a new-born infant's head (left image). Sub-domain division in the coupled model (right image): the CSF-regions (dark grey), the sub-domain Ω_ϕ (light grey), and the DA sub-domain Ω_Φ (white). The source location is marked with a triangle.

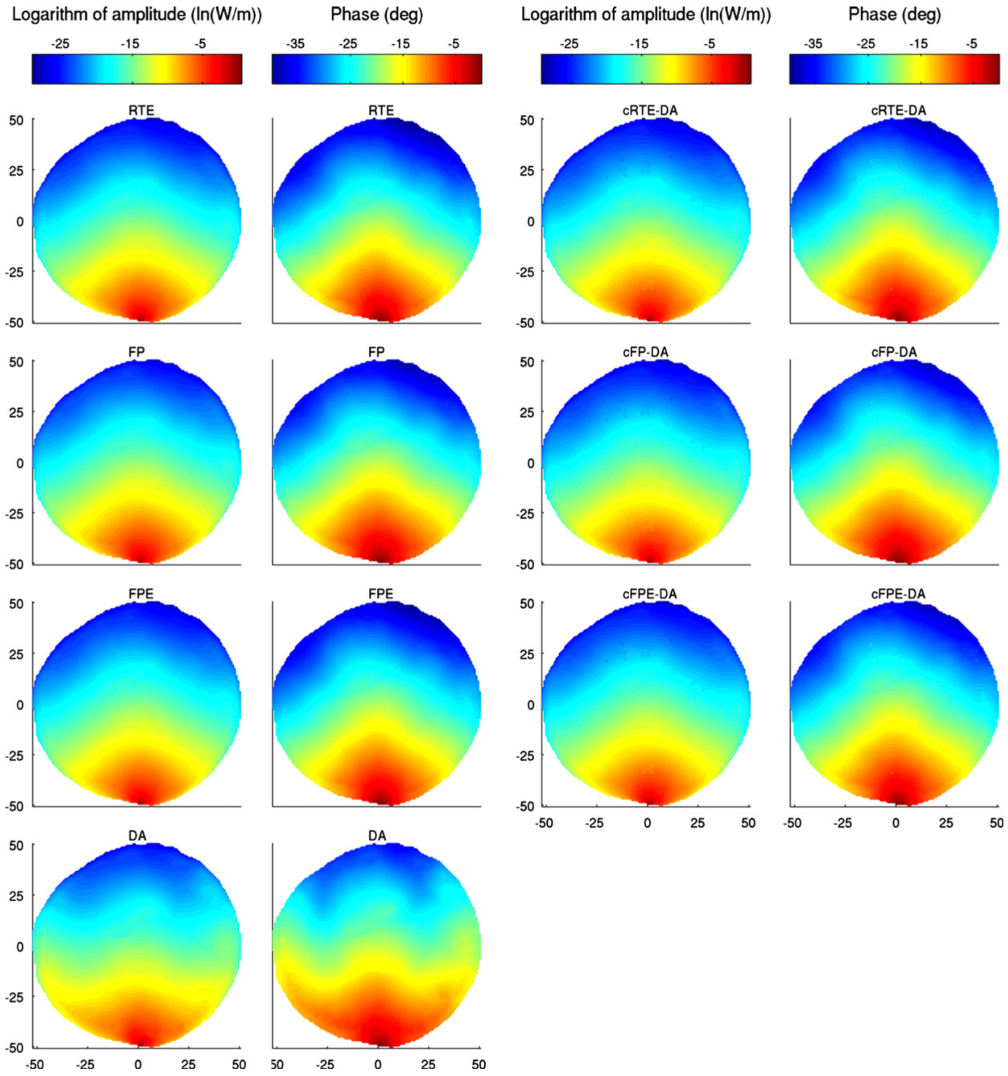

Fig. 8. Logarithm of amplitude (first and third column) and phase shift (second and fourth column) of photon density computed using the RTE, FP, FPE, and DA (first and second columns from top to bottom in respective order) and using the cRTE-DA, cFP-DA, and cFPE-DA (third and fourth columns from top to bottom in respective order) within realistic head geometry.

5. Conclusions

In this paper, the forward-peaked scattering approximations of the radiative transport equation, namely the Fokker–Planck and Fokker–Planck–Eddington equations, were used to form a coupled model with the diffusion approximation to model light propagation in medium with tissue-like optical properties. In the coupled model, the computational domain is divided into two different sub-domains . Light propagation in regions in which the DA is not valid, such as close to the source, boundaries and in low-scattering regions, is modeled using the more accurate Fokker–Planck equation or Fokker–Planck–Eddington equation. The DA is used elsewhere in the domain. The models are coupled at the interfaces of the sub-domains with boundary conditions and solved simultaneously using the finite element method.

The results of the coupled models were compared with the previously developed coupled RTE-DA model, and the solutions of the FP, FPE, DA and RTE. The effect of the coupling interface location on the solution of the coupled models was investigated as well as the computational

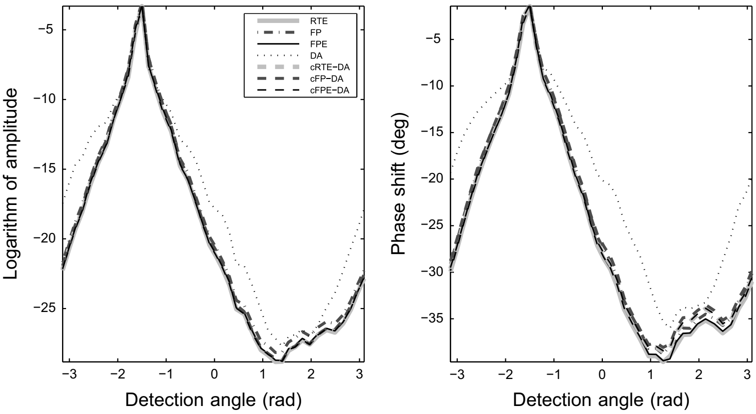

Fig. 9. Logarithm of amplitude (left) and phase shift (right) of photon density at the boundary using different models.

load. In addition, the models were tested in a realistic head geometry with tissue-like optical properties. The results show that the coupled models can be used to describe light propagation in heterogeneous tissues, also with low-scattering regions such as the cerebrospinal fluid in the brain, with almost the same accuracy as the RTE but with reduced computational load.

Acknowledgments

The authors would like to thank associate professor Arnold D. Kim and professor Simon Arridge for useful discussions. This work has been supported by the Academy of Finland (projects 136220, 140984, and 250215 Finnish Centre of Excellence in Inverse Problems Research), Finnish Doctoral Programme in Computational Sciences (FICS), Magnus Ehrnrooth foundation and by the strategic funding of the University of Eastern Finland.

References

[1] Arridge S. Optical tomography in medical imaging. Inverse Probl 1999;15:41.
[2] Gibson A, Hebden J, Arridge S. Recent advances in diffuse optical imaging. Phys Med Biol 2005;50(4):1–43.
[3] Arridge S, Schotland J. Optical tomography: forward and inverse problems. Inverse Probl 2009;25(123010):123010.
[4] Bal G. Inverse transport theory and applications. Inverse Probl 2009;25:053001. (48pp).
[5] Arridge S, Methods in diffuse optical imaging. Philos Trans R Soc A: Math Phys Eng Sci 2011;369 (195):4558–76.
[6] Wang L, Wu H. Biomedical optics: principles and imaging. Wiley-Blackwell; 2007.
[7] Ishimaru A. Wave propagation and scattering in random media. Academic, New York: IEEE Press; 1978.
[8] Hielscher A, Alcouffe R, Barbour R. Comparison of finite-difference transport and diffusion calculations for photon migration in homogeneous and heterogeneous tissues. Phys Med Biol 1998;43(5): 1285–302.
[9] Wang L, Jacques S. Hybrid model of Monte Carlo simulation and diffusion theory for light reflectance by turbid media. J Opt Soc Am A 1993;10(8):1746–52.
[10] Arridge S, Dehghani H, Schweiger M, Okada E. The finite element model for the propagation of light in scattering media: a direct method for domains with nonscattering regions. Med Phys 2000;27(1):252–64.
[11] Dehghani H, Arridge S, Schweiger M, Delpy D. Optical tomography in the presence of void regions. J Opt Soc Am A 2000;17(9): 1659–70.
[12] Hayashi T, Kashio Y, Okada E. Hybrid Monte Carlo-diffusion method for light propagation in tissue with a low-scattering region. Appl Opt 2003;42(16):2888–96.
[13] Alexandrakis G, Farrell T, Patterson M. Monte Carlo diffusion hybrid model for photon migration in a two-layer turbid medium in the frequency domain. Appl Opt 2000;39(13):2235–44.
[14] Alexandrakis G, Busch D, Faris G, Patterson M. Determination of the optical properties of two-layer turbid media by use of a frequency-domain hybrid Monte Carlo diffusion model. Appl Opt 2001;40(22): 3810–21.
[15] Bal G, Maday Y. Coupling of transport and diffusion models in linear transport theory. Math Modelling Numer Anal 2002;36(01): 69–86.
[16] Tarvainen T, Vauhkonen M, Kolehmainen V, Kaipio J. Hybrid radiative-transfer-diffusion model for optical tomography. Appl Opt 2005;44(6):876–86.
[17] Tarvainen T, Vauhkonen M, Kolehmainen V, Kaipio J. Finite element model for the coupled radiative transfer equation and diffusion approximation. Int J Numer Methods Eng 2006;65(3):383–405.
[18] Gorpas D, Yova D, Politopoulos K. A three-dimensional finite elements approach for the coupled radiative transfer equation and diffusion approximation modeling in fluorescence imaging. J Quant Spectrosc Radiat Transfer 2010;111(4):553–68.
[19] Wright S, Schweiger M, Arridge S. Reconstruction in optical tomography using the PN approximations. Meas Sci Technol 2007;18:79–86.
[20] Mohan PS, Tarvainen T, Schweiger M, Pulkkinen A, Arridge SR. Variable order spherical harmonic expansion scheme for the radiative transport equation using finite elements. J Comput Phys 2011;230(19):7364–83.
[21] Pomraning G. The Fokker–Planck operator as an asymptotic limit. Math Models Methods Appl Sci 1992;2:21–36.
[22] Leakeas C, Larsen E. Generalized Fokker–Planck approximations of particle transport with highly forward-peaked scattering. Nucl Sci Eng 2001;137(3):236–50.
[23] Kim A, Keller J. Light propagation in biological tissue. J Opt Soc Am A 2003;20(1):92–8.
[24] González-Rodríguez P, Kim A. Light propagation in tissues with forward-peaked and large-angle scattering. Appl Opt 2008;47(14): 2599–609.
[25] González-Rodríguez P, Kim A. Comparison of light scattering models for diffuse optical tomography. Opt Express 2009;17(11): 8756–74.
[26] Phillips K, Lancellotti C. On the accuracy of generalized Fokker–Planck transport equations in tissue optics. Appl Opt 2009;48(2): 229–41.
[27] Lehtikangas O, Tarvainen T, Kolehmainen V, Pulkkinen A, Arridge S, Kaipio J. Finite element approximation of the Fokker–Planck

equation for diffuse optical tomography. J Quant Spectrosc Radiat Transfer 2010;111:1406–17.

[28] Olbrant E, Frank M. Generalized Fokker–Planck theory for electron and photon transport in biological tissues: application to radiotherapy. Comput Math Methods Med 2010;11(4):313–39.

[29] Han W, Eichholz J, Wang G. On a family of differential approximations of the radiative transfer equation. J Math Chem 2011;11: 1–14.

[30] Case K, Zweifel P. Linear transport theory. USA: Addison-Wesley Educational Publishers Inc.,; 1967.

[31] Chandrasekhar S. Radiative transfer. London: Oxford University Press; 1950.

[32] Henyey L, Greenstein J. Diffuse radiation in the Galaxy. The Astrophys J 1941;93:70–83.

[33] Cheong W, Prahl S, Welch A. A review of the optical properties of biological tissues. IEEE J Quantum Electron 1990;26(12): 2166–85.

[34] Larsen E, Keller J. Asymptotic solution of neutron transport problems for small mean free paths. J Math Phys 1974;15:75–82.

[35] Habetler G, Matkowsky B. Uniform asymptotic expansions in transport theory with small mean free paths, and the diffusion approximation. J Math Phys 1975;16:846–54.

[36] Kim A. Correcting the diffusion approximation at the boundary. J Opt Soc Am A 2011;28(6):1007–15.

[37] Heino J, Somersalo E. Estimation of optical absorption in anisotropic background. Inverse Probl 2002;18:559–73.

[38] Schweiger M, Arridge S, Hiraoka M, Delpy D. The finite element method for the propagation of light in scattering media: boundary and source conditions. Med Phys 1995;22:1779.

[39] Tarvainen T, Vauhkonen M, Kolehmainen V, Arridge S, Kaipio J. Coupled radiative transfer equation and diffusion approximation model for photon migration in turbid medium with low-scattering and non-scattering regions. Phys Med Biol 2005;50(20):4913–30.

[40] Tarvainen T, Kolehmainen V, Arridge SR, Kaipio JP. Image reconstruction in diffuse optical tomography using the coupled radiative transport-diffusion model. J Quant Spectrosc Radiat Transfer 2011;112(16):2600–8.

[41] Kanschat G. A robust finite element discretization for radiative transfer problems with scattering. East West J Numer Math 1998;6: 265–72.

[42] Kim A, Moscoso M. Beam propagation in sharply peaked forward scattering media. J Opt Soc Am A 2004;21(5):797–803.

Paper **IV**

O. Lehtikangas, T. Tarvainen, A.D.
Kim, S.R. Arridge,
"Finite element approximation of
the radiative transport equation in
a medium with piece-wise
constant refractive index,"

Submitted for publication

Finite element approximation of the radiative transport equation in a medium with piece-wise constant refractive index

O. Lehtikangas[a,*], T. Tarvainen[a,b], A.D. Kim[c], S.R. Arridge[b]

[a]*Department of Applied Physics, University of Eastern Finland, P.O. Box 1627, 70211 Kuopio, Finland*
[b]*Department of Computer Science, University College London, Gower Street, London WC1E 6BT, United Kingdom*
[c]*Applied Mathematics Unit, School of Natural Sciences, University of California, Merced, California 95343, USA*

Abstract

The radiative transport equation can be used as a light transport model in a medium with scattering particles, such as biological tissues. In the radiative transport equation, the refractive index is assumed to be constant within the medium. However, in biomedical media, changes in the refractive index can occur between different tissue types. In this work, light propagation in a medium with piece-wise constant refractive index is considered. Light propagation in each sub-domain with a constant refractive index is modeled using the radiative transport equation and the equations are coupled using boundary conditions describing Fresnel reflection and refraction phenomena on the interfaces between the sub-domains. The resulting coupled system of radiative transport equations is numerically solved using a finite element method. The approach is tested with simulations. The results show that this coupled system describes light propagation accurately through comparison with the Monte Carlo method. It is also shown that neglecting the internal changes of the refractive index can lead to erroneous boundary measurements of scattered light.

Keywords:

---

[*] Corresponding author at: Department of Applied Physics, University of Eastern Finland, P.O. Box 1627, 70211 Kuopio, Finland. Tel.: +358 40 3553913; fax: +358 17 162585
Email address: `Ossi.Lehtikangas@uef.fi` (O. Lehtikangas)

Preprint submitted to Journal of Computational Physics *January 3, 2014*

Radiative transport equation, Refractive index, Finite element method

---

1. Introduction

The radiative transport equation (RTE) can be used to model propagation of particles such as neutrons and photons in a scattering medium [1–3]. Applications can be found in atmospheric and ocean optics [4], astrophysics [5], nuclear reactor physics [6] and biomedical optics [7]. In biomedical diffuse optical tomography (DOT), images of the optical properties of the target are reconstructed from measurements of near-infrared light made on the surface of the target. The image reconstruction procedure in DOT requires a model for light propagation inside the target in which the RTE can be utilized [8–11].

The RTE takes into account absorption and multiple scattering inside tissues and treats photons as particles which propagate along straight lines between scattering and absorption events. The refractive index is assumed to be a constant inside tissues. However, the refractive index can change between different tissues types inside the target even though these changes are typically neglected in DOT.

A more general version of the RTE with a spatially dependent refractive index was derived in [12], and more recently investigated in [13–21]. This model allows curved photon paths between absorption and scattering events based on the gradient field of the refractive index. Therefore, the refractive index is assumed to be a smooth continuous function such that the gradient is well defined. However, in biomedical applications the refractive index can have jumps between different tissue types, such as between skull and cerebrospinal fluid in the brain, and a smooth function may not approximate these jumps correctly.

The RTE with piecewise constant refractive index with Fresnel reflection and transmission between the regions has been considered [22–28]. The approach was developed for an one dimensional spherically symmetric case in [22, 23] and for multilayered media in [24–27]. Furthermore, an one dimensional plane parallel geometry with multilayered media was considered in [28]. In this paper, this approach is extended to general geometry. Light propagation in each sub-domain with a constant refractive index is modeled using the RTE and the equations are coupled using boundary conditions describing Fresnel reflection and transmission on the interfaces between the sub-domains. This leads to a coupled system of radiative transport equations (cRTE).

In the numerical solution of the RTE, different discretization methods have been applied for both the spatial and angular parts of the solution. For the spatial part, a finite difference method [29–31], a finite element method (FEM) [32–35] and a finite volume method [36–38] have been the most commonly applied approaches. For the angular part, a discrete ordinate method [29–31, 33, 36, 38], the FEM [34, 35, 39–41] and a spherical harmonics method (P_n) [42–45] have been utilized.

In this work, the cRTE is numerically solved using the FEM both in the space and in the angle. In the approach, the boundary conditions are formulated in a general form. Hence, the model is applicable in complex geometries represented by finite element meshes with an arbitrary number of sub-domains and inhomogeneous parameter distributions. Moreover, using the FEM for the angular part enables an accurate and simple implementation of the boundary conditions.

The rest of the paper is organized as follows. In Section 2, the RTE and the boundary conditions between piece-wise constant regions of refractive index are reviewed and the coupled system of RTEs is described. In Section 3, the numerical approximation of the coupled system of the RTEs using the FEM is described. In Section 4, simulation results are shown. Section 5 gives the conclusions.

2. Radiative transport equation with piece-wise constant refractive index

Let $\Omega \subset \mathbb{R}^d$ be the physical domain with a boundary $\partial\Omega$, and $d = 2{,}3$ be the dimension of the domain. In addition, let $\hat{\mathbf{s}} \in \mathbb{S}^{d-1}$ denote a unit vector in the direction of interest on the unit sphere $\mathbb{S}^{d-1}$. Let the refractive index n be a piece-wise constant within N disjoint sub-domains Ω_k, $k = 1, ..., N$. An interface between the sub-domains Ω_k and Ω_n with different refractive indices n_k and n_n is denoted by $\Gamma_{k,n} = \partial\Omega_k \cap \partial\Omega_n$ as shown in Figure 1. Further, the union of the interfaces of the sub-domain Ω_k can be written as $\Gamma_k = \cup_{n=1,n\neq k}^{N} \Gamma_{k,m}$. With these notations, the boundary of the sub-domain Ω_k can be divided into the outer boundary and the union of the interfaces $\partial\Omega_k = \partial\Omega_{k,\mathrm{out}} \cup \Gamma_k$. Light propagation in each sub-domain Ω_k can be modeled using the RTE and the equations are coupled using the boundary conditions at the interfaces $\Gamma_{k,n}$.

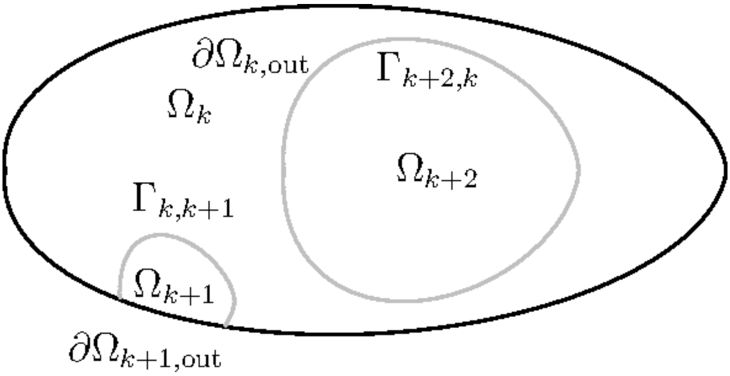

Figure 1: A sketch of sub-domains having different refractive indices. The interfaces Γ between the sub-domains are marked with gray color and the outer boundaries $\partial\Omega_{\mathrm{out}}$ with black color.

2.1. Radiative transport equation

The frequency domain version of the RTE in the sub-domain Ω_k can be written as [8]

$$\left(\frac{\mathrm{i}\omega}{c_k} + \hat{\mathbf{s}} \cdot \nabla + \mu_{\mathrm{a}}\right) \phi_k(\mathbf{r}, \hat{\mathbf{s}}) = \mu_{\mathrm{s}} \mathcal{L} \phi_k(\mathbf{r}, \hat{\mathbf{s}}) \tag{1}$$

where i is the imaginary unit, ω is the angular modulation frequency of the input signal, $c_k = c_0/n_k$ is the speed of light in the sub-domain Ω_k, c_0 is the speed of light in a vacuum, $\phi_k(\mathbf{r}, \hat{\mathbf{s}})$ is the radiance in the sub-domain Ω_k, and $\mu_{\mathrm{s}} = \mu_{\mathrm{s}}(\mathbf{r})$ and $\mu_{\mathrm{a}} = \mu_{\mathrm{a}}(\mathbf{r})$ are the scattering and absorption coefficients of the medium, respectively [1, 2]. The scattering operator $\mathcal{L}$ is

$$\mathcal{L}\phi_k(\mathbf{r}, \hat{\mathbf{s}}) = -\phi_k(\mathbf{r}, \hat{\mathbf{s}}) + \int_{\mathbb{S}^{d-1}} \Theta(\hat{\mathbf{s}} \cdot \hat{\mathbf{s}}') \phi_k(r, \hat{\mathbf{s}}') \mathrm{d}\hat{\mathbf{s}}'. \tag{2}$$

The scattering phase function $\Theta(\hat{\mathbf{s}} \cdot \hat{\mathbf{s}}')$ describes the probability for a photon with an initial direction $\hat{\mathbf{s}}'$ to scatter in a direction $\hat{\mathbf{s}}$. In this work, the Henyey-Greenstein scattering function [46] is used

$$\Theta(\hat{\mathbf{s}} \cdot \hat{\mathbf{s}}') = \frac{1}{|\mathbb{S}^{d-1}|} \frac{1 - g^2}{(1 + g^2 - 2g\hat{\mathbf{s}} \cdot \hat{\mathbf{s}}')^{d/2}}, \tag{3}$$

where $g \in [-1, 1]$ is the anisotropy parameter defining the shape of the probability distribution. In biological tissues, g is typically close to one

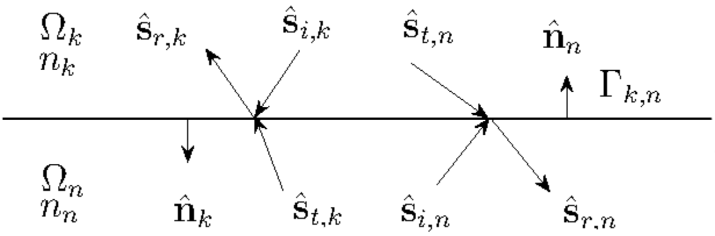

Figure 2: Interface $\Gamma_{k,n}$ between the sub-domains Ω_k and Ω_n with different refractive indices n_k and n_n. The direction of incoming radiance to the interface is denoted by $\hat{\mathbf{s}}_i$, the direction of reflected radiance by $\hat{\mathbf{s}}_r$ and the direction of radiance which transmits through the interface is denoted by $\hat{\mathbf{s}}_t$. Outward unit normal is denoted by $\hat{\mathbf{n}}$.

indicating that scattering is forward-peaked. Further, $|\mathbb{S}^{d-1}|$ is the surface measure of $\mathbb{S}^{d-1}$ ($|\mathbb{S}^1| = 2\pi$ and $|\mathbb{S}^2| = 4\pi$). The fluence is defined as an integral of the radiance over the angular directions [8]

$$\Phi_k(\mathbf{r}) = \int_{\mathbb{S}^{d-1}} \phi_k(\mathbf{r}, \hat{\mathbf{s}}) \mathrm{d}\hat{\mathbf{s}}. \tag{4}$$

2.2. Boundary conditions

The boundary condition in the sub-domain Ω_k at the interface $\Gamma_{k,n}$ in an inward direction $\hat{\mathbf{s}}_{r,k}$ takes into account the reflected radiance from a direction $\hat{\mathbf{s}}_{i,k}$ and the transmitted radiance from the sub-domain Ω_n from a direction $\hat{\mathbf{s}}_{t,k}$ as shown in Figure 2. The boundary condition can be written as

$$\phi_k(\mathbf{r}, \hat{\mathbf{s}}) = R_{k,n}\phi_k(\mathbf{r}, H_k^{-1}\hat{\mathbf{s}}) + T_{n,k}\phi_n(\mathbf{r}, K_{n,k}^{-1}(\hat{\mathbf{s}})), \quad \mathbf{r} \in \Gamma_{k,n}, \quad \hat{\mathbf{s}} \cdot \hat{\mathbf{n}}_k < 0, \tag{5}$$

where $R_{k,n} = R_{k,n}(\hat{\mathbf{s}}_{i,k}, \hat{\mathbf{n}}_k, n_k, n_k)$ is the Fresnel reflection coefficient between the sub-domain Ω_k and Ω_n

$$R_{k,n} = \frac{1}{2}\left(\frac{n_k \cos\theta_k - n_n \cos\theta_n}{n_k \cos\theta_k + n_n \cos\theta_n}\right)^2 + \frac{1}{2}\left(\frac{n_k \cos\theta_n - n_n \cos\theta_k}{n_k \cos\theta_n + n_n \cos\theta_k}\right)^2, \tag{6}$$

where

$$\cos\theta_k = \hat{\mathbf{n}}_k \cdot \hat{\mathbf{s}}_{i,k}, \tag{7}$$

$$\cos\theta_n = \sqrt{1 - \left(\frac{n_k}{n_n}\right)^2 (1 - (\cos\theta_k)^2)}. \tag{8}$$

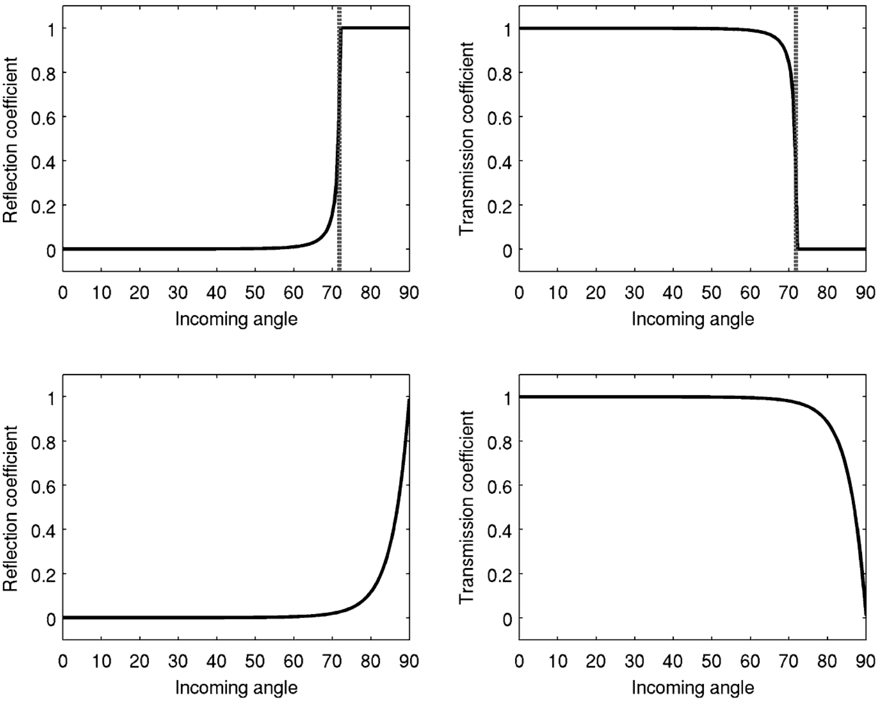

Figure 3: Fresnel reflection coefficient R (left column) and transmission coefficient T (right column) between sub-domains with refractive indices $n_1 = 1.4$ and $n_2 = 1.33$ (top row) and refractive indices $n_1 = 1.33$ and $n_2 = 1.4$ (bottom row) as a function of incoming angle. The critical angle $\theta_{\text{crit}} = \sin^{-1}(n_2/n_1)$ is marked with a gray vertical line when total internal reflection occurs.

Further, $T_{n,k}$ is the Fresnel transmission coefficient between the sub-domains Ω_n and Ω_k

$$T_{n,k} = 1 - R_{n,k}. \tag{9}$$

Figure 3 shows the Fresnel reflection coefficient R and the transmission coefficient T as a function of an incident angle.

The mapping H_k^{-1} is the inverse reflection law giving the initial direction of the radiance $\hat{\mathbf{s}}_{i,k}$ for a given direction of the reflected radiance $\hat{\mathbf{s}}_{r,k}$. The reflection law can be written in a vector form as $H_k : \hat{\mathbf{s}}_{i,k} \to \hat{\mathbf{s}}_{r,k}$

$$\hat{\mathbf{s}}_{r,k} = H_k \hat{\mathbf{s}}_{i,k}, \tag{10}$$

$$H_k = \left(\mathbf{I} - 2\hat{\mathbf{n}}_k \hat{\mathbf{n}}_k^T\right), \tag{11}$$

where $\mathbf{I}$ is an identity matrix. The inverse reflection law H_k^{-1} can be computed

$$\hat{\mathbf{s}}_{i,k} = H_k^{-1} \hat{\mathbf{s}}_{r,k} = H_k \hat{\mathbf{s}}_{r,k}, \tag{12}$$

since the matrix H_k is a Householder transformation and thus $H_k^{-1} = H_k$.

The mapping $K_{n,k}^{-1}$ is the inverse Snell's law giving the direction $\hat{\mathbf{s}}_{t,k}$ from which the radiance is transmitted from the sub-domain Ω_n into the sub-domain Ω_k for a given direction $\hat{\mathbf{s}}_{r,k}$. The Snell's law for the refraction of the radiance between the sub-domain Ω_n and Ω_k can be written in a vector form $K_{n,k} : (\hat{\mathbf{s}}_{\mathrm{t,k}}, \hat{\mathbf{n}}_n, n_n, n_k) \to \hat{\mathbf{s}}_{r,k}$

$$\hat{\mathbf{s}}_{r,k} = \frac{n_n}{n_k} \hat{\mathbf{s}}_{t,k} + \left(\cos\varphi_k - \frac{n_n}{n_k} \cos\varphi_n\right) \hat{\mathbf{n}}_n, \tag{13}$$

where

$$\cos\varphi_n = \hat{\mathbf{n}}_n \cdot \hat{\mathbf{s}}_{t,k}, \tag{14}$$

$$\cos\varphi_k = \sqrt{1 - \left(\frac{n_n}{n_k}\right)^2 (1 - (\cos\varphi_n)^2)}. \tag{15}$$

The inverse Snell's law $K_{n,k}^{-1} : (\hat{\mathbf{s}}_{r,k}, \hat{\mathbf{n}}_n, n_n, n_k) \to \hat{\mathbf{s}}_{t,k}$ can be computed as $K_{n,k} : (-\hat{\mathbf{s}}_{r,k}, -\hat{\mathbf{n}}_n, n_k, n_n) \to -\hat{\mathbf{s}}_{t,k}$ due to the reciprocity principle of light propagation.

The boundary condition for the outer boundary in the sub-domain Ω_k takes into account a boundary source $\phi_{0,k}(\mathbf{r}, \hat{\mathbf{s}})$ and the reflection of the radiance due to a mismatch in refractive indices at the outer boundary

$$\phi_k(\mathbf{r}, \hat{\mathbf{s}}) = \phi_{0,k}(\mathbf{r}, \hat{\mathbf{s}}) + R_{k,\mathrm{out}} \phi_k(\mathbf{r}, H_k \hat{\mathbf{s}}), \quad \mathbf{r} \in \partial\Omega_{k,\mathrm{out}}, \quad \hat{\mathbf{s}} \cdot \hat{\mathbf{n}}_k < 0, \tag{16}$$

where $R_{k,\mathrm{out}} = R_{k,\mathrm{out}}(\hat{\mathbf{s}}_{i,k}, \hat{\mathbf{n}}_k, n_k, n_{\mathrm{out}})$ is the reflection coefficient between the sub-domain Ω_k and the exterior of the domain Ω with the refractive index n_{out}.

2.3. Coupled system of radiative transport equations

The coupled system of RTEs for N sub-domains with different refractive indices can be written as

$$\left(\frac{\mathrm{i}\omega}{c_k} + \hat{\mathbf{s}} \cdot \nabla + \mu_\mathrm{a}\right) \phi_k(\mathbf{r}, \hat{\mathbf{s}}) = \mu_\mathrm{s} \mathcal{L} \phi_k(\mathbf{r}, \hat{\mathbf{s}}), \quad \mathbf{r} \in \Omega_k \tag{17a}$$

$$\phi_k(\mathbf{r}, \hat{\mathbf{s}}) = \phi_{0,k}(\mathbf{r}, \hat{\mathbf{s}}) + R_{k,\mathrm{out}} \phi_k(\mathbf{r}, H_k \hat{\mathbf{s}}), \quad \mathbf{r} \in \partial\Omega_{k,\mathrm{out}}, \quad \hat{\mathbf{s}} \cdot \hat{\mathbf{n}}_k, < 0, \tag{17b}$$

$$\phi_k(\mathbf{r}, \hat{\mathbf{s}}) = R_{k,n} \phi_k(\mathbf{r}, H_k \hat{\mathbf{s}}) + T_{n,k} \phi_n(\mathbf{r}, K_{n,k}^{-1}(\hat{\mathbf{s}})), \quad \mathbf{r} \in \Gamma_{k,n}, \quad \hat{\mathbf{s}} \cdot \hat{\mathbf{n}}_k < 0, \tag{17c}$$

$$n, k = 1, \ldots, N.$$

3. Finite element approximation of the coupled system

In this work, the solution of the cRTE (17) is numerically approximated using the FEM. In the FEM, a variational formulation of the original problem is derived, and then this infinite dimensional problem is discretized using a suitable set of basis functions.

To derive the variational formulation of the coupled system, we follow a similar procedure as in [34, 47–50]. Thus, first each of the equations in (17a) are multiplied by a test function v_k and integrated over the domain $\Omega_k \times \mathbb{S}^{d-1}$. Then, by using the Green's theorem [51], separating the resulting boundary integrals over the outer boundary $\partial\Omega_{k,\mathrm{out}}$ and over the interfaces $\Gamma_{k,n}$, and utilizing the boundary conditions (17b) and (17c), the variational formulation is obtained. The variational formulation of the cRTE (17) with a streamline diffusion modification [32, 48, 52] can be written as

$$
\begin{aligned}
&\sum_{k=1}^{N}\Big(\int_{\Omega_k}\int_{\mathbb{S}^{d-1}}\frac{\mathrm{i}\omega}{c_k}\phi_k(\mathbf{r},\hat{\mathbf{s}})v_k(\mathbf{r},\hat{\mathbf{s}})\mathrm{d}\hat{\mathbf{s}}\mathrm{d}\mathbf{r}-\int_{\Omega_k}\int_{\mathbb{S}^{d-1}}\hat{\mathbf{s}}\cdot\nabla v_k(\mathbf{r},\hat{\mathbf{s}})\phi_k(\mathbf{r},\hat{\mathbf{s}})\mathrm{d}\hat{\mathbf{s}}\mathrm{d}\mathbf{r}\\
&+\int_{\partial\Omega_k}\int_{\mathbb{S}^{d-1}}(\hat{\mathbf{s}}\cdot\hat{\mathbf{n}}_k)_+\phi_k(\mathbf{r},\hat{\mathbf{s}})v_k(\mathbf{r},\hat{\mathbf{s}})\mathrm{d}\hat{\mathbf{s}}\mathrm{d}S-\int_{\partial\Omega_{k,\mathrm{out}}}\int_{\mathbb{S}^{d-1}}(\hat{\mathbf{s}}\cdot\hat{\mathbf{n}}_k)_-R_{k,\mathrm{out}}\phi_k(\mathbf{r},H_k\hat{\mathbf{s}})v_k(\mathbf{r},\hat{\mathbf{s}})\mathrm{d}\hat{\mathbf{s}}\mathrm{d}S\\
&-\sum_{n=1,n\neq k}^{N}\int_{\Gamma_{k,n}}\int_{\mathbb{S}^{d-1}}(\hat{\mathbf{s}}\cdot\hat{\mathbf{n}}_k)_-R_{k,n}\phi_k(\mathbf{r},H_k\hat{\mathbf{s}})v_k(\mathbf{r},\hat{\mathbf{s}})\mathrm{d}\hat{\mathbf{s}}\mathrm{d}S\\
&-\sum_{n=1,n\neq k}^{N}\int_{\Gamma_{k,n}}\int_{\mathbb{S}^{d-1}}(\hat{\mathbf{s}}\cdot\hat{\mathbf{n}}_k)_-T_{n,k}\phi_n(\mathbf{r},K_{n,k}^{-1}(\hat{\mathbf{s}}))v_k(\mathbf{r},\hat{\mathbf{s}})\mathrm{d}\hat{\mathbf{s}}\mathrm{d}S+\int_{\Omega_k}\int_{\mathbb{S}^{d-1}}\mu_{\mathrm{a}}\phi_k(\mathbf{r},\hat{\mathbf{s}})v_k(\mathbf{r},\hat{\mathbf{s}})\mathrm{d}\hat{\mathbf{s}}\mathrm{d}\mathbf{r}\\
&-\int_{\Omega_k}\int_{\mathbb{S}^{d-1}}\mathcal{L}\phi_k(\mathbf{r},\hat{\mathbf{s}})v_k(\mathbf{r},\hat{\mathbf{s}})\mathrm{d}\hat{\mathbf{s}}\mathrm{d}\mathbf{r}+\int_{\Omega_k}\int_{\mathbb{S}^{d-1}}\delta\frac{\mathrm{i}\omega}{c}\phi_k(\mathbf{r},\hat{\mathbf{s}})\hat{\mathbf{s}}\cdot\nabla v_k(\mathbf{r},\hat{\mathbf{s}})\mathrm{d}\hat{\mathbf{s}}\mathrm{d}\mathbf{r}\\
&+\int_{\Omega_k}\int_{\mathbb{S}^{d-1}}\delta(\hat{\mathbf{s}}\cdot\nabla\phi_k(\mathbf{r},\hat{\mathbf{s}}))(\hat{\mathbf{s}}\cdot\nabla v_k(\mathbf{r},\hat{\mathbf{s}}))\mathrm{d}\hat{\mathbf{s}}\mathrm{d}\mathbf{r}+\int_{\Omega_k}\int_{\mathbb{S}^{d-1}}\delta\mu_{\mathrm{a}}\phi_k(\mathbf{r},\hat{\mathbf{s}})v_k(\mathbf{r},\hat{\mathbf{s}})\mathrm{d}\hat{\mathbf{s}}\mathrm{d}\mathbf{r}\\
&-\int_{\Omega_k}\delta\int_{\mathbb{S}^{d-1}}\mathcal{L}\phi_k(\mathbf{r},\hat{\mathbf{s}})(\hat{\mathbf{s}}\cdot\nabla v_k(\mathbf{r},\hat{\mathbf{s}}))\mathrm{d}\hat{\mathbf{s}}\mathrm{d}\mathbf{r}-\int_{\partial\Omega_{k,\mathrm{out}}}\int_{\mathbb{S}^{d-1}}(\hat{\mathbf{s}}\cdot\hat{\mathbf{n}}_k)_-\phi_{0,k}(\mathbf{r},\hat{\mathbf{s}})v_k(\mathbf{r},\hat{\mathbf{s}})\mathrm{d}\hat{\mathbf{s}}\mathrm{d}S\Big)=0
\end{aligned}
\tag{18}
$$

where δ is a streamline-diffusion modification parameter and $(\hat{\mathbf{s}}\cdot\hat{\mathbf{n}}_k)_+$ and $(\hat{\mathbf{s}}\cdot\hat{\mathbf{n}}_k)_-$ denote the positive and negative parts of the function $(\hat{\mathbf{s}}\cdot\hat{\mathbf{n}}_k)$.

The FE-approximation is obtained by approximating the solutions $\phi_k(\mathbf{r},\hat{\mathbf{s}})$ of the variational formulation (18) with a linear combination of the basis functions

$$\phi_k(\mathbf{r},\hat{\mathbf{s}})\approx\sum_{i=1}^{N_{s,k}}\sum_{l=1}^{N_{a,k}}\alpha_{il}^{k}\psi_{i,k}(\mathbf{r})\psi_{l,k}(\hat{\mathbf{s}}),\tag{19}$$

where $\psi_{i,k}(\mathbf{r})$ and $\psi_{l,k}(\hat{\mathbf{s}})$ are the nodal basis functions of the spatial and angular discretizations of $\Omega_k\times\mathbb{S}^{d-1}$, α_{il}^{k} is the radiance in spatial nodal point i into angular direction l in the sub-domain Ω_k, and $N_{s,k}$ and $N_{a,k}$ are the number of spatial and angular nodes in the sub-domain Ω_k, respectively. Therefore, different number of angular directions can be used in different sub-domains if that is feasible. In this work, we use a piecewise linear basis for both spatial and angular parts of the solution. The FE-approximation of the coupled model can be written in a matrix form as

$$\begin{pmatrix} A_1 & C_{1,2} & \cdots & \cdots & C_{1,N} \\ C_{2,1} & A_2 & \ddots & \ddots & \vdots \\ \vdots & \ddots & \ddots & \ddots & \vdots \\ C_{N-1,1} & \ddots & \ddots & A_{N-1} & C_{N-1,N} \\ C_{N,1} & \cdots & \cdots & C_{N,N-1} & A_N \end{pmatrix} \begin{pmatrix} \alpha_1 \\ \vdots \\ \alpha_N \end{pmatrix} = \begin{pmatrix} b_1 \\ \vdots \\ b_N \end{pmatrix}, \qquad (20)$$

where the vector of radiances in the different sub-domains is $\alpha = (\alpha_1, \ldots, \alpha_N) = (\alpha^1_{1,1}, ..., \alpha^1_{1,N_{a,1}}, ..., \alpha^1_{N_{s,1},N_{a,1}}, ..., \alpha^N_{N_{s,N},N_{a,N}})^T \in \mathbb{C}^{\sum_{k=1}^N N_{s,k}N_{a,k}}$. The matrix $A_k \in \mathbb{C}^{N_{s,k}N_{a,k} \times N_{s,k}N_{a,k}}$ contains the FE-approximation of the RTE in the sub-domain Ω_k

$$A_k = A_{0,k} + A_{1,k} + A_{2,k} + A_{3,k} + A_{4,k}, \qquad (21)$$

where

$$\begin{aligned}A_{0,k}(h,s) =&\frac{\mathrm{i}\omega}{c_k}\left(\int_{\Omega_k}\psi_i(\mathbf{r})\psi_j(\mathbf{r})\mathrm{d}r\int_{\mathbb{S}^{d-1}}\psi_l(\hat{\mathbf{s}})\psi_m(\hat{\mathbf{s}})\mathrm{d}\hat{\mathbf{s}}\right.\\ &\left.+\int_{\Omega_k}\delta\int_{\mathbb{S}^{d-1}}\hat{\mathbf{s}}\cdot\nabla\psi_j(\mathbf{r})\psi_m(\hat{\mathbf{s}})\psi_l(\hat{\mathbf{s}})\mathrm{d}\hat{\mathbf{s}}\psi_i(\mathbf{r})\mathrm{d}\mathbf{r}\right),\end{aligned}\tag{22a}$$

$$\begin{aligned}A_{1,k}(h,s) =&-\int_{\Omega_k}\int_{\mathbb{S}^{d-1}}\hat{\mathbf{s}}\cdot\nabla\psi_j(\mathbf{r})\psi_m(\hat{\mathbf{s}})\psi_l(\hat{\mathbf{s}})\mathrm{d}\hat{\mathbf{s}}\psi_i(\mathbf{r})\mathrm{d}\mathbf{r}\\ &+\int_{\Omega_k}\delta\int_{\mathbb{S}^{d-1}}(\hat{\mathbf{s}}\cdot\nabla\psi_i(\mathbf{r}))(\hat{\mathbf{s}}\cdot\nabla\psi_j(\mathbf{r}))\psi_l(\hat{\mathbf{s}})\psi_m(\hat{\mathbf{s}})\mathrm{d}\hat{\mathbf{s}}\mathrm{d}\mathbf{r},\end{aligned}\tag{22b}$$

$$\begin{aligned}A_{2,k}(h,s) =&\int_{\partial\Omega_k}\psi_i(\mathbf{r})\psi_j(\mathbf{r})\mathrm{d}S\int_{\mathbb{S}^{d-1}}(\hat{\mathbf{s}}\cdot\hat{\mathbf{n}}_k)_+\psi_l(\hat{\mathbf{s}})\psi_m(\hat{\mathbf{s}})\mathrm{d}\hat{\mathbf{s}}\\ &-\int_{\partial\Omega_{k,\mathrm{out}}}\psi_i(\mathbf{r})\psi_j(\mathbf{r})\mathrm{d}S\int_{\mathbb{S}^{d-1}}(\hat{\mathbf{s}}\cdot\hat{\mathbf{n}}_k)_-R_{k,\mathrm{out}}\psi_l(H\hat{\mathbf{s}})\psi_m(\hat{\mathbf{s}})\mathrm{d}\hat{\mathbf{s}}\\ &-\int_{\Gamma_{k,n}}\psi_i(\mathbf{r})\psi_j(\mathbf{r})\mathrm{d}S\int_{\mathbb{S}^{d-1}}(\hat{\mathbf{s}}\cdot\hat{\mathbf{n}}_k)_-R_{k,n}\psi_l(H\hat{\mathbf{s}})\psi_m(\hat{\mathbf{s}})\mathrm{d}\hat{\mathbf{s}},\end{aligned}\tag{22c}$$

$$\begin{aligned}A_{3,k}(h,s) =&\int_{\Omega_k}\mu_\mathrm{a}\psi_i(\mathbf{r})\psi_j(\mathbf{r})\mathrm{d}\mathbf{r}\int_{\mathbb{S}^{d-1}}\psi_l(\hat{\mathbf{s}})\psi_m(\hat{\mathbf{s}})\mathrm{d}\hat{\mathbf{s}}\\ &+\int_{\Omega_k}\delta\mu_\mathrm{a}\psi_i(\mathbf{r})\int_{\mathbb{S}^{d-1}}(\hat{\mathbf{s}}\cdot\nabla\psi_j(\mathbf{r}))\psi_m(\hat{\mathbf{s}})\psi_l(\hat{\mathbf{s}})\mathrm{d}\hat{\mathbf{s}}\mathrm{d}\mathbf{r},\end{aligned}\tag{22d}$$

$$\begin{aligned}A_{4,k}(h,s) =&\int_{\Omega_k}\mu_\mathrm{s}\psi_i(\mathbf{r})\psi_j(\mathbf{r})\mathrm{d}\mathbf{r}\int_{\mathbb{S}^{d-1}}\psi_l(\hat{\mathbf{s}})\psi_m(\hat{\mathbf{s}})\mathrm{d}\hat{\mathbf{s}}\\ &+\int_{\Omega_k}\delta\mu_\mathrm{s}\psi_i(\mathbf{r})\int_{\mathbb{S}^{d-1}}(\hat{\mathbf{s}}\cdot\nabla\psi_j(\mathbf{r}))\psi_m(\hat{\mathbf{s}})\psi_l(\hat{\mathbf{s}})\mathrm{d}\hat{\mathbf{s}}\mathrm{d}\mathbf{r}\\ &-\int_{\Omega_k}\mu_\mathrm{s}\psi_i(\mathbf{r})\psi_j(\mathbf{r})\mathrm{d}\mathbf{r}\int_{\mathbb{S}^{d-1}}\int_{\mathbb{S}^{d-1}}\Theta(\hat{\mathbf{s}}\cdot\hat{\mathbf{s}}')\psi_l(\hat{\mathbf{s}}')\mathrm{d}\hat{\mathbf{s}}'\psi_m(\hat{\mathbf{s}})\mathrm{d}\hat{\mathbf{s}}\\ &-\int_{\Omega_k}\delta\mu_\mathrm{s}\int_{\mathbb{S}^{d-1}}(\hat{\mathbf{s}}\cdot\nabla\psi_j(\mathbf{r}))\psi_m(\hat{\mathbf{s}})\int_{\mathbb{S}^{d-1}}\Theta(\hat{\mathbf{s}}\cdot\hat{\mathbf{s}}')\psi_l(\hat{\mathbf{s}}')\mathrm{d}\hat{\mathbf{s}}'\mathrm{d}\hat{\mathbf{s}}\psi_i(\mathbf{r})\mathrm{d}\mathbf{r},\end{aligned}\tag{22e}$$

where $h = N_{a,k}(j-1)+m$, $s = N_{a,k}(i-1)+l$ ($j,i = 1,\ldots,N_{s,k}$, $m,l = 1,\ldots,N_{a,k}$, and $h,s = 1,\ldots,N_{s,k}N_{a,k}$). Further, the matrix $C_{n,k}\in\mathbb{R}^{N_{s,n}N_{a,n}\times N_{s,k}N_{a,k}}$ contains the coupling conditions on the interface $\Gamma_{k,n}$ due to the radiance transmitted from the sub-domain Ω_n into the sub-domain Ω_k. Note that the matrix $C_{n,k}$ is non-zero only if Ω_n and Ω_k share an interface $\Gamma_{k,n}$. The matrix

$C_{n,k}$ can be written as

$$C_{n,k}(p,s) = -\int_{\Gamma_{k,n}} \psi_i(\mathbf{r})\psi_e(\mathbf{r})\mathrm{d}S \int_{\mathbb{S}^{d-1}} (\hat{\mathbf{s}}\cdot\hat{\mathbf{n}}_k)_- T_{n,k}\psi_l(K_{n,k}^{-1}(\hat{\mathbf{s}}))\psi_u(\hat{\mathbf{s}})\mathrm{d}\hat{\mathbf{s}}, \quad (23)$$

where $p = N_{a,n}(e-1)+u$, $(e = 1,\ldots,N_{s,n},\ u = 1,\ldots,N_{a,n}$, and $p = 1,\ldots,N_{s,n}N_{a,n})$. The source vector in the sub-domain Ω_k is

$$b_k(h) = \int_{\partial\Omega_{k,\mathrm{out}}} \psi_j(\mathbf{r})\mathrm{d}S \int_{\mathbb{S}^{d-1}} (\hat{\mathbf{s}}\cdot\hat{\mathbf{n}}_k)_- \phi_{0,k}(\mathbf{r},\hat{\mathbf{s}})\psi_m(\hat{\mathbf{s}})\mathrm{d}\hat{\mathbf{s}}. \quad (24)$$

4. Results

The performance of the proposed cRTE model was tested with 2D simulations. The solution of the cRTE was compared with the solution of the Monte Carlo (MC) simulation. In the MC simulations, a photon packet method, originally developed in [53] was modified to allow computation in complex inhomogeneous geometries represented by finite element meshes with piecewise constant refractive indices [54].

The cRTE was solved using the FEM as described in Section 3. The FE-approximation was computed using Eq. (20). The quantity of interest was the fluence, Eq. (4), inside the domain and at the boundary.

4.1. Reflection from an oblique surface with mismatched refractive indices

First, a reflection from an oblique surface due to a mismatch in the refractive indices was investigated. The simulation domain Ω was a square $[-20,20]\times[-20,20]$ mm^2 shown in Figure 4. The domain was divided into two sub-domains with different refractive indices. The FE-mesh for the spatial discretization of the sub-domain Ω_1 is marked with dark grey and the sub-domain Ω_2 is marked with light grey in Figure 4. The FE-meshes consisted of 1710 and 1091 nodes and 3261 and 2043 triangular elements for the sub-domains Ω_1 and Ω_2, respectively. The angular domain $\mathbb{S}^1$ was discretized using 64 equally spaced angular directions for the both sub-domains.

The scattering and absorption properties of the domain were: $\mu_{\mathrm{s},1} = 0.1$ mm^{-1}, $\mu_{\mathrm{s},2} = 0.1$ mm^{-1}, $\mu_{\mathrm{a},1} = 0.01$ mm^{-1}, $\mu_{\mathrm{a},2} = 0.01$ mm^{-1}, $g_1 = 0.8$ and $g_2 = 0.8$. These values correspond to a low-scattering medium with a forward-peaked scattering. Hence, the reflection from a surface with mismatched refractive indices should be clearly visible. The refractive index of the sub-domain Ω_1 was $n_1 = 2$ and the refractive index of the sub-domain Ω_2 was given values

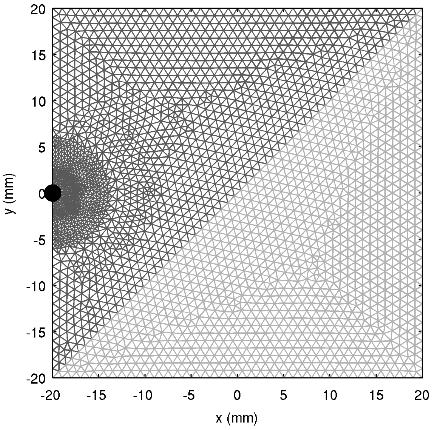

Figure 4: Mesh for the domain with an oblique surface between the sub-domains with different refractive indices. The sub-domain Ω_1 is marked with dark grey and the sub-domain Ω_2 with light grey. The source is marked with a black circle.

$n_2 = 1, 1.3, 1.6, 1.8$. The refractive index of the exterior of the domain Ω was $n_{\text{out}} = 1$. The modulation frequency of the input signal was 100 MHz. A collimated source with a narrow gaussian angular dependence was located at $(x, y) = (-20, 0)$ mm and it is marked with a black circle in Figure 4.

The fluence computed using the cRTE and the MC is shown in Figure 5. As it can be seen, when $n_2 = 1$, most of the light reflects from the surface due a large mismatch in the refractive indices. In this case the critical angle is $\theta_{\text{crit}} = \sin^{-1}(n_2/n_1) = 30$ deg (with respect to the unit normal). This means that only the photons which hit the interface almost perpendicularly can transmit through the interface. Thus, in this case when the medium is low-scattering, most of the photons from the collimated source retain their initial direction before hitting the interface at 45 deg angle and undergo total internal reflection. When the refractive index of the second sub-domain is increased, more light transmits through the surface with a refraction.

When the cRTE and the MC solutions are compared, a good agreement is obtained except close to the source due to different discretization approaches. In the MC, the solution and the source are element-wise constant whereas in the FEM piece-wise linear basis is used. This difference is distinguishable since the medium is small and low-scattering.

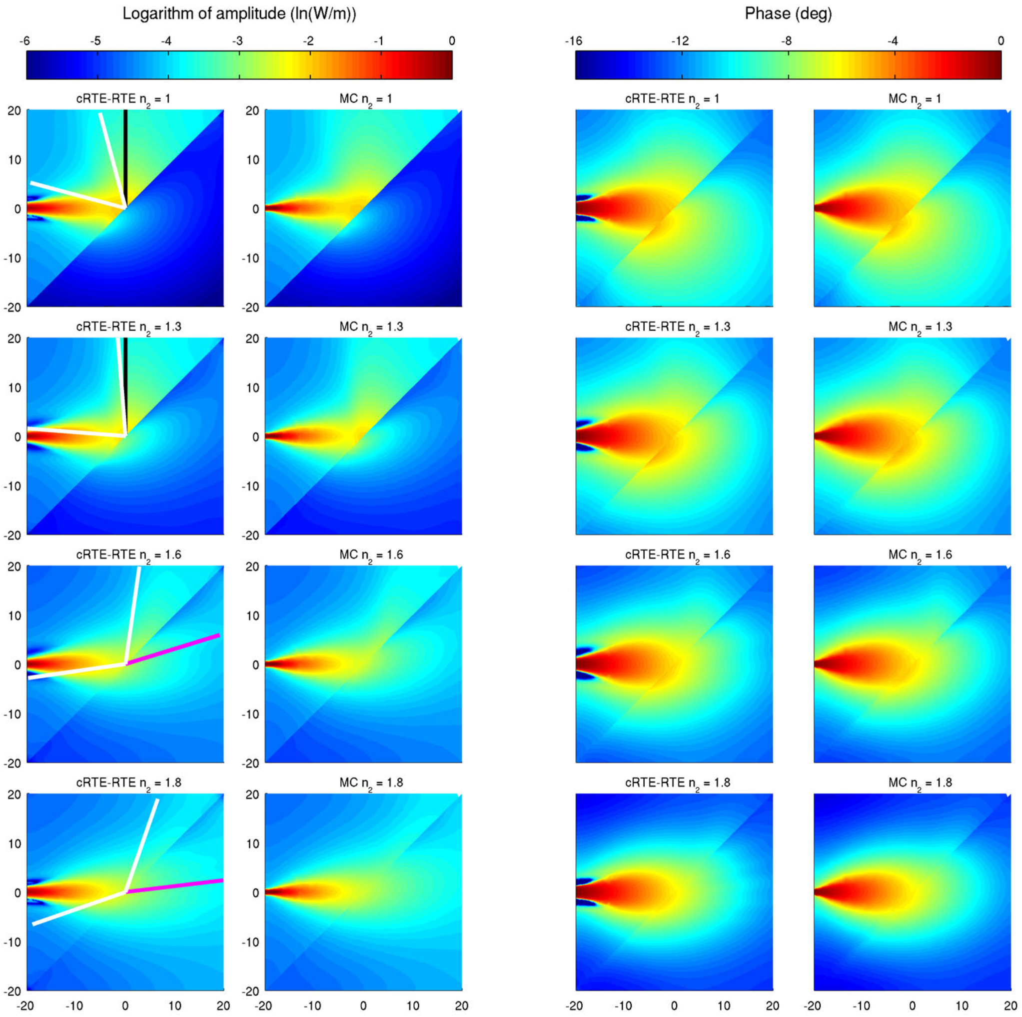

Figure 5: Logarithm of the amplitude (first and second column) and the phase shift (third and fourth column) of the fluence computed using the cRTE model (first and third column) and using the MC (second and fourth column) due to reflection from the oblique surface. Refractive index of the second sub-domain is $n_2 = 1$ (first row), $n_2 = 1.3$ (second row), $n_2 = 1.6$ (third row) and $n_2 = 1.8$ (fourth row). Directions of reflected and transmitted light with incoming angle of 45 deg are marked with black and purple lines, respectively, and the critical angle is marked with a white line.

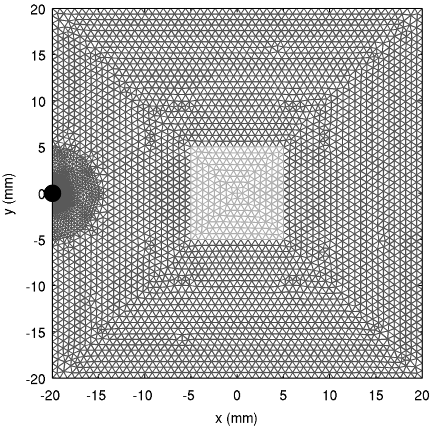

Figure 6: Mesh for the domain with a square inclusion inside the target. The sub-domain Ω_1 is marked with dark grey and the sub-domain Ω_2 with light grey. The source is marked with a black circle.

4.2. Effect of the internal refractive index change on the boundary measurements

Next, the effect of the internal refractive index change on the boundary measurements was investigated. Two different cases were considered. In the first case, the inclusion with different refractive indices was located deep inside the target and in the second case the inclusion was located close to the boundary of the target.

4.2.1. Inclusion inside the target

First, the inclusion was located inside the target as shown in Figure 6. The FE-mesh for the spatial discretization of the sub-domain Ω_1 is marked with dark grey and the sub-domain Ω_2 is marked with light grey. The FE-meshes consisted of 3476 and 1051 nodes and 6398 and 1179 triangular elements for the sub-domains Ω_1 and Ω_2, respectively. The angular domain $\mathbb{S}^1$ was discretized using 64 equally spaced angular directions.

The scattering and absorption properties were: $\mu_{\mathrm{s},1} = 1\ \mathrm{mm}^{-1}$, $\mu_{\mathrm{s},2} = 1\ \mathrm{mm}^{-1}$, $\mu_{\mathrm{a},1} = 0.01\ \mathrm{mm}^{-1}$, $\mu_{\mathrm{a},2} = 0.01\ \mathrm{mm}^{-1}$, $g_1 = 0.8$ and $g_2 = 0.8$. The refractive index of the sub-domain Ω_1 was $n_1 = 1.4$ and the refractive index of the sub-domain Ω_2 was $n_2 = 1, 1.05, ..., 2$. The refractive index of the exterior was $n_{\mathrm{out}} = 1$.

The fluences computed using the cRTE and the MC are shown in Figure

7. In addition, per cent relative error of the fluence computed using the cRTE against the MC is shown. Figure 8 shows the fluence at the boundary computed using the cRTE for $n_2 = 1$ (grey line), $n_2 = 1.4$ (black line) and $n_2 = 2$ (dashed line) as a function of distance along the boundary. In addition, per cent relative difference against the case with $n_2 = 1.4$ (matched refractive indices) is shown. The mean of the relative difference of the boundary measurements against the case with $n_2 = 1.4$ was computed for the amplitude and for the phase as

$$\Delta_{|\Phi|} = \text{mean}\left(\left|\frac{|\Phi(\mathbf{r})| - |\Phi_{\text{ref}}(\mathbf{r})|}{|\Phi_{\text{ref}}(\mathbf{r})|}\right|\right), \tag{25}$$

$$\Delta_{\arg(\Phi)} = \text{mean}\left(\left|\frac{\arg(\Phi(\mathbf{r})) - \arg(\Phi_{\text{ref}}(\mathbf{r}))}{\arg(\Phi_{\text{ref}}(\mathbf{r}))}\right|\right), \tag{26}$$

where $\Phi_{\text{ref}}(\mathbf{r})$ is the solution with $n_2 = 1.4$, $|\cdot|$ is the absolute value and $\arg(\cdot)$ is the phase angle. This quantity is shown in Figure 9 for the amplitude (left image) and for the phase (right image).

The results in Figure 7 show that when the refractive index of the inclusion is lower ($n_2 = 1$) than the refractive index of the background ($n_1 = 1.4$) strong reflection occurs when light enters the inclusion. In contrast, when the refractive index is larger ($n_2 = 2$) than that of the background, more light is transmitted into the inclusion and total internal reflection takes place when light exits the inclusion. When the cRTE and the MC solutions are compared, a very good agreement is found and the relative error is under three per cent for both the amplitude and the phase further from the source.

The results show that the fluence at the boundary is changed when the refractive index is not constant within the target. When the refractive index of the inclusion is lower ($n_2 = 1$) than that of the background, larger values for the amplitude can be measured next to the source due to the reflection from the inclusion. At the opposite side of the target, the amplitude is up to 10 % lower compared to the fluence without the inclusion. For the phase, smaller values can be measured next to the source since photons can arrive earlier to the boundary due to the possible reflection. If the refractive index is larger ($n_2 = 2$) than that of the background, the amplitude is one to four per cent lower compared to the fluence obtained without the inclusion. For the phase, up to 8 % larger values are obtained since photons can arrive later to the boundary due to the internal reflection inside the inclusion.

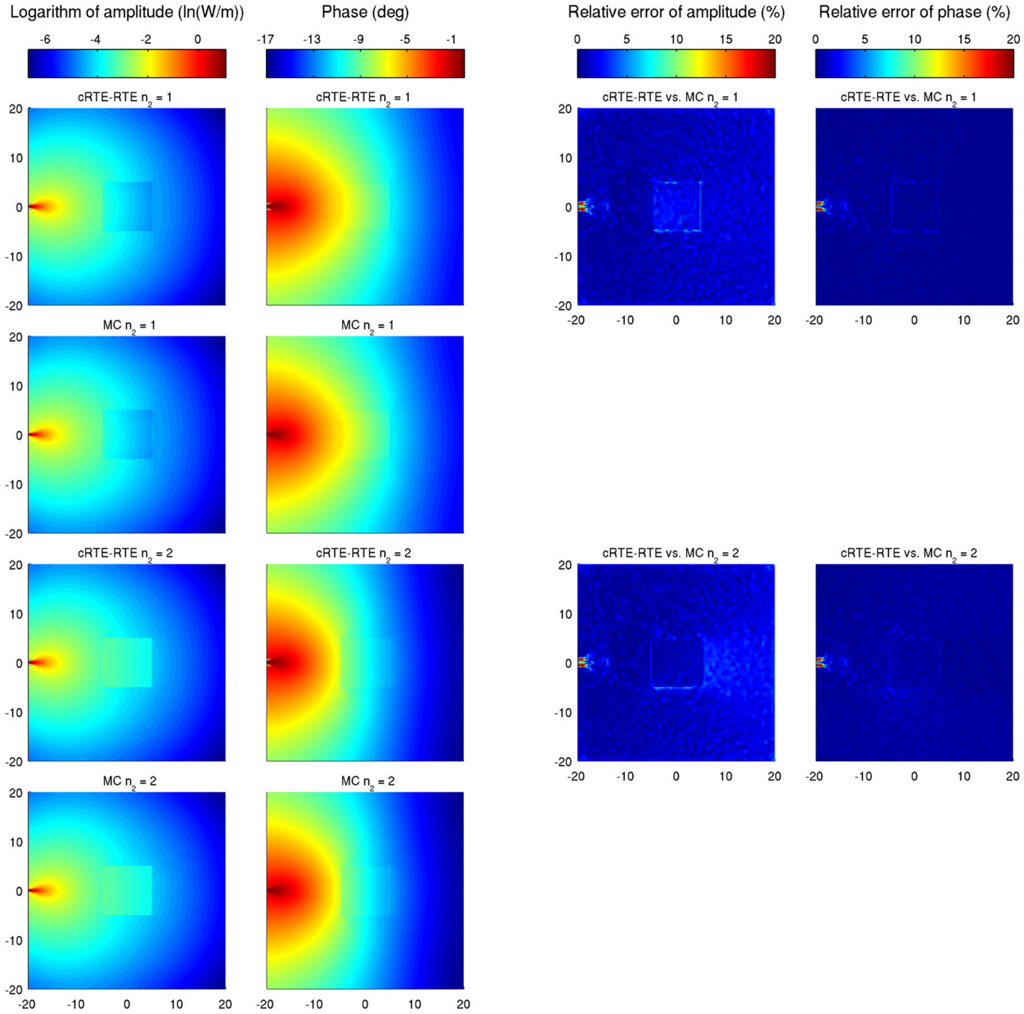

Figure 7: Logarithm of the amplitude (first column) and the phase shift (second column) of the fluence computed using the cRTE model (first and third row) and using the MC (second and fourth row) due to reflection from the square inclusion inside the target. Refractive index of the inclusion is $n_2 = 1$ (first and second row) and $n_2 = 2$ (third and fourth row). Per cent relative error of the amplitude and the phase shift against the MC are shown in third and fourth columns.

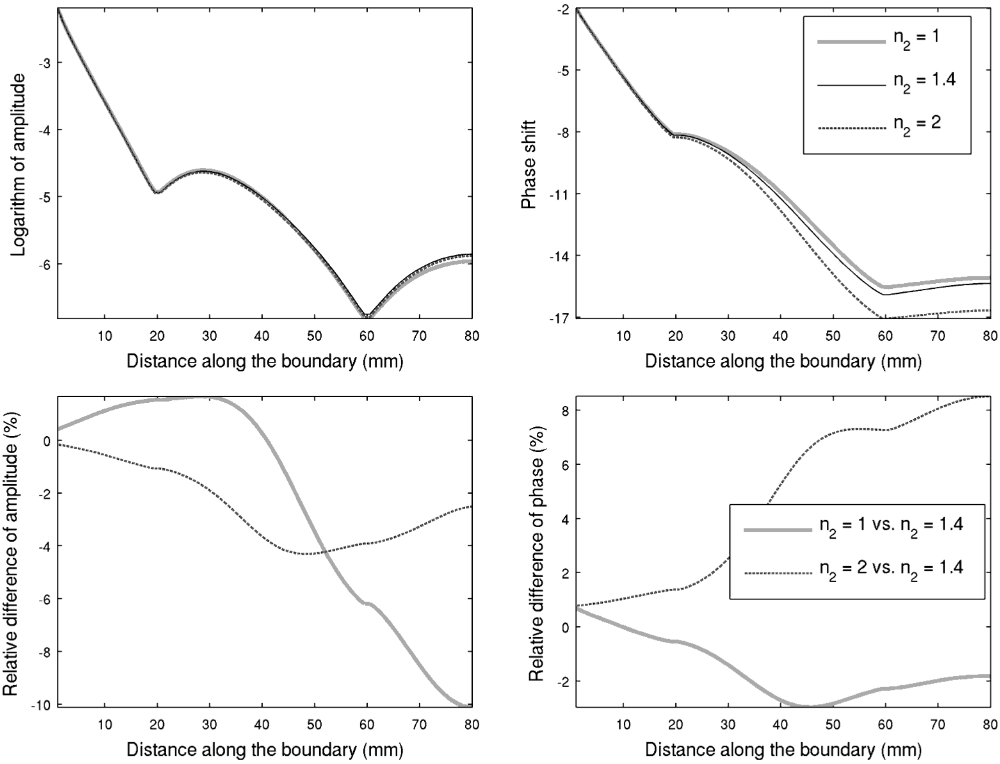

Figure 8: Logarithm of the amplitude (top left) and the phase shift (top right) of the fluence at the boundary computed using the cRTE model for $n_2 = 1$ (grey line), $n_2 = 1.4$ (black line) and $n_2 = 2$ (dashed line) as a function of distance along the boundary. Per cent relative difference of the amplitude (bottom left) and the phase shift (bottom right) against the case $n_2 = 1.4$ are shown on the bottom row.

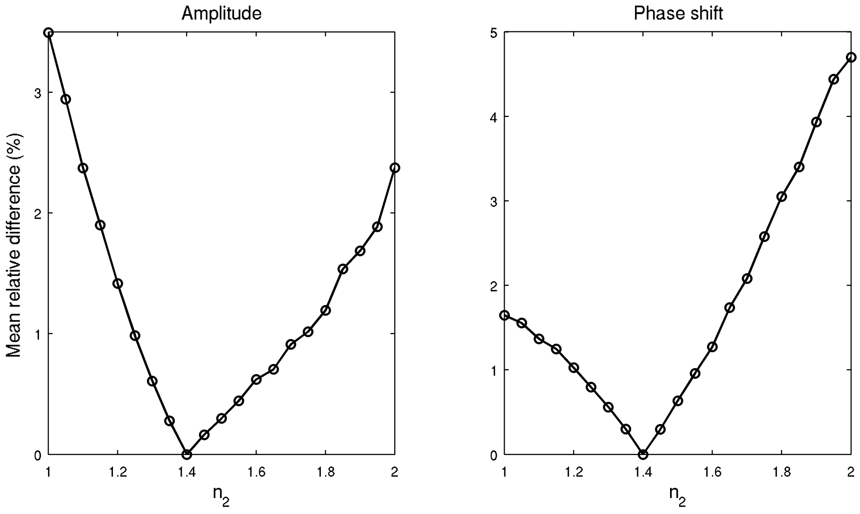

Figure 9: Mean per cent relative difference of the amplitude (left) and the phase shift (right) of the fluence at the boundary as a function of refractive index of the inclusion n_2.

4.2.2. Inclusion close to the boundary of the target

In the second case, the inclusion located close to the boundary of the target as shown in Figure 10. The number of spatial and angular nodes and elements were the same as before. In addition, the scattering and absorption properties were the same as in the first case in Section 4.2.1. Again, we set the refractive index of the background to $n_1 = 1.4$ and varied the refractive index of the layer n_2.

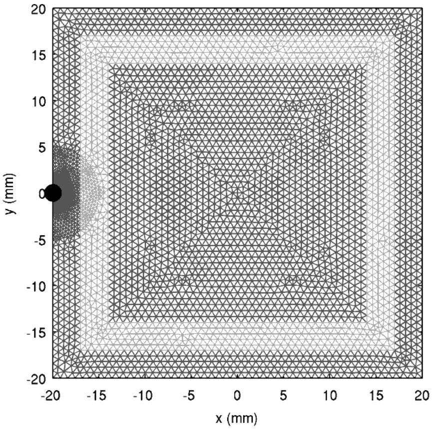

Figure 10: Mesh for the domain with a layer inclusion close to the boundary of the domain. The sub-domain Ω_1 is marked with dark grey and the sub-domain Ω_2 with light grey. The source is marked with a black circle.

The fluences computed using the cRTE and the MC are shown in Figure 11 for $n_2 = 1$ and for $n_2 = 2$. In addition, per cent relative error of the fluence computed using the cRTE is shown. Figure 12 shows the fluence at the boundary for $n_2 = 1$, $n_2 = 1.4$ and for $n_2 = 2$. The mean of the relative difference of the boundary measurements against the case with $n_2 = 1.4$ (matched refractive indices) is shown in Figure 13.

The results in Figure 11 show that for a smaller refractive index value ($n_2 = 1$) strong reflection occurs in front of the source when light enters the layer. As a result, a major portion of light remains between the layer and the boundary of the target. In addition, the part of the light which is transmitted through the layer in the front of the source gets reflected at the opposite side of the layer. Hence, some part of the light remains trapped inside the inner boundary of the layer. In contrast, for a larger refractive index ($n_2 = 2$) more light is transmitted into the layer and light propagates

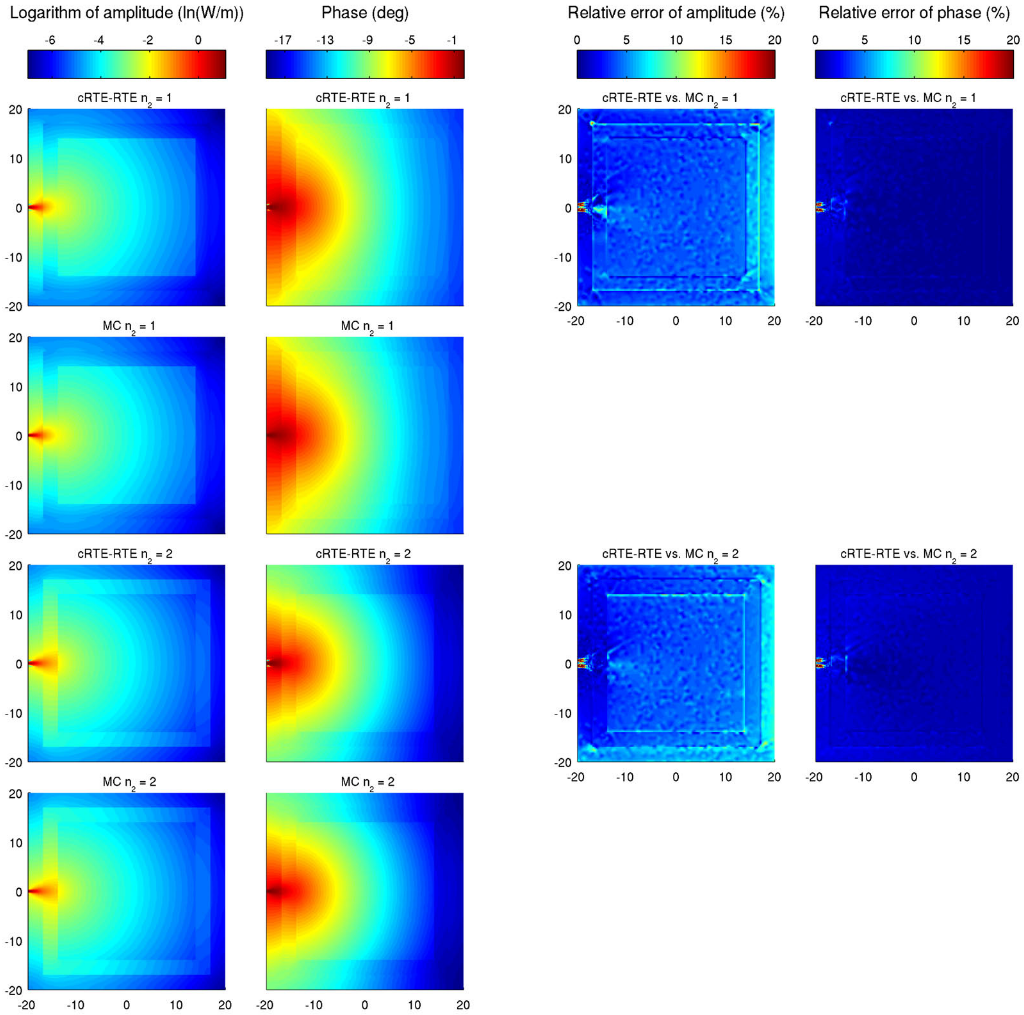

Figure 11: Logarithm of the amplitude (first column) and the phase shift (second column) of the fluence computed using the cRTE model (first and third row) and using the MC (second and fourth row) due to reflection from the layer inclusion close to the boundary of the target. Refractive index of the inclusion is $n_2 = 1$ (first and second row) and $n_2 = 2$ (third and fourth row). Per cent relative error of the amplitude and the phase shift against the MC are shown in third and fourth columns.

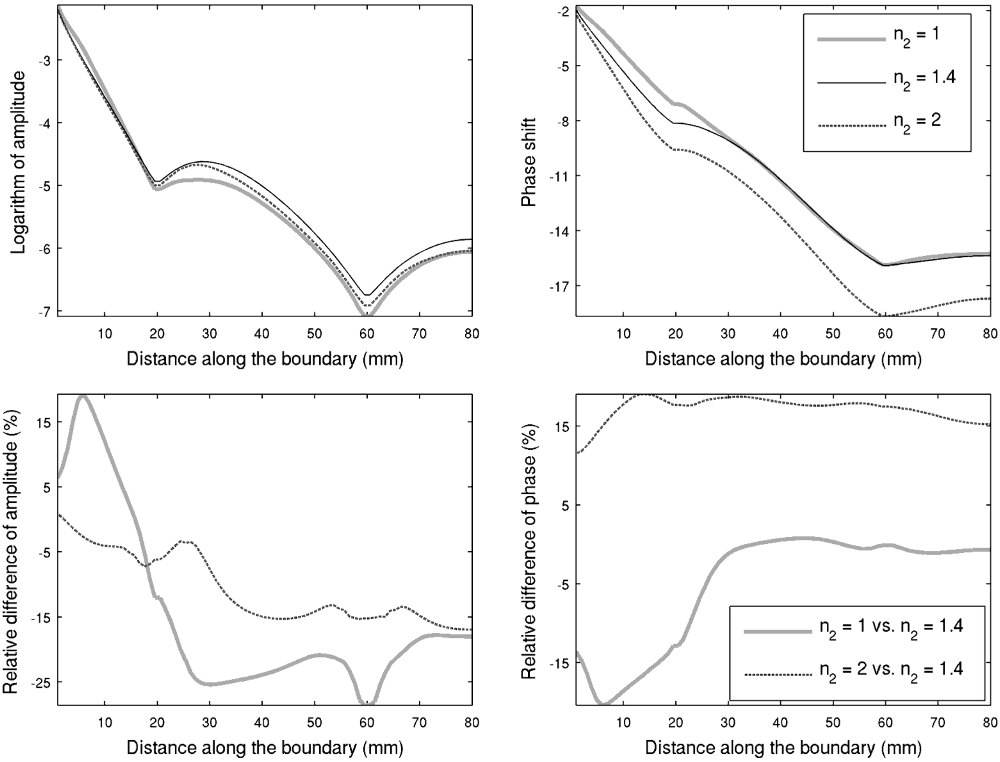

Figure 12: Logarithm of the amplitude (top left) and the phase shift (top right) of the fluence at the boundary computed using the cRTE model for $n_2 = 1$ (grey line), $n_2 = 1.4$ (black line) and $n_2 = 2$ (dashed line) as a function of distance along the boundary. Per cent relative difference of the amplitude (bottom left) and the phase shift (bottom right) against the case $n_2 = 1.4$ are shown on the bottom row.

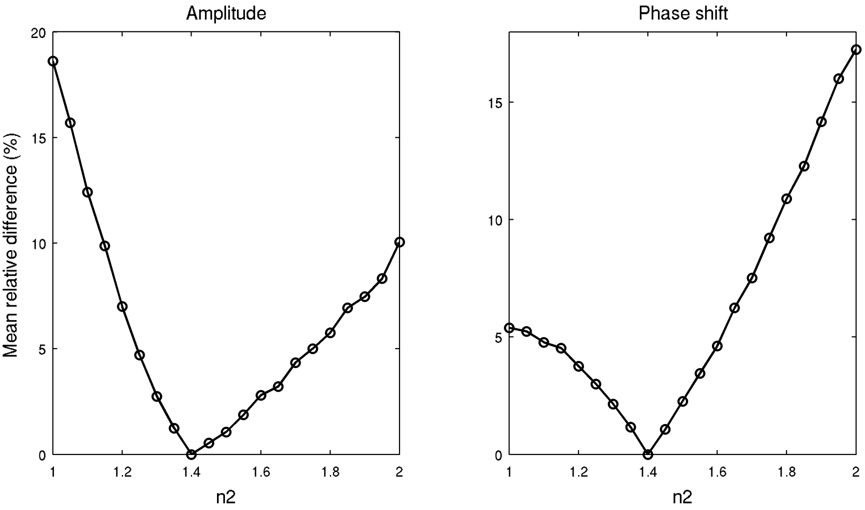

Figure 13: Mean per cent relative difference of the amplitude (left) and the phase shift (right) of the fluence at the boundary as a function of refractive index of the layer n_2.

along the layer. This is due the total internal reflection. The cRTE and the MC solutions agree relative well even though some differences can be seen at the right-hand side of the target between the layer and the boundary of the target.

The results in Figure 12 show that up to 15 % larger and 25 % smaller values can be measured for the amplitude next to the source and at the opposite side of the target, respectively, when the refractive index n_2 is smaller than the background in comparison to the fluences computed without the inclusion. For the phase, up to 15 % difference can be obtained. Based on the results it can be concluded that if the internal refractive index change occurs close to the boundary, significant changes in the boundary measurements can be obtained.

5. Conclusions

In this work, light propagation in a scattering medium with piece-wise constant refractive index using the radiative transport equation was studied. Light propagation in each sub-domain with a constant refractive index was modeled using the RTE and the equations were coupled using boundary conditions describing Fresnel reflection and transmission phenomenas on the interfaces between the sub-domains. The resulting coupled system of RTEs was numerically solved using the FEM. The proposed model was tested using simulations and was compared with the solution of the Monte Carlo method. The results show that the coupled RTE model describes light propagation accurately in comparison with the Monte Carlo method. In addition, results show that neglecting internal refractive index changes can lead to erroneous boundary measurements of scattered light. This indicates that the quality of the DOT reconstructions could possible be increased by incorporating a model for internal refractive index changes in the image reconstruction procedure.

Acknowledgments

The authors would like to thank Aki Pulkkinen for providing the Monte Carlo simulation solver. This work has been supported by the Academy of Finland (projects 136220, 140984, and 250215 Finnish Centre of Excellence in Inverse Problems Research), Finnish Doctoral Programme in Computational Sciences (FICS), Magnus Ehrnrooth foundation and by the strategic funding of the University of Eastern Finland.

References

[1] S. Chandrasekhar, Radiative transfer, Oxford University Press, London, 1950.

[2] K. Case, P. Zweifel, Linear transport theory, Addison-Wesley Educational Publishers Inc., US, 1967.

[3] A. Ishimaru, Wave Propagation and Scattering in Random Media (Academic, New York), IEEE Press, 1978.

[4] G. E. Thomas, K. Stamnes, Radiative transfer in the atmosphere and ocean, Cambridge University Press, 2002.

[5] G. B. Rybicki, A. P. Lightman, Radiative processes in astrophysics, John Wiley & Sons, 2008.

[6] E. E. Lewis, W. F. Miller, Computational methods of neutron transport, John Wiley and Sons, Inc., New York, NY, 1984.

[7] L. Wang, H. Wu, Biomedical optics: principles and imaging, Wiley-Blackwell, 2007.

[8] S. Arridge, Optical tomography in medical imaging, Inverse problems 15 (1999) 41–41.

[9] S. Arridge, J. Schotland, Optical tomography: forward and inverse problems, Inverse Problems 25 (2009) 123010.

[10] G. Bal, Inverse transport theory and applications, Inverse Problems 25 (2009) 053001 (48pp).

[11] S. Arridge, Methods in diffuse optical imaging, Philosophical Transactions of the Royal Society A: Mathematical, Physical and Engineering Sciences 369 (2011) 4558–4576.

[12] G. C. Pomraning, The equations of radiation hydrodynamics, Courier Dover Publications, 1973.

[13] H. Ferwerda, The radiative transfer equation for scattering media with a spatially varying refractive index, J. Opt. A: Pure Appl. Opt 1 (1999) L1–L2.

[14] J.-M. Tualle, E. Tinet, Derivation of the radiative transfer equation for scattering media with a spatially varying refractive index, Optics communications 228 (2003) 33–38.

[15] L. Martí-López, J. Bouza-Domínguez, J. Hebden, S. Arridge, R. Martín, Validity conditions for the radiative transfer equation, J. Opt. Soc. Am. A 20 (2003) 2046–2056.

[16] M. L. Shendeleva, Radiative transfer in a turbid medium with a varying refractive index: comment, J. Opt. Soc. Am. A 21 (2004) 2464–2467.

[17] M. Premaratne, E. Premaratne, A. J. Lowery, The photon transport equation for turbid biological media with spatially varying isotropic refractive index, Opt. Express 13 (2005) 389–399.

[18] L. Martí-López, J. Bouza-Domínguez, R. Martínez-Celorio, J. Hebden, An investigation of the ability of modified radiative transfer equations to accommodate laws of geometrical optics, Optics Communications 266 (2006) 44 – 49.

[19] G. Bal, Radiative transfer equations with varying refractive index: a mathematical perspective, J. Opt. Soc. Am. A 23 (2006) 1639–1644.

[20] J.-M. Tualle, Link between the laws of geometrical optics and the radiative transfer equation in media with a spatially varying refractive index, Optics Communications 281 (2008) 3631 – 3635.

[21] J. Boulanger, O. Balima, A. Charette, Refractive index imaging from radiative transfer equation-based reconstruction algorithm: Fundamentals, Journal of Quantitative Spectroscopy and Radiative Transfer 112 (2011) 1222 – 1228.

[22] J. Cassell, M. Williams, Radiation transport and internal reflection in a sphere, Journal of Quantitative Spectroscopy and Radiative Transfer 101 (2006) 16 – 28.

[23] J. Cassell, M. Williams, Radiation transport and internal reflection in a two region, turbid sphere, Journal of Quantitative Spectroscopy and Radiative Transfer 104 (2007) 400 – 427.

[24] Z. Jin, K. Stamnes, Radiative transfer in nonuniformly refracting layered media: atmosphere-ocean system, Applied optics 33 (1994) 431–442.

[25] R. Elaloufi, S. Arridge, R. Pierrat, R. Carminati, Light propagation in multilayered scattering media beyond the diffusive regime, Appl. Opt. 46 (2007) 2528–2539.

[26] R. Garcia, C. Siewert, A. Yacout, On the use of fresnel boundary and interface conditions in radiative-transfer calculations for multilayered media, Journal of Quantitative Spectroscopy and Radiative Transfer 109 (2008) 752 – 769.

[27] B. Bulgarelli, V. B. Kisselev, L. Roberti, Radiative transfer in the atmosphere-ocean system: the finite-element method, Applied optics 38 (1999) 1530–1542.

[28] K. G. Phillips, S. L. Jacques, Solution of transport equations in layered media with refractive index mismatch using the P_N-method, JOSA A 26 (2009) 2147–2162.

[29] O. Dorn, A transport-backtransport method for optical tomography, Inverse Problems 14 (1998) 1107–1130.

[30] A. Hielscher, R. Alcouffe, R. Barbour, Comparison of finite-difference transport and diffusion calculations for photon migration in homogeneous and heterogeneous tissues, Physics in Medicine and Biology 43 (1998) 1285–1302.

[31] J. Boulanger, A. Charette, Reconstruction optical spectroscopy using transient radiative transfer equation and pulsed laser: a numerical study, Journal of Quantitative Spectroscopy and Radiative Transfer 93 (2005) 325 – 336.

[32] G. Kanschat, A robust finite element discretization for radiative transfer problems with scattering, East West Journal of Numerical Mathematics 6 (1998) 265–272.

[33] G. Abdoulaev, A. Hielscher, Three-dimensional optical tomography with the equation of radiative transfer, Journal of Electronic Imaging 12 (2003) 594.

[34] T. Tarvainen, M. Vauhkonen, V. Kolehmainen, J. Kaipio, Hybrid radiative-transfer-diffusion model for optical tomography, Applied Optics 44 (2005) 876–886.

[35] H. Gao, H. Zhao, A fast-forward solver of radiative transfer equation, Transport Theory and Statistical Physics 38 (2009) 149–192.

[36] K. Ren, G. Abdoulaev, G. Bal, A. Hielscher, Algorithm for solving the equation of radiative transfer in the frequency domain, Optics Letters 29 (2004) 578–580.

[37] K. Ren, G. Bal, A. Hielscher, Frequency domain optical tomography based on the equation of radiative transfer, SIAM Journal on Scientific Computing 28 (2006) 1463–1489.

[38] F. Asllanaj, S. Fumeron, Applying a new computational method for biological tissue optics based on the time-dependent two-dimensional radiative transfer equation, Journal of Biomedical Optics 17 (2012) 075007–1–075007–11.

[39] J. Tervo, P. Kolmonen, M. Vauhkonen, L. M. Heikkinen, J. P. Kaipio, A finite-element model of electron transport in radiation therapy and a related inverse problem, Inverse Problems 15 (1999) 1345.

[40] E. Boman, J. Tervo, M. Vauhkonen, Modelling the transport of ionizing radiation using the finite element method, Physics in Medicine and Biology 50 (2005) 265–280.

[41] T. Tarvainen, V. Kolehmainen, S. R. Arridge, J. P. Kaipio, Image reconstruction in diffuse optical tomography using the coupled radiative transport-diffusion model, Journal of Quantitative Spectroscopy and Radiative Transfer 112 (2011) 2600–2608.

[42] E. Aydin, C. De Oliveira, A. Goddard, A comparison between transport and diffusion calculations using a finite element-spherical harmonics radiation transport method, Medical Physics 29 (2002) 2013.

[43] S. Wright, M. Schweiger, S. Arridge, Reconstruction in optical tomography using the pn approximations, Measurement Science and Technology 18 (2007) 79–86.

[44] P. S. Mohan, T. Tarvainen, M. Schweiger, A. Pulkkinen, S. R. Arridge, Variable order spherical harmonic expansion scheme for the radiative transport equation using finite elements, Journal of Computational Physics 230 (2011) 7364–7383.

[45] K. Grella, C. Schwab, Sparse tensor spherical harmonics approximation in radiative transfer, Journal of Computational Physics 230 (2011) 8452 – 8473.

[46] L. Henyey, J. Greenstein, Diffuse radiation in the Galaxy, The Astrophysics Journal 93 (1941) 70–83.

[47] T. Tarvainen, M. Vauhkonen, V. Kolehmainen, J. Kaipio, Finite element model for the coupled radiative transfer equation and diffusion approximation, International Journal for Numerical Methods in Engineering 65 (2006) 383–405.

[48] T. Tarvainen, M. Vauhkonen, V. Kolehmainen, S. Arridge, J. Kaipio, Coupled radiative transfer equation and diffusion approximation model

for photon migration in turbid medium with low-scattering and non-scattering regions, Physics in Medicine and Biology 50 (2005) 4913–4930.

[49] O. Lehtikangas, T. Tarvainen, A. Kim, Modeling boundary measurements of scattered light using the corrected diffusion approximation, Biomed. Opt. Express 3 (2012) 552–571.

[50] O. Lehtikangas, T. Tarvainen, Hybrid forward-peaked-scattering–diffusion approximations for light propagation in turbid media with low-scattering regions, Journal of Quantitative Spectroscopy and Radiative Transfer 116 (2013) 132–144.

[51] G. Arfken, H. Weber, H. Weber, Mathematical methods for physicists, Academic press New York, 1985.

[52] S. Richling, E. Meinköhn, N. Kryzhevoi, G. Kanschat, Radiative transfer with finite elements, Astronomy and Astrophysics 380 (2001) 776–788.

[53] S. Prahl, M. Keijzer, S. Jacques, A. Welch, A Monte Carlo model of light propagation in tissue, in: SPIE Proceedings of Dosimetry of Laser Radiation in Medicine and Biology, pp. 102–111.

[54] T. Tarvainen, V. Kolehmainen, A. Pulkkinen, M. Vauhkonen, M. Schweiger, S. Arridge, J. Kaipio, An approximation error approach for compensating for modelling errors in DOT, Inverse Problems 26 (2010) 015005.

OSSI LEHTIKANGAS

Approximations and Hybrid Models for Modeling Light Propagation in Biological Tissues

Diffuse optical tomography is a non-invasive biomedical imaging modality that is used to reconstruct images of the optical properties of tissues based on boundary measurements of transmitted near-infrared light. Reconstruction of the tomographic images requires an accurate and computationally feasible mathematical model for light propagation inside tissues. In this thesis, computational methods for modeling light propagation in tissue-like media are developed. These methods aim at reducing the computational load, and increasing the accuracy compared to the conventional methods.

UNIVERSITY OF
EASTERN FINLAND

PUBLICATIONS OF THE UNIVERSITY OF EASTERN FINLAND
Dissertations in Forestry and Natural Sciences

ISBN 978-952-61-1627-3